Lecture Notes in Civil Engineering

C. N. V. Satyanarayana Reddy
K. Muthukkumaran
Ravikiran Vaidya *Editors*

Stability of Slopes and Underground Excavations

Proceedings of Indian Geotechnical Conference 2020 Volume 3

Springer

Lecture Notes in Civil Engineering

Volume 185

Lecture Notes in Civil Engineering (LNCE) publishes the latest developments in Civil Engineering—quickly, informally and in top quality. Though original research reported in proceedings and post-proceedings represents the core of LNCE, edited volumes of exceptionally high quality and interest may also be considered for publication. Volumes published in LNCE embrace all aspects and subfields of, as well as new challenges in, Civil Engineering. Topics in the series include:

- Construction and Structural Mechanics
- Building Materials
- Concrete, Steel and Timber Structures
- Geotechnical Engineering
- Earthquake Engineering
- Coastal Engineering
- Ocean and Offshore Engineering; Ships and Floating Structures
- Hydraulics, Hydrology and Water Resources Engineering
- Environmental Engineering and Sustainability
- Structural Health and Monitoring
- Surveying and Geographical Information Systems
- Indoor Environments
- Transportation and Traffic
- Risk Analysis
- Safety and Security

To submit a proposal or request further information, please contact the appropriate Springer Editor:

– Pierpaolo Riva at pierpaolo.riva@springer.com (Europe and Americas);
– Swati Meherishi at swati.meherishi@springer.com (Asia - except China, and Australia, New Zealand);
– Wayne Hu at wayne.hu@springer.com (China).

All books in the series now indexed by Scopus and EI Compendex database!

More information about this series at https://link.springer.com/bookseries/15087

C. N. V. Satyanarayana Reddy ·
K. Muthukkumaran · Ravikiran Vaidya
Editors

Stability of Slopes and Underground Excavations

Proceedings of Indian Geotechnical Conference 2020 Volume 3

Springer

Editors
C. N. V. Satyanarayana Reddy
Geotechnical Engineering Division
Department of Civil Engineering
Andhra University College of Engineering
Visakhapatnam, Andhra Pradesh, India

K. Muthukkumaran
Geotechnical Engineering Division
Department of Civil Engineering
National Institute of Technology
Trichy, Tamil Nadu, India

Ravikiran Vaidya
Vadodara, India

ISSN 2366-2557 ISSN 2366-2565 (electronic)
Lecture Notes in Civil Engineering
ISBN 978-981-16-5600-2 ISBN 978-981-16-5601-9 (eBook)
https://doi.org/10.1007/978-981-16-5601-9

This Springer imprint is published by the registered company Springer Nature Singapore Pte Ltd.
The registered company address is: 152 Beach Road, #21-01/04 Gateway East, Singapore 189721, Singapore

Contents

About the Editors

Dr. C. N. V. Satyanarayana Reddy is a Professor of Civil Engineering at College of Engineering, Andhra University, Visakhapatnam, India, and has 28 years of teaching, research, and consultancy experience. His expertise and research interests are in the areas of reinforced soils, ground improvement, landfills, soil retention in excavations, deep foundations, and forensic geotechnical engineering. He obtained B.Tech. in Civil Engineering from Nagarjuna University, M.Tech. in Geotechnical Engineering from Indian Institute of Technology (IIT) Madras, M.E. (Structures) from Andhra University, and Ph.D. from National Institute of Technology (NIT) Warangal, India. He has guided 8 Ph.D. scholars and 92 M.Tech. dissertations. He has more than 110 publications in various national and international journals and seminars/conference proceedings. He has organized more than 30 seminars, workshops, and training programs. He is fellow of Indian Geotechnical Society, The Institution of Engineers (India) and Life member of Indian Roads Congress, Indian Concrete Institute, Indian Society for Technical Education, Indian Society for Rock Mechanics and tunneling Technology. He handled several research projects funded by DST, UGC and AICTE. He received the Engineer of the Year 2006 Award from Govt. of Andhra Pradesh and The Institution of Engineers (India) A.P. State Centre, Best Academician Award for the year 2014 from Andhra University and Andhra Pradesh Scientist Award 2020 in Civil Engineering Discipline from A.P. State Council of Science and Technology, Govt. of A.P. He served as National Executive Committee member of Indian Geotechnical Society during the period 2013-2020. He served as a member in H-4 Committee on Embankment, Ground Improvement and Drainage Committee of Indian Roads Congress (IRC) for the term 2018-2020. He is serving as member of TC 213 on "Scour and Erosion" of International Society for Soil mechanics and Geotechnical Engineering (ISSMGE).

Dr. K. Muthukkumaran is currently Professor of Civil Engineering at National Institute of Technology (NIT), Tiruchirappalli, India. He obtained his Ph.D. in Marine Geotechnical Engineering from Indian Institute Technology (IIT) Madras. He has published more than 120 papers in international and national journals and conferences. He has completed 5 R&D (including ISRO Chandrayaan-2 Mission project) &

50 major consultancy projects in geotechnical engineering and published two patents. Dr. Muthukkumaran's area of research is in geotechnical engineering, which includes pile foundation, soil–structure interaction, marine geotechnics & foundations, field instrumentation, geotechnical physical modeling, ground improvement, and forensic geotechnical engineering. He has received DST Young Scientist Award, IGS-Smt. Indra Joshi Biennial Award and Keynote Paper Award—GEOMATE Conference 2015 at Osaka, Japan. He has guided 8 PhD, 5 MS (by research) and more than 40 M.Tech. students in Geotechnical and allied research areas. He is a member of Technical Committee (TC-301 on "Preservation of Historic Sites") of International Society for Soil Mechanics and Geotechnical Engineering. He served as a member of IGS National Executive Committeeduring the period 2017-18. He has received DST Young Scientist Award, IGS- Smt. Indra Joshi Biennial Award and Keynote Paper Award – GEOMATE Conference 2015 at Osaka, Japan. He has received NIT Trichy Achiever Awards for research publications, research projects, maximum citation and consultancy projects. He is a recipient of Bharat Vikas Award -2018.

Mr. Ravikiran Vaidya is Principal Engineer and Founder of Geo Dynamics, a company involved in deep foundation testing. He has been instrumental in popularizing and pioneering various methods for deep foundation testing in India. It is to his credit that methods like high strain dynamic testing, integrity testing, sonic logging, etc., are now routinely used all over India to verify pile foundations and also form a part of all specifications of all major projects. He has recently worked on thermal integrity profiling for bored piles and indigenized the bidirectional load testing technology. He has written several technical papers on the subject, and his work has been cited by several authors in various articles and dissertations. He is also Guest Lecturer at academic and industry forums.

Prediction of Stability of an Infinite Slope Using Geospatial Techniques

Srirama Dinesh, Chirasmayee Savitha, and Arif Ali Baig Moghal

1 Introduction

Geospatial techniques comprise Remote Sensing, Photogrammetric, Geographical Information Systems (GIS), and Global Positioning Systems (GPS). They deal with acquisition, processing, storing, manipulating, storing, and disseminating spatial data. Remote sensing of the earth is a science and art of obtaining information about natural and artificial features. GIS refers to the analysis, capturing manipulating spatially related data. Photogrammetry refers to the acquisition processing of data using photographs. GPS refers to satellites positioned in space, which provides accurate and precise location information of the earth's features. Information collected from conventional and geospatial techniques can perform various spatial and temporal analyses of various land resources. Soil, one of the natural materials, has different properties and varies both spatially and temporally. Soil properties, index, and engineering properties help predict the soil's suitability as foundation and construction material. Engineering property, shear strength, is used to determine the slope's stability, bearing capacity, and the earth's pressure on one of the significant parameters, soil moisture.

Slope stability assumes a significant job in structural building, particularly in the design of expressways, railways, channels, surface mining, decline removal earth banks, and dams, just like numerous other human exercises, including construction

S. Dinesh (✉) · A. A. B. Moghal
Department of Civil Engineering, NIT, Warangal, Telangana 506004, India
e-mail: dinesh1991@student.nitw.ac.in

A. A. B. Moghal
e-mail: baig@nitw.ac.in

Present Address:
C. Savitha
Department of Civil Engineering, Vidya Jyothi Institute of Technology, Hyderabad 500075, India

C. N. V. Satyanarayana Reddy et al. (eds.), *Stability of Slopes and Underground Excavations*, Lecture Notes in Civil Engineering 185,
https://doi.org/10.1007/978-981-16-5601-9_1

and unearthing. Changes in external loads and pore water may cause slope failure and mass movement of the well-stabilized slopes [1]. Highway alignments, established along the hilly or mountainous terrain, taking or without considering hazard maps, are subjected to slope failures. The mass movement of soil succeeded by slope failure poses a high risk of damage to both lives and infrastructure. Quantitative and qualitative assessment of such mass movement of soil, its exact configuration, and spatial location is complicated to predict. However, depending on the in situ data and a few analytical postulates, quantitative assessments can be made. This quantitative examination decides the safety characteristics considering taking into account the causes that constitute the condition of strength and potential outcomes of the slopes to fail, regularly turned in a lead indicator called Factor of Safety (FOS). However, these assessments have a few limitations due to the difficulties in obtaining, checking, and processing large spatial and temporal data sets and varying soil moisture. With limited site investigation data and a lack of temporally varied data, useful slope failure analysis in mountainous areas, especially in mountainous urban areas, has become a paramount concern. With its potential and versatility for processing spatial data and temporal data, geospatial technologies have attracted significant attention to assessing soil and its properties. By establishing a statistical relationship between the slope stability and the factors influencing it and utilizing geospatial technologies in both acquisitions of spatial and temporal data and utilizing GIS, the FOS data can be created, assessed, and a map can be disseminated. The maps thus prepared help ease the planning of infrastructure before construction and indicate the possible failure zones or the risk-prone areas near the existing infrastructure.

In India, 15% of the area is prone to landslides [2]. Numerous landslides triggered by unusually high rainfall in India's Western Ghats regions caused widespread damage to property and life and resulted in 14.9% of landslides in the moderate slopes area in Karnataka state [3]. Considering the necessities and possibilities of geospatial techniques, the stability of an infinite slope was carried out near the Ballari area, which covers a part of National Highway 150A (NH 150A); a motorway in Karnataka state that connects Jewargi and Chamarajanagar employing the limit equilibrium method for the stability of an infinite slope is predicted. The infinite slope model used to calculate an FOS based on limit equilibrium analysis determines the balance between shear stress and shear strength. The necessary input parameters in developing the infinite slope model are (i) Cohesion, (ii) Angle of Shearing Resistance, (iii) Unit Weight of Soil, and (iv) Soil moisture. Soil water content is assessed from field observations; the estimations of these variables (c, φ, γ) are evaluated through the correlations. Digital Elevation Model (DEM) obtained from Cartosat-1 from Bhuvan is utilized in this study (Fig. 1).

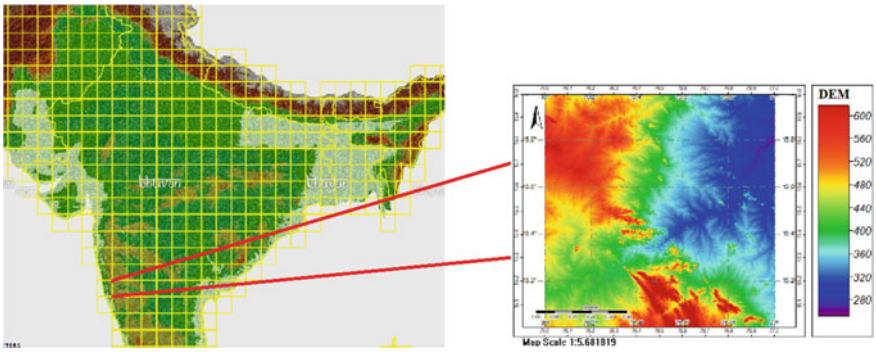

Fig.1 Cartosat Dem data from Bhuvan website

2 Objectives

The primary advance in this paper is by utilizing geospatial technologies to assess the sensitivity of the infinite slope over a spatial extent. To make the study achieve effectively, the explicit goals of this exploration are as follows:

1. Soil moisture maps to be prepared.
2. To determine the slope angle from Cartosat-1 DEM data.
3. Slope stability modeling using (i) Cohesion, (ii) Angle of Shearing Resistance, and (iii) Unit Weight of Soil.
4. To predict the Factor of Safety (FOS) of infinite slope from SAGA GIS.

3 Materials and Methods

3.1 Materials

Primary Data collected during field investigation, including satellite data and ancillary data, is used in this research. For satellite data, Cartosat-1 DEM was used. The Cartosat-1 Digital Elevation Model (CartoDEM) is a National DEM developed by the Indian Space Research Organization (ISRO), having a resolution of 2.5 m. The data extent was from 76–77°E and 15–16°N. However, the data was clipped further specific to the study area extent, i.e., 76.60–77°E and 15–15.32°N. The extent of NH150A obtained from urban land use and land cover map acquired from the Bhuvan website used in preparing a road network map for the study area is shown in Fig. 2. The extent of the NH150A, along with its terrain characteristics, is shown in Fig. 3.

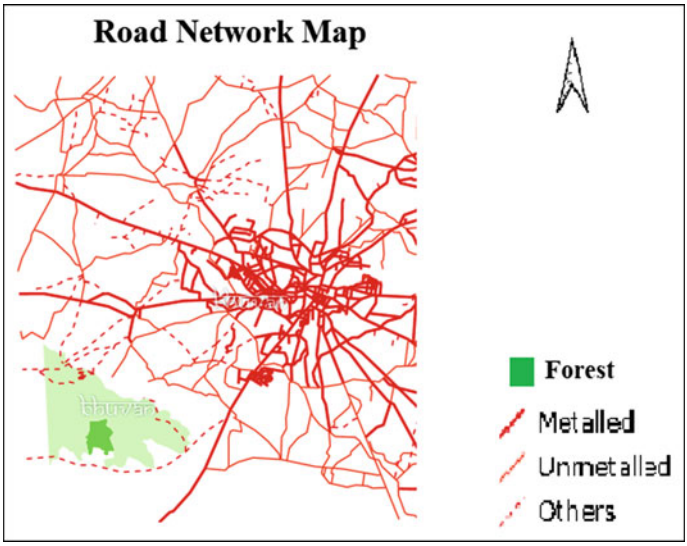

Fig.2 Overlaid map of the study area

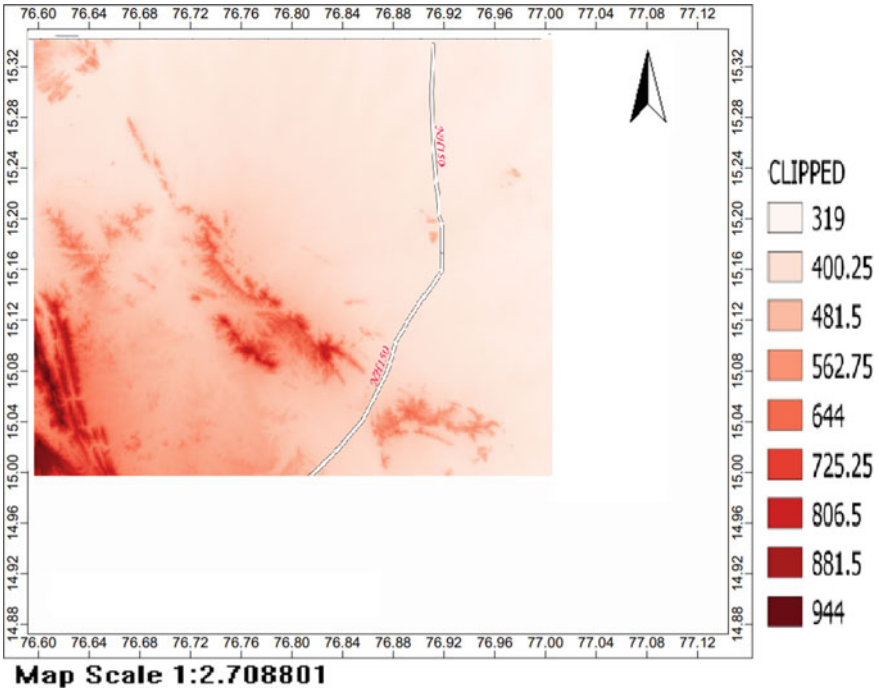

Fig.3 Topographic feature of the study area

3.2 Methods

3.2.1 Field Observation

Variables such as soil water content and soil samples of 20 selected points from the study region were obtained during the field investigation that was performed on Wednesday, January 2, 2019. Open-source software such as QGIS is used for mapping. SAGA GIS software is used for image processing.

3.2.2 Infinite Slope Stability Modeling

The slope's stability is a function of various parameters and depends on the soil geotechnical properties, land use land cover, and geological features. Frictional resistance of the soil is affected by the presence of water and pore water pressure. As the quantity of interstitial fluid rises, the soil weight increases, further destabilizing the slope. Evaluating the slope's stability using the infinite slope model provides simple equations for determining the Factor of Safety (FOS) with a surface of plane failure parallel to the slope surface. By adapting Factor of Safety (FOS) [4] for the hydrostatic condition used in this research for the infinite model, we get

$$\begin{aligned} \mathrm{FS} \;=\; & (\tan\phi/\tan\alpha) \;+\; (\mathrm{c}/(\gamma(\mathrm{D}-\mathrm{y}))\,(1/(\sin\alpha\cos\alpha)) \\ & +\; (\mathrm{y}/(\mathrm{D}-\mathrm{y}))(\gamma\omega/\gamma)\,(\tan\phi/\tan\alpha) \end{aligned} \tag{1}$$

where D assumed as 10 m is the height of soil from the water table, and y estimated to be a constant 2.5 m is the thickness of the slab, reflecting the average debris-flow thickness in the region of the study area [4] and recommended for a shallow landslide [5].

Considering the influence of geotechnical parameters alone on the stability of an infinite slope using limit state equilibrium condition and modeling in the QGIS software, an FOS map can be developed. The necessary input parameters in developing the infinite slope model are (i) Cohesion, (ii) Angle of Shearing Resistance, (iii) Unit Weight of Soil, and (iv) Slope Angle. Utilizing the relationship between the soil moisture (ω) and geotechnical parameters, adapted in [6, 7], the cohesion of the soil (c), angle of shearing resistance (ø), and unit weight of the soil (γ) for an infinite slope are determined from the QGIS model maker from the equations below.

(i) The cohesion of the soil (c in kPa):

$$c = -1.2009\omega^2 + 56.412\omega - 587.87 \tag{2}$$

(ii) Angle of shearing resistance:

$$\phi = 11212\omega^{-1.1929} \tag{3}$$

(iii) The unit weight of the soil (γ in kN/m^3):

$$Y = -0.1337\omega + 17.457 \tag{4}$$

The values thus obtained served as input parameters for determining the Factor of Safety.

4 Results

As shown in Fig. 4, the soil moisture map prepared from soil moisture measurements made at 11 points in the field serves as an essential input parameter to determine the (i) Cohesion, (ii) Angle of Shearing Resistance, and (iii) Unit Weight of Soil. Measurement of slope angle is made from Carosat-1 DEM data. Figure 5 presents the Factor of Safety Map for the entire study area. Each pixel in the image represents the value of FOS. It provides a quantitative sign of slope stability. A value of FOS = 1.0 indicates that the slope is at the verge of failure; under the current condition value of FOS, less than 1.0 points out that the slope is unstable, and a value of FOS greater than 1.0 points toward a stable slope [8]. Figure 5 explains the dependence of conditionally stable elements on the soil moisture within the elevation. The least

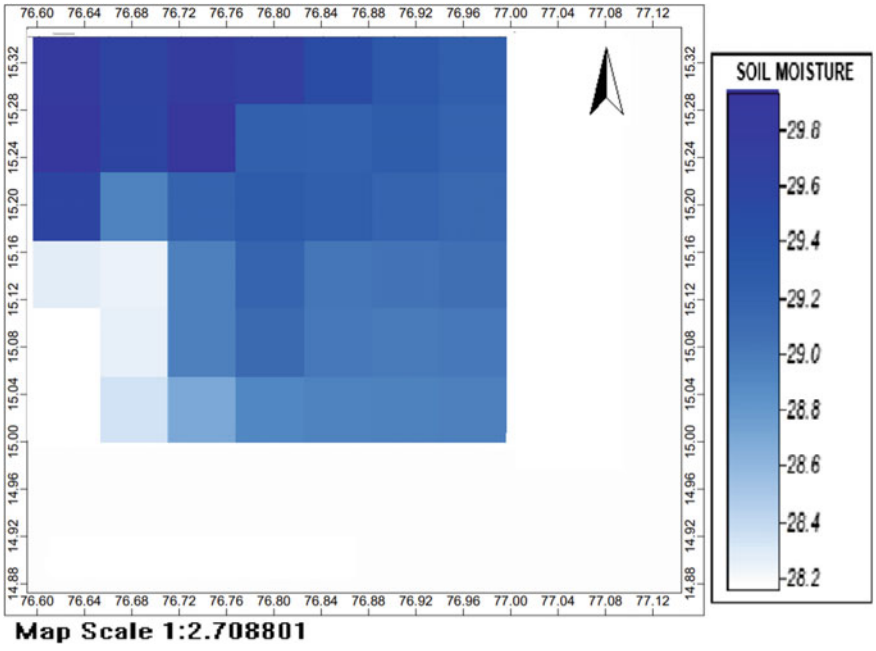

Fig. 4 Soil moisture mapped interpolated from field observations

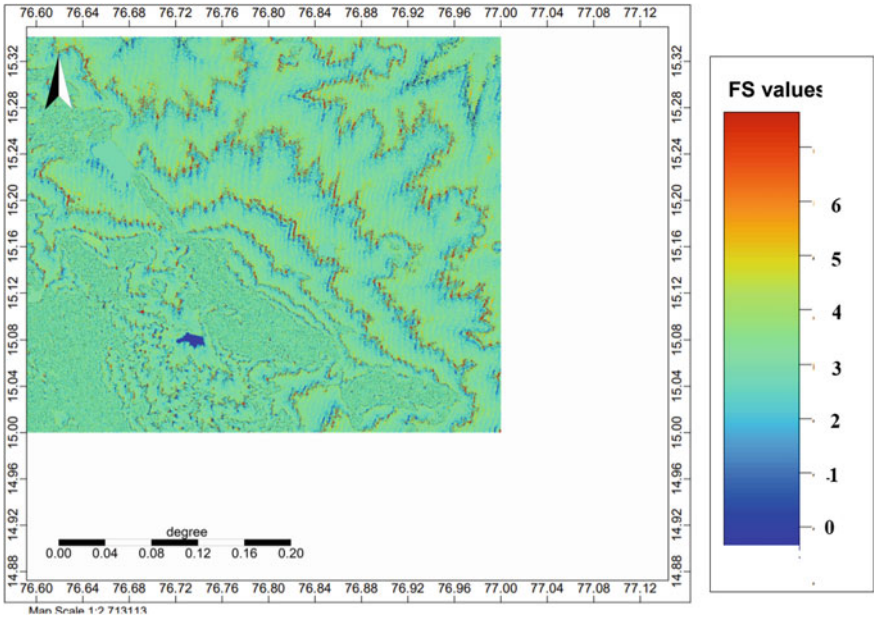

Fig. 5 Slope stability map depicting location of unstable slopes

factor of safety in the southwest part of the study area is attributed to forest cover having more soil moisture. Frictional resistance dependant on the soil moisture is least in the southwest region with high elevations. Further, the factor of safety values more significant than the one with the least slope failure is concentrated in regions with low soil moisture.

For validating the model, laboratory experiments were carried out. Table 1 shows the comparative analysis of soil parameters of 11 observation samples.

5 Conclusions

This paper presents the prediction of the infinite slope stability of NH150A across the Ballari region using geospatial techniques. The model created in QGIS estimates where a failure phenomenon could occur by simulating most geotechnical parameters and assessing its stability based on the infinite slope model. The application of geospatial techniques in predicting the stability of an infinite slope demonstrates the model's ability to perform according to input parameters and terrain topography; moreover, it highlights the strengths of the model that can be disseminated at the spatial extent. Soil moisture, one of the critical parameters, varies both spatially and temporally. Further enhancement of the model in predicting the stability of an infinite

Table 1 Comparative analysis of soil parameters

Borehole	Geospatial				Experimental		
	Soil moisture (%)	Cohesion (kPa)	Friction angle (°)	Unit weight (kN/m^3)	Cohesion (kPa)	Friction angle (°)	Unit weight (kN/m^3)
1	30	23.7	19.39	13.45	15.31	16.34	19.42
2	25	71.9	24.10	14.11	65.4	22.19	20.06
3	24.98	71.9	24.12	14.12	68.09	24.27	18.33
4	28	50.2	21.05	13.71	41.11	17.02	19.25
5	28.1	49.1	20.96	13.70	40.21	17.12	19.41
6	25.1	71.5	23.98	14.10	67.85	24.25	19.87
7	26.1	66.4	22.89	13.97	61.28	22.61	19.92
8	28.3	46.8	20.79	13.67	39.66	17.37	18.45
9	30.1	22.1	19.31	13.43	15.45	18.43	18.03
10	28.01	50.1	21.04	13.71	41.06	21.55	19.63
11	27.3	57.2	21.70	13.81	53.55	23.61	20.71

slope at the temporal scale from satellite-derived soil moisture data is possible using geospatial techniques. However, the accuracy and reliability of the model should be validated with the ground truth measurements. Natural soil moisture varies seasonally, and which in turn influences the stability of slopes, which need to be considered. The R^2 values of 0.991, 0.657, and 0.523 for c, φ, and γ, respectively, are found to be statistically significant. The proposed model has the ability to represent a visual and virtual geotechnical laboratory as correlations are arrived at using soil moisture with slope and geotechnical parameters.

References

1. Park, S., Kim, W., Lee, J., Baek, Y.: Case study on slope stability changes caused by earthquakes—focusing on Gyeongju 5.8 M_L EQ. Sustain. **10**, 3441 (2018)
2. Walde, S., Kale, K., Kundu, S., Nagaraj, P., Shelar, T., Shukla, VK.: GIS-based landslide susceptibility assessment of Malin area: a case study in the watershed India. In: 17th Esri India User Conference 2017, New Delhi (2017)
3. Martha, T.R., Roy, P., Khanna, K., Mrinalni, K., Vinod Kumar, K.: Landslides mapped using satellite data in the Western Ghats of India after excess rainfall during August 2018. Curr. Sci. **117**(5):804–812. (2019) https://doi.org/10.18520/cs/v117/i5/804-812
4. Rahardjo, H., Lim, T.T., Chang, M.F., Fredlund, D.G.: Shear-strength characteristics of a residual soil. Can. Geotech. J. **32**, 60–77 (1995)
5. Terlien, M.: The determination of statistical and deterministic hydrological landslide-triggering thresholds. Environ. Geol. **35**, 124–130 (1998)
6. Cocka, E., Erol, O., Armangil, F.: Effects of compaction moisture content on the shear strength of an unsaturated clay. Geotech. Geol. Eng. **22**, 285–297 (2004)

7. Omar, H., Ibrahim, A.L., Hashim, M.: Slope stability analysis using remote sensing data in department of remote sensing, faculty of geoinformation science and engineering. Universiti Teknologi Malaysia. Vol, Proceeding of AARS-ACR (2007)
8. Duncan, J.M., Wright, S.G.: Soil Strength and Slope Stability. Wiley, Hoboken, New Jersey (2005)
9. Dickson. Qin, Z., Karnieli, A., Berliner, P.: A mono-window algorithm for retrieving land surface temperature from landsat TM data and its application to the Israel–Egypt border region. Int. J. Remote. Sens. **22**(18), 3719–3746 (2001)
10. Raj, J.K.: Characterization of the weathering profile developed over porphyritic biotite granite in Peninsular Malaysia. Bull. Int. Assoc. Eng. Geol. Paris. **32**, 121–127 (1985)

Application of Bi-directional Extreme Learning Machine in Predicting Stability of Slope of Railway Embankment in Seismic Condition

Abidhan Bardhan, B. Dhilipkumar, Lakshmi Mulagala, and Pijush Samui

1 Introduction

Railway tracks are normally built on the natural ground surface or the elevated formation and the tracks are laid on a prepared bed called Permanent way, prepared either in cutting, filling of earthwork, or combination of both. Necessary longitudinal gradients and cross slopes are provided during the construction of the formation bed. The rails are attached to the sleeper with help of fasteners and the sleepers rest on a ballast cushion. All these elements together are called 'rail track system' and act as a single unit. In general, railway projects are carried out with large earthwork which leads to high initial expenditure during the course of the construction of permanent way. Therefore, for the safety of the entire system, a detailed analysis should be done before the track system comes into actual use.

Evaluation of slope stability is a challenging task for geotechnical engineers which is the most encountered problem in the transport network. The heterogeneous property of soil makes it difficult for engineers to assess reliability accurately. Nowadays, several methods are available to determine the slope stability of the embankment. These methods are of two types, i.e. deterministic or probabilistic [1–4]. Methods like the Strength reduction method (SRM), Limit equilibrium method (LEM), and Limit analysis method comes under deterministic type. The deterministic analysis is

A. Bardhan (✉) · B. Dhilipkumar · P. Samui
Department of Civil Engineering, National Institute of Technology Patna, Patna 800005, India
e-mail: abidhan@nitp.ac.in

P. Samui
e-mail: pijush@nitp.ac.in

L. Mulagala
Geotechnical Expert NK Consortium (NK-OC-JTC-NKI-QCI-RITES), PMC-DFCCIL, New Delhi, India
e-mail: m.lakshmi.p3@nkindia.in

C. N. V. Satyanarayana Reddy et al. (eds.), *Stability of Slopes and Underground Excavations*, Lecture Notes in Civil Engineering 185,
https://doi.org/10.1007/978-981-16-5601-9_2

based on the evaluation of the factor of safety which will determine the stability of the embankment. Among the various slip surfaces, the one which gives a minimum factor of safety is termed as a critical slip surface and the corresponding factor of safety is termed as a critical factor of safety. For the determination of the critical factor of safety, a trial and error approach is normally being used.

On the other hand, undesirable constituents such as pebbles, wastes, organic matter, etc. develop spatial variability within the soil and uncertainties in soil parameters, i.e. cohesion, internal friction, and unit weight. Because of these uncertainties involved, the deterministic methods have limitations in their application. Using the LEM, satisfactory results can only be obtained when the soil parameters are correctly accessed. Therefore, due to the complex and multi-factorial interactions between factors that affect slope stability, the task of assessment of slope stability remains a significant challenge for geotechnical engineers [5]. Considering these phenomena, this study implements a soft computing approach, i.e. Bi-Directional extreme learning machine (Bi-ELM) for the assessment of slope stability. The remainder of this paper is structured as follows including the Instruction section. In the next section, the methodological details of LEM techniques along with the employed soft computing techniques, i.e. ELM and Bi-ELM are furnished. This is followed by, discussion of the analysis of slope stability and results and discussion. At the end, a summary and conclusion is furnished.

2 Methodology

2.1 Conventional Analysis of Slopes

In the LEM technique, the factor of safety of slopes can be defined as the ratio between resistance and disturbance along a probable slope surface. Many available methods that are based on the method of slices [6] can be used to determine the factor of safety. For a typical slope given in Fig. 1, the factor of safety can be determined using the Bishop's simplified method given by

$$FOS = \frac{\sum_{i=1}^{n} [C_i \Delta x_i + (W_i - u_i \Delta x_i) \tan(\phi_i)] \frac{sec\alpha_i}{1+\tan(\phi_i)\tan(\alpha_i)/FOS}}{\sum_{i=1}^{n} (W_i \tan \alpha_i)} \quad (1)$$

where W_i are Δx_i are the weight and width of the ith slice, respectively, ϕ_i and C_i represent the angle of internal friction and cohesion, respectively, at the base of ith slice, u_i is the pore water pressure and α_i is the tangential angle, respectively, at the base of ith slice and n denotes the total number of the slice. To calculate the critical factor of safety, a trial and error method is used.

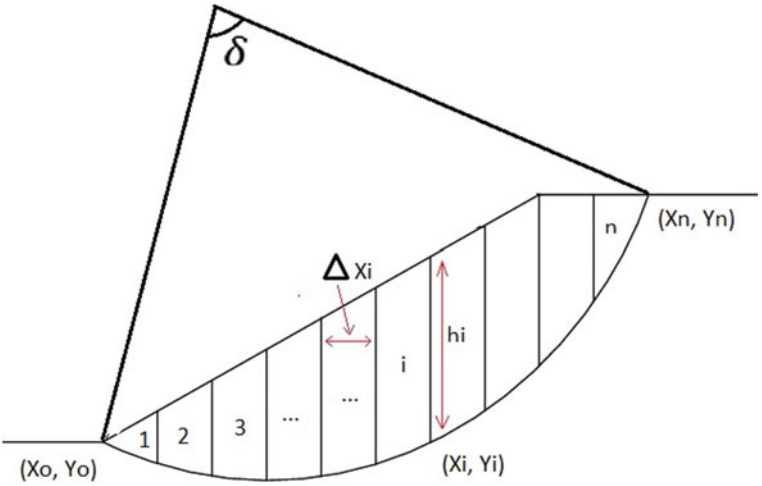

Fig. 1 Sectional details of a typical soil slope

2.2 Extreme Learning Machine

ELM, proposed by Huang et al. [5] is a type of single layer feed-forward network used in the classification and regression problem. During training, weights and biases are assigned at random and then the output weights are calculated with a defined number of the hidden layer neurons and activation function. Network structure of ELM is shown in Fig. 2 with a single hidden layer having 2 neurons.

Now, for example, a set with input $X_i = [X_{i1}, X_{i2}, X_{i3} \ldots .., X_{in}]^T \in \mathbb{R}^n$ and output $Y_i = [Y_{i1}, Y_{i2}, Y_{i3} \ldots .., Y_{im}]^T \in \mathbb{R}^m$ where $i = 1, 2, 3, \ldots ..p$, then the structure of the ELM can be mathematically expressed as

$$t_j = \sum_{k=1}^{p} \beta_k g\left(\mathrm{w}_k, b_k, z_j\right) \tag{2}$$

where w_k and b_k represent the input weight and biases of the kth hidden node, $z_j = \left[z_{ij}, z_{2j}, z_{3j} \ldots .., z_{nj}\right]^T$ is the output weight, $g(w_k, b_k, z_j)$ represents the output of the kth hidden node to the input of z_j, t_j represents the predicted output of the corresponding input z_j and j is the number of training samples. Right after the generation of input weight and biases randomly, ELM estimates β using the following expression:

$$\beta_{min} = ||H \times \beta - T|| \tag{3}$$

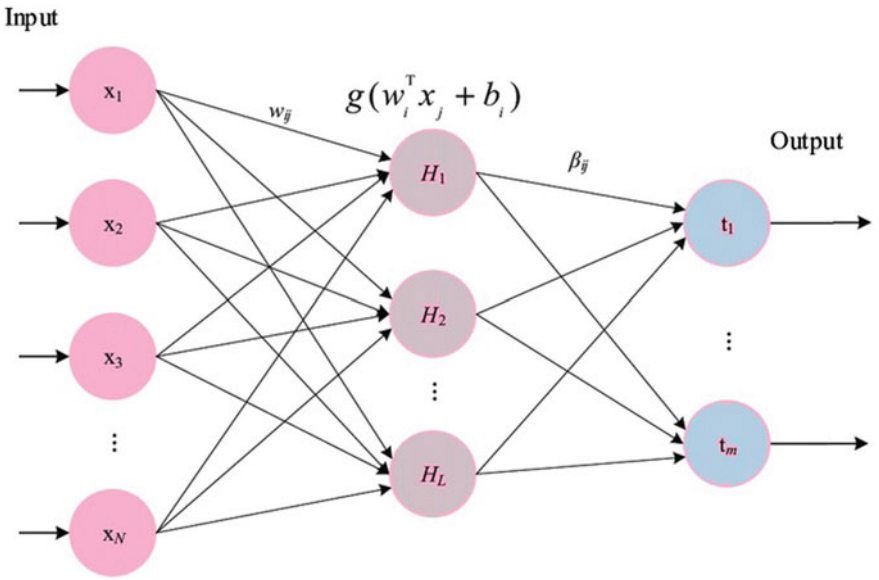

Fig. 2 A basic structure of ELMs

And, in the next step, the output weights are calculated using the linear equation given by

$$\beta_{min} = H * pinv(Y) \tag{4}$$

where H represents the output vector coming from the hidden layer and $pinv(Y)$ represents the Moore–Penrose pseudoinverse training data. The output vector can be written as

$$H = \begin{bmatrix} g(\mathrm{w}_1, b_1, x_1) & \cdots & g(\mathrm{w}_p, b_p, x_1) \\ \vdots & \ddots & \vdots \\ g(\mathrm{w}_1, b_1, x_q) & \ldots & g(\mathrm{w}_p, b_p, x_q) \end{bmatrix} \tag{5}$$

Lastly, the output weight from the hidden layer is used to get the desired output for a new set of data, i.e. testing data as follows:

$$Y_{i-new} = X_{i-new} * z_j \tag{6}$$

2.3 Bi-directional ELM

Although the structure of ELM seems simple and has much faster training speed than traditional tuning-based learning methods, but the selection of an optimum number of neurons in the hidden layer still remains an intractable challenge. Generally, the number of hidden neurons is predefined by the users and the trial and error approach has been followed to obtain the optimal no. of hidden neurons. Thus, this process can't always obtain the best network structure which likely causes under-fitting or over-fitting.

To avoid this problem, Yang et al. [7] proposed Bi-ELM, in which Yang divides the training operation into two parts. When the number of hidden nodes $L \in \{2n+1, n \in Z\}$, the hidden node parameter (ω_i,b_i) is generated randomly. When the number of hidden nodes $L \in \{2n, n \in Z$, the hidden node parameter ω_i, b_i is obtained as per the following expressions:

$$\widehat{\omega}2n = g^{-1}(u(H_{2n})) \cdot x^{-1} \tag{7}$$

$$\widehat{b}2n = \sqrt{mse\left(g^{-1}(u(H_{2n})) - \omega 2n \cdot x\right)} \tag{8}$$

$$\widehat{H}2n = u^{-1}\left(g^{-1}\omega 2n \cdot x + b2n\right) \tag{9}$$

where u^{-1} and g^{-1} indicate the inverse functions of u and g, respectively.

Several applications of Extreme Learning Machine are available in the literature [8–11] and researchers are using this technique in predicting the desired output in every field of engineering.

3 Slope Stability Analysis

As mention in the previous section, the limit equilibrium approach is used in this study in estimating the stability of slopes. To perform the analysis, 50 data sets are generated randomly considering the lower limit and upper limit of the soil parameter (Table 1) and then the slope stability analysis has been performed in SLOPE-W software separately for static as well as seismic conditions. A 12.293 m high embankment with 2H:1 V side slopes is considered in the analysis. The shear strength properties for different layers are presented in Fig. 3. The typical section of the proposed formation comprises of sleeper and ballast cushion (350 mm depth) at the top followed by a 600 mm thick blanket layer and which is underlaid by a 1000 mm thick prepared subgrade. The prepared subgrade is an integral part of the embankment fill of varying height.

Table 1 Statistical details of soil parameters for different layers

Parameters	Min	Max	Mean	Median	Std. error	Std. dev	Variance	Kurtosis	Skewness
γ_1	17.00	18.43	17.76	17.78	0.05	0.46	0.21	−1.47	−0.02
C_1	2.00	10.00	5.70	5.68	0.22	2.23	4.97	−1.09	0.08
ϕ_1	26.00	33.70	29.67	29.75	0.23	2.34	5.50	−1.26	0.07
γ_2	15.50	18.60	16.96	17.11	0.08	0.80	0.64	−0.83	−0.07
C_2	0.00	155.00	83.88	91.00	4.41	44.06	1941.52	−0.90	−0.37
ϕ_2	9.80	34.00	21.70	21.05	0.74	7.40	54.83	−1.18	0.12
γ_3	16.00	17.70	16.88	16.89	0.05	0.47	0.22	−1.10	−0.09
C_3	0.00	0.00	0.00	0.00	0.00	0.00	0.00	–	–
ϕ_3	27.00	31.00	28.99	28.96	0.10	1.03	1.05	−0.76	−0.03

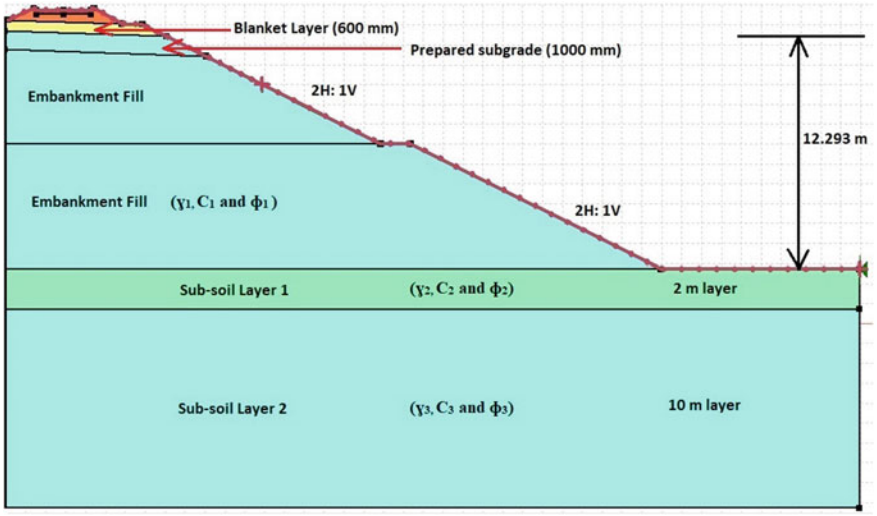

Fig. 3 Cross-sectional details of 12.293 m high embankment

For the embankment fill, the values of shear parameters considered as γ_1, C_1 and ϕ_1, for the sub-soil layer-1, it is γ_2, C_2 and ϕ_2 and for sub-soil layer-2, it is γ_3, C_3 and ϕ_3. The statistical details of the shear parameters of different layers considered in the analysis are given in Table 1.

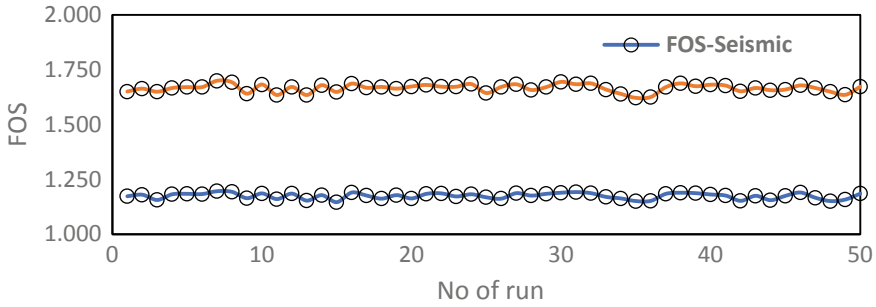

Fig. 4 Variation in FOS in static and seismic condition in different cases

4 Results and Discussion

4.1 Evaluation of FOS in Static and Seismic Conditions

The values of the factor of safety have been calculated in SLOPE-W software in static conditions as well as seismic conditions. To determine the factor of safety in seismic conditions, the values of co-efficient of ground acceleration k_h and k_v are considered as 0.16 and $0.08g$, respectively, for Zone III. The values of Z, I and S are taken as 0.16, 1.5 and 2.0. Figure 4 represents the variation of factor of safety for different values of cohesion, angle of internal friction and unit weight of soils. The values of the critical factor of safety in static and seismic conditions are obtained as 1.622 and 1.146, respectively. Figures 5 and 6 the critical failure surface, respectively, for static analysis and seismic-based analysis.

4.2 Assessment of Bi-directional ELM Model

Now, prior to the development of the model, the total dataset has been normalized between 0 and 1, and then divided into two portions, i.e. training and testing. In the training portion, 75% of the entire dataset has been selected randomly and the balance 25% of data is considered as a testing dataset. The training dataset is used to develop the Bi-ELM model, while the testing dataset is used to validate the developed model. Once the model is developed, the capability of the developed model is then assessed using five performance parameters, namely, Adjusted R^2 ($Adj.R^2$), mean absolute error (MAE), determination co-efficient (R^2), root mean square error ($RMSE$) and weighted mean absolute percentage error ($WMAPE$), which can be mathematically expressed as [12–15]:

$$Adj.R^2 = 1 - \frac{(n-1)}{(n-p-1)}(1-R^2) \tag{10}$$

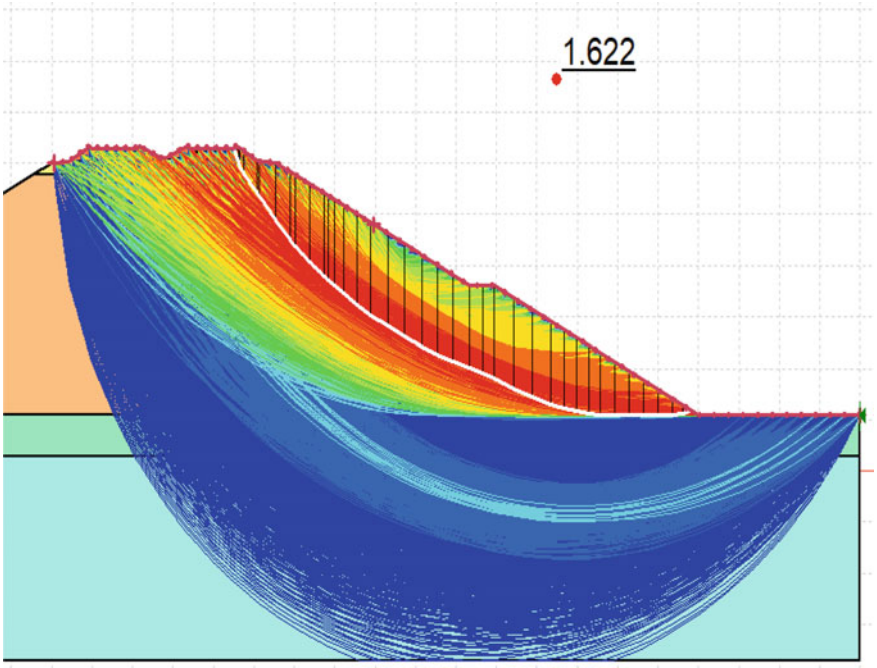

Fig. 5 Analysis of factor of safety in static condition showing all failure surface

$$MAE = \frac{1}{n}\sum_{i=1}^{n}\left|\left(\hat{y}_i - a_i\right)\right| \tag{11}$$

$$R^2 = \frac{\sum_{i=1}^{n}(a_i - a_{mean})^2 - \sum_{i=1}^{n}(a_i - p_i)^2}{\sum_{i=1}^{n}(a_i - a_{mean})^2} \tag{12}$$

$$RMSE = \sqrt{\frac{1}{n}\sum_{i=1}^{n}(a_i - p_i)^2} \tag{13}$$

$$WMAPE = \frac{\sum_{i=1}^{n}\left|\frac{a_i - p_i}{y_i}\right| \times a_i}{\sum_{i=1}^{n} a_i} \tag{14}$$

where a_i and p_i are the observed and predicted ith value, n is the number of samples in a dataset, a_{mean} is the mean of the observed values. For a perfect model, the value of these statistical parameters should be equal to their ideal value as $Adj.R^2 = 1$, $MAE = 0$, $R^2 = 1$, $RMSE = 0$ and $WMAPE = 0$.

Table 2 represents the details of performance parameters determined for the developed model in the training and testing phase. As can be seen, the values of all the performance parameters are quite close to their ideal value. The Bi-ELM model achieved 100% accuracy in terms of R^2 value ($R^2 = 0.9983$ i.e., 99.83%) in the

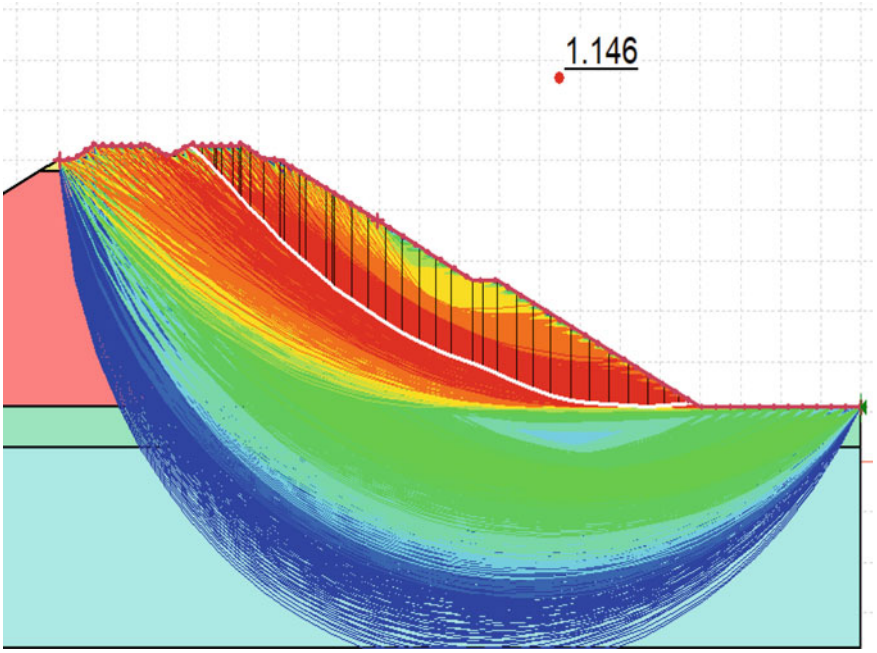

Fig. 6 Analysis of factor of safety in seismic condition showing all failure surface

Table 2 Performance parameters of the developed model in training and testing phase

Parameters	Bi-ELM (Training)	Bi-ELM (Testing)
Adj.R^2	0.9980	0.9971
MAE	0.0149	0.0150
R^2	0.9983	0.9983
RMSE	0.0184	0.0181
WMAPE	0.0312	0.0259

training phase as well as in the testing phase. Also, the values of MAE (0.0149 in training and 0.0150 in testing phase) and RMSE (0.0184 in the training and 0.0181 in the testing phase) show that the model has very good generalization capability in both the phase. It is also understood from the other performance parameters that the capability in predicting the factor of safety in the static as well as seismic conditions of the developed model is quite satisfactory (Fig. 7).

Also, the match between the actual and predicted values of the factor of safety is shown in Fig. 8 in the form of a scatter plot. As can be seen, all the values predicted by Bi-ELM lie on the line of the ideal model, and hence the developed Bi-ELM model can be considered as a perfect model to predict the factor of safety of any railway embankment provided that the wide range of data is available.

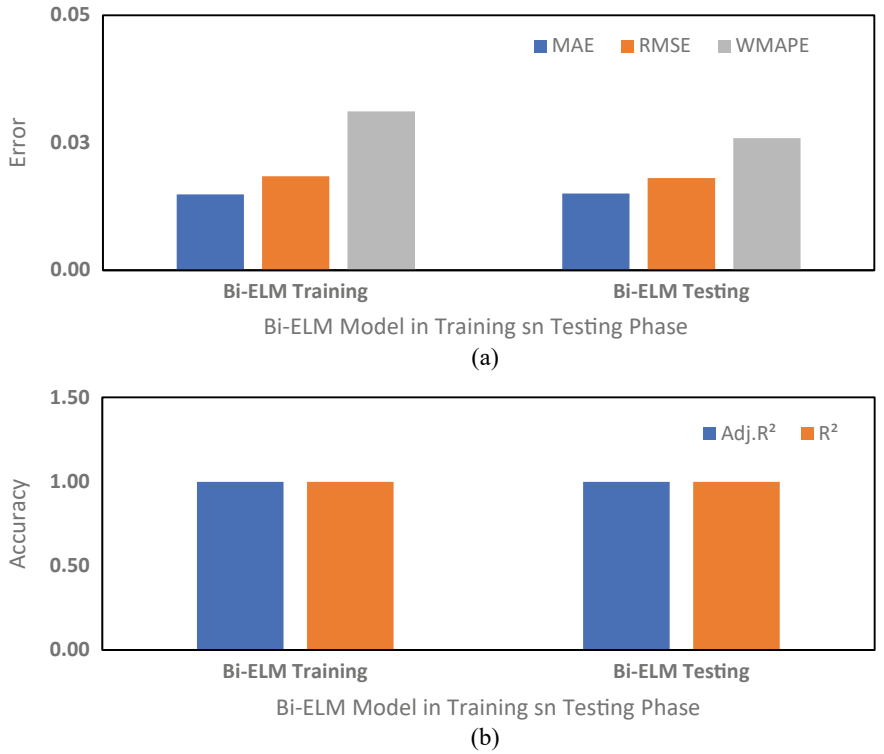

Fig. 7 Graphical representation of the performance of the Bi-ELM model Fig. **a** showing MAE, RMSE and WMAPE, and Fig. **b** showing Adj. R^2 and R^2

5 Summary and Conclusion

In this study, the authors developed a soft computing model, i.e. Bi-Directional Extreme Learning Machine to predict the slope stability of railway embankment. For this, the values of shear strength parameters of soils are generated randomly and considered in the analysis. A 12.293 m high embankment is considered with embankment fill, sub-soil layer-1 and sub-soil layer-2. Different values of cohesion, angle of internal friction and unit weight are considered for all three layers. A set of 50 data was generated randomly and assigned in each run to obtained the factor of safety in the static case as well as in the seismic case separately.

In the next stage, the values of $\gamma_1, C_1, \phi_1, \gamma_2, C_2, \phi_2 \gamma_3, C_3, \phi_3, k_h$ and *fos* is used to develop the soft computing model. However, prior to the development of the model, the entire dataset has been normalized between 0 and 1 and then divided into training and testing datasets. Right after the data partitioning, the training dataset is used to develop the Bi-ELM model. Later, the developed model is assessed in terms of performance parameters ($Adj.R^2$, MAE, R^2, $RMSE$ and WMAPE). It is

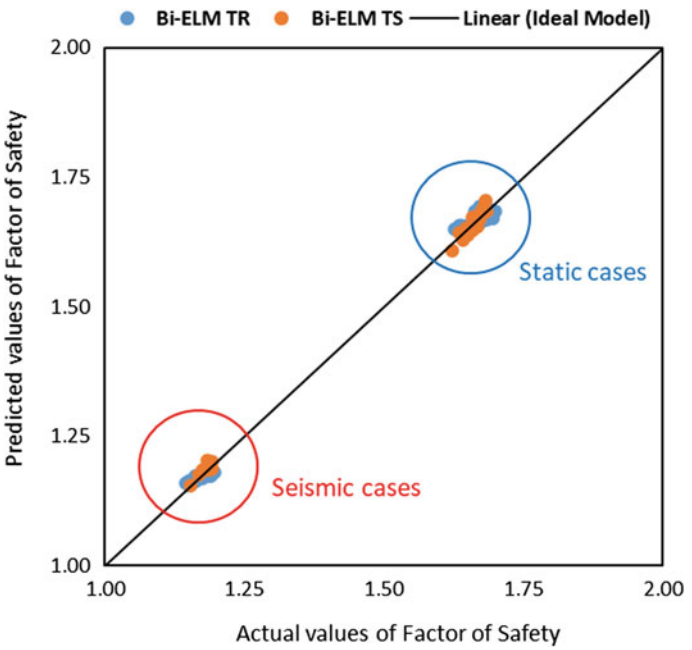

Fig.8 Scatter plot showing the match between actual and predicted values of factor safety

understood from the results of the performance parameters that the developed model is capable enough of predicting the factor of safety. Overall, the Bi-ELM model is highly recommended as an intelligent tool to assist the decision-making process for the assessment of slope stability.

References

1. Assefa, E., Lin, L.J., Sachpazis, C.I., Feng, D.H., Shu, S.X., Xu, X.: Slope stability evaluation for the new railway embankment using stochastic finite element and finite difference methods. Electron. J. Geotech. Eng. **22**, 51–79 (2017)
2. Cheng, Y.M., Lansivaara, T., Wei, W.B.: Two-dimensional slope stability analysis by limit equilibrium and strength reduction methods. Comput. Geotech. **34**(3), 137–150 (2007)
3. Reale, C., Xue, J., Pan, Z., Gavin, K.: Deterministic and probabilistic multi-modal analysis of slope stability. Comput. Geotech. **66**, 172–179 (2015)
4. Tran, C., Srokosz, P.: The idea of PGA stream computations for soil slope stability evaluation. Comptes Rendus Mécanique **338**(9), 499–509 (2010)
5. Huang, G.B., Zhu, Q.Y., Siew, C.K.: Extreme learning machine: theory and applications. Neurocomputing **70**(1–3), 489–501 (2006)
6. Bishop, A.W.: The use of the slip circle in the stability analysis of slopes. Geotechnique **5**(1), 7–17 (1955)
7. Yang, Y., Wang, Y., Yuan, X.: Bidirectional extreme learning machine for regression problem and its learning effectiveness. IEEE Trans. Neural Netw. Learn. Syst. **23**(9), 1498–1505 (2012)
8. Kumar, M., Samui, P.: Reliability analysis of pile foundation using ELM and MARS. Geotech. Geol. Eng. **37**(4), 3447–3457 (2019)
9. Mouyeaux, A., Carvajal, C., Bressolette, P., Peyras, L., Breul, P., Bacconnet, C.: Probabilistic stability analysis of an earth dam by stochastic finite element method based on field data. Comput. Geotech. **101**, 34–47 (2018)
10. Samui, P., Kim, D.: Minimax probability machine regression and extreme learning machine applied to compression index of marine clay (2017)
11. Samui, P., Kim, D., Jagan, J., Roy, S.S.: Determination of uplift capacity of suction caisson using Gaussian process regression, minimax probability machine regression and extreme learning machine. Iran. J. Sci. Technol., Trans. Civ. Eng. **43**(1), 651–657 (2019)
12. Raja, M.N.A., Shukla, S.K.: An extreme learning machine model for geosynthetic-reinforced sandy soil foundations. In: Proceedings of the Institution of Civil Engineers-Geotechnical Engineering, pp. 1–21 (2020)
13. Raja, M.N.A., Shukla, S.K.: Multivariate adaptive regression splines model for reinforced soil foundations. Geosynthetics Int. 1–23 (2021)
14. Raja, M.N.A., Shukla, S.K., Khan, M.U.A.: An intelligent approach for predicting the strength of geosyntheticreinforcedsubgrade soil. Int. J. Pavement Eng. 1–17 (2021)
15. Raja, M.N.A., Shukla, S.K.: Predicting the settlement of geosynthetic-reinforced soil foundations using evolutionary artificial intelligence technique. Geotext. Geomembr. (2021)

Risk Assessment and Early Warning System for Landslides in Himalayan Terrain

R. K. Panigrahi and Gaurav Dhiman

1 Introduction

Landslides hazards are the most occurring among the hydro geological hazards because the aftermath of landslides disaster is both in loss of life and property. The term landslides hazard is described by many authors among which the definitions given by Burton et al. [1], Varnes [2], Rezig et al. [3], and Guzzetti [4] are important. It also cause severe disruptions to the environment and large part of mountains area and in India most of the landslides occurrence has been seen in the hilly ranges of the country because these regions are both affected by landmass movement and anthropological activities. Some of the most devasting landslides has been seen in Himachal Pradesh, Maharashtra, Nagaland, West Bengal, Uttrakhand and Kerala (NDMA [5]). The development of new trends for landslides mitigation and remediation both depends upon the pros and cons of the existing methods of implementation. The following are the recent developments in the mitigation of landslides disasters.

2 Early Warning System for Landslides (LEWS)

Landslides are one of the most difficult disaster to predict because of the factors involved that affect slope stability vary in both space and time, but the advancement in the satellite imaging, mapping, and rainfall estimations have made it possible to develop a system to monitor the real time assessment of landslides hazards threat across the country. The Landslide Early Warning System (LEWS) is based on the type of landslides, the targeted geological area and the population under risk. The

R. K. Panigrahi (✉) · G. Dhiman
CSIR-Central Road Research Institute, New Delhi 110025, India

C. N. V. Satyanarayana Reddy et al. (eds.), *Stability of Slopes and Underground Excavations*, Lecture Notes in Civil Engineering 185,
https://doi.org/10.1007/978-981-16-5601-9_3

LEWS can be for a single landslides based on the movement sensor or for a large area using rainfall threshold and for a very large area based on the weather prediction. The LEWS subdivision consists of design, monitoring, forecasting, and education. The design of EWS is based on the geological knowledge of the area to be included in EWS. The recent developments in remote sensing and Geographical Information System (GIS) are being used in accessing landslide hazards (Pardeshi et al. [6]). The key factors that are to be considered while designing a EWS for landslides is (a) to know the vulnerabilities of the population at risk and (b) determining the geologic and meteorological settings and conditions that lead to landslides initiation. Monitoring in EWS refers to the installation of instrument and the analysis of data communication throughout the life of the EWS. The component forecasting is the core element in EWS system, as this component is very crucial to know the threshold of any type such as rainfall intensity, movement velocity, and mass movement (Nadim et al. [7]). Finally, education is very necessary to cover all the social and logistic issues that every EWS must consider to be people centric (Twigg [8]). The main objective of this component is to aware public with risk perception and to correct behaviors during landslides occurrence events to prevent damage or losses. The subdivision diagram for typical Landslide Early Warning System is shown in Fig. 1.

The block diagram of typically Landslide Early Warning System is shown in Fig. 2.

Besides the advancement in LEWS in India there are many shortcomings which are needed to overcome to provide a more productive and societal beneficial EWS which is both economic as well people centric. A well-illustrated and functional rainfall threshold model is not yet available in India due the missing corresponding daily/hourly rainfall data. Information on the time of landslides based on real time monitoring is still lacking in India. The existing network and technology are not sufficient to tackle landslide predictions, and there is a need of extensive research in the literature of EWS; the single EWS should be modified and used as multi-hazard EWS.

If the implementation of EWS is done without the consideration of the social aspects, in particular without considering the public response, this results in an incomplete EWS. There is also problem for installing the sensors because of the inaccessible locations and later maintenance problems. Another important issue is inclement weather such as high winds, low temperatures, snowfall, and rainfall, which may affect the sensors and/or the communication lines. Snow may block radar reflectors; heavy rainfall may cause leakages, rotting, or corrosion; high winds may destroy antennas, signs, or aerial cables (NDMA Report [5]).

3 Landslides Zonation Mapping

Landslide zoning is division of the hills or mountains with respect to their degree of slope susceptible to landslide hazard or risk. There are several methods of Landslide Hazard Zonation (LHZ) viz. heuristic, semi quantitative, quantitative, probabilistic, and multi-criteria decision making process. However, no one method is

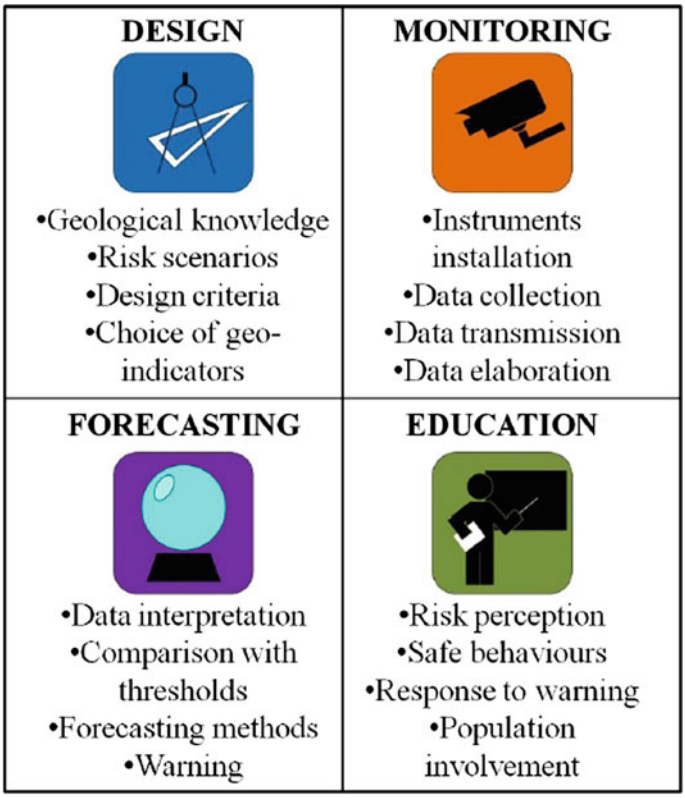

Fig.1 Subdivision of a generic EWS in four fundamental components

accepted universally for effective assessment of landslide hazards. The aim of zonation mapping is to provide a broad trend of landslides potential zones, and also if it is done at macro level, it can lead to concrete insight into the landslide hazards. A brief outline of different methods for LHZ is shown in Fig. 3 and are explained further.

Direct method

The direct method consists of geomorphological mapping where the earth scientist evaluates the direct relationship between the hazard and the environmental setting during the survey at the site of the hazard event.

Indirect method

The indirect methods include two different approaches, namely, the heuristic (knowledge driven) and statistical (data driven) techniques. To overcome the problem of the "hidden rules" in geomorphological mapping, heuristic approach has been developed based on factors influencing landslides, such as rock type, slope, landform, and land use.

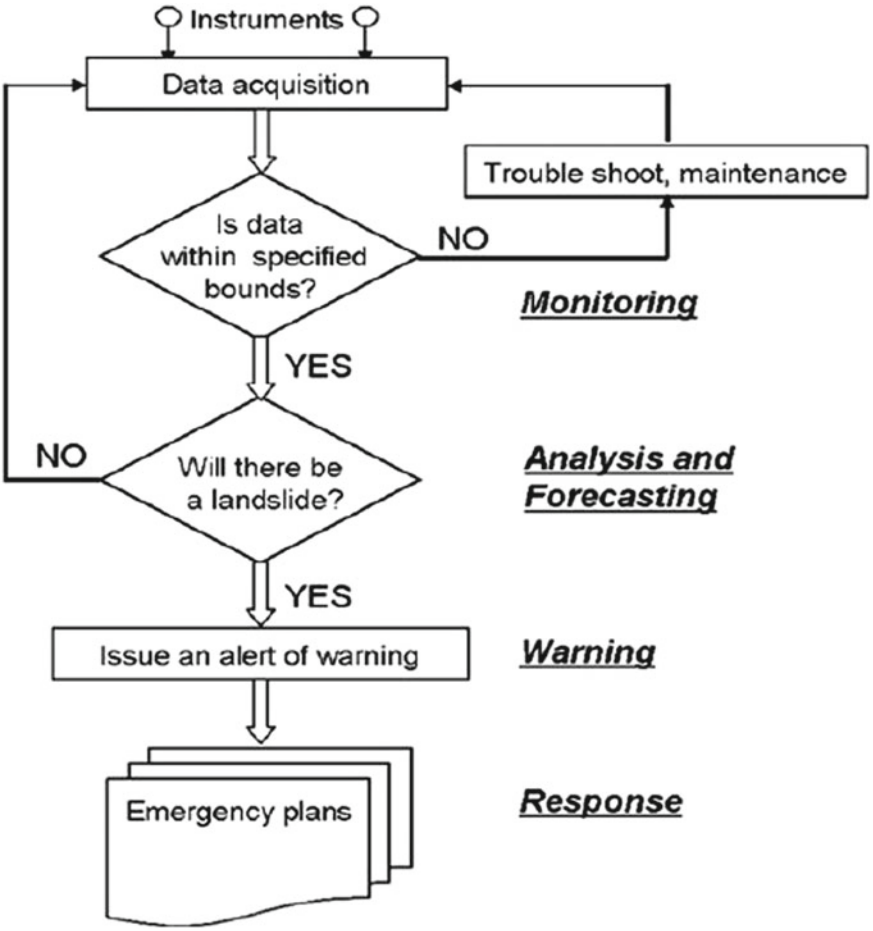

Fig. 2 Block diagram of a typical landslide early warning system DiBiagio and Kjekstad [9]

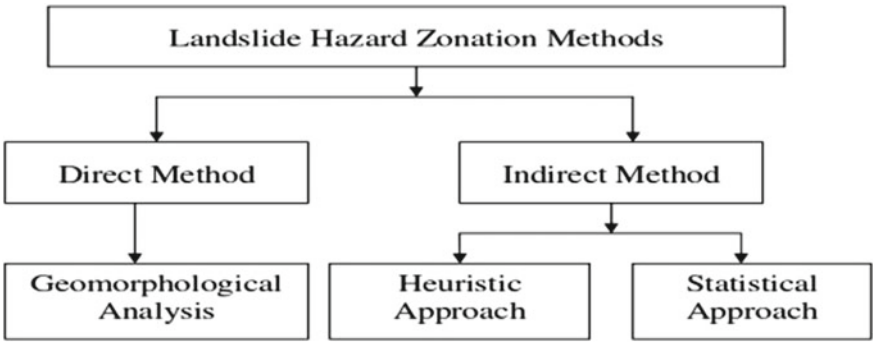

Fig. 3 Various approaches for LHZ

Table 1 Categories of slopes

Slope type	Slope angle	
1	Cliff	> 80°
2	Precipitous	50–80°
3	Very steep or steep	20–50°
4	Moderate	6–20°
5	Gentle slope	1–6°
6	Flat terrain	< 1°

Table 2 Various scales used in LZM (Landslide Zonation Mapping)

1	National scale	< 1:1000,000
2	Regional and synoptic scale	1:100,000–1:1000,000
3	Medium scale	1:25,000–1,50,000
4	Large scale	1:5,000–1:15,000

The categories of slope and the common scale used in LHZ maps is given below in Tables 1 and 2.

The assessment of hazard, vulnerability, and risk is a crucial element in landslide hazard. The following definition given by Varnes [2] is generally accepted.

Natural Hazard (H): The probability of occurrence of a potentially damaging phenomenon within a specified period of time and within a given area.

Vulnerability (V): The degree of loss to a given element or set of elements at risk resulting from the occurrence of a natural phenomenon of a given magnitude. It is expressed on a scale from 0 (no damage) to 1 (total loss).

Specific Risk (Rs): The expected degree of loss due to a particular natural phenomenon. It may be expressed by the product of H and V.

Element at Risk (E): The population, properties, economic activities, including public service, etc., at risk in a given area.

Total Risk (Rt): The expected number of lives lost, persons injured, damage to property, or disruption of economic activity due to a particular natural phenomenon. It is therefore the product of specific risk (Rs) and elements at risk (E) which gives the total risk as given in the Eq. (1.1).

$$\mathrm{Rt} = \mathrm{E}\,(*)(\,\mathrm{Rs}) = \mathrm{E}\,(*)(\,\mathrm{H} * \mathrm{V}) \tag{1}$$

The landslide zoning is further divided into following subtypes.

3.1 Landslide Susceptibility Zoning (LSZ)

This type of zoning is done after studying the past landslides that occurred in that area following to future prediction of susceptible areas and likelihood of landslides in future. The LSZ maps are formed after critically studying the topography, geology, geotechnical properties, and climate of the vulnerable area. It also focus to study vegetation and anthropogenic factors such as development and clearing of vegetation.

3.2 Landslide Risk Zoning (LRZ)

The LRZ maps are created for planning and allocation of resources before occurrence of landslides. In the recent developments the landslide hazard zonation mapping for a small area using a hazard evaluation factor rating scheme was done by S. Sarkar et al. [10] which divides the zone into two classes, viz. high hazard zones and high frequency of landslides. The macro hazards maps prepared using LHEF techniques have predicted landslide hazards little better than SRZ subjective regional zonation and ORZ objective regional zonation maps. The MHZ maps are shown below in Fig. 3, and the hazard classes for MHZ maps are shown in Table 3 and (Fig 4).

LHZ maps are very useful in identifying delineate unstable hazard prone areas and to choose favorable locations for sitting development schemes. But besides several applications landslide zonation mapping in India is still lacking in giving complete use of them because of the various reasons such as only LSZ maps are mostly available in India; the maps are not available for states wise/district wise, northeastern states, and eastern and western Ghats. Most of the LSZ maps are prepared with 1:50,000 scale only. Most of the LSZ maps are lacking in incorporating the details of past landslides details, and active landslide zones of smaller dimensions having sizes of 50×50 m appear as a dot (1×1 mm) on 1:50,000 scale map. Existing LHM maps do not address the crucial aspects of overloading and or under cutting of hill slope due to anthropogenic activities and, therefore, provide no clear guidelines for removal of those manmade constructions in particular which are overloading or undercutting the hill slope or blocking, diverting or narrowing the natural drainage courses.

Table 3 Landslide density of hazard classes for MHZ Map

Hazard class	Area (km^2)	Number of landslides	Landslide density
Very low	4.54	0	0.00
Low	15.64	2	0.13
Moderate	27.62	20	0.72
High	19.78	23	1.16
Very high	10.42	14	1.34

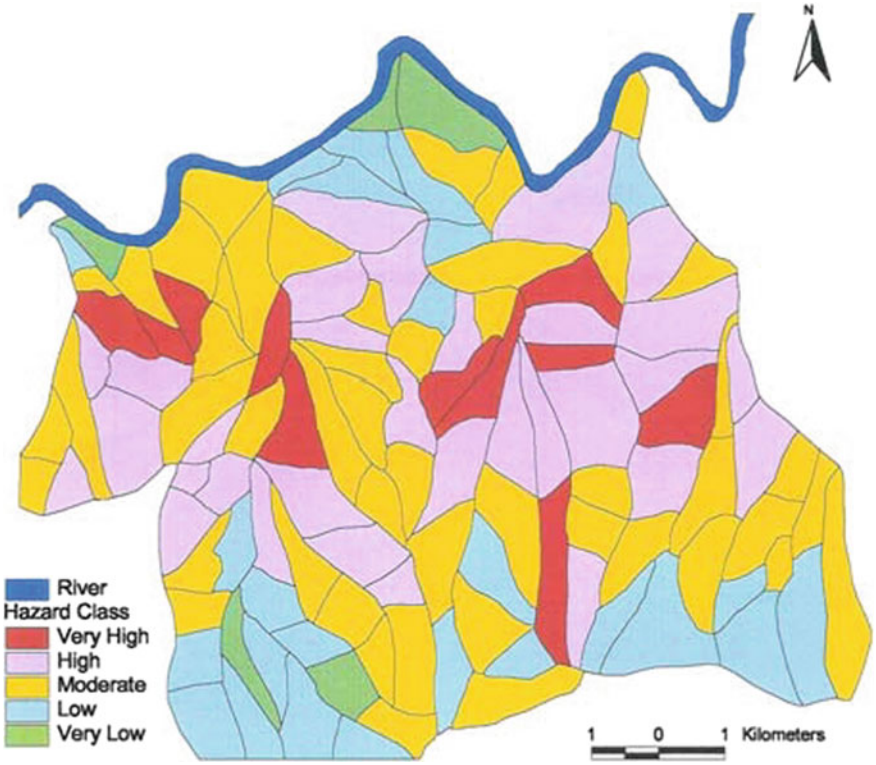

Fig. 4 MHZ Map using LHEF factor technique

The improvements needed in landslides zonation should focus on Preliminary to intermediate level risk zoning for local areas and the advanced stages of planning for large engineering structures, roads and railways Detailed (Site specific zoning) > 5,000 1–10 km^2 • Intermediate and advanced level hazard and risk zoning for local and site-specific areas and for the design phase of large engineering structures, roads and railways. The landslide hazard mapping techniques are so many, but the selection of method should be based on the scale of mapping, data availability, and nature of hazards.

4 Mountains Zones Regulations

In India the hilly regions are vulnerable to landslides and this results in loss of property, lives, and economy. The wide study of these natural disasters shows that the construction plans are ill implemented and do not follow standard norms. The cities of the Himalayas are growing and beginning to turn into the mountains of garbage and plastic, untreated sewage, chronic water shortages, unplanned urban growth,

and even local air pollution because of vehicles (NDMA report [5]). There is need to formulate new policies or improvement of existing methods of construction and strict adherence to the construction norms. There should be use of bio engineering methods in the landslides affected areas. There is a need of making strategies for utilization of land use in these areas. The existing building bye laws and construction methods used in these areas are needed to improvement considering the present scenario.

5 Existing Methods of Landslide Remediation and Mitigation

The designing of landslide remedial measure is done after studying field investigation data and cause of landslide. The remedial measures are broadly classified into three main categories.

(a) Reinforcement measures

This type of remedial measure consists of Earth Reinforcing structures which involve insertion of tensile resisting materials such as steels rods, metal strips, geosynthetics of cloths and steel angles into the soil to improve stability. Soil nailing is also a reinforcement technique in which closely spaced parallel steels bars are installed into the face of a slope or vertical cut to improve stability. This technique consists of improving the soil resistance to failure and to deformation by the inclusion of elements which are resistant to tensile, compressive shear, and/or bending forces. Reinforcement remedial measures are widely used because of flexibility, ease of construction and are inexpensive as compared to large retaining walls but these methods have limitations such as soil nailing technique has to occur above ground-water level and away from seepage location. Also, the surface runoff water should also be intercepted before reaching a soil nailed wall, and any collected water should be disposed of rapidly.

(b) Retaining structures

The restraining structures such as gravity walls, cantilever walls, tied back walls, sausage walls, and mass gravity Gabion walls are designed to retain rock/soil and are generally economically cheaper as compared to other categories of remedial measures but have numerous drawbacks such as water drainage problem in sausage walls, base sliding failure in concrete gravity walls, need of bearing surface in case of anchored walls, etc. (Panigrahi and Dhiman [11]).

(c) Surface—sub surface drainage measures

Drainage measures which are most effective in the geological condition which allow interference with natural water regime.

(d) Bio-Engineering remedial measures

Bioengineering techniques are useful approaches to prevent landslides as they improve slope stability and maintain ecological balance. They are mostly suitable to be deployed in developing countries because of their cost effectiveness and environmentally friendly nature. The effectiveness of Bio-Engineering technique further depends upon the survival and growth rate of plants.

6 Conclusions

The risk assessment of landslides in predicting the occurrence of hazard is very critical task in landslide mitigation and remediation. Landslides are influenced by several preparatory and triggering factors which vary significantly from region to region. The paper provides a substantial contribution in knowing the latest trends in EWS and improvement of existing methods which will lead to developments of new standards. The EWS are becoming one the main pillars of hazard prevention in areas where mitigation strategies are not up to the mark. The modern sensor networks, like ad hoc wireless sensor networks, have the advantage over currently existing landslide monitoring systems that they can be used as very variable and the installation is quite simple. The advancements in geo-spatial technologies have opened the doors for detailed and accurate assessment of landslide. The accuracy of the LHZ maps is improved with the use of high resolution satellite data combined with GIS. The LHZ maps if are prepared with accuracy can result in designing cost effective methods such as bio-engineering (grass plantation, shrubs plantation, and tree plantation) in conjunction with small civil engineering structures. It is also concluded that the mitigation approach in landslide hazards is much more cost effective than construction cost. The use of improved methods of EWS, LHZ, and improved mountainous areas policies will help in delineating the hazards caused by landslides in a concrete manner.

Acknowledgements Author is grateful to Director, Central Road Research Institute, New Delhi, for his kind permission to publish this paper.

References

1. Burton, I., Kates, R., White, G.: The environment as hazard. Oxford University Press, New York (1978)
2. Varnes, D.: Landslide hazard zonation: a review of principles and practice, pp. 1–6. United Nations Scientific and Cultural Organization, Paris (1984)
3. Rezig, S., Favre, J., Leroi, E.: The probabilistic evaluation of landslide risk. In: Sennset (ed) Landslides. Rotterdam, Balkema, pp. 351–355. (1996)

4. Guzzetti, F.: Landslide Hazard Assessment and Risk Evaluation: Limits and Perspectives. In: Proceedings of the 4th EGS Plinius Conference held at Mallorca, Spain, pp. 1–4. University de les Illes Balears, Spain. (2003)
5. NDMA Report.: National Landslides Risk Management Strategy Report (2019)
6. Pardeshi, S.D., Autade, S.E., Pardeshi, S.S.: Landslide hazard assessment: recent trends and techniques. SpringerPlus (2013)
7. Intrieri, E., Gigli, G., Casagli, N., Nadim, F.: Landslide Early Warning System: toolbox and general concepts. Nat. Hazards Earth Syst. Sci. **13**, 85–90 (2013)
8. Twigg, J.: Disaster early warning systems: people, politics and economics, benfield hazard research centre disaster studies. Working Paper, No. 16 pp. 1–4 (2006)
9. DiBiagio, E., Kjekstad, O.: Early warning, instrumentation and monitoring landslides. In: Proceedings of the 2nd Regional Training Course, RECLAIM II, 29th January– 3rd February 2007 2007.
10. Sarkar, S., Anbalagan, R.: Landslides hazards zonation mapping and comparative analysis of hazard zonation maps. J. Mount. Sci. (2008)
11. Panigrahi, R.K., Dhiman, G.: Critical review of different types of remedial measures for landslides. Indian Highways J Indian Road Cong New Delhi **10**(3), 38–45 (2020)

Numerical Analysis of the Stability of Soil Slope Subjected to Rainwater Infiltration

H. R. Bhanuprakash and Adarsh S. Chatra

1 Introduction

Slope failures and landslides are some of the major geological processes occurring frequently in the world. Landslides affect 15% of the land area of India. The term, 'landslide' is defined as the movement of a mass of a rock, debris or earth down a slope under the influence of gravity (Cruden [1]). The subject of stability analysis of rain-induced failures in soil is an interesting, important and challenging one in geotechnical engineering. The slope failures and landslides occur when hill slopes become mechanically unstable, because of geologic and hydrogeologic processes and pose a serious threat to human life and built environments. The process of rainwater infiltration into the soil and its movement in unsaturated soils has been studied by hydrologists, geologists and geotechnical engineers by carrying out field and numerical examinations [2–6]. The physics-based and numerical models are capable of reproducing the physical processes during rainfall intrusion and failure initiation in the variably saturated soils during the process of slope failures and subsequent mass movement. Landslides are also referred as landslips, slump or slope failure. These landslides not only cause extensive damage to the property but also cause loss of lives. The triggering factors responsible for landslides are rainfall, rapid snowmelt, earthquakes and anthropogenic activities.

Anderson and Pope [7] studied unsaturated flow into a hydrological model to investigate the stability of a typical slope in Hong Kong. The authors concluded that saturated permeability is not a constant value in the unsaturated zone and is the function of the degree of saturation. Collins and Znidarcic [8] investigated the failure mechanisms of slopes subjected to rainwater infiltration. Significant buildup of positive pore-water pressure in the soil due to the rise of groundwater leads to failure. Authors concluded that slope failure is mainly because of a reduction in shear strength

H. R. Bhanuprakash (✉) · A. S. Chatra
Basaveshwar Engineering College, Bagalkot 587102, India

C. N. V. Satyanarayana Reddy et al. (eds.), *Stability of Slopes and Underground Excavations*, Lecture Notes in Civil Engineering 185,
https://doi.org/10.1007/978-981-16-5601-9_4

of soil due to reduction in the magnitude of matric suction. Zhou et al. [9] investigated the effects of rainfall duration, rainfall intensity and soil weakening on stability of slope. Seepage-stress coupling model is used to examine an actual disastrous event in Yulin China. Authors conclude that the safety factor drops sharply at first and then gradually declines to 1.05 during additional two days of intense rainfall indicating the slope is at the verge of failure. Gidon and Sahoo [10] conducted numerous studies and used many innovative techniques to understand the problems due to slope instability under rainfall. The authors suggested that bamboos can be widely used as a reinforcement material for soil stabilization. The process of rainwater infiltration into the soil and its movement in unsaturated soils have been studied by several researchers by carrying out numerical simulations [3, 4, 11].

The study presented in this paper focuses on the relationship between the stability of soil slope and rainfall intensity and duration. The effects of hydraulic characteristics of soil, rainfall intensity and duration on the stability of soil slopes are studied in detail. The main rainfall events are applied to the slope right after the application of the antecedent rainfall. The antecedent rainfall is applied to simulate the initial conditions normal just before the occurrence of the major rainfall events. The variations in pore-water pressure in slopes under different rainfalls are calculated using Finite Difference Analysis (FDA) of transient water flow through unsaturated soils. These pore-water pressures are then used along with the strength reduction technique to calculate the Factor of Safety (FOS) using FDA. All the finite difference calculations have been performed using FLAC [12].

2 Slope Geometry and Boundary Conditions

In this study, the slope geometry mechanical and hydraulic properties are considered. Figure 1 shows the Finite Difference (FD) mesh of homogeneous slope having specific slope geometry and boundary conditions. The slope angle of 35°, slope height of 8 m and initial height of groundwater table from the bottom of the slope is taken as 6 m in the analysis. The boundary conditions were utilized for the seepage analysis. Along the sides of the slope below the water table, a boundary condition equal to the total head is applied.

3 Initial Conditions

First, an antecedent total rainfall of 2565.7 mm ($I = 8.133 \times 10^{-8}$ m/s) prior to the main rainfall event is applied to the surface of slope for 1 year in order to simulate the antecedent groundwater conditions in the slope section. The pore-water pressure, degree of saturation, shear strain, etc. are calculated at the end of the main rainfall events. The plots corresponding to the above response variables are drawn against

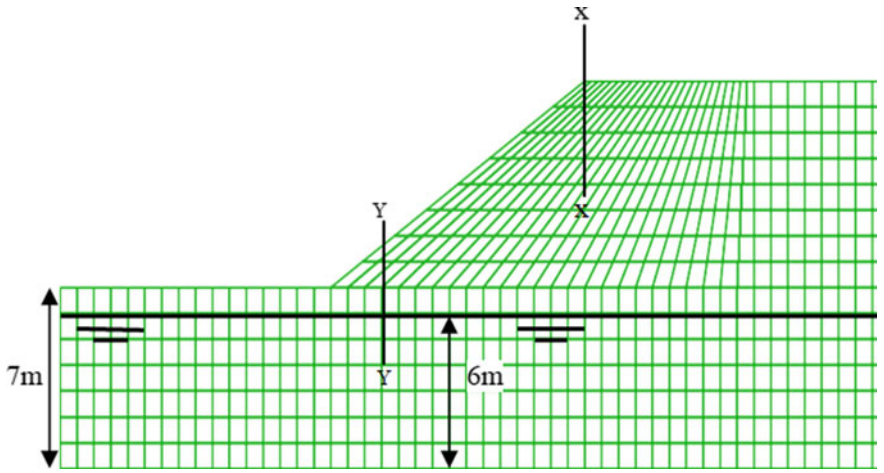

Fig. 1 Finite difference mesh of finite slope

the time from the slope surface at the selected locations in the top (Section x-x) and bottom (Section y-y) portion of the slope.

4 Soil Properties

For FDA, the slope section having the following soil properties is considered. The Mohr–Coulomb soil parameters and van Genuchten hydraulic parameters are given in Tables 1 and 2, respectively. The soil properties are considered to study the response slope subjected to main rainfall event. The rainfall is applied after the antecedent conditions created in the slope section. The properties of the soil types are given in Table 2, in which γ_d = dry unit weight, n = porosity, φ' = friction angle P_0 = Scaling suction m = Shape parameter and θ_r = Residual saturation.

Table 1 Soil parameters for Mohr–Coulomb model

Soil Property	Measured Value	Unit
Mechanical parameters		
Bulk modulus (K)	12.7	MPa
Shear modulus (G)	3.91	MPa
Effective cohesion	3.1	kPa
Effective friction angle	26	Degrees

Table 2 Mechanical and hydraulic properties of the soil.

Soil Property	Measured Value	Unit
Young's modulus (E)	10.7	MPa
Poisson's ratio (μ)	0.37	
Cohesion (c')	3.1	kPa
Shape parameter (m)	0.86	
Scaling suction (P_0)	9.81	kPa
Residual saturation (θ_r)	0.0954	

5 Results and Discussion

The typical rainfall intensities ($I = 4.05 \times 10^{-7}$, 1.39×10^{-6}, 1.119×10^{-6}, 1.10×10^{-6}, 1.38×10^{-6} m/s) are applied on the slope section to study the effects of rainfall intensities on the stability. Before the application of these main rainfall intensities, an antecedent rainfall of 2565.7 mm ($I = 8.133 \times 10^{-8}$ m/s) in 1-year period is applied over the slope section. The abovementioned rainfall intensities are applied over the homogeneous soil slope. The pore-water pressure at time, t = 0 h represents the pore-water pressure measured after the antecedent rainfall. After the application of main rainfall event, the increase in pore-water pressure is observed for the soil slopes. The results in the form of variations in pore-water pressure distribution, degree of saturation, shear strain increment at Sections x-x and y-y are provided.

5.1 Effect of Rainfall on Pore-Water Pressure Generation

An antecedent total rainfall of 2565.7 mm ($I = 8.133 \times 10^{-8}$ m/s) is applied to the slope section up to 1-year period in order to simulate the antecedent groundwater conditions prior to the main rainfall event. Figure 2a, b shows the evolution of pore-water pressures with rainfall duration. Figure 2a shows the variation of pore pressure at Section x–x. The variations in pore pressures at 1, 2 and 3 m depth are − 9.8, − 10.67 and − 8.4 kPa, respectively, at time t = 0 h. At time t = 120 h, the pore pressure values at 1, 2 and 3 m depth are − 0.77, 5.7 and 8.51 kPa, respectively. Figure 2b shows the variation of pore pressure at Section y–y. The pore pressure up to 48 h increases. Thereafter, the pore pressure remains constant.

5.2 Effect of Rainfall on the Stability of Slope

The changes in FOS values with rainfall duration for the slope sections are shown in Fig. 3. The rate of decrease in FOS values as the rainfall duration increases. For the slope section, a FOS of 1.41 is obtained at the end of antecedent rainfall duration

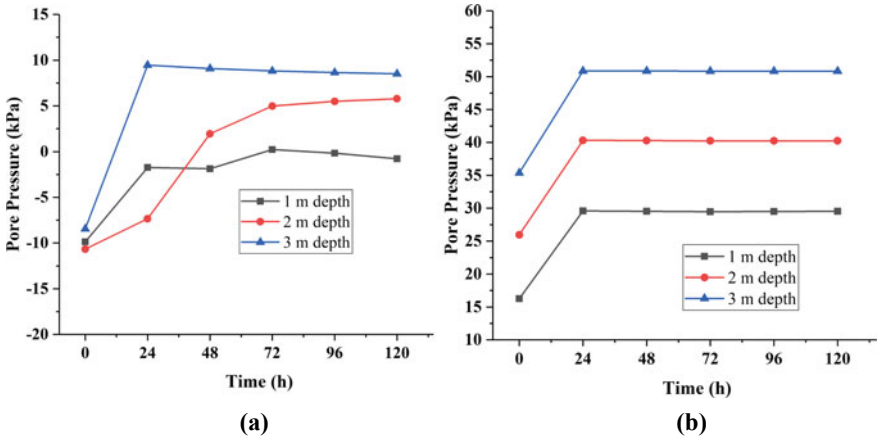

Fig. 2 (**a**) Variation of pore pressure at Section x-x and (**b**) Variation of pore pressure at Section y-y

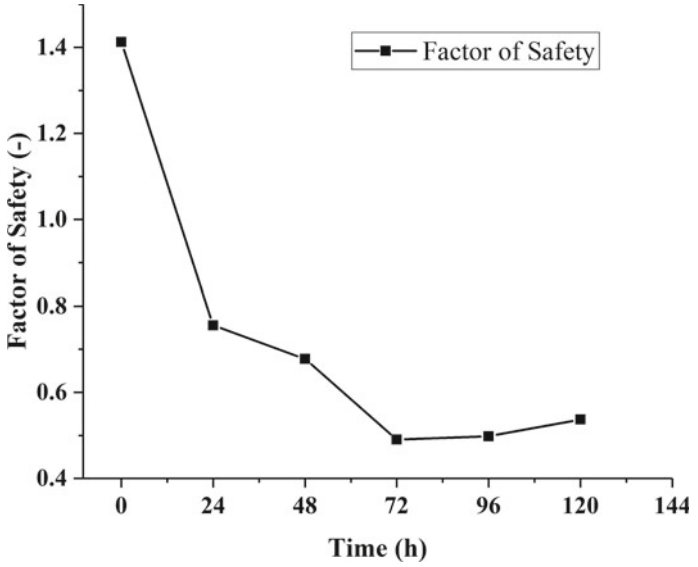

Fig. 3 Variation of factor of safety with time

(i.e. t = 0 h). The FOS values at time t = 18 h reduce to unity indicating slope is on the verge of failure. Further increase in rainfall duration the FOS values reduces less than unity indicating slope has failed. For the same slope with rainfall duration at time t = 120 h, i.e. end of rainfall the FOS value reduced to 0.537.

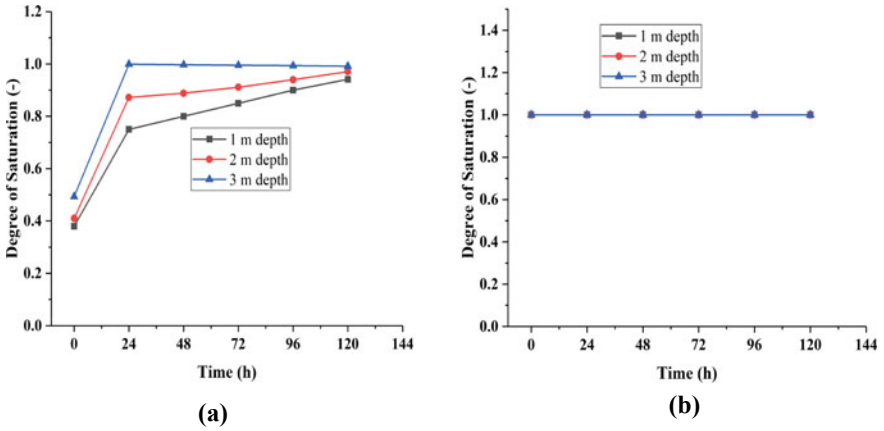

Fig. 4 (**a**) Variation of degree of saturation at Section x-x and (**b**) Variation of degree of saturation at Section y-y

5.3 Effect of Rainfall on Degree of Saturation

Figure 4a and b shows the variations of degree of saturation with time. Figure 4a shows the variation of degree of saturation at (Section x–x). At 1 m depth, the degree of saturation gradually increases. At 3 m depth, the degree of saturation increases from 49 to 100%, thereafter the degree of saturation remains constant. Figure 4(b) shows the variation of degree of saturation for (Section y–y). The rainwater infiltrated all along with the depth of the slope thereby fully saturating the slope.

5.4 Strain Response of Slope During Rainfall

The rainfall infiltration that leads to a decrease in matric suction also changes the shear strength and unit weight of the soil. The plots of shear strain increment with time are shown in Fig. 5a and b. Figure 5a depicts the variation of shear strain increment along (Section x-x). At 1, 2 and 3 m depths, the shear strain increment increases gradually. Figure 5b depicts the variation of shear strain increment along (Section y-y). The shear strain increment increases and thereafter remain constant.

6 Conclusions

The numerical simulations of rain-induced fluctuation are performed with finite difference method using FLAC. The effects of rain intrusion on the progressive slope

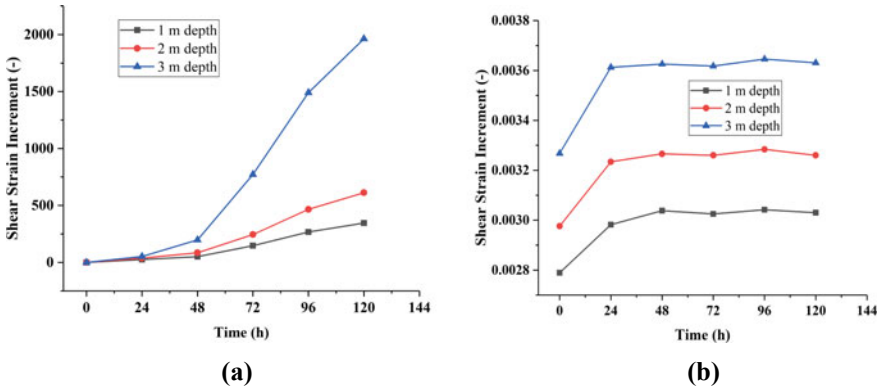

Fig. 5 (**a**) Variation of shear strain increment at Section x-x and (**b**) Variation of shear strain increment at Section y-y

deformations and the formation of a shear failure mechanism are studied. The rainfall intensities are applied over the slope right after the antecedent rainfall, which provided initial conditions for the stability analysis. The variations of pore-water pressure and FOS under these rainfall intensities are evaluated for the saturated–unsaturated slope section. The strain responses of the slopes are evaluated under rainfall intrusion. The numerical results of the present study have greater assurance in the practical stability analysis of the rain-induced earth slope instability. Actual rainfall data can be utilized in the simulation of pore pressure generation thereby giving instruction about the stability of the slope. Based on the results obtained for the selected slope section, soil properties and rainfall intensities, the following results are drawn:

1. During rainfall infiltration, the pore pressures increased due to the dissipation of matric suction and increase in the groundwater table corresponding to the antecedent conditions of the slope. For the slope, pore-water pressure increases for all the rainfall intensities.
2. For the slope section, a FOS of 1.41 is obtained at the end of antecedent rainfall duration. The FOS values at 18 h reduce to unity indicating the slope is unstable.
3. The degree of saturation decreases after the applied antecedent total rainfall and thereafter remains constant.
4. Shear strain values indicate that the soil first becomes unstable at the bottom then the instability extends to the top part of the slope.

References

1. Cruden, D.M.: A simple definition of landslide. Bull. Int. Assoc. Eng. Geol. 27–29 (1991)

2. Ali, A., Huang, J., Lyamin, A.V., Sloan, S.W., Cassidy, M.J.: Boundary effects of rainfall-induced landslides. Comput. Geotech. **61**, 341–354 (2014)
3. Cai, F., Ugai, K.: Numerical analysis of rainfall effects on slope stability. Int. J. Geomech. ASCE **4**(2), 69–78 (2004)
4. Chatra, A.S., Dodagoudar, G.R., Maji, V.B.: Numerical modelling of rainfall effects on the stability of soil slopes. Int. J. Geotech. Eng. **03**(5), 425–437 (2019)
5. Ng, C.W.W., Zhan, L.T., Bao, C.G., Fredlund, D.G., Gong, B.W.: Performance of an unsaturated expansive soil slope subjected to artificial rainfall infiltration. Geotechnique **53**(2), 143–157 (2003)
6. Tsaparas, I., Rahardjo, H., Toll, D.G., Leong, E.C.: Controlling parameters for rainfall-induced landslides. Comput. Geotech. **29**, 1–27 (2002)
7. Anderson, M.G., Pope, R.G.: The incorporation of soil water physics models in geotechnical studies of landslide behavior. In: Proceedings of the 4th International Symposium on Landslides, vol. 4, pp. 349–354 (1984)
8. Collins, B.D., Znidarcic, D.: Stability analyses of rainfall induced landslides. J. Geotech. Geoenviron. Eng. **130**(4), 362–372 (2004)
9. Zhou, D., Zhang, Z., Li, J., Wang, X.: Seepage-stress coupled modeling for rainfall induced loess landslide. Theor. Appl. Mech. Lett. **9**, 7–13 (2019)
10. Gidon, J.S., Sahoo, S.: Rainfall-induced slope failures and use of bamboo as a remedial measure: a review. Indian Geotechn. Soc. **50**, 766–783 (2020)
11. Rabie, M.: Comparison study between traditional and finite element methods for slopes under heavy rainfall. Hous. Build. Natl. Res. Center **10**, 160–168 (2014)
12. FLAC Flac Manual: Fluid-mechanical interaction. Itasca Consulting Group Inc., Minneapolis (2011)

Response of Sand at Low Normal Stresses Using Gravity Shear Test

Konda Kiranmai, Kadali Srinivas, and Madhav Madhira

1 Introduction

Liner systems on slopes are a combination of various materials like soil and geosynthetics. Designing of such systems on slopes necessitates prior knowledge of angle of shear resistance between various layers, as the critical failure plane is usually located at the interface between these components. Shear strength of materials can be characterized either by a direct shear test [1] or an inclined plane or a tilt test [2]. Tilting frame or a gravity-induced shear test is used to measure shear/frictional characteristics of soil, soil-geosynthetic or geosynthetic-geosynthetic interfaces where shearing occurs for a material placed on an inclined surface under gravity. Shear strength behaviour of a soil and geosynthetic interfaces on an inclined plane has been studied at different test conditions by Palmeria et al. and Lopes et al. [3, 4]. Several studies have been reported comparing the two methods (direct shear and inclined plane/tilt) and they conclude that "Gravity Induced Shear test" is more suitable for conditions under low normal stress of less than 10 kPa [5] and direct shear performs well under conditions of relatively high normal stresses [4–7]. The above studies measure only the strength and not the shear stress–displacement responses of the material or the interface.

In this study, gravity-induced shear test set-up was developed to measure the shear stress–displacement response considering the factors affecting the test results. Tests have been performed for a normal load of 0.7 kPa, 0.9 kPa and 1.6 kPa at 50 and 75% density index and the angle of shearing resistance was evaluated. A graph has been plotted between shear stress and horizontal displacement. It is observed that the plot (shear stress vs Displacement) depicts a stick–slip phenomenon, i.e., as the shear stress increased the displacement remained constant and then gradually increased,

K. Kiranmai · K. Srinivas (✉) · M. Madhira
VNR Vignana Jyothi Institute of Engineering and Technology, Hyderabad 500090, India
e-mail: srinivas_kadali@vnrvjiet.in

C. N. V. Satyanarayana Reddy et al. (eds.), *Stability of Slopes and Underground Excavations*, Lecture Notes in Civil Engineering 185,
https://doi.org/10.1007/978-981-16-5601-9_5

later the displacement continued persistent and thereafter with no rise in the shear stress the horizontal displacement increased. A similar analysis has been carried for direct shear tests performed at normal loads of 9.8 kPa, 24.5 kPa, 49.0 kPa, 98.1 kPa and 147.1 kPa and the test results depicted a gradual increase in the shear stress with an increase in the horizontal displacement.

2 Methodology

To measure the shear stress–horizontal displacement response, a test set-up was fabricated as shown in Fig. 1. A shear box of size 6 × 6 cm is mounted on a fabricated table which can be inclined. A lifting jack is provided to allow the inclination of the box. To record the displacement of the shear box, a horizontal dial gauge is fixed. A graduation scale is erected to measure the angle of inclination of the test box.

The forces acting on the test specimen are represented in Fig. 2. The net normal stress and the shear stress are calculated as per Eqs. 1 and 2, respectively.

$$Normal\ stress = \frac{W_s \cos\theta + W_p \cos\theta}{A} \tag{1}$$

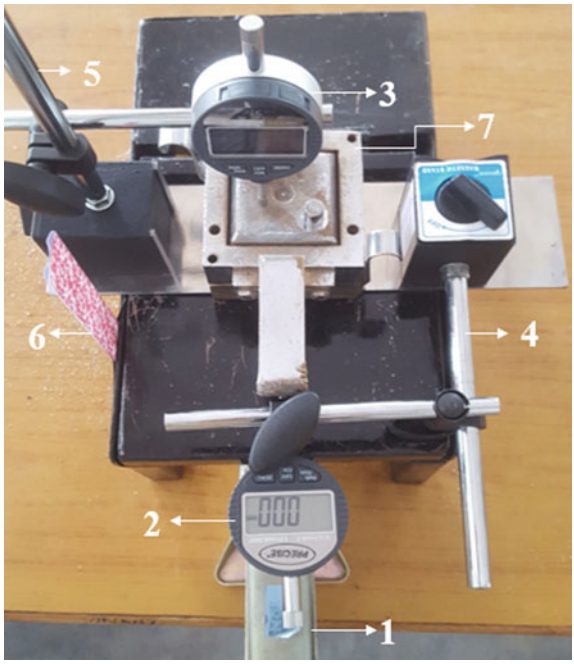

Fig. 1 Gravity Induced shear test set-up (1) Lifting jack, (2) Dial gauge (to measure horizontal displacement), (3) Dial gauge (to measure dilation), (4 & 5) Magnetic stands, (6) Graduation scale and (7) Shear box (6 × 6 cm)

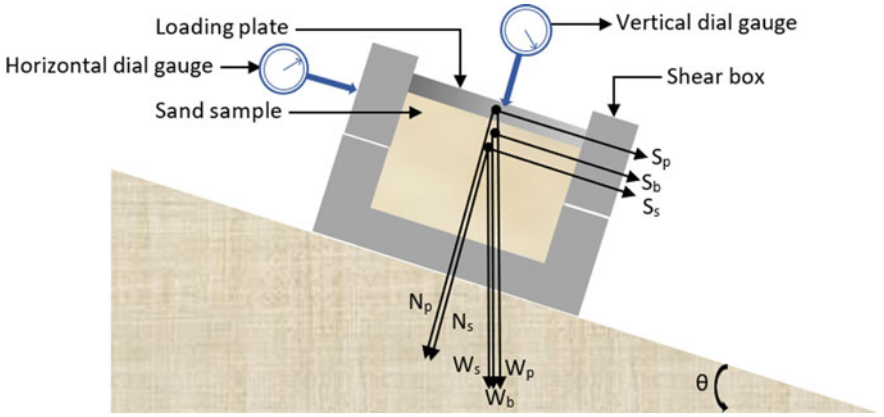

Fig. 2 Forces acting on the shear box

$$Shear\ stress = \frac{W_s \sin\theta + W_p \sin\theta + W_b \sin\theta}{A} \tag{2}$$

where W_s = Weight of soil in the upper half; W_p = Weight of loading plates; W_b = Weight of upper half of box; N_s = normal component of soil weight = $W_s\cos\theta$; N_p = normal component of weight of plates = $W_p\cos\theta$; S_s = shear component of soil weight = $W_s\sin\theta$; S_P = shear component of weight of plates = $W_p\sin\theta$; S_b = shear component of weight of upper half of box = $W_b\sin\theta$; A = Area of the specimen.

3 Results and Discussion

Naturally available sand is considered for the study. A sieve analysis [8] has been performed to evaluate the particle size distribution (refer Fig. 3) of the representative sample. The Cu and Cc values were recorded to be 2.63 and 0.92, respectively, it is clearly observed that the soil is classified as poorly graded sand.

A relative density test [9] has been carried to estimate the in-situ dry density of the sample with density index equal to 50 and 75% and is measured to be 1.61 g/cm^3 and 1.64 g/cm^3 respectively (refer Table 1).

With known density and volume, the weight of the sand is assessed and is filled in a standard size shear box (6 × 6 cm) which is then placed on the tabletop. Stainless steel loading plates of size 6 × 6 cm are placed on top of the shear box to act like a normal load. The horizontal dial gauge is positioned to measure the shear displacement. A graduation scale is provided to estimate the test box inclination. The inclination of the shear box is advanced with the help of a lifting jack to measure stress–displacement response and also the angle of shearing resistance of the representative sand. Figure 4 shows the failure of the test specimen under gravity.

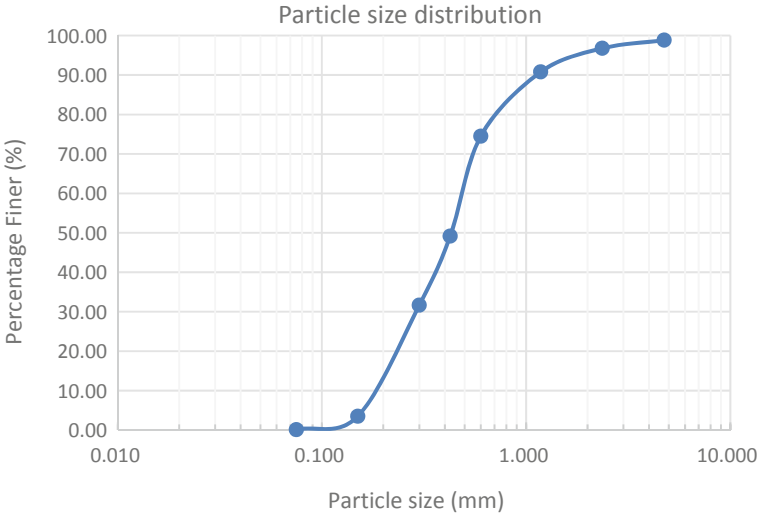

Fig. 3 Particle size distribution of sand sample

Table 1 Relative density test results of sand sample

	Density value (g/cm^3)
Minimum density	1.56
Maximum density	1.67
Dry density	
RD = 50%	1.61
RD = 75%	1.64

Fig. 4 Failure of sand sample under gravity

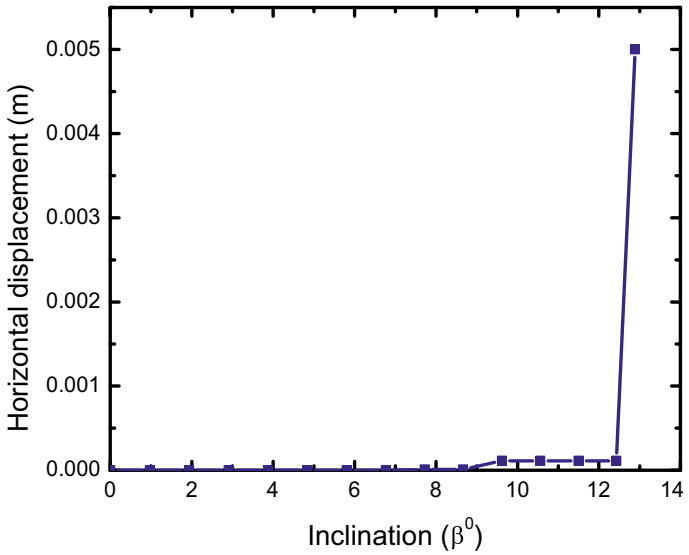

Fig. 5 Inclined shear test box without sand

To know the frictional resistance between the boxes, a test has been carried for the test box without sand. From Fig. 5, it is envisioned that the horizontal displacement remained constant up to an inclination of 12.4° and the displacement increased extremely causing sudden sliding of the test box indicating no friction between the boxes.

3.1 Gravity Induced Shear Test Results

The test result with three normal loading conditions (0.7 kPa, 0.9 kPa and 1.6 kPa) has been plotted (Fig. 6). Figure 6a reflects the plots for shear stress vs normal stress at a density index of 50%. It is observed that as the test is advanced, the normal stress decreased from 0.7 kPa to 0.6 kPa. The shear stress increased from 0 kPa to 1.4 kPa and the friction angle is evaluated to be 66.6° at failure. Likewise, for a loading condition of 0.9 kPa, the normal stress decreased from 0.9 kPa to 0.8 kPa and the shear stress increased from 0 kPa to 1.9 kPa with the friction angle equal to 65.7° at failure. And hence for 1.6 kPa normal loading condition, the normal stress reduced to 1.5 kPa and shear stress increased to 2.3 kPa for a friction angle being 56.7° at failure. The details of the failure condition for all the three test cases were tabulated in Table 2.

Figure 6b represents the shear stress vs displacement curve for normal loads of 0.7 kPa, 0.9 kPa and 1.6 kPa with density index being 50%. A stick–slip phenomenon is depicted from the test results. For a loading condition of 0.7 kPa, the shear stress

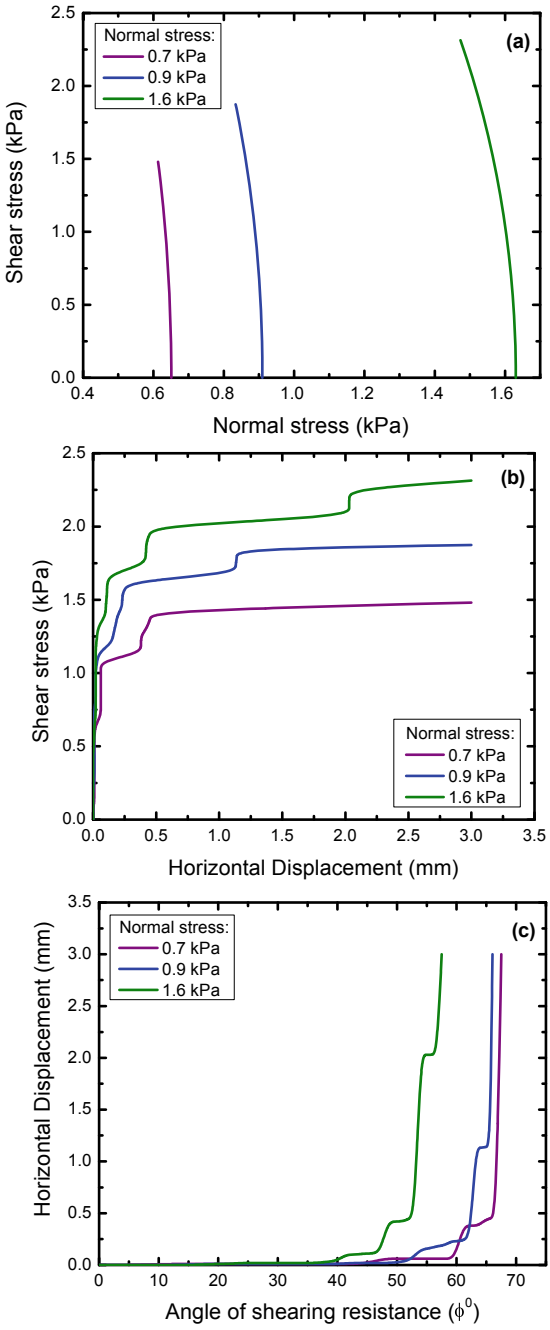

Fig. 6 Gravity induced shear test results at 50% density index

Table 2 Gravity induced shear test results at failure condition for 50% density index

Density (g/cc)	Initial normal stress (kPa)	Normal stress at failure (kPa)	Shear stress at failure (kPa)	Angle of shearing resistance (ϕ^0)
1.61	0.7	0.6	1.4	66.6
1.61	0.9	0.8	1.9	65.7
1.61	1.6	1.5	2.3	56.7

increased from 0 kPa to 0.6 kPa with no increase in the displacement. Later, with a minor increase in the displacement, the shear stress increased to 1.1 kPa. Thereafter, with a small increase in the shear stress, the displacement increased from 0.06 mm to 0.38 mm. Now, the displacement remained constant and the shear stress increase to 1.4 kPa. Later, with no increase in the shear stress, the displacement augmented. Likewise, for normal loads of 0.9 kPa and 1.6 kPa, an equivalent response is noticed. Figure 6c depicts the plots of displacement vs angle of shearing resistance. A similar phenomenon (stick–slip) has been observed, the displacement progressively augmented and then nearly maintained continually. Later, the displacement increased drastically.

A similar analysis has been carried with an increase in density index from 50 to 75% (refer Fig. 7). The details of the failure condition for the three loading conditions were tabulated (refer Table 3). Comparing the test results from Tables 2 and 3, it is envisioned that with an increase in density, a minor increase in the normal load is observed. However, with the slight increase in the normal load, there is a rise of 2–4° in the friction angle. This is due to the influence of the sand particles with varying densities.

3.2 Direct Shear Test Results

Direct shear tests have been carried for normal loads of 9.8 kPa, 24.5 kPa, 49.0 kPa, 98.1 kPa and 147.1 kPa at 50% and 75% density index. Shear stress vs horizontal displacement curve has been plotted for the test results. Figure 8a shows the plots for a relative density of 50% and Fig. 8b for 75% density index. It is observed that the shear stresses at failure were recorded to be 9.84 kPa, 21.1 kPa, 36.6 kPa, 65.4 kPa and 93.5 kPa for the normal loads of 9.8 kPa, 24.5 kPa, 49.0 kPa, 98.1 kPa and 147.1 kPa, respectively, with a density index of 50%. Similarly, for a density index of 75%, the shear stresses at failure are 11.2 kPa, 23.2 kPa, 40.8 kPa, 72.4 kPa and 104.7 kPa for normal loads of 9.8 kPa, 24.5 kPa, 49.0 kPa, 98.1 kPa and 147.1 kPa, respectively. It is hence concluded that the shear stress increased gradually with an increase in the horizontal displacement.

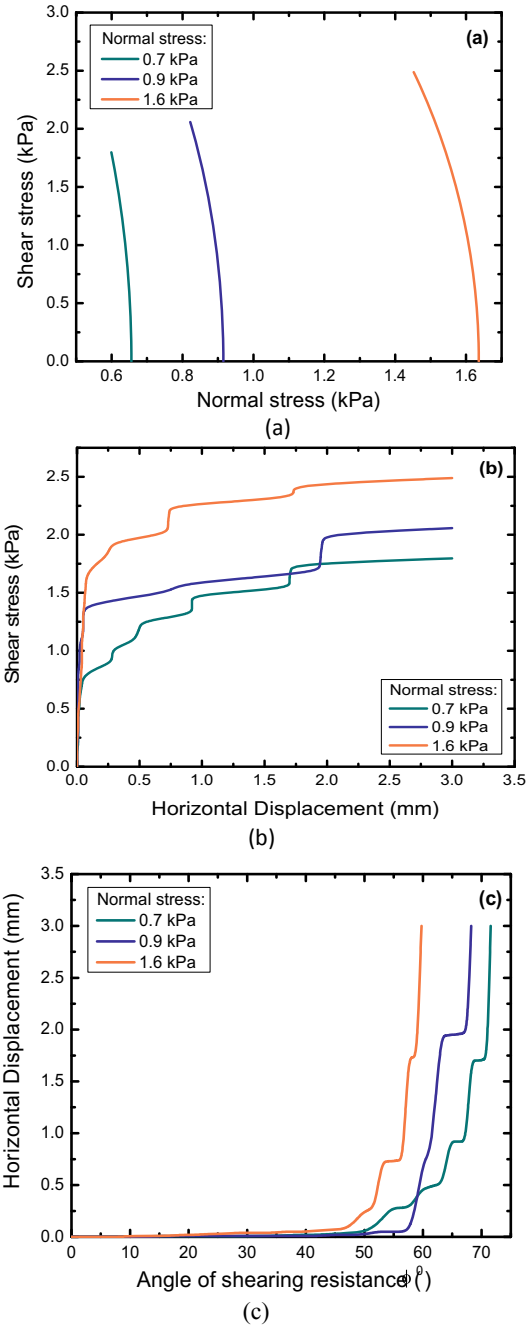

Fig. 7 Gravity induced shear test results at 75% density index

Table 3 Gravity induced shear test results at failure condition for 75% density index

Density (g/cc)	Initial normal stress (kPa)	Normal stress at failure (kPa)	Shear stress at failure (kPa)	Angle of shearing resistance (ϕ^0)
1.64	0.7	0.6	1.8	71.0
1.64	0.9	0.8	2.0	67.6
1.64	1.6	1.4	2.4	59.0

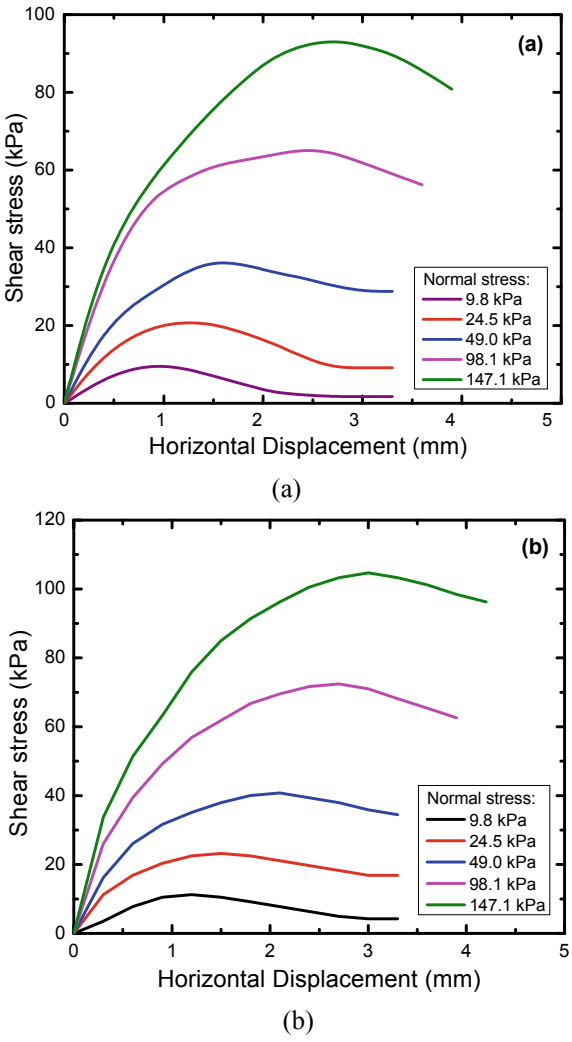

Fig. 8 Direct shear test results at **a** 50% density index **b** 75% density index

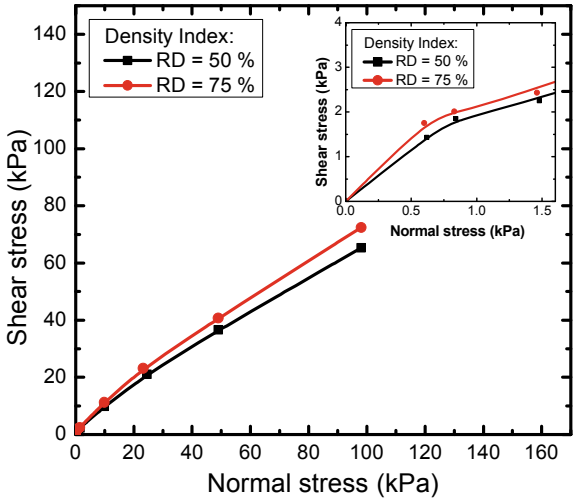

Fig. 9 Unified Mohr–Coulomb envelope

3.3 Strength Envelope

A unified Mohr–Coulomb envelope has been plotted combining the test results from gravity-induced and the direct shear tests at 50% and 75% density indices (Fig. 9). The normal stresses range from a low 0.7 kPa through 0.9 kPa, 1.6 kPa, 9.8 kPa, 24.5 kPa, 49.0 kPa to a maximum of 98.1 kPa. An inset graph has also been plotted to visualize the normal stresses of 0.7 kPa, 0.9 kPa and 1.6 kPa. A non-linear Mohr–Coulomb envelope is obtained indicating the angle of shearing resistance to be a function of normal stress. The angle of shearing resistance reduces from 66.6° at a normal stress of 0.7 kPa to 33.7° at 98.1 kPa for a 50% density index. Likewise, for a 75% density index, the angle of shearing resistance decreases from 71° at a normal stress of 0.7 kPa to 36.4° at maximum stress of 98.1 kPa. Fannin et al. [10] report a similar result.

4 Conclusions

The present study reports the development of the gravity-induced shear test set-up to measure the shear stress–displacement responses at low normal stresses. Three low normal loading conditions of 0.7 kPa, 0.9 kPa and 1.6 kPa at 50 and 75% density indices were considered. A similar study has been carried using direct shear tests at normal stresses of 9.8 kPa, 24.5 kPa, 49.0 kPa, 98.1 kPa and 147.1 kPa. A unified Mohr–Coulomb envelope represented by a non-linear curve indicates the angle of shearing resistance is a function of normal stress, decreasing with increasing normal stresses.

References

1. IS 2720-Part 13: Methods of Test for Soils—Direct Shear Test. Soils and Foundation Engineering (1986)
2. EN ISO 12957-Part 2: Determination of Friction Characteristics—Inclined Plane Test. European Committee for Standardization, Brussels (2005)
3. Lopes, M.L., Ferreira, F., Carneiro, J.R., Vieira, C.S.: A new procedure for measuring geosynthetic friction with an inclined plane. Int. J. Geotech. Eng. **8**(3), 335–342 (2014)
4. Palmeira, E.M., Lima, Jr. N.R., Mello, L.G.R.: Interaction between soils and geosynthetic layers in large-scale ramp tests. Geosynth. Int. **9**(2), 149–187 (2002)
5. Reyes, R.R., Gourc, J.P.: Use of the inclined plane test in measuring geosynthetic interface friction relationship. Geosynth. Int. **10**(5), 165–175 (2003)
6. Izgin, M., Wasti, Y.: Geomembrane-sand interface frictional properties as determined by inclined board and shear box tests. Geotext. Geomembr. **16**, 207–219 (1998)
7. Pitanga, H.N., Gourc, J.P., Vilar, O.M.: Interface shear strength of geosynthetics: evaluation and analysis of inclined plane tests. Geotext. Geomembr. **27**, 435–446 (2009)
8. IS 2720-Part 4: Methods of Test for Soils—Grain Size Analysis. Soil and Foundation Engineering (1985)
9. IS 2720-Part 14: Methods of Test for Soils—Determination of Density Index of Cohesionless Soils. Soil and Foundation Engineering (1983)
10. Fannin, R.J., Eliadorani, A., Wilkinson, J.M.T.: Shear strength of cohesionless soils at low stress. Geotechnique **55**(6), 467–478 (2005)

Rock Slope Stability Analysis of a Metro Station Excavation

R Rajaraman and Gundeti Sumanth Kumar

1 Introduction

In the present-day of urban transportation infrastructure, demand for utilization of underground space surges at a high speed. Construction of stations in metro projects in urban environments involves huge challenges to the safety and creates an impact on adjacent structures. In a metro project in southern part of India, excavation of a station involves deep rock excavation of around 20 m. A vertical cut was proposed without any bench due to space constraints imposed on the area by adjacent major buildings and structures. All types of failure likely to occur for rock slopes were considered for analysis. Analysis has been conducted using empirical, analytical, and numerical methods so that the most suitable support system is recommended with application of adequate engineering judgement.

2 Site Description and Geology

The excavated bedrock was of fresh and hard strong to very strong granitic gneiss. The discontinuities were tight in nature with low persistence making lower portion of the excavation stable and massive in nature. Damp to moist conditions of seepage were noticed mainly. Outcrops were assigned Rock Mass Rating (RMR) of 42–79. The outcrops observed during excavation are presented below (Fig. 1).

R. Rajaraman · G. S. Kumar (✉)
EDRC Metro, Heavy Civil Infrastructure, L&T Construction, Chennai, Tamil Nadu, India
e-mail: sumanth-gundeti@lntecc.com

C. N. V. Satyanarayana Reddy et al. (eds.), *Stability of Slopes and Underground Excavations*, Lecture Notes in Civil Engineering 185,
https://doi.org/10.1007/978-981-16-5601-9_6

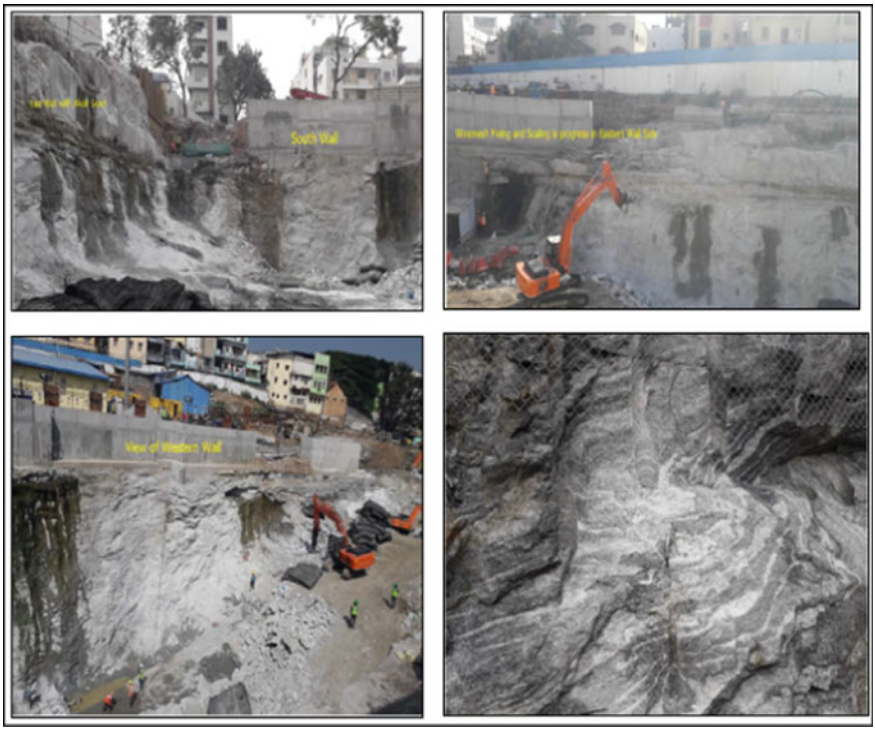

Fig. 1 Outcrops observed during excavation

2.1 Major Discontinuities

The discontinuity data collection has been carried out for the rock outcrops, and joints considered for kinematic analysis are presented in Table 1. All these joints are not discreet and distinct. For a conservative estimation, all these joints have been considered for kinematic analysis.

3 Geotechnical Parameters for Analysis and Design

3.1 Rock Mass

Hoek–Brown strength criterion is used to determine the principal stress and normal-shear strength plots for the rock mass at various depths. The equivalent Mohr–Coulomb parameters have been calculated by fitting the linear Mohr–Coulomb relationship. Typical plots derived by RocData software for one such case is presented in Fig. 2.

Table 1 Details of joints mapped at site

Sl. No.	Joint No.	Dip (degrees)	Dip Direction (degrees)
1	J1	20	360
2	J2	80	40
3	J3	18	180
4	J4	80	310
5	J5	65	230
6	J6	70	135
7	J7	30	100
8	J8	85	110
9	J9	35	310
10	J10	45	125
11	J11	30	110
12	J12	80	10
13	J13	80	210
14	J14	29	102
15	J15	25	320
16	J16	85	210

Table 2 Summary of geotechnical parameters of rock mass

Case No	Height of rock (m)	GSI	UCS (MPa)	Cohesion (kPa)	Friction angle (degrees)	Modulus of Deformation (MPa)
1	5	15	33	31	45	418
2		30	75	81	60	1416
3		40	162	193	67	4952
4	10	15	33	49	40	418
5		30	75	121	56	1416
6		40	162	252	64	4952
7	15	15	33	63	37	418
8		30	75	155	53	1416
9		40	162	304	62	4952
10	20	15	33	76	35	418
11		30	75	186	51	1416
12		40	162	353	60	4952

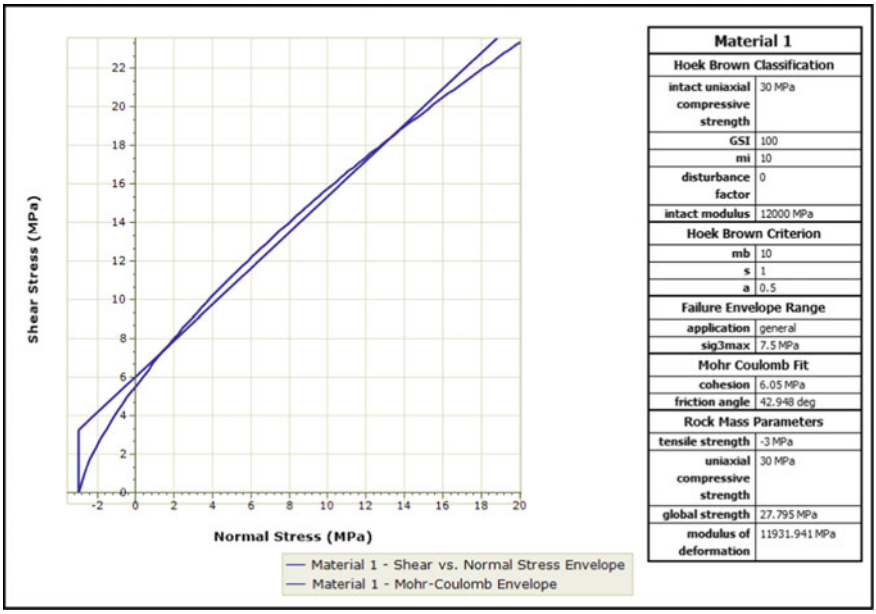

Fig. 2 Typical plot derived by RocData software

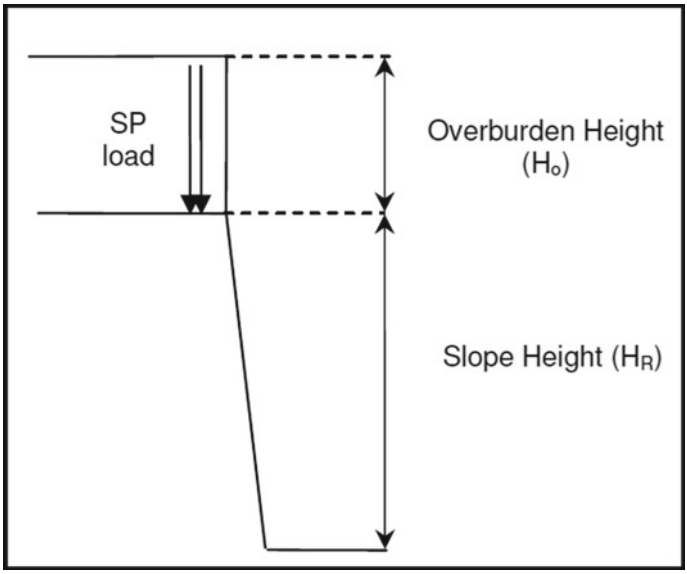

Fig. 3 Idealised Model of Slope

Analyses have been carried out for three rock mass classes represented by GSI ranges; GSI > 40; 20 < GSI < 40 and GSI < 20. These class ranges represent the possible conditions of rock mass likely to be encountered at site. The geotechnical parameters as estimated are presented in the following (Table 2).

3.2 Rock-Rock Joints

Shear strength parameters of rock-rock joints are to be assigned empirically in the absence of field test results. The joint characteristics have been defined by the geologist during site mapping. Accordingly, shear strength parameters of the rock-rock joint in accordance with IS 13365 Re-excavation [1] and Hoek [2] are assigned as below in Table 3.

4 Design Methodology

Analysis of rock slope stability and design of support system will only be holistic when there is a proper link between design and geological assessment at the site. The design must cater to all types of rock mass classes likely to be encountered at site. The flexibility of selection of support system must be entrusted upon the site geologist. Considering this, slope support system has been designed for three rock mass classes characterized by GSI. Analyses have been carried out for various ranges of overburden height and height of rock slope for each GSI range to determine the factor of safety for each scenario as shown in Fig. 4. Rock dowels of varying dimension and spacing are employed to improve stability where static FoS greater than 1.3 and seismic FoS greater than 1.1 was not achieved.

Table 3 Shear strength parameters of rock-rock joints

Material	Cohesion (MPa)	Friction angle (degrees)
Rock-Rock joint	0.05	35

Table 4 Estimated values of SMR at site

S.No	Face	Wall direction	SMR (Range)	Recommended support system
1	Face 1	East	35–79	Important corrective measure–occasional supports
2	Face 2	South	42–77	Systematic supports–occasional supports
3	Face 3	West	57–79	Systematic supports–occasional supports
4	Face 4	North	18–60	Re-excavation[a]–systematic supports

[a]This face needs special attention and effective support system to be provided depending upon site conditions

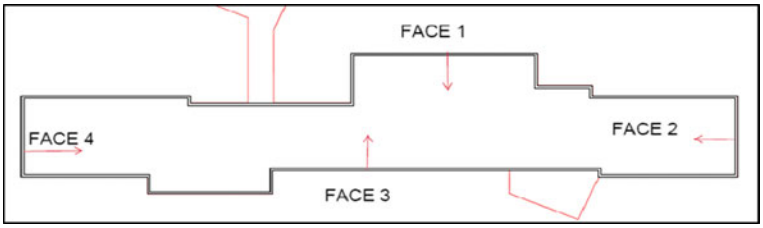

Fig. 4 Details of cut slopes at metro station

The bonded length is a function of the bar diameter, hole diameter and allowable bond stress. An allowable bond stress of 500 kPa has been selected for all anchorages based on typical conservative values presented by Duncan [3]. The unbonded length and required tension force per meter width of slope, T, has been provided where the FoS of either a sliding or rotating block does not reach 1.3. The tension force T is anticipated to be spread between several individual anchorages to distribute the load across the sliding block. For the rock mass assessment in the GSI > 40 range, the application of the secant pile (SP) loading causes local failure below the toe of the pile only, with the remainder of the slope remaining stable. A single row of rock dowels below the secant pile footing is generally adequate to prevent localized failure.

In order to analyse the stability of rock slope, possible four modes of failure were checked, i.e., Wedge failure, Planar failure, Toppling failure and Circular failure.

5 Analysis

5.1 Assumptions and Loading

As per available geotechnical investigations at the metro station location, it has been found that ground water table varies between 1.8 and 6.40 m deep from ground level. To stabilize the slope, drainage holes are recommended for the rock slope at regular intervals. Hence, zero uplift pressure has been considered on the joint plane conforming to Clause 10.2 of IS 14448 [4].

Pseudo static analysis has been undertaken to model the effects of earthquake. Seismic coefficients have been used as follows:

$A_h = 0.12$ has been used for design horizontal seismic co-efficient.

$A_v = 0.08$ has been used for design vertical seismic co-efficient.

Live loading from vehicles, e.g., cranes, at ground surface has been incorporated into the secant pile loading applied at rock head level. Details of various faces of cut slope considered for analysis are presented in Fig. 5.

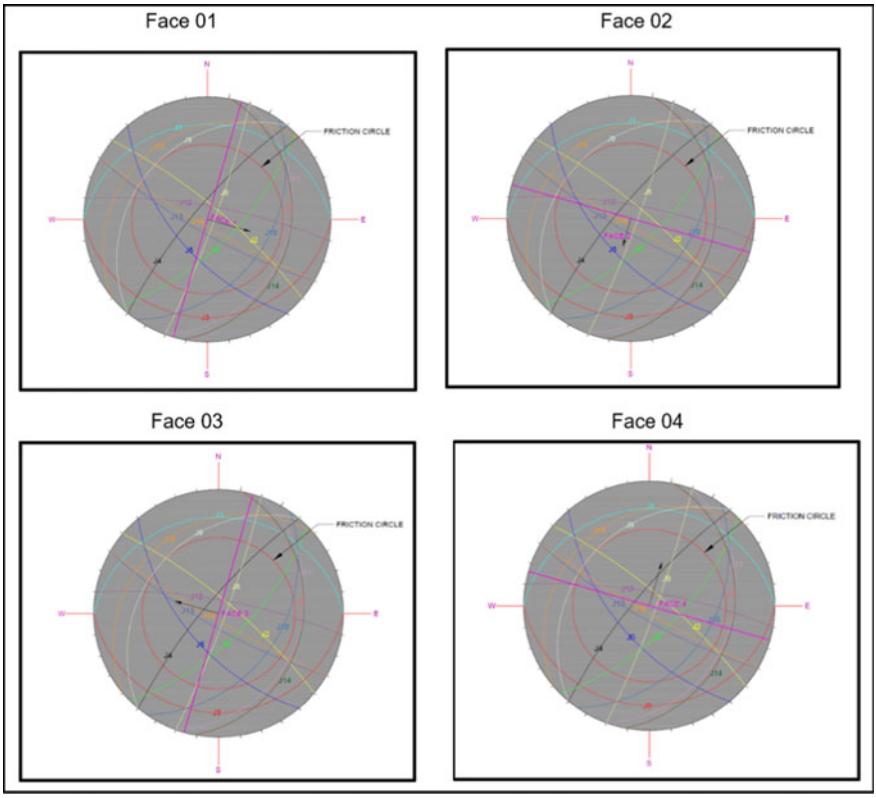

Fig. 5 Stereographic projection of joints mapped at site

5.2 Analytical Method

Identification of modes of failure. The stereographic projection of joints has been used for identifying the mode of failure of slope as in Fig. 6.

Wedge Failure. In order for the wedge failure to occur, three primary conditions are to be satisfied. They are as follows:

- Two planes will always intersect in a line.
- The plunge of the line of intersection must be flatter than the dip of the face and steeper than the average friction angle of the two slide planes.
- The line of intersection must dip in a direction out of the face for sliding to be feasible.

Planar Failure. A plane failure is a comparatively rare sight in rock slopes because it is only occasionally that all geometric conditions required to produce such a failure occur in an actual slope. Still, the possibility of such failure has been studied. In order for the planar failure to occur, three primary conditions are to be satisfied. They are as follows:

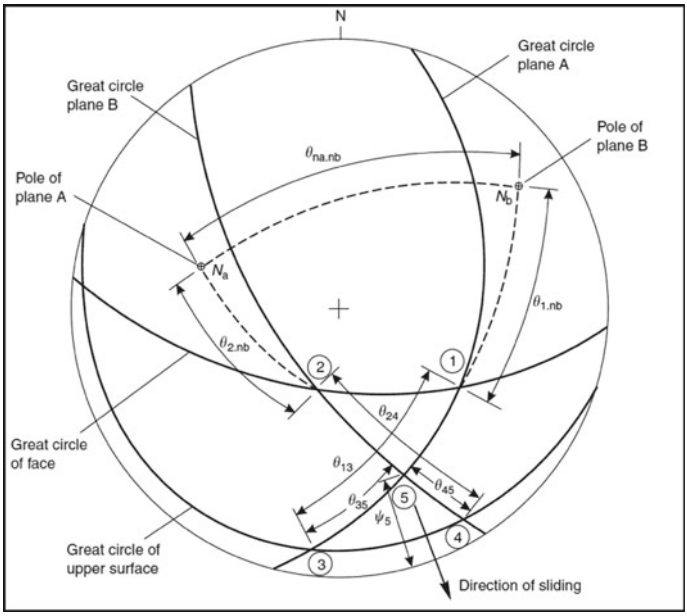

Fig. 6 Stereoplot of data required for wedge stability analysis

- Joint plane dipping out of the face.
- Dip of the joint must be less than the dip of slope face.
- The plane on which sliding occurs must strike parallel or nearly parallel (within approximately ±20) to the slope face.

*Toppling Failure***.** In order for the toppling failure to occur, two primary.

conditions are to be satisfied. They are as follows:

- Joints dipping into the face must be within about 10°.
- $(90° - \psi f) + \phi j < \psi p$, given by Goodman and Bray [5].

Where ψf is the cut slope angle, ϕj is the friction angle, and ψp is the dip of joint.

Circular Failure. In the case of a closely fractured or highly weathered rock, a strongly defined structural pattern no longer exists, and the slide surface is free to find the line of least resistance through the slope. Observations of slope failures in these materials suggest that this slide surface generally takes the form of a circle, and most stability theories are based upon this observation.

Assessment of factor of safety. Factor of safety of slopes identified in the kinematic analyses are further analysed using the formula below given in IS 14448 [4]

$$FOS = \frac{c_j A + \tan \Phi \left(\mathrm{W} \cos \Psi_p - \alpha_h \, \mathrm{W} \sin \Psi_p - V \sin \Psi_p - U \right)}{\mathrm{W} \sin \Psi_p + \alpha_h \mathrm{W} \cos \Psi_p + \mathrm{V} \cos \Psi_p} \tag{1}$$

FOS = Factor of safety.
c_j = Cohesion of rock-rock joint.
ψ_p = Dip of joint plane.
A = H cosec ψ_p.
Φ = Friction angle of rock-rock joint.
W = Weight of wedge = ½ Υ H^2 (cot ψ_p – cot ψ_f).
V = 0 (in the absence of tension crack).
α_h = 0.1 (for earthquake condition).
U = Uplift on joint plane = 0 (as per Clause 10.2 of IS 14448[4] for drained slope).

Hoek et al. [6], gave a formula for Factor of Safety (FoS) against wedge failure as given below:

$$\frac{3}{\Upsilon_r H}(c_A X + c_A Y) + \left(A - \frac{\Upsilon_W X}{2\Upsilon_r}\right)\tan \Phi_A + \left(B - \frac{\Upsilon_W Y}{2\Upsilon_r}\right)\tan \Phi_B \quad (2)$$

Υ = Unit weight of rock = 26 kN/m3.
H = Cut slope Height.
$c_A = c_B$ = Cohesion of rock-rock joint = 50 kPa.
$\Phi_A = \Phi_B$ = Friction angle of joint = 35°

$$X = \frac{\sin \theta_{24}}{\sin \theta_{45} \cos \theta_{2,na}} \quad (3)$$

$$Y = \frac{\sin \theta_{13}}{\sin \theta_{35} \cos \theta_{1,nb}} \quad (4)$$

Υ = Unit weight of water = 9.81 kN/m^3.

Effect of water pressure has not been considered in the analysis as the drainage.

arrangement is proposed. A and B are derived from Friction only charts available in Duncan [3]. Other parameters are defined in Fig. 7.

The factor of safety against circular failure has been determined with the aid of circular failure charts, given in Duncan C [3]. These were produced by running a search routine to find the most critical combination of slide surface and tension crack for each of a wide range of slope geometries and ground water conditions. Circular chart corresponding to fully drained slope has been adopted for stability analysis.

5.3 Empirical Method

Slope Mass Rating (SMR). As per IS 13365 [1], Slope Mass Rating (SMR) can be used for preliminary assessment of the stability of rock slopes. The approach is based on modification of RMR system using adjustment factors related to discontinuity

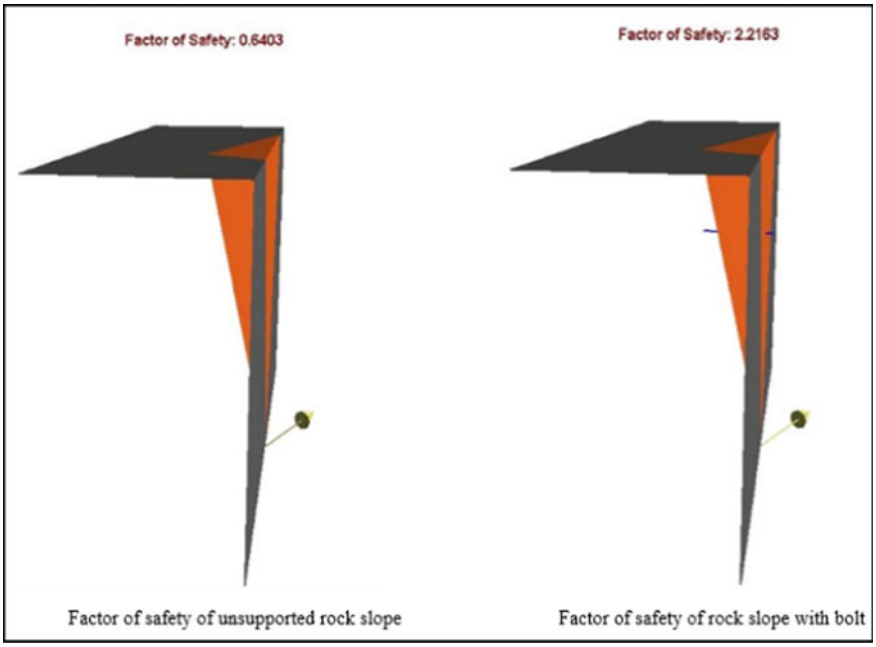

Fig. 7 Typical results of SWedge analysis of metro station excavation

orientation with reference to slope as well as failure mode and slope excavation methods.

$$\text{Slope mass rating (SMR)} = \text{RMR}_{\text{basic}} + (\text{FI} \times \text{F2} \times \text{F3}) + \text{F4} \quad (5)$$

The values of F1, F2, F3, and F4 have been taken from IS 13365 [1]. The adjustment rating for joints and excavation in rock slopes depends on the following factors:

F1: Factor which is dependent on parallelism between the slope and the discontinuity.

F2: Factor which is dependent on the dip of discontinuity.

F3: Factor which is dependent on the relationship of dip of discontinuity and inclination of slope.

F4: Factor which depends on whether the slope under investigation is a natural one or excavated by pre-splitting, smooth blasting, mechanical excavation or poor blasting (Table 4).

Northern side has been found as critical and the support system shall be finalized only after a proper assessment of joint conditions by site geologist.

5.4 Numerical Analysis

Analyses to assess the overall stability of the slopes have been carried out using softwares—SWedge, RocPlane, RocTopple and RS^2.

Wedge failure analysis. SWedge is a software developed by Rocscience Inc. This is based on the method developed by Goodman and Shi [7]. Factor of safety of the identified wedges has been evaluated using SWedge software. Analysis has been considered by incorporating both static and dynamic conditions for both supported and unsupported wedges. Typical results of SWedge are presented in Fig. 8.

Planar failure analysis. Identified cases of Planar failure have been further analysed using RocPlane software of Rocscience Inc. Factor of safety has been determined for all planar failures likely to be formed in the slope. Analysis has been performed for both static and dynamic loading conditions considering the reinforcement as required. Typical results of planar failure are presented in Fig. 9.

Toppling failure analysis. RocTopple software of Rocscience Inc. has been used to determine the factor of safety of identified toppling blocks. This software is based on the limit equilibrium analysis. Typical result of toppling failure analysis is presented in Fig. 9.

Circular failure analysis. Detailed circular analysis has been carried out by RS^2 software [8] of Rocscience Inc. for various combinations of rock slope height and overburden possible at the site. Critical Strength Reduction Factor (SRF), equivalent to factor of safety has been evaluated for all possible scenarios. Factor of safety has been determined in both static and dynamic loading conditions to ensure the safety of the rock slope in adverse conditions. Typical result of failure analysis is presented in Fig. 10.

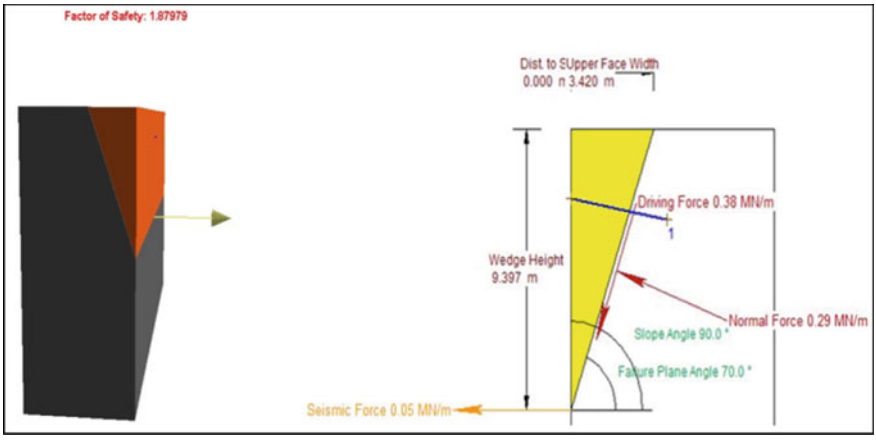

Fig. 8 Typical results of RocPlane failure analysis of metro station excavation

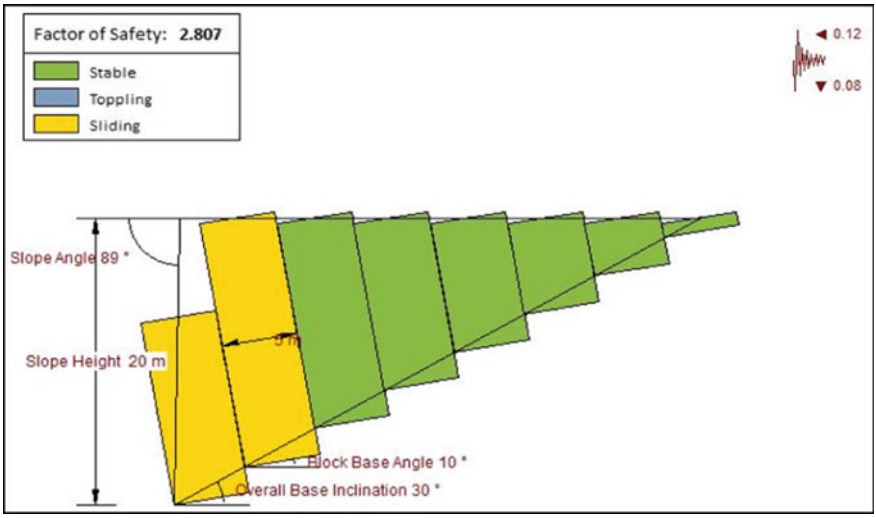

Fig. 9 Typical result of RocTopple failure analysis of metro station excavation

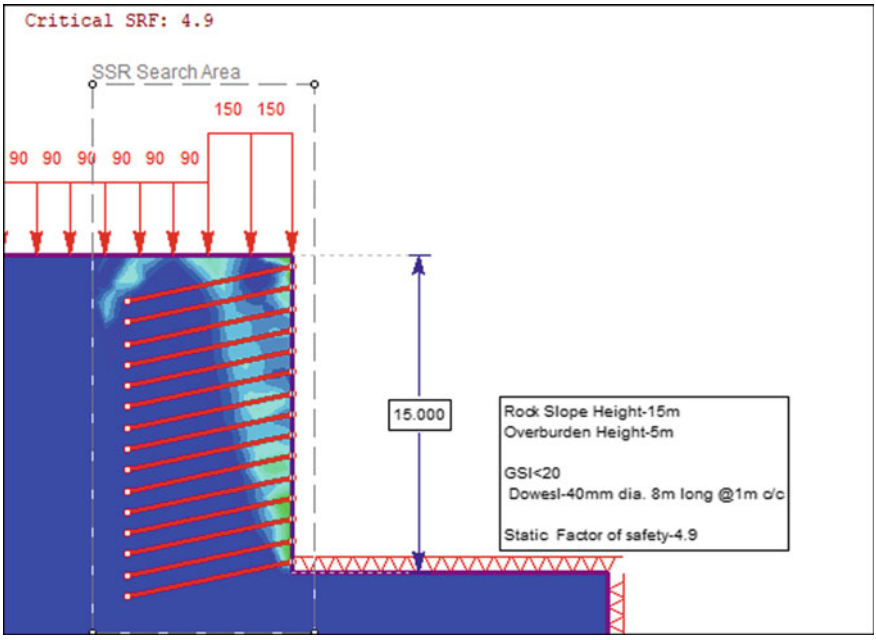

Fig. 10 Typical result of circular failure analysis of metro station excavation

Hoek Brown failure criterion has been used to represent the strength of the rock mass. Analyses have been carried out for three rock mass classes represented by GSI ranges: GSI > 40, GSI 20 to 40 and GSI < 20 and for all possible ranges of overburden against height of rock slope to determine the factor of safety for each case. Overburden thickness above rock head is applied as a surcharge at rock head level.

From the analysis, it has been estimated that spot bolting length of 4 m is required for slope stability. The length and spacing of rock bolts required for systematic bolt has been determined from the analysis for various cases of rock mass quality and depths of overburden and rock mass.

6 Instrumentation and Monitoring

Instrumentation and Monitoring forms an integral part of design. This has been recommended during the excavation of station to verify/alert the designer/contractor about the recorded values. In this regard, optical targets were installed on the rock slope to measure the 3D deformations of soil and rock mass within the excavation. Load cells are also installed at some dowels to understand whether the actual forces are same as anticipated forces or not.

7 Comparative Analysis

Methods for rock slope stability can be categorized into three: (1) Analytical methods by limit equilibrium analysis, (2) Empirical methods and (3) Numerical methods. In limit equilibrium analysis, factor of safety of the slope is calculated with unique procedures for wedge, plane, circular and toppling failures. Slope Mass Rating (SMR) is an empirical method developed to use in slopes as a sequel of Bieniawski's Rock Mas Rating (RMR) system by Romana [9]. Guidelines were proposed based on SMR for application of remedial measures.

Numerical analysis by RS^2 of Rocscience Inc. has been used to estimate a critical strength reduction factor which is equivalent to factor of safety of the slope. The basic concept is to reduce the strength parameters by a certain factor and to compute finite element stress analysis. The process is repeated for different values of Strength Reduction Factor (SRF) until the model becomes unstable, which corresponds to the critical Strength Reduction Factor (critical SRF) of the slope.

All methods have their own advantages and disadvantages. Empirical method by means of SMR can be used to predict the support system from rock mass classification and geological characterization of rock-rock joints. This method helps us to predict the probable type of failure and to alert the designer and site engineers about the critical face of excavation. Analytical methods by limit equilibrium analysis do not help us to predict the mode of failure. But this method helps to determine the

stability of slope by calculating the factor of safety. Unlike other methods, numerical analysis considers more geotechnical parameters and results of the analysis are to be interpreted by keeping in mind degree of uncertainty involved in estimation of parameters. Reliability of results of numerical analysis is dependent upon the quality of input parameters and the assumptions involved.

8 Conclusions

Rock cut slope of the metro station has been analysed for wedge failure, planar failure, toppling failure and circular failure, and appropriate support arrangement is recommended. Analysis performed leads to the conclusion that the planned cut slope will be safe with the recommended support system varying from spot bolting arrangement to systematic bolting arrangement depending upon the site conditions encountered.

From the analysis, it has been estimated that spot bolting length of 4 m is required for slope stability. The length and spacing of rock bolts required for systematic bolt has been determined from the analysis for various cases of rock mass quality and depths of overburden and rock mass. Since the rock slope is vertical, shotcrete of 100–150 mm thickness with wire mesh is recommended to be applied for safety during excavation and to prevent erosion and weathering of rock-rock joints. 75 mm dia. 3 m long drainage holes have been recommended to release the water pressure from the rock slope.

During excavation, no slope more than 2.5 m depth was not kept unsupported. The extent of blasting matched with the rock condition so as not to over fracture the rock mass. Wire mesh was always fully covered with shotcrete to prevent corrosion by wetting and drying cycles. Whenever the joint conditions assumed for the analysis did not match with design assumptions, slope support system was revised to suit to the site conditions encountered.

Rock slope stability involves estimation of parameters of rock mass and rock-rock joint. The parameters shall be applied with adequate engineering judgement and after elaborate discussion among the stakeholders. The design approach must be followed in such a way that all the available methods shall be exploited to the core. Scenarios corresponding to each and every probability shall be forecasted. The parameters are to be assigned by considering the safety of the metro station. Risks involved in the omission and admission of all the scenarios shall be identified and mitigation system shall be derived accordingly.

References

1. IS 13365-Part 3: Quantitative Classification System of Rock Mass—Guidelines: Determination of Slope Mass Rating. Bureau of Indian Standards, New Delhi (1997)
2. Hoek, E.: Practical Rock Engineering (2006)
3. Wyllie, D.C., Mah, W.: Rock Slope Engineering, 4th edn. CRC Press (2004)
4. IS 14448: Code of Practice for Reinforcement of Rock Slopes with Plane Wedge Failure. Bureau of Indian Standards, New Delhi (1997)
5. Goodman, R.E., Bray, J.W.: Toppling of rock slopes. In: Proceedings of the Specialty Conference Rock Engineering for Foundations and Slopes, pp. 201–234. American Society of Civil Engineers, Boulder, CO. (1976)
6. Hoek, E., Bray, J., Boyd, J.: The stability of a rock slope containing a wedge resting on two intersecting discontinuities. Quart. J. Engng Geol. **6**(1), 22–35 (1973)
7. Goodman, R., Shi, G.: Block Theory and its Application to Rock Engineering. (1985)
8. RS^2 v9.0. Elasto-plastic Finite Element stress analysis program for underground or surface excavations in rock or soil. (2016)
9. Romana, M.: New adjustment ratings for application of Bieniawski classification to slopes. In: Proceedings of the International Symposium on the Role of Rock Mechanics in Excavations for Mining and Civil Works. International Society of Rock Mechanics, pp. 49–53, Zacatecas. (1985)
10. IS: 1893-Part 1: Criteria for earthquake resistance design of structures. Bureau of Indian Standards, New Delhi (2002)
11. RocData Version 5.007, Rocscience Inc

Design of Core of Earthen Dam by Replacement with Geosynthetics

Asif Ali Mohammed, S. Sasanka Mouli, and J. Y. V. Shiva Bhushan

1 Introduction

Earthen dams are constructed with easily available soil in the surrounding area. The main components of the embankment consist of an outer shell, inner core, and drainage layer. Seepage is one of the prominent concerns in earthen dams since they are constructed by porous soil. Many embankments were failed due to seepage problems [1]. The major role of the inner core is to control the seepage through the embankment. Hence, the core material is chosen in such a way that it has low permeability. However, the availability of compatible clay in the vicinity of the embankment construction site might be difficult and may incur so much transportation cost to transfer the clay to the site. In various conditions, the volume of core might be increased to a large extent in order to control seepage through the earthen dam. The stability of slopes may be critical if the pore water pressures in the dams increase beyond the permissible limits [2]. Hence, proper care has to be taken in the construction of the embankment to control the seepage amount [3].

Nowadays, geosynthetics have many applications in the construction field. Over the past few decades, these have been widely used as they serve various functions in Embankment dams. Some of them are drainage, filtration, reinforcement, water barrier, and surficial erosion control. The main aim of using geosynthetics in dams is to prevent excessive leakage and minimize the material cost of the core section of the earthen dam. This study introduces geosynthetic clay liners into the core region instead of drains to control seepage. GCL will perform as a water barrier which is

A. A. Mohammed (✉) · S. S. Mouli · J. Y. V. S. Bhushan
VNR Vignana Jyothi Institute of Engineering and Technology, Hyderabad 500090, India

S. S. Mouli
e-mail: sasankamouli_s@vnrvjiet.in

C. N. V. Satyanarayana Reddy et al. (eds.), *Stability of Slopes and Underground Excavations*, Lecture Notes in Civil Engineering 185,
https://doi.org/10.1007/978-981-16-5601-9_7

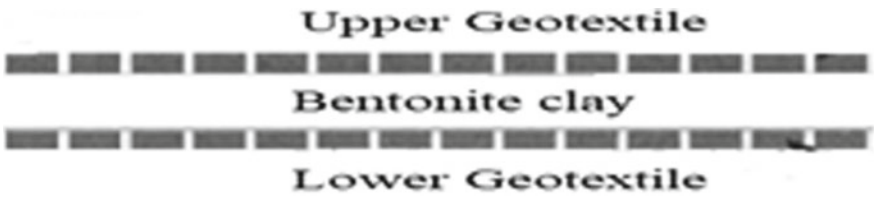

Fig. 1 Geosynthetic Clay Liner

made up of bentonite clay sandwiched with geotextile or geomembrane as shown in Fig. 1 [4]. Aoyama [5] concluded that Geosynthetic Clay Liners can be used in earthen dams in the way it was used in the landfill.

2 Methodology

An earthen dam was considered and the seepage and slope stability analysis was carried out with and without the geosynthetic Clay Liners. In the present study, limit equilibrium software-GeoStudio 2012 [6, 7] was used for the analysis. This software is capable of performing stability analysis of embankment in steady and transient seepage conditions with 2D geometry [8].

The geometrical dimensions are considered from Chahar [9] as shown in Fig. 2. The upstream slope of the dam was considered as 1 Vertical: 3 Horizontal. The downstream slope of the dam was taken as 1 Vertical: 2.5 Horizontal. The depth of water from the base in the reservoir is 30 m. However, the total height of the embankment was 33 m. The slope of the centrally symmetric core was considered

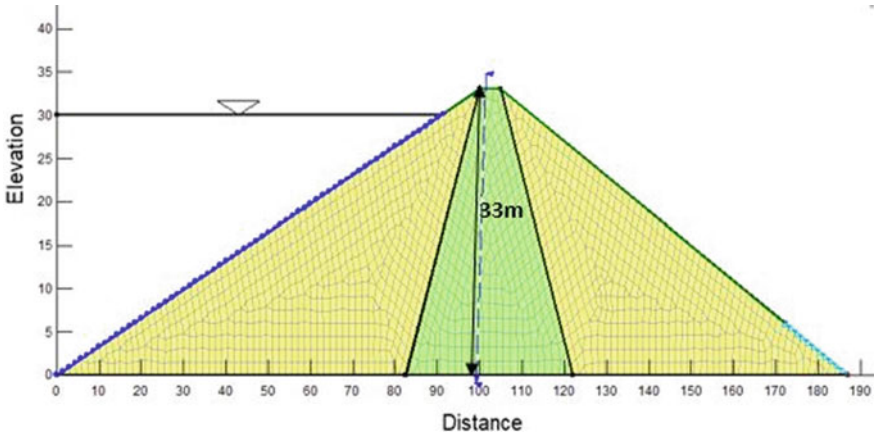

Fig. 2 Sketch of earthen dam

Table 1 Parameter used in seep/w analysis

Material	k (m/s)	θ_s (cm^3/cm^3)	θ_r (cm^3/cm^3)
Sandy clay	1×10^{-5}	0.4300	0.1090
Clay core	1×10^{-9}	0.4750	0.0900
GCL	1×10^{-11}	0.500	0.0700

1 V:0.5 H. The outer shells of the dam were constructed with homogeneous material (sandy soils) and the core with clayey deposits.

Calamak and Yanmaz [10] described van Genuchten technique used in SEEP/W modeling for saturated/unsaturated conditions of soil material. The parameters required for van Genuchten technique are mentioned in Table 1, where k is hydraulic conductivity, θ_s is saturated water content, and θ_r residual water content. Seepage analysis of the embankment for both steady state and sudden drawdown (transient state) conditions were analyzed using SEEP/W [6]. In the modeling of the earthen embankment, medium mesh size was adopted and other boundary conditions were specified. Filter was modeled at the toe of the downstream side. In the steady-state flow condition, the bottom 5 m of the downstream face was considered as a potential seepage face. Geosynthetic Clay Liner was placed at the upstream of the core of the dam. GCL was introduced in the core of the earthen dam, in the form of steps (1 m rise and 0.3 m wide) for the ease of construction. GCL layer was simulated as a single material with 10 mm thickness and hydraulic conductivity as 1e-11 m/s. Later a 3 m clay strip was replaced with outer shell material as shown in Fig. 3.

After the seepage analysis, the updated pore water pressures were used for the slope stability for both the upstream and downstream slopes using SLOPE/W [7]. Slope stability analysis was examined after the steady-state and transient seepage

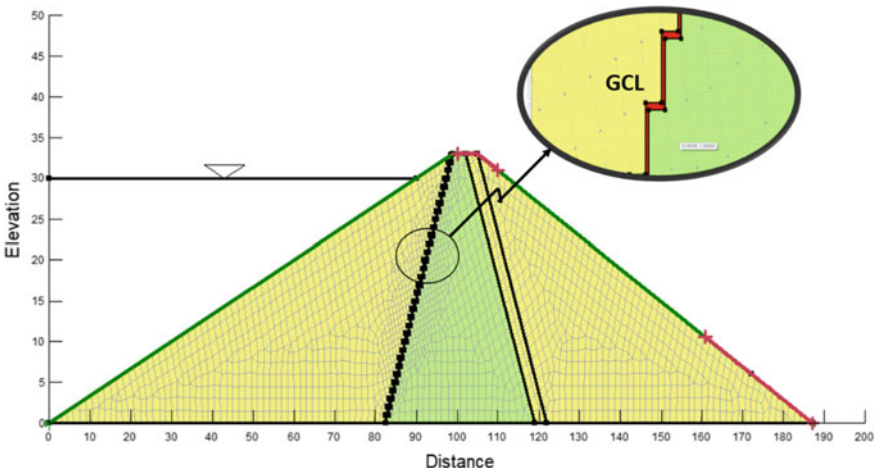

Fig. 3 Inclusion of GCL with reduction of the core area

Table 2 Soil properties for slope stability analysis

Material	Υ (kN/m^3)	φ (degrees)	c (kPa)
Sandy clay	19	34	10
Clay core	17	26	100
GCL	15	20	120

analysis. The Morgenstern–Price method was adopted for the slope stability analysis. The entry-exit method was adopted for the calculation. The properties used for analysis are unit weight (Υ), cohesion (c), and angle of shearing strength (ϕ) listed with values in Table 2.

3 Results

The seepage analysis was performed and discharge quantity was found through SEEP/W. Slope stability analysis was done in continuation of it through SLOPE/W and the factor of safety was found.

3.1 Embankment Without the Inclusion of GCL

In Fig. 4, results from the seepage analysis were shown. Contour lines represent the pore pressure in the embankment and the top blue line represents the phreatic line.

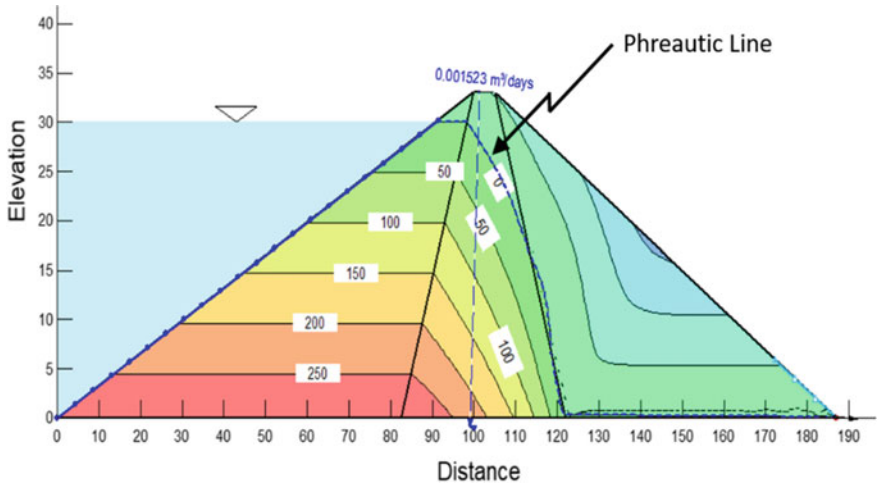

Fig. 4 Steady-state seepage and discharge across the sections of embankment

The discharge flow through the embankment was observed to be 1.52e-3 m^3/day. Pore water pressure was about $\Upsilon_s H$ on the upstream side. However, the pore water pressure reduced drastically in the core because the outer shell in the upstream side of the core will dissipate water from low-permeable zone. It is found that the critical slip surface of the downstream side of embankment in case of steady seepage flow gives a factor of safety of 1.9 which is safe for the stability of earthen dams (Fig. 5).

A rapid drawdown condition was also considered for the analysis. It was assumed that the water level in the reservoir was emptied suddenly to zero level in 5 days. In this condition, the soil in the upstream slope experiences undrained loading. Figure 6 shows the pore water pressure contours in the transient condition. It can be observed that water seepage is observed from the upstream side. In this condition, upstream side slope stability is critical as the pore water pressures are high in the upstream

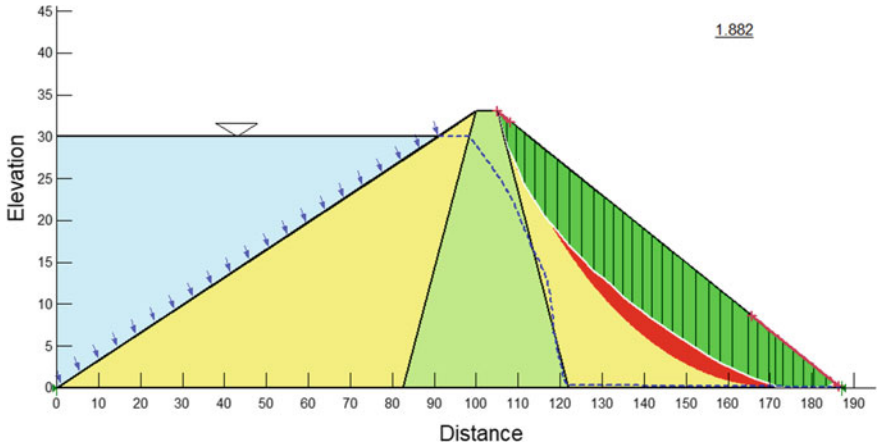

Fig. 5 Critical slip surface of the downstream slope in steady-state seepage analysis

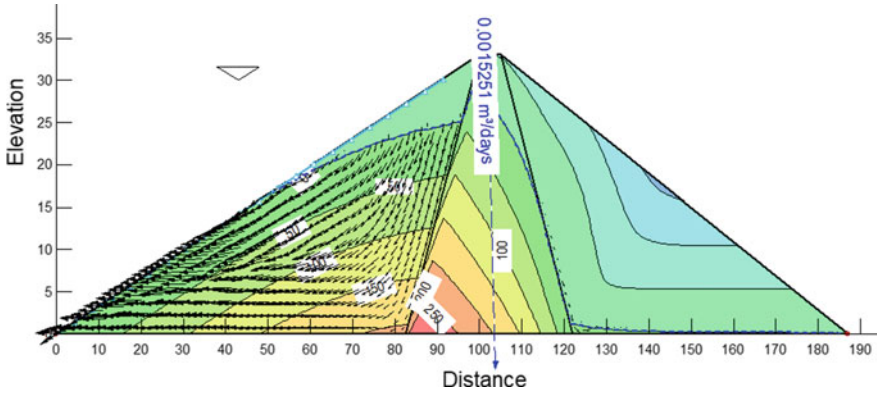

Fig. 6 Pore water pressure contours in transient seepage condition without GCL case

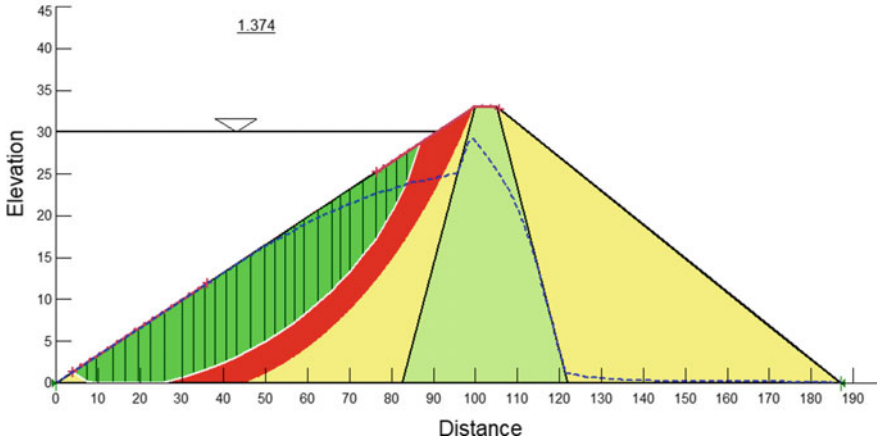

Fig. 7 Critical slip surface of the upstream slope in transient seepage analysis

side slope. The capillary action influences the stability of the upstream side of the embankment, whose factor of safety is 1.374 (Fig. 7).

3.2 Embankment with Inclusion of GCL

Geosynthetic Clay Liner was introduced in the embankment as shown in Fig. 3, which has lower permeability than that of the core material. Figure 8 shows the steady seepage flow in the embankment with GCL. In this case, the clay core section was reduced by 15% (by volume). The discharge rate was observed to be 1.19e-3 m^3/day through the cross-section of the embankment. The discharge rate was observed to be reduced by about 22% from the case without GCL. In Fig. 9, in the steady seepage

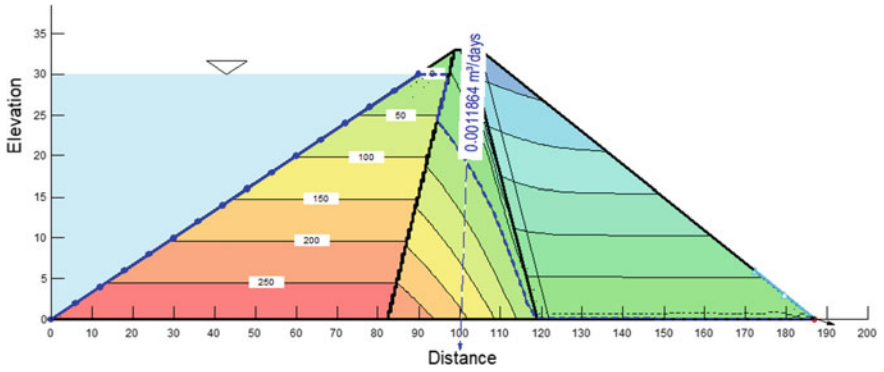

Fig. 8 Steady-state seepage and discharge flow

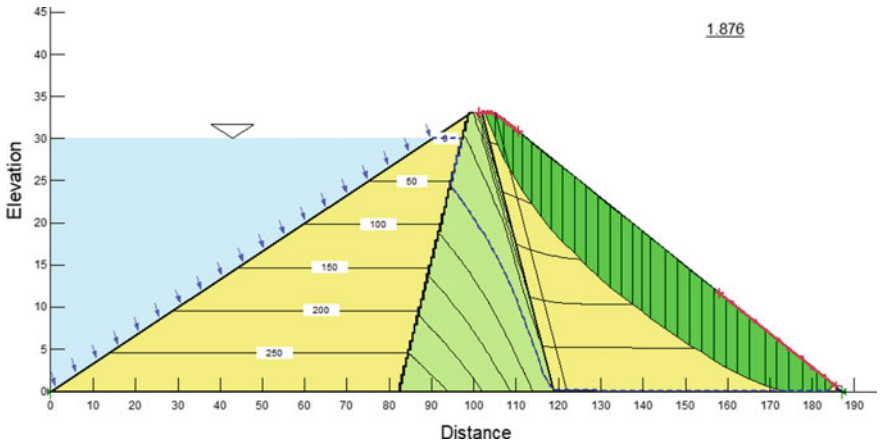

Fig. 9 Critical slip surface in steady seepage analysis

flow condition, the factor of safety of the downstream side slope after the inclusion of GCL was 1.87 which is slightly lower than that of without the inclusion of GCL. However, the reduction was negligible.

Rapid drawdown state of embankment after introducing geosynthetic clay liners and by partially replacing with core lowers the phreatic line as shown in Fig. 10.

Negligible change in the pore water pressures with and without providing the GCL layer. However, the factor of safety of the upstream side of the embankment is 1.58 (Fig. 11).

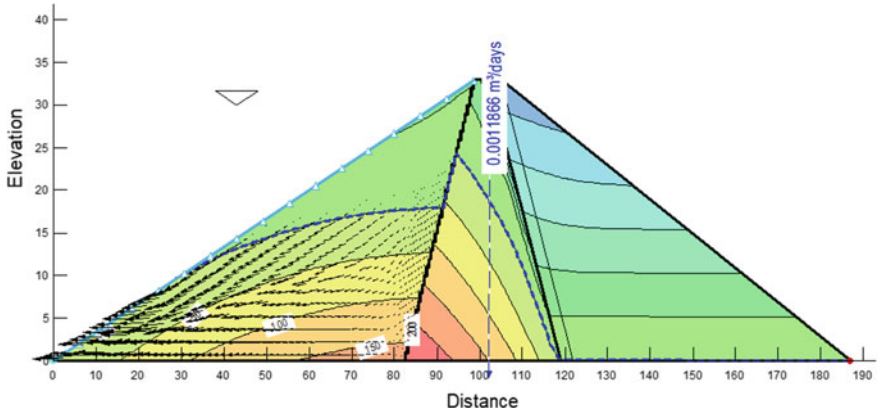

Fig. 10 Transient seepage and discharge flow

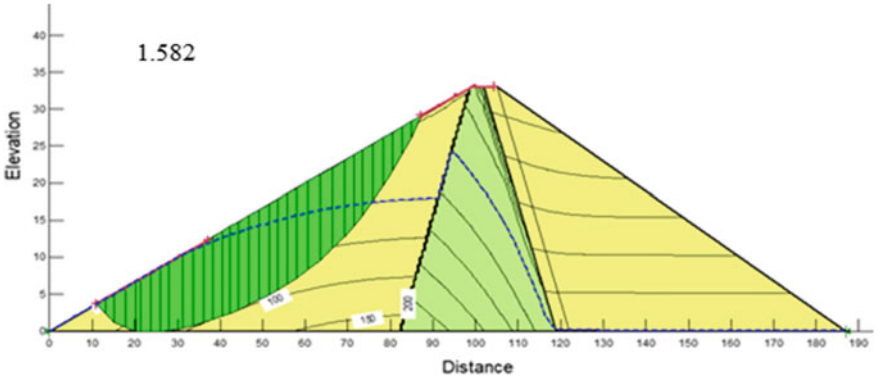

Fig. 11 Critical slip surface for the upstream side in rapid drawdown condition

4 Conclusion

The analysis was carried in both steady seepage and transient conditions. The effect of providing GCL on seepage flow and the factor of safety was well understood. The following conclusions were drawn from the study:

1. With the inclusion of GCL, discharge quantity through the embankment dam was reduced by 22% in both static and transient conditions.
2. Reducing clay core size by including Geosynthetic Clay Liners does not alter the upstream and downstream stability in both transient and steady seepage state of the embankment. Hence, the GCLs can be used at places where the clay availability is scarce.

References

1. Foster, M., Fell, R., Spannagle, M.: The statistics of embankment dam failures and accidents. Can. Geotech. J. **37**, 1000–1024 (2000). https://doi.org/10.1139/t00-030
2. Singh, B.R.S.V.: Engineering for embankment dams. A.A._Balkema_Publishers (1995)
3. Calamak, M., Yilmaz, A.N., Yanmaz, A.M.: Performance evaluation of internal drains of earthen dams. J. Perform. Constr. Facil. **32**, 04018085 (2018). https://doi.org/10.1061/(asce)cf.1943-5509.0001232
4. Shukla, S.K., Yin, J.-H.: Fundamentals of Geosynthetic Engineering. Taylor and Francis Ltd. (2006)
5. Aoyama, M.: Rehabilitation of irrigation ponds using bentonite sheets. Water L Envi. Eng. **79** (2011)
6. Geo-slope international (2012) Seepage modeling with SEEP/W. Calgary, Canada
7. Geo-slope international (2012) Stability Analysis with SLOPE/W. Calgary, Canada
8. Calamak, M., Melih Yanmaz, A., Kentel, E.: Probabilistic evaluation of the effects of uncertainty in transient seepage parameters. J. Geotech. Geoenvi. Eng. **143**:06017009 (2017). https://doi.org/10.1061/(asce)gt.1943-5606.0001739

9. Chahar, B.R.: Determination of length of a horizontal drain in homogeneous earth dams. J. Irrig. Drain. Eng. **130**, 530–536 (2004). https://doi.org/10.1061/(asce)0733-9437(2004)130:6(530)
10. Calamak, M., Yanmaz, A.M.: Uncertainty quantification of transient unsaturated seepage through embankment dams. Int. J. Geomech. **17**, 04016125 (2017). https://doi.org/10.1061/(asce)gm.1943-5622.0000823

Investigation and Design of Remedial Measures for Landslide in Hunthar Veng, Mizoram—A Case Study

M. Vinoth, P. S. Prasad, Sudhir Mathur, and Kishor Kumar

1 Introduction

Aizawl city is the capital of Mizoram and Hunthar Veng is one of the important areas of Aizawl town. Hunthar Veng is situated in the Western limb of Aizawl anticlinal ridge, which is below Chanmari West [1]. The area is located at a height of 1188 m above Mean sea level (MSL). The proposed problematic area, i.e. landslide and sinking area below Vaivakawn, Hunther Veng, Aizawal, is located on NH-54 at Km 179.50. The Hunthar landslide area, as informed by neighbouring people of the area and reported by PWD Mizoram, has started during the years 1993 (June), continued in 1995 (June), 2009 (July) and 2012 (August); the road formation had sunk for a length of 100 to 120 m. (Approx.). However, in the year 2016 alone it has sunk up to 2 m. It gets reactivated every year after the torrential rain. On August 2016, landslide took place due to heavy and incessant rains. The area currently affected by landslide covers 126886 sqm, affecting more than 100 houses as shown in Fig. 1. The total affected length is about 490m and with a width of 185m at the top and gradually tapering at toe portion. If this landslide remains unchecked even for one more monsoon, it could result in total blockage of highway which would result in shortage of food and essential daily basic needs of Aizawl city. In order to ensure safety of the people living near the slide area and for people travelling through this area daily and also for the entire economy of Mizoram, it was decided to stabilise the slope with suitable remedial measures with no further delays. This paper describes the complete analysis as carried out on the affected slope and remedial measures for mitigating the landslide. Remedial measures were worked out especially to stabilise the upper thick layer of debris that are located along the affected area as no bed rock

M. Vinoth (✉)
CSIR-Central Building Research Institute, Roorkee, India

P. S. Prasad · S. Mathur · K. Kumar
CSIR-Central Road Research Institute, New Delhi, India

C. N. V. Satyanarayana Reddy et al. (eds.), *Stability of Slopes and Underground Excavations*, Lecture Notes in Civil Engineering 185,
https://doi.org/10.1007/978-981-16-5601-9_8

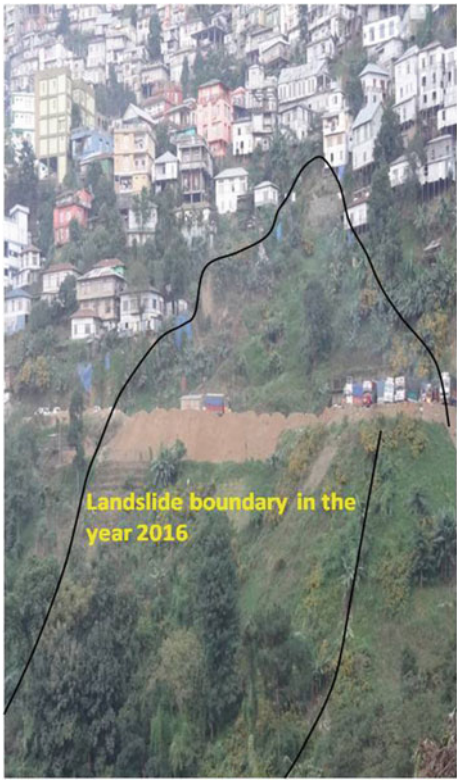

Fig. 1 Hunthar landslide and sinking area (Ch: 179/500 km on NH-54)

has been observed in the subsidence zone. Another major factor considered in the stability analysis was water table, because most of the landslides in the region are found to occur during the monsoon period. During monsoon, overburden material gets saturated, resulting in the reduction of its shear strength and increase in pore water pressure, which decreases the slope stability.

2 Geology

The soil formation in the Hunthar Veng area, in general, is of loose sedimentary type with high porosity and permeability. The top of hills being capped by sandstone having sufficient porosity, rainwater infiltrates down to interface with impervious clayey shale layers (Fig. 2) and exit to the surface due to gravity. While coming out through the shale/silty soil layers, the water carries with it the slope forming material from down below. It results into the subsidence of the area. It was also indicated that there are lot of water channels in the landslide affected area, out of which some are visible and some of them are required to be unearthed.

Fig. 2 Shale and interbedded siltstone–shale at the road section of NH-54

3 Site Description and Assessment of Causative Factors for Landslide

In order to investigate the causes of the sinking/sliding area and to suggest suitable measures for permanent stabilisation of the sinking/sliding area, which affect Vaivakawn, Chandmary West and Hunther Area of Aizawal City by designing the suitable scheme of remedial measures in form the of appropriate structures and a network of drainage systems, the entire area was surveyed by the investigating team. The photograph of the affected slide above the National highway is shown in Fig 3. It was observed that the total affected area due to the landslide was 1,21,107.00 sq.m, however, the length of NH affected was 420 metres. Fig 4 shows the affected area on the down side slope of the highway. It can be seen that the down side slope almost sank by 2 m from the existing road level. In order to drain out the surface

Fig. 3 Affected area above national highway

Fig. 4 Sinking/sliding of national highway

runoff water from the uphill side of the slope, two water channels as shown in Fig. 5 were provided but it was observed that it was choked and broken and therefore not very effective in draining out surface runoff.

Based on the site visit and preliminary investigations, the following factors were found to be the causative factors triggering landslide:

- **Hydrological condition**: It is one of the most important parameters for triggering landslide and slope instability. Most of these landslides occur during the monsoon period. During monsoon, the rock and overburden material gets saturated, resulting in reduction of its shear strength and increase in pore water pressure, which decreases the slope stability.

Fig. 5 Condition (eroded and broken) of side drains adjacent to affected slide

- **Surface water**: During investigation, it was observed that the area is lacking improper road side and surface drainage system and also sewage system which induced instability of slopes that triggered landslides.
- **Toe erosion by nala**: During monsoon season/periods of intense rain, heavy discharge of rainwater in the Vaivakawn stream and Biakin (Church) Kawr nala scours the toe of nala bank slopes and induces slumping tendency in the overburden material which causes the instability (subsidence) in the area.
- **Gully erosion**: The subsidiary drains/gullies formed in the slide/subsidence zone have also contributed instability in the area due to erosion along slope.
- **Habitation**

  (a) Existence of massive multi-storey buildings at the crown and side part of the slide.
  (b) Construction of buildings without taking into account the natural slope factors.
  (c) Foundation of the houses/building, are found to be anchored in the overburden material, which has a higher risk of sliding down.
  (d) Loads of the buildings reduce the bearing capacity as well as shear strength of the overburden material resulting in development of ground cracks and distresses in the houses.

- **Anthropogenic activities**

  (a) Changing the existing slope by cutting slopes unscientifically.
  (b) For construction of Civil Structure and houses, existing slope angle has been cut steeply.
  (c) Over large area vegetation cover has been removed, which lead to high surface runoff.
  (d) NH is constructed through the slide area where some portion is cut and filled which is not well compacted.

4 Subsurface Profile and Design Parameters

Sub-soil investigation in Hunthar Veng area was carried out through three bore holes (BH-1, BH-2 and BH-3) as shown in Figure 6. Table 1 shows the typical sub-soil profile obtained from BH-3. The sub-soil profile in the region consists of two types of materials, top loose debris and followed by Highly Weathered Rock (HWR) (Fig. 7). Survey has been carried out in landslide area and the typical cross-section of affected landslide area is shown in Fig. 8. The entire stretch has been split into three sections (top, middle and lower). The vertical and horizontal depth of debris varies along these sections which are given in Table 2.

Choosing proper input parameters is an important step in slope stability analysis. Therefore, input parameters like shear strength of the soil and rock, bulk density and degree of saturation for different sub-soil layers needs to be selected meticulously.

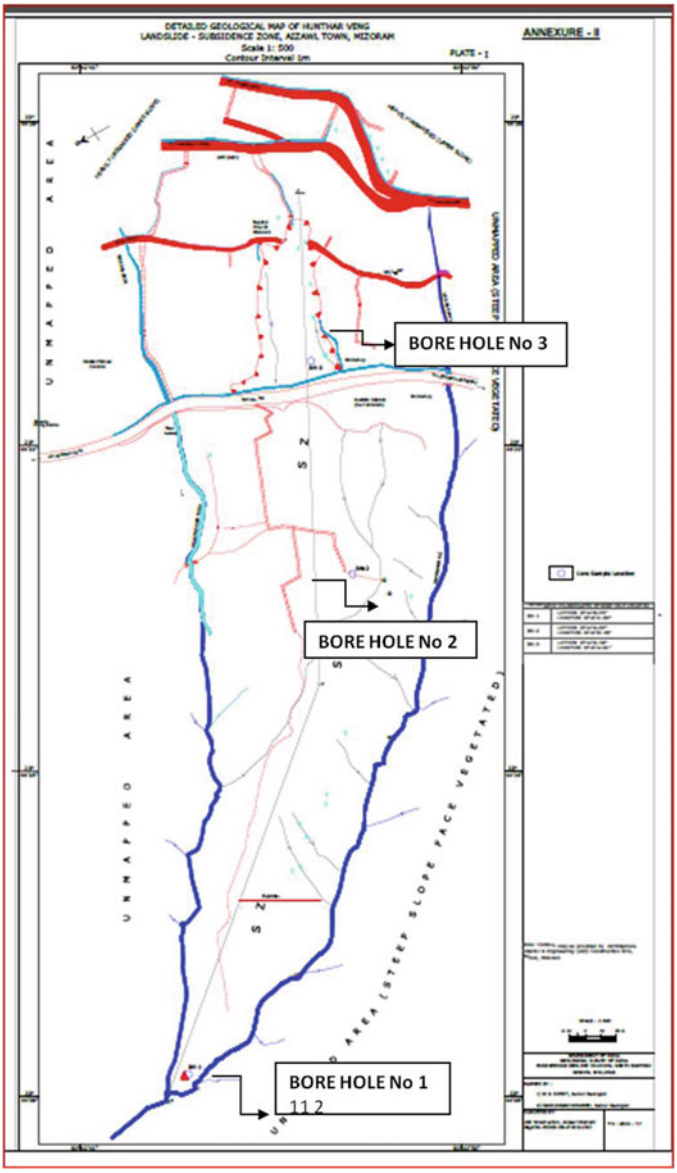

Fig. 6 Location of boreholes

Table 1 Sub-soil profile in the landslide area

Depth, m	Rock type
0.0−1.50	Sandy soil + shale type rock
1.50−3.00	Silt + shale type rock
3.00−4.50	Greyish silt + fine silty stone
4.50−6.00	Greyish silt + fine silty stone
6.00−7.50	Reddish silt + weathered silty stone
7.50−9.00	Greyish silt + silty stone
9.00−10.50	Greyish silt + silty stone + fine grained sandstone
10.50−12.00	Reddish silty + weathered sandstone
12.00−13.50	Reddish sandy clay + partly weathered sandstone
13.50−15.00	Partly weathered sandstone
15.00−16.50	Partly weathered sandstone
16.50−18.00	Weathered sandstone + fresh sandstone
18.00−19.50	Fresh sandstone
19.50−21.00	Partly weathered sandstone
21.00−22.50	Partly weathered sandstone + Fresh sandstone
22.50−24.00	Partly weathered sandstone
24.00−25.50	Partly weathered sandstone
25.50−27.00	Partly weathered sandstone
27.00−28.50	Partly weathered sandstone
28.50−30.00	Fresh and partly weathered sandstone

Existing shear properties were available only for top loose debris layer and not available for HWR. In order to obtain the HWR shear parameters, back analysis was carried out using Geo5 software [2–4]. Back analysis was carried out on the basis that slope is just safe (say FoS is 1) under dry condition. In back analysis, rock shear parameters were varied in order to get a FoS of 1 under dry condition. The results from the back analysis are given in Table 3.

From the back analysis, HWR shear parameters were determined. The parameters used in the slope stability analysis are given in Table 4. All the analysis was carried out under the following conditions:

- Water table at the surface of the slope (i.e. Fully saturated condition).
- Dry density condition (i.e. without water table).

As per IS 1893 (Part-1): 2016, Aizawl city falls under seismic zone category V. Hence, earthquake factors (EQ) were also included in the analysis.

Fig. 7 Rock showing poor core recovery

5 Stability Analysis

After finalising the shear parameters for debris and highly weathered rock (HWR), stability analysis of the existing slope was carried out at saturated condition and it was found prone to slide. Therefore, attempts were made to stabilise the saturated slope with various possible techniques [5]. The following options were tried to stabilise the slope and the results of the same are given in Table 5. All these options were carried in the Geo 5 Software.

- **Option 1:** Inclined and Vertical Grouted Nails.
- **Option 2:** Removal of Debris and Installation of Grouted Nails.
- **Option 3:** Stepped Slope with Cut-off Wall.

Some of the common design details adopted in all the options are given below,

- Top section was installed with both inclined and vertical grouted nails.

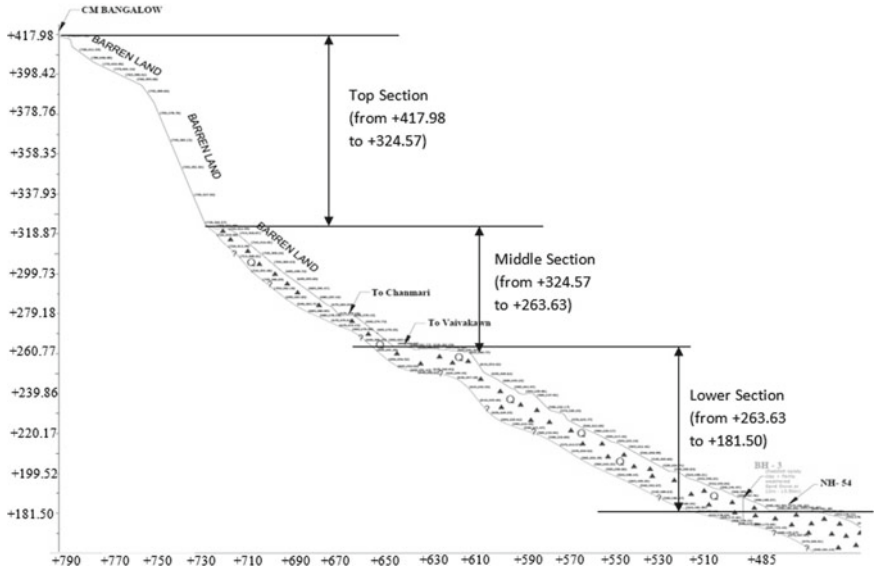

Fig. 8 C/s of affected landslide area

Table 2 Thickness of debris along affected area

Section	Thickness (m)	
	vertical	Horizontal
Top	3.0–12.0	10.0–15.0
Middle	6.0–11.0	10.0–35.0
Lower	11.0–19.0	15.0–35.0

Table 3 Back analysis results

φ'_{ef}°	Cohesion, kPa	FoS
20	150	0.77
25	150	0.88
35	100	0.93
36	75	0.85
36	100	0.95
37	75	0.87
37	100	0.98
38	50	0.76
38	75	0.89
38	100	1

Table 4 Design parameters

Description	Debris	HWR
Unit weight, γ (kN/m^3)	20	22
Angle of internal friction, φ'_{ef}°	11	38
Cohesion of soil, c_{ef} (kPa)	20	100

Table 5 Stabilised slope stability analysis results

Options	Length of nail, m	Force, kN	FoS	Stabilisation measures
1	24/36	1000/500	1.02	Grouted nails
2	36	1000/500	1.05	Berms + Grouted nails
3	24	1000	1.31	Grouted nails in top portion + cut-off walls at middle and lower portions

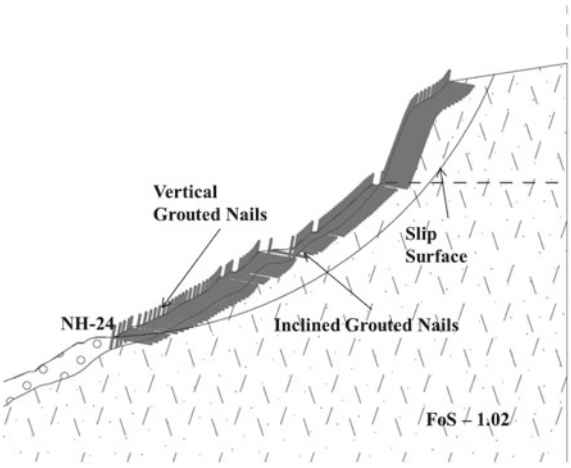

Fig. 9 Slip surface for option 1

- The length of grouted nails installed in the top section is 24m.
- Horizontal and vertical spacing adopted for grouted nail were 2 × 2 m.
- Inclined grouted nails were installed at an angle of 10° to the horizontal surface.
- 100mm diameter grouted nail was considered for the analysis.

Based on the length of nail embedment into HWR, the bond strength was considered. For top section (+790m to +730m) of the slope, HWR is located at the surface itself; hence, nail forces were considered to be 1000kN. Middle section (+730m to +645m) and lower section (+645m to +480m) of the slope debris are found at the surface; hence, nail force has been reduced accordingly to 500kN and 250kN, respectively. The above-mentioned nail forces are valid for nail lengths of 24m, when 36m long nails are used in lower section, forces in this section are increased to 500kN.

Figure 9 presents the stabilisation measures in option 1 (Inclined and Vertical Grouted Nails) with grouted nails. It can be seen that the Factor of Safety (FoS) is still less than the required limit set by the standards (1.25 [6]). Slip surface passes well below the reinforced region and it starts from the crown of the affected area and ends at the toe of the affected area; they still lead to a translational failure.

In order to improve the stability of the slope, in option 2 (Removal of Debris and Installation of Grouted Nails), it was further thought to remove the debris by 5m in vertical direction from bottom to top and making berms of suitable width, and nails were installed on the slopes created in such a manner. The results of the analysis are shown in Fig. 10. It may please be noted that even with such an arrangement, the factor of safety was found to be less than 1 as face failure occurs.

Figure 11 presents the final option 3 (Stepped Slope with Cut-off Wall). In option 3, cut-off walls were provided in the form of continuous piles (very close to each

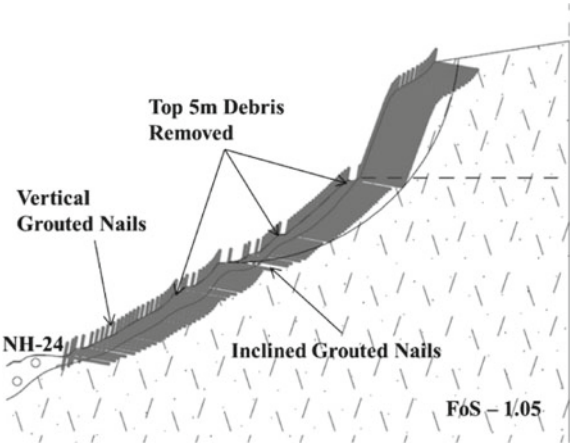

Fig. 10 Slip surface for otion 2

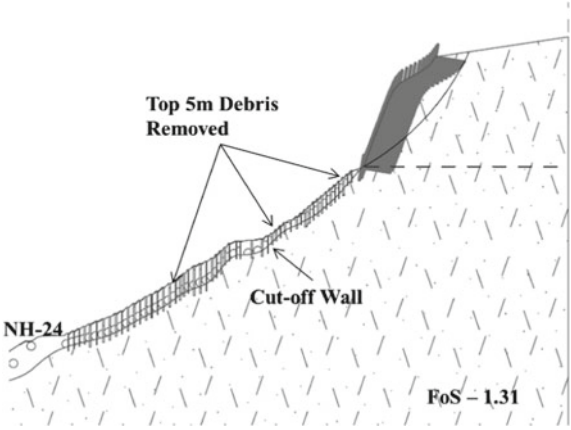

Fig. 11 Slip surface for option 3

other horizontally so that it forms a wall). They were provided from middle portion to lower portion at a vertical distance of 3m and up to a depth, where the piles are embedded into HWR at least up to a depth of 3D to 5D. Only with this arrangement a factor of safety greater than 1.2 could be obtained. All the above slope stability analysis results are indicated in Table 5.

6 Conclusions

Based on the stability analysis, it was found that the slope above the National Highway-54 is highly unstable. The factor of safety of the slope after applying different measures was not adequate except in one condition, where cut-off walls of large depth, i.e. up to 20m in depth at a spacing of 2.5–3 m from top to bottom was provided. Such a solution though analytically appears to be satisfactory would involve high cost. This may also invite many unforeseen construction related problems for which highly experienced professionals may be required to be involved.

In view of the above detailed analysis, it is opined that the remedial measures such as provision of drainage (Longitudinal and Transverse drains, RCC tube wells), vegetation and turfing, construction of retaining wall at the toe of the slope, etc., including evacuation of population close to the affected slide area be implemented.

Acknowledgement The financial support from the Disaster Management and Rehabilitation (DM&R) is gratefully acknowledged.

References

1. Detailed project report for restoration of national high way & mitigation of sinking area at Hunthar Veng, Aizawl
2. GEO 5, Geotechnical software. https://www.finesoftware.eu/geotechnical-software/
3. Moni, M., Sazzad, M.: Stability analysis of slopes with surcharge by LEM and FEM. Int. J. Adv. Struct. Geotech. Eng. **4**(3), 216–225 (2015)
4. Sazzad, M., Rahman, F.I. and Mamun, A.A.: Effects of water-level variation on the stability of slope by LEM and FEM. In: Proceedings of the 3rd International Conference on Civil Engineering for Sustainable Development (2016)
5. CRRI report on detailed investigation of problematic Hunthar landslide/sinking areas at km 179.5 on NH-54 and design schemes for suitable remedial measures
6. M 46-03.12 (2019), Geotechnical Design Manual. Washington State Department of Transportation

Stability Analysis of Tailings Dam Using Finite Element Approach and Conventional Limit Equilibrium Approach

Surender Singh, Abhishek Kumar, and T. G. Sitharam

1 Introduction

The demand of mineral products has increased substantially in the recent years due to rise in economic development resulting in the production of significant volume of tailings. 'Tailings' are the left over waste generated by the mining industries during the extraction of metals (Fe, Ni, Mn, Au, etc.), minerals (diamond, gypsum, asbestos, etc.) or mineral fuels (coal, etc.) from their respective ores. These tailings generally are fine grained crushed rocks having size predominately ranging from sandy to silty [3]. The ratio of concentrate mineral to tailings is generally considered approximately around 1:200 [6]. Hence, mining operations discharge huge volume of tailings which needs to be disposed-off effectively. Different types of approaches, such as riverine disposal, submarine disposal, backfilling, dry stacking and storage behind dammed impoundments, are used to dispose the tailings waste [6]. In order to avoid formation of surface dust (due to oxidation) and acid mine drainage, tailings are mostly stored behind water holding dams (more often called as "tailings dam") [5].

Construction of tailings dam is a continuous process where dam embankments are raised depending upon the volume of tailings waste being generated by the mining operations. By doing so, the initial cost of construction is reduced considerably. The materials used for the construction of embankments can be either borrowed (generally obtained from the impoundment area) or from the tailings itself [3]. In most cases, tailings are more often used for constructing the embankments subjected to meeting the permeability, compressibility and shear strength requirements of embankments [3]. However, use of tailings as a construction material makes the tailings dam susceptible to liquefaction, internal piping and highly erodible surfaces [12]. Based on the

S. Singh (✉) · A. Kumar · T. G. Sitharam
Department of Civil Engineering, IIT Guwahati, Assam 781039, India
e-mail: surendersingh@iitg.ac.in

C. N. V. Satyanarayana Reddy et al. (eds.), *Stability of Slopes and Underground Excavations*, Lecture Notes in Civil Engineering 185,
https://doi.org/10.1007/978-981-16-5601-9_9

relative position of crest, there are three methods which are used to construct a tailings dam, i.e., U/S method (see Fig. 1), D/S method (see Fig. 2) and centreline method (see Fig. 3) [12].

The probability of failure in tailings dams is generally found to be much greater than the conventional water retention dams. The rate of failure, in case of tailings dams, is found to vary between 1 in 700 and 1 in 1750 as compared to 1 in 10,000 (approximately) for water retention dams [2]. Further, the rate of failure is found much higher (83%) for active tailings dams as compared to inactive ones (15%) [8]. The causes of tailings dam failure can be broadly categorised into foundation failure, slope instability, liquefaction, overtopping, piping or seepage, structural and others (snow melt, mine subsidence, etc.) [8]. Moreover, it is also observed that 66% of failures occurred in those tailings dams which were built using U/S construction technique

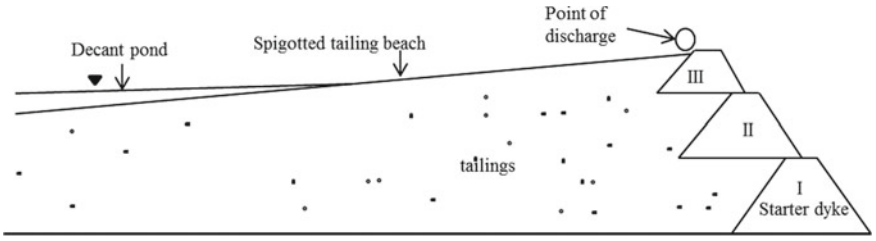

Fig. 1 U/S method of tailings dam construction (recreated after [12])

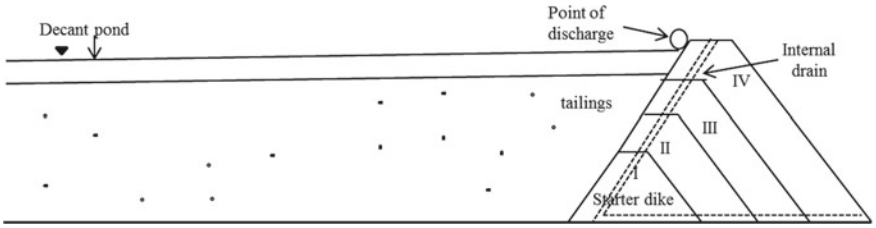

Fig. 2 D/S method of tailings dam construction (recreated after [12])

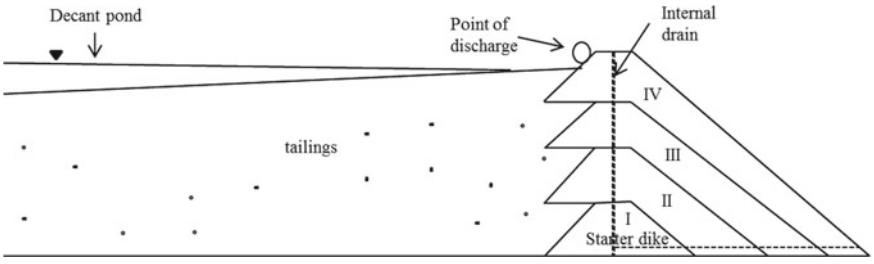

Fig. 3 Centreline method of tailings dam construction (recreated after [12])

[10]. Further, it is observed from the existing literature that the slope instability is one of the major causes, contributing more often to the failure of the tailings dams. Due to this reason, the stability of tailings dams has drawn much attention as significant numbers of tailings dam's failure had been reported worldwide in the recent years.

The present work focuses on evaluating the slope stability of existing tailings dam by using FEM as well as conventional LEMs under static loading conditions. SSR technique has been incorporated (by using 2D finite-element based package RS^2) in order to find out the potential modes of failure whereas Rocscience SLIDE-2D has been utilised to evaluate the stability of tailings dam based on LEM. The results obtained from the analyses utilizing both FEM and LEM are compared in terms of their global FOS and SRF. Further, an attempt has been made to explore the stability of different types of tailings dams, based on their method of construction (i.e., U/S method and D/S method).

2 Site Description

The data for the present stability analyses is taken from [10] related to an existed tailings dam. The reported tailings dam is situated in Rampura Agucha Mine (RAM) in Rajasthan, India (see Fig. 4). The primary product being extracted from the mine is zinc whereas it generates lead as secondary product [10]. Plan area of tailings pond is approximately 1200 m × 800 m. Figure 5 shows the dimensions of already existing tailings dam, the height of which was required to be raised from 27 to 51 m [10]. The tailings dam has U/S slope of 2H:1 V whereas D/S slope angle was considered as 36°. The top width of tailings dam (crest width) was provided as 30 m.

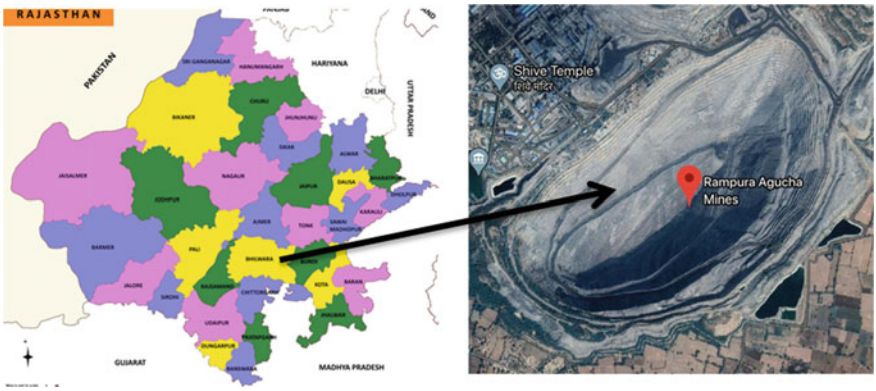

Fig. 4 RAM location (Google maps, accessed on 15th July 2020)

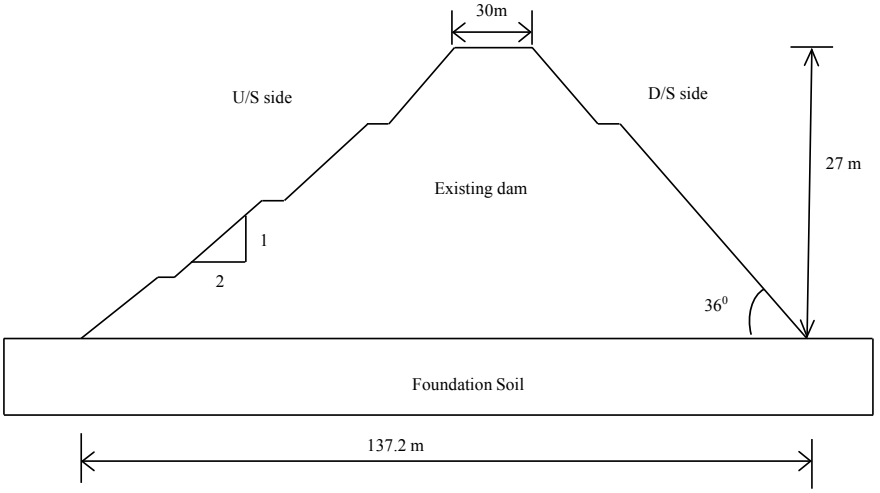

Fig. 5 Typical cross-section of RAM tailings dam used for the analysis [10]

3 Foundation Soil and Tailings Properties

The RAM tailings dam was built over low permeability soil (0.8×10^{-8} to 1×10^{-8} m/s), which was underlain by rocky strata. Table 1 presents various properties of foundation soil and tailings used in the present work. Embankments were built using mine spoil which is crushed rock waste produced during mining operations.

Table 1 Properties of materials used for the study [10]

Properties	Foundation soil	Mine spoil	Settled mine tailings
Bulk unit weight, γ (kN/m^3)	22	20.7	20
Cohesion, c (kN/m^2)	20	2	1
Friction angle, φ (°)	38	39	35
Bulk modulus, K (MPa)	40	20	10
Shear modulus, G (MPa)	20	10	5

4 Construction of Dam Embankments

It should be noted that a dam already exists of 27 m height, and in this work, the stability of dam is analysed against rise of embankment. Such rise of embankments can be done by adopting U/S method, D/S method and centreline method of construction. In the present wok, however, only D/S and U/S methods are considered as most of the existing tailings dams are constructed using these methods. In D/S method, dam embankments are raised by shifting the centreline of crest towards D/S side of tailings dam (see Fig. 6). In U/S method of construction, the height of dam embankment is raised in such a way that the centreline of crest moves towards the U/S side of tailing dam (see Fig. 7). Thus, the foundations of subsequent embankments in the

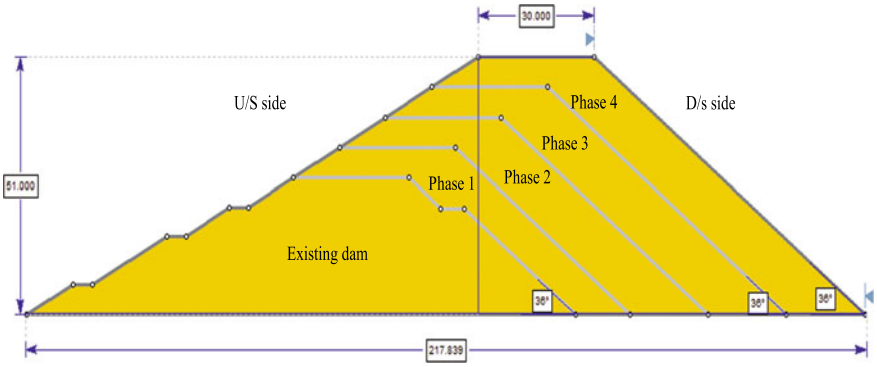

Fig.6 A typical cross-section of tailings dam at the end of construction using D/S method of construction

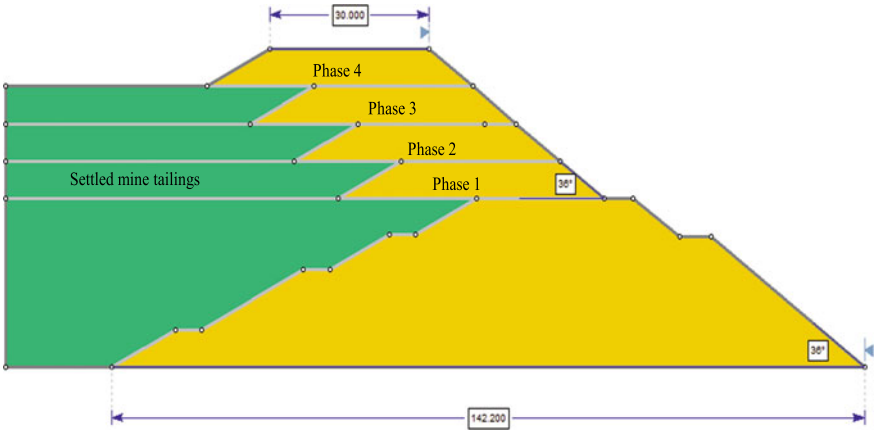

Fig. 7 A typical cross-section of tailings dam at the end of construction using U/S method of construction

U/S approach will rest over the already deposited tailings. For the present analysis, construction of tailings dam in each method is allowed to complete in four phases. In each phase, the height of embankments is raised by 6 m. In addition, the D/S slope, U/S slope and crest width in each phase are kept the same as that of already existing dam. Further, stability analyses using LEM and FEM are performed as discussed in the further section.

5 Stability Analysis Using LEM

In general, the stability of dams is assessed for three cases, i.e., at the end of construction, sudden drawdown and steady seepage. The concerned tailings dam is analysed only for the 'end of construction (only for static loading)' case as the other two cases hold negligible importance for the present tailings dam (due to material properties) (as highlighted by Sitharam and Hegde [10]). SLIDE-2D by Rocscience is utilised in the present study, which performs the stability analysis by incorporating different LEM methods. Further, Bishop's method [1], Janbu's simplified method [4], Spencer's method [11] and Morgenstern-Price method [7] are used to perform the stability of embankment slopes. Only circular slip surface is assumed for each method as the embankment material is homogeneous in nature. Moreover, slopes having slope angle >30° (36° in present case) has been mostly observed to have circular failure surface [9]. Stability analysis (for both U/S and D/S case) is performed after completion of each phase of construction.

5.1 Results and Discussion

Obtained results of stability analysis during different phases of construction and using D/S method are summarized in Table 2. It can be observed from Table 2 that the FOS value decreases as the height of tailings dam increases. However, FOS can be kept unchanged by providing suitable berm width at the end of each phase and thus maintaining the constant height of embankment [10]. By doing so, the overall

Table 2 FOS for D/S slope observed during different stages of construction using D/S method

Stages of construction	FOS based on			
	Bishop's method	Janbu's method	Spencer's method	Morgenstern-price method
Phase 1	1.228	1.204	1.223	1.224
Phase 2	1.220	1.195	1.216	1.216
Phase 3	1.210	1.188	1.205	1.206
Phase 4	1.201	1.183	1.197	1.197

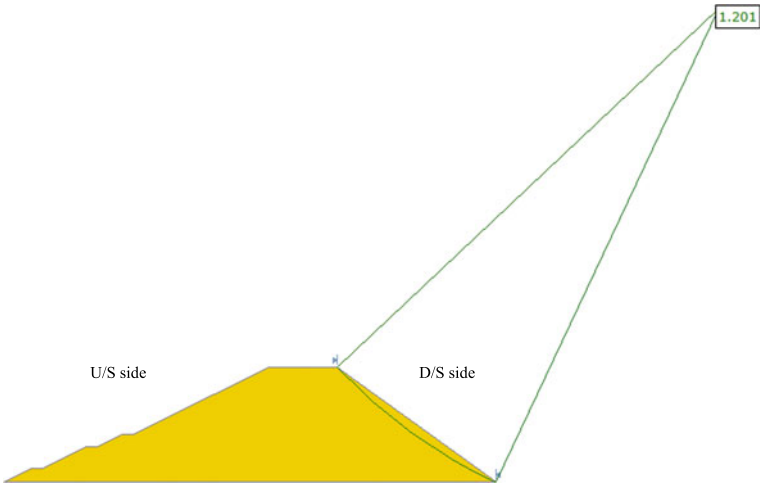

Fig. 8 A typical stability analysis result of D/S slope constructed by D/S method of construction

area occupied by dam will increase, thus increasing the material required for the construction of embankments. Further, it was observed from Table 2 that choice of different slope stability methods have negligible effect on the obtained FOS in all phases of construction. Figure 8 shows the FOS obtained for D/S slope at the end of phase 4 constructed by D/S method of construction following Bishop's method.

In case tailings dam is constructed using U/S method of construction, U/S slope might behave as a critical slope. This is due to the reason that in case of U/S method, the foundation of subsequent embankments directly rests over the tailings stored in the previous embankments (see Fig. 9). Hence, rate of raising the embankment is an important factor while raising the embankment using U/S method of construction. Moreover, in comparison to D/S method of construction, U/S method can have both U/S and D/S slopes as critical. Therefore, in order to make the outcomes of analysis

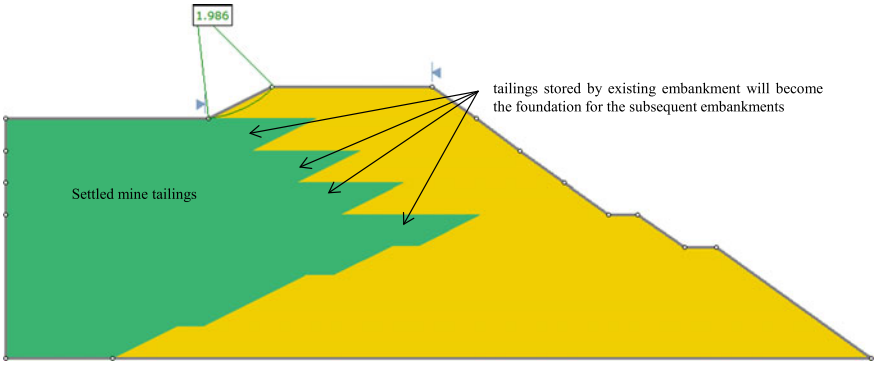

Fig. 9 A typical stability analysis result of U/S slope constructed using U/S method of construction

more reliable, FOS in the present work is calculated for both U/S slope (see Fig. 9) as well as for D/S slope (see Fig. 10). Obtained results based on the analysis, for each phase of construction and following different stability analyses methods, are summarized in Table 3 and Table 4 for D/S and U/S slope, respectively. From Table 3, the trend in the FOS is observed to be the same as it was observed in case of D/S method. It can be observed from Table 4 that the FOS is the same for the U/S slope during all phases of construction. This is due to the fact that the slope geometry used for the construction of U/S slope was kept the same in all phases of construction.

Comparing the outcomes based on both methods of construction, it can be noticed that the FOS for the embankments constructed by D/S method is less as compared to embankment constructed by U/S method. This is due to the reason that in case of D/S method, the entire D/S slope behaves as a critical slope (see Fig. 8) whereas for U/S method, only a part of D/S slope is found to be critical (see Fig. 10). However, as discussed earlier, this value of FOS can be increased for D/S slope by providing a berm of suitable width (as shown in Fig. 8), which will reduce the slope height and hence will increase the FOS [10] of D/S slope.

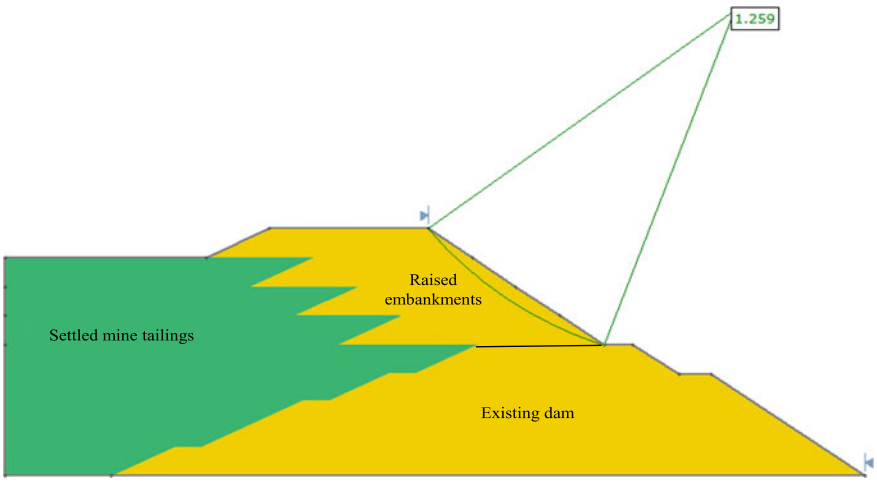

Fig. 10 A typical stability analysis result of D/S slope constructed using D/S method of construction

Table 3 FOS for D/S slope observed during different stages of construction using U/S method

Stages of construction	FOS based on			
	Bishop's method	Janbu's method	Spencer's method	Morgenstern-price method
Phase 1	1.267	1.236	1.265	1.263
Phase 2	1.267	1.236	1.265	1.263
Phase 3	1.267	1.236	1.265	1.263
Phase 4	1.259	1.230	1.253	1.255

Table 4 FOS for U/S slope observed during different stages of construction using U/S method

Stages of construction	FOS based on			
	Bishop's method	Janbu's method	Spencer's method	Morgenstern-price method
All Phases (i.e. for phase 1, phase 2, phase 3 and phase 4)	1.986	1.870	1.986	1.986

6 Stability Analysis Using FEM

Although LEM used in previous section is simple to perform, but it has certain limitations. Firstly, the technique does not consider the stress–strain behaviour of materials while calculating the FOS values. Secondly, in order to ensure the static determinacy, LEM uses arbitrary assumptions regarding the inter-slice forces. Therefore, to avoid the inaccuracy caused due to inherent drawbacks of LEM, FEM has been used more frequently in the recent years. In the present work, another set of analyses is done using RS^2 by Rocscience, which performs analysis using FEM approach. SSR technique is used to assess the stability of slopes where shear strength of a material is reduced (by reducing shear strength parameters, i.e., cohesion and angle of internal friction) in each stage, until the slope fails completely. Further, Mohr–Coulomb model is adopted to simulate the behaviour of both foundation soil as well as embankment material (mine spoil). Bottom boundaries are restrained in both vertical and horizontal direction, whereas side boundaries are restrained in horizontal direction only. These boundary conditions represent the slope stability problem in a better way. At the bottom boundary there will be hardly any displacement in x and y directions due to confinement from all the directions. Similarly, along the side boundaries, soil will be less confined in y-direction due to low overburden pressure and thus the soil particles can be allowed to displace vertically. Further, referring to Table 1, all material properties are assigned.

6.1 Results and Discussion

The accuracy of results obtained based on FEM depends upon various factors such as boundary conditions, mesh fineness, mesh gradation, and mesh shape. Therefore, optimum values of these parameters are found initially and then those values are used in the analysis. The results obtained by the FEA of the tailings dam developed using U/S method and D/S method of construction is shown in Table 5. The variation of SRF (analogous to FOS in LEM) with height is found to be similar to FOS as observed in case of LEM. SRF is observed to decrease with increase in the height of embankment. Even in FEM based analysis, the D/S slope is found critical for both the cases (i.e., for U/S method of construction and D/S method of construction) as

Table 5 Strength reduction factor (SRF) obtained for tailings dam during different stages of construction

Stages of construction	SRF	
	U/S method	D/S method
Phase 1	1.28	1.20
Phase 2	1.27	1.19
Phase 3	1.25	1.17
Phase 4	1.24	1.15

can be observed from Fig. 11 and Fig. 12, respectively. Further, the failure surface for critical slopes is observed to be approximately circular (see Fig. 12) which is in agreement with the assumption made in the LEM based analysis carried out in previous section.

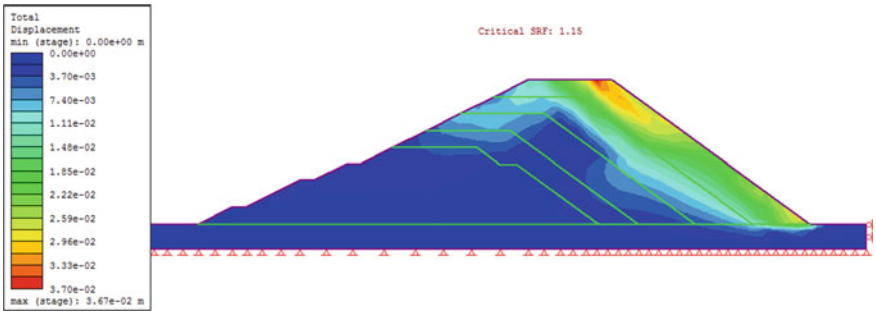

Fig. 11 SRF observed at the end of phase 4 construction using D/S method of construction

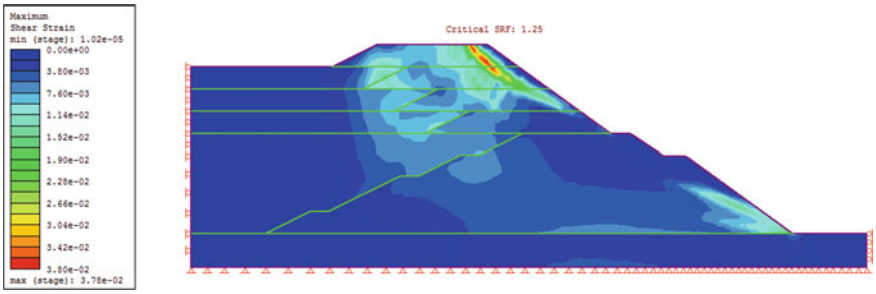

Fig. 12 SRF observed at the end of phase 4 construction using D/S method of construction

7 Comparison of Results Obtained from Lem and Fem

Previous sections highlighted the results obtained from stability analysis performed using LEM and FEM. Figures 13 and 14 show the comparison between the results obtained from FEM and LEM for both methods of construction. It can be noticed from Fig. 13 that the results obtained from FEM is a bit conservative as compared to the results obtained from LEM for the slope constructed using U/S method of construction. However, the difference between the SRF and FOS values is very less, which makes the stability analysis and hence the design quite reliable. Further, it can

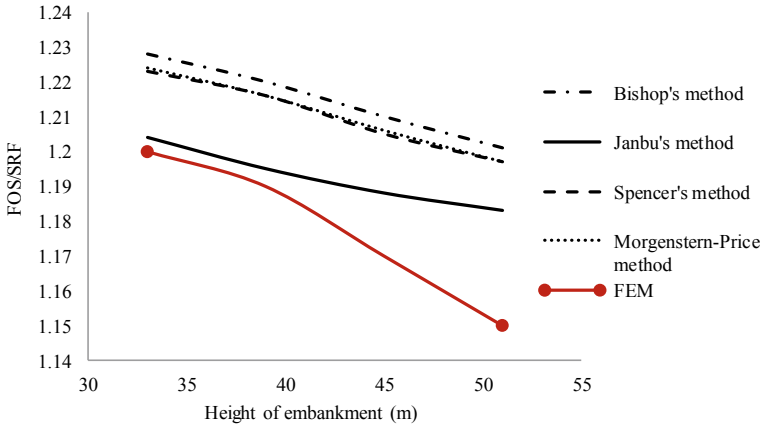

Fig. 13 Comparison of results obtained from LEM and FEM for D/S slope constructed using D/S method of construction

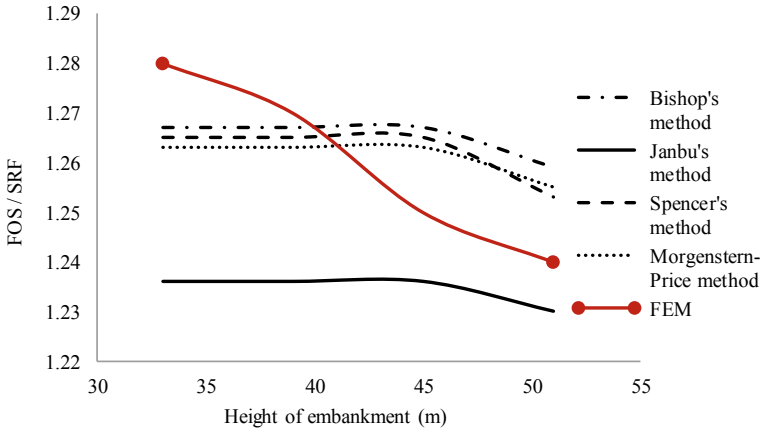

Fig. 14 Comparison of results obtained from LEM and FEM for D/S slope constructed using U/S method of construction

be also observed from Fig. 14 that FOS from Janbu's method shows least value of FOS in comparison to other slope stability methods and is U/S method of construction. Further, except for Janbu's method, FEM gives lesser SRF values at large heights (>42 m) in comparison to other LEMs. Overall, FEM gives a bit conservative results as compared to LEMs.

8 Conclusions

The current work attempts the stability analysis (static loading only) for RAM tailings dam located in Rajasthan, India, the height of which was planned to be raised from 27 to 51 m. The two widely used method of construction, i.e., U/S method and D/S method are adopted to raise the tailings dam. The stability analysis of the embankments is initially performed in SLIDE-2D program which is based on LEM. Bishop's method, Janbu's method, Spencer's method and Morgenstern-price methods of slope stability are used to perform the stability analysis. In addition, FEM is incorporated further to carry out the slope stability analysis. The FEM based analyses is carried out by using RS^2 program which uses SSR technique to perform the analysis. Results obtained from both the methods are then compared in order to make the outcome of slope stability analysis more reliable. Results obtained from LEM and FEM are found in good agreement with each other. Further, it is observed that the FOS and SRF values decreases as the height of embankment is raised. In addition, the failure surface is found to be circular in FEM for most of the critical slopes which support the assumptions of circular slip surface in LEMs. Moreover, the critical slope liable to failure is found to be D/S slope for the embankments either built by U/S method of construction or by D/S method of construction. In general, the results obtained from the FEM are found to be a bit conservative as compared to the results obtained by utilising limit equilibrium approach.

References

1. Bishop, A.W.: The use of the slip circle in the stability analysis of slopes. Geotechnique **5**(1), 7–17 (1955)
2. Davies, M.P.: Impounded mine tailings: what are the failures telling us?. CIM Bulletin., 53–59 (2001)
3. EPA: Design and evaluation of tailings dam. United State environmental protection agency, office of solid waste, Washington, DC (1994)
4. Janbu, N.: Slope Stability Computations. Wiley. Incorporated (1973)
5. Kossoff, D., Dubbin, W.E., Alfredsson, M., Edwards, S.J., Macklin, M.G., Hudson-Edwards, K.A.: Mine tailings dams: Characteristics, failure, environmental impacts, and remediation. Appl. Geochem. **51**, 229–245 (2014)
6. Lottermoser, B.: Mine Wastes: Characterisation, Treatment and Environmental Impacts. Springer, Berlin, Heidelberg, New York (2007)

7. Morgenstern, N.R., Price, V.E.: The analysis of the stability of general slip surfaces. Geotechnique **15**, 79–93 (1965)
8. Rico, M., Benito, G., Salgueiro, A.R., Díez-Herrero, A., Pereira, H.G.: Reported tailings dam failures: a review of the European incidents in the worldwide context. J. Hazard. Mater. **152**(2), 846–852 (2008)
9. Salmasi, F., Pradhan, B., Nourani, B.: Prediction of the sliding type and critical factor of safety in homogeneous finite slopes. Appl. Water Sci. **9**(7), 158 (2019)
10. Sitharam, T.G., Hegde, A.: Stability analysis of rock-fill tailing dam: an Indian case study. Int. J. Geotech. Eng. **11**(4), 332–342 (2017)
11. Spencer, E.: A method of analysis of the stability of embankments assuming parallel inter-slice forces. Geotechnique **17**(1), 11–26 (1967)
12. Vick, S.G.: Planning, Design, and Analysis of Tailings Dams. BiTech, Richmond, BC, Canada (1990)

Stability Analysis of Slopes at a Landslide Prone Area: A Case Study on the Landslide at Madikere, India

J. Sumalatha

1 Introduction

Landslides due to excessive rainfall are devastating natural disasters which occur on soil slopes due to seepage of water and cause destruction of a large range of resources (Sassa [1, 2]; Zêzere et al. [3]; Chang and Chiang [4]; Petley [5]; Shokouhi et al. [6]; Kim et al. [7]; Promper and Glade [8]; Peruccacci et al. [9]; Salvati et al. [10]). Investigations on landslides are often concluded that the failures occur when the angle of soil slope (i) exceeds the critical angle of the slope (i_c) in saturated conditionor sometimes due to the reduction in shear strength of soil caused by high levels of rainfall which increases the pore water pressure within the slope (Bishop [11]; Brand et al. [12]; Larsen and Simon [13]; Tsaparas et al. [14]; Craig [15]; Chien-Yuan et al. [16]; Dahal and Hasegawa [17]; Gui and Han [18]; Niroumand et al. [19]; Tay and Selaman [20]).

Once the slope failure is started at one part of a slope, it progresses toward the rest of the slope and becomes tough to control at the site (Wang and Sassa, 2001, [21]). From the relationship between pore water pressure and occurrence of landslide, it is obvious that the presence of an undrained soil layer multiplies the chances of landslide, if subjected to excessive rainfall (Cogan and Gratchev [22]).When a natural hazard occurs, various kinds of losses occur, but the losses related to buildings, roads, rail tracks, and other infrastructure will be given much focus (Iovine and Parise [23]; Calcaterra et al. [24]; Calò et al. [25]; Del Soldato et al. [26]). Yet, when rural areas are considered, the major losses are related to agricultural fields and land damage which cause threat to the economic development of a country.

The risk analysis for any natural hazard often considers the future damage as it provides the essential basis for strategies related to risk reduction and planning (Van Westen et al. [27]; Vranken et al. [28]). In this regard, an attempt is made to identify

J. Sumalatha (✉)
Department of Civil Engineering, M S Ramaiah Institute of Technology, Bangalore, India

C. N. V. Satyanarayana Reddy et al. (eds.), *Stability of Slopes and Underground Excavations*, Lecture Notes in Civil Engineering 185,
https://doi.org/10.1007/978-981-16-5601-9_10

the suitable ground improvement technique to avoid future landslides in this area. Two additives, fly ash and rice husk ash, were studied in different proportions, and the stability analysis was carried out to know the effect of these additives on the stability of slopes. The fly ash addition to the soil increases the strength and stability of a slope up to a height of 14.0 m (Rajak et al. [29]). Rice husk which is obtained from rice milling contains a vast amount of silica, and its global annual production is about 108 tons (Alhassan [30]). As the rice husk ash (RHA) is an abundantly available agriculture by-product, utilization of RHA in soil stabilization seems to be cost-effective, particularly in the rice-producing countries (Choobbasti et al. [31]). The aim of this paper is to study the influence of addition of fly ash and RHA on the soil strength and factors of safety (FoS) of the slopes. The slope stability analysis was carried out using Taylor's method and using GEO5 software tool.

2 Materials and Methods

2.1 Study Area

The study area is located at Makkandur, Kodagu district located in the Western Ghats of India (Fig. 1). In 2018, high rainfall was recorded (2718 mm as per Karnataka State Natural Disaster Monitoring Center (KSNDM)). This caused severe landslides, flooding, and large scale displacement of soil. More than a thousand houses were destroyed, about five thousand people were displaced, and at least 16 were killed. The average rainfall data of Kodagu district is as shown in Fig. 2.

To examine the in-situ properties of the soil at the study area, the soil samples were collected (Fig. 3) at the landslide area. The slope angle and height of the slope were also measured. The slope angles are varying from 45 to 55°, and the heights

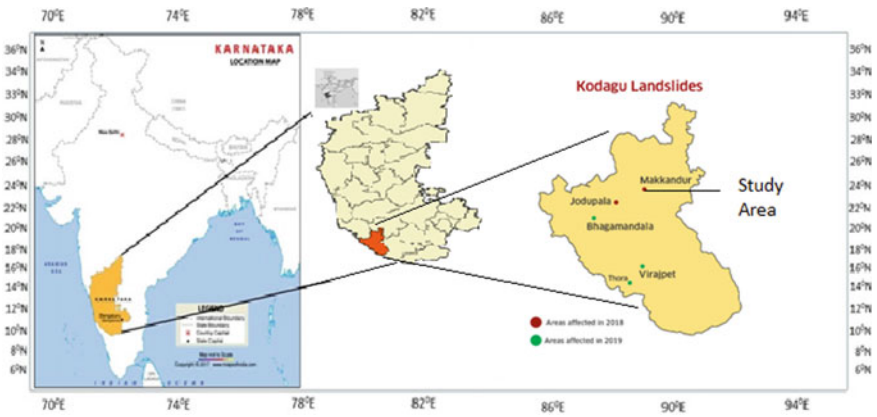

Fig.1 Site location in India map

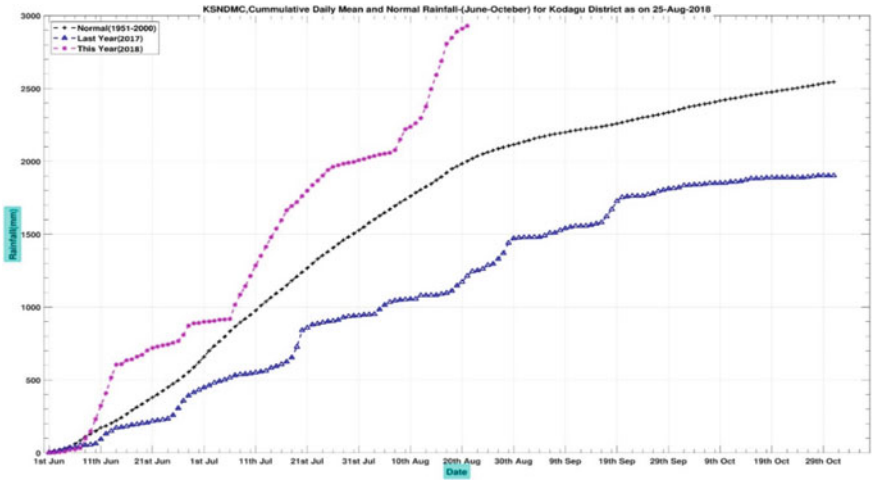

Fig.2 Average rainfall data as per Karnataka state natural disaster monitoring center (KSNDM))

of the slopes were ranging between 10 and 15.2 m. The soil is free from impurities like heavy metals. The in-situ density of soil was determined by core cutter method at 0.5 m depth.

2.2 Properties of Soil

The index and engineering properties of soil samples were as per IS 2720. The in-situ density and moisture content of the soil determined by core cutter method are 1.9 g/cc and 25%, respectively. The in-situ dry unit weight is 14.91 kN/m^3. The wet sieve analysis was carried out as per IS 2720, and the fines were analyzed using hydrometer analysis. The composition of the soil is 0.75% gravel, 40.25% sand, and 59% fines. It is classified as clay of intermediate plasticity (CI) as per Indian Standard classification. The physical properties of soil are specified in Table 1.

2.3 Properties of Amended Soil

To examine the influence of admixtures on the factor of safety of slopes, two industrial wastes, fly ash and rice husk ash, were selected. The admixtures of 5 and 10% were mixed with the soil samples, and the properties of these mixtures are as given in Table 1.

Fig.3 Collection of soil samples at landslide affected area

2.4 Stability Analysis of Slopes

The heights of slopes in the study area are varying between 10 and 15.2 m. Hence the factors of safety were estimated for 10 and 15.2 m height slopes using Taylor's method. As the slope angles are varying between 45 and 55°, an average value of 50° was taken for the analysis. The factors of safety of the slope were also estimated using the GEO5 software tool using the Bishop's method. As the degree of saturation varies with depth, the bulk unit weights at different depths were calculated and the

Table 1 Properties of soil with and without additives

S. No	Soil parameter	Soil alone	Soil amended with 5% Fly Ash	Soil amended with 10% Fly Ash	Soil amended with 5% Rice Husk Ash	Soil amended with 10% Rice Husk Ash
1	Specific gravity	2.70	2.69	2.67	2.64	2.61
2	Maximum dry unit weight (kN/m^3)	18.89	17.54	16.48	16.88	16.58
3	Plastic limit (%)	24.44	23.21	22.10	23.89	22.36
4	Liquid limit (%)	39.8	37.8	36.6	38.2	36.9
5	Shrinkage limit (%)	9.21	9.68	10.57	11.28	11.9
6	OMC (%)	16.98	18.45	20	18.52	19.1
7	Unconfined compressive strength (q_u) (kN/m^2)	70.60	92.80	97.09	90.22	94.14
8	Undrained cohesion ($Cu = q_u/2$) (kN/m^2)	35.3	46.4	48.54	45.11	47.07
9	Shear strength parameters from triaxil test (UU Test)	$C = 28$ kN/m^2 $Ø = 22^0$	$C = 32$ kN/m^2 $Ø = 28^0$	$C = 38$ kN/m^2 $Ø = 32^0$	$C = 33$ kN/m^2 $Ø = 20^0$	$C = 36$ kN/m^2 $Ø = 18.5^0$

slope is prepared using the interface option in the GEO5 software tool. The soil slope was divided into different zones depending on the degree of saturation, and the pore pressure ratio (Ru) was given as 0.5.

3 Results and Discussions

The estimated factors of safety using Taylor's method for slopes of heights 10 and 15.2 m with and without the admixtures are shown in Tables 2 and 3. The results of slope stability analysis carried out on the slopes using GEO5 software tool are shown in Figs. 4 and 5. From the values of factors of safety obtained, it was observed that the addition of 5% fly ash to the soil considerably increases the factor of safety and there is only a minimal increase in factor of safety with 10% fly ash when compared with 5% fly ash. A similar trend was followed for the rice husk ash when compared with the results corresponding to 5 and 10% rice husk ash. It was also observed that

Table 2 Factors of Safety for 10 m height slope using Taylor's method

S. No	Material of slope	FoS
1	Soil only	1.29
2	Soil amended with 5% Fly Ash	1.95
3	Soil amended with 10 Fly Ash	2.04
4	Soil amended with 5% RHA	1.90
5	Soil amended with 10% RHA	1.94

Table 3 Factors of Safety for 15.2 m height slope using Taylor's method

S. No	Material of slope	FoS
1	Soil only	0.93
2	Soil amended with 5% Fly Ash	1.24
3	Soil amended with 10 Fly Ash	1.32
4	Soil amended with 5% RHA	1.21
5	Soil amended with 10% RHA	1.24

the factors of safety are less for a slope of 15.2 m height when compared with a 10 m height slope. Hence, it is evident that the addition of fly ash/RHA to the soil improves the stability of soil slopes in the study area.

From Tables 2 and 3, it can be observed that the factors of safety, estimated for 10 m slope stabilized with fly ash and rice husk ash, are above 1.5. But the factors of safety, estimated for 15.2 m slope stabilized with the same additives, have not improved the factors of safety above 1.5. From this analysis, it was understood that the selected additives are effective only for the slopes of height up to 10 m and beyond which it requires additional reinforcement to achieve higher factors of safety.

4 Conclusions

The landslide prone area located at Makkandur, Karnataka State, India, was studied to know the effect of addition of admixtures on the stability of existing slopes at this location. The additives, fly ash and rice husk ash, were added in different proportions, and the changes in the soil properties were observed. With the addition of fly ash and rice husk ash, the unconfined compressive strength of soil increased significantly. The factors of safety were estimated for 10 and 15.2 m height slopes using Taylor's method and using GEO5 software tool by considering the field conditions. It was observed that for the existing slope of 10 m, the factors of safety have considerably increased with the addition of fly ash and rice husk ash. But for 15.2 m slope, the estimated factors of safety of using both the methods were less than 1.5. Hence it can

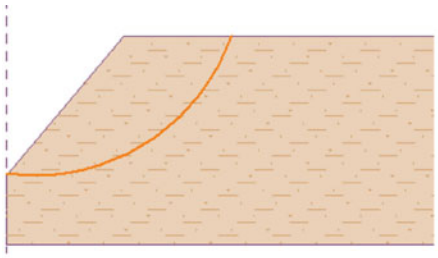

(a)

Slope stability verification (Bishop)
Sum of active forces : F_a = 633.91 kN/m
Sum of passive forces : F_p = 881.51 kN/m
Sliding moment : M_a = 9508.70 kNm/m
Resisting moment : M_p = 13222.66 kNm/m
Factor of safety = 1.39 < 1.50
Slope stability NOT ACCEPTABLE

(b)

Slope stability verification (Bishop)
Sum of active forces : F_a = 598.70 kN/m
Sum of passive forces : F_p = 1205.32 kN/m
Sliding moment : M_a = 8980.44 kNm/m
Resisting moment : M_p = 18079.77 kNm/m
Factor of safety = 2.01 > 1.50
Slope stability ACCEPTABLE

(d)

Slope stability verification (Bishop)
Sum of active forces : F_a = 598.70 kN/m
Sum of passive forces : F_p = 1148.43 kN/m
Sliding moment : M_a = 8980.44 kNm/m
Resisting moment : M_p = 17226.45 kNm/m
Factor of safety = 1.92 > 1.50
Slope stability ACCEPTABLE

(c)

Slope stability verification (Bishop)
Sum of active forces : F_a = 598.70 kN/m
Sum of passive forces : F_p = 1084.18 kN/m
Sliding moment : M_a = 8980.44 kNm/m
Resisting moment : M_p = 16262.65 kNm/m
Factor of safety = 1.81 > 1.50
Slope stability ACCEPTABLE

(f)

Slope stability verification (Bishop)
Sum of active forces : F_a = 598.70 kN/m
Sum of passive forces : F_p = 1055.77 kN/m
Sliding moment : M_a = 8980.44 kNm/m
Resisting moment : M_p = 15836.53 kNm/m
Factor of safety = 1.76 > 1.50
Slope stability ACCEPTABLE

(e)

Fig. 4 Stability analysis of 10 m height slope using GEO5 (**a**) cross section of the slope, (**b**) soil alone, (**c**) soil + 5% fly ash, (**d**) soil + 10% fly ash, (**e**) soil + 5% RHA, and (**f**) soil + 10% RHA

be concluded that addition of fly ash or rice husk ash is effective for slopes of height upto 10 m and for slopes of height beyond 15 m needs soil reinforcement either in the form of soil nails or geosynthetics to achieve a factor safety above 1.5. The stability analysis carried out with and without additives is useful to select suitable admixture to improve the slope stability of soil presented at the site. Thus, this research work is useful to design the ground improvement techniques at the area studied to avoid landslides in the future.

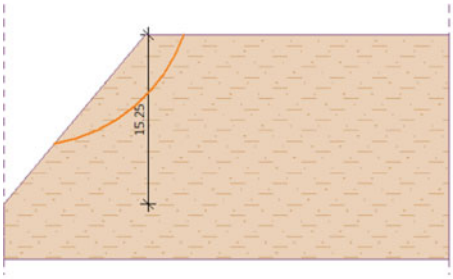

(a)

Slope stability verification (Bishop)
Sum of active forces : F_a = 406.23 kN/m
Sum of passive forces : F_p = 431.03 kN/m
Sliding moment : M_a = 6093.40 kNm/m
Resisting moment : M_p = 6465.40 kNm/m
Factor of safety = 1.06 < 1.50
Slope stability NOT ACCEPTABLE

(b)

Slope stability verification (Bishop)
Sum of active forces : F_a = 406.23 kN/m
Sum of passive forces : F_p = 495.74 kN/m
Sliding moment : M_a = 6093.40 kNm/m
Resisting moment : M_p = 7436.15 kNm/m
Factor of safety = 1.22 < 1.50
Slope stability NOT ACCEPTABLE

(c)

Slope stability verification (Bishop)
Sum of active forces : F_a = 406.23 kN/m
Sum of passive forces : F_p = 578.70 kN/m
Sliding moment : M_a = 6093.40 kNm/m
Resisting moment : M_p = 8680.55 kNm/m
Factor of safety = 1.42 < 1.50
Slope stability NOT ACCEPTABLE

(d)

Slope stability verification (Bishop)
Sum of active forces : F_a = 406.23 kN/m
Sum of passive forces : F_p = 473.63 kN/m
Sliding moment : M_a = 6093.40 kNm/m
Resisting moment : M_p = 7104.41 kNm/m
Factor of safety = 1.17 < 1.50
Slope stability NOT ACCEPTABLE

(e)

Slope stability verification (Bishop)
Sum of active forces : F_a = 406.23 kN/m
Sum of passive forces : F_p = 541.97 kN/m
Sliding moment : M_a = 6093.40 kNm/m
Resisting moment : M_p = 8129.58 kNm/m
Factor of safety = 1.33 < 1.50
Slope stability NOT ACCEPTABLE

(f)

Fig. 5 Stability analysis of 15.2 m height slope using GEO5 (**a**) cross section of the slope, (**b**) soil alone, (**c**) soil + 5% fly ash, (**d**) soil + 10% fly ash, (**e**) soil + 5% RHA, and (**f**) soil + 10% RHA

References

1. Sassa, K.: Analysis on slope stability: II. Mainly on the basis of the indoor experiments using the standard sand produced in Toyoura, Japan. J. Jpn. Soc. Erosion Control Eng. **26**(3), 8–19 (1974)
2. Sassa, K.: The mechanism starting liquefied landslides and debris flows. In: Proceedings of 4th International Symposium on Landslides, Toronto, Canada, vol. 2, pp 349–354 (1984)
3. Zêzere, J.L., Garcia, R.A.C., Oliveira, S.C., Reis, E.: Probabilistic landslide risk analysis consideringdirect costs in the area north of Lisbon (Portugal). Geomorphology **94**, 467–495 (2008)
4. Chang, K., Chiang, S.: An integrated model for predicting rainfall-induced landslides. Geomorphology **105**, 366–373 (2009)
5. Petley, D.: Global patterns of loss of life from landslides. Geology **40**, 927–930 (2012)

6. Shokouhi, A., Gratchev, I., Kim, D.: Rock slope stability problems in Gold Coast area Australia. Int. J. Geomate **4**(1), 501–504 (2013)
7. Kim, H.D., Gratchev, I., Balasubramaniam, A.: Determination of joint roughness coefficient (JRC) for slope stability analysis; a case study from the Gold Coast area Australia. Landslides **10**(5), 657–664 (2013)
8. Promper, C., Glade, T.: Multilayer-exposure maps as a basis for a regional vulnerability assessment for landslides: applied in Waidhofen/Ybbs. Austria. Nat. Hazards **82**, 111–127 (2016)
9. Peruccacci, S., Brunetti, M., Gariano, S., Melillo, M., Rossi, M., Guzzetti, F.: Rainfall thresholds for possible landslides occurrence in Italy. Geomorphology **290**, 39–57 (2017)
10. Salvati, P., Petrucci, O., Rossi, M., Bianchi, C., Pasqua, A.A., Guzzetti, F.: Gender, age and circumstances analysis of flood and landslide fatalities in Italy. Sci. Total Environ. **610–611**, 867–879 (2018)
11. Bishop, A.W.: The influence of an undrained change in stress on the pore pressure in porous media of low compressibility. Géotechnique **23**(3), 435–442 (1973)
12. Brand, E.W., Premchitt, J., Phillipson, H.B.: Relationship between rainfall and landslides in Hong Kong. In: Proceedings of the 4th International Symposium On Landslides, Downsview, Ontario, Canada, pp. 377–384 (1984)
13. Larsen, M., Simon, A.: A rainfall intensity–duration threshold for landslides in a humid-tropical environment, Puerto Rico. Geografiska Annaler Ser. A Phys. Geogr. **75**, 13–23 (1993)
14. Tsaparas, I., Rahardjo, H., Toll, D., Leong, E.: Controlling parameters for rainfall-induced landslides. Comput. Geotechn. **29**, 1–27. (2002)
15. Craig, R.F.: Craig's Soil Mechanics. New Fetter Lane, London (2004)
16. Chien-Yuan, C., Tien-Chien, C., Fan-Chieh, Y., Wen-Hui, Y., Chun-Chieh, T.: Rainfall duration and debris-flow initiated studies for real-time monitoring. Environ. Geol. **47**(5), 715–724 (2005)
17. Dahal, R., Hasegawa, S.: Representative rainfall thresholds for landslides in the Nepal Himalaya. Geomorphology **100**, 429–443 (2008)
18. Gui, M., Han, K.: Landslides and Engineering slopes. A case study on rainfall infiltration effect on the stability of two slopes, pp. 1737–1743 (2008)
19. Niroumand, H., Kassim, K.A., Ghafooripour, A., Nazir, R., Far, S.Y.Z.: Investigation of slope failures in soil mechanics. Electron. J. Geotech. Eng. **17**, 2703–2718 (2012)
20. Tay, J.E., Selaman, O.S.: A study on the rainfall and landslide along Sarawak Road using antecedent rainfall analysis (2019)
21. Wang, G., Sassa, K.: Pore-pressure generation and movement of rainfall-induced landslides: effects of grain size and fine-particle content. Eng. Geol. **69**(1), 109–125 (2003)
22. Cogan, J., Gratchev, I.: A study on the effect of rainfall and slope characteristics on landslide initiation by means of flume tests. Landslides **16**(12), 2369–2379 (2019)
23. Iovine, G., Parise, M.: Schema classificativo per il rilievo dei danni da frana in aree urbane. Mem. Soc. Geol. Ital. **57**, 595–603 (2002)
24. Calcaterra, D., Ramondini, M., Calò, F., Longobardi, V., Parise, M., Galzerano, C.M.: DInSAR techniques for monitoring slow-moving landslides in landslides and engineered slopes. In: Cheng, Z., Zhang, J., Li, Z., Wu, F., Ho (Xi'an) K. (eds) Proceedings of the 10th International Symposium on Landslides, pp. 1095–1101 (2008)
25. Calò, F., Calcaterra, D., Iodice, A., Parise, M., Ramondini, M.: Assessing the activity of a large landslide in southern Italy by ground-monitoring and SAR interferometric techniques. Int. J. Remote Sens. **33**, 3512–3530 (2012)
26. Del Soldato, M., Bianchini, S., Calcaterra, D., De Vita, P., Di Martire, D., Tomás, R.: A new approach for landslide-induced damage assessment. Geomat. Nat. Hazards Risk **8**, 1524–1537 (2017)
27. Van Westen, C.J., Asch, T.W.J., Soeters, R.: Landslide hazard and risk zonation—why is it still so difficult? Bull. Eng. Geol. Environ. **65**, 167–184 (2006)
28. Vranken, L., Van Turnhout, P., Van Den Eeckhaut, M., Vandekerckhove, L., Poesen, J.: Economic valuation of landslide damage in hilly regions: a case study from Flanders Belgium. Sci. Total Environ. **447**, 323–336 (2013)

29. Rajak, T.K., Yadu, L., Pal, S.K.: Analysis of slope stability of fly ash stabilized soil slope. In: Geotechnical Applications, pp. 119–126. Springer, Singapore (2019)
30. Alhassan, M.: Permeability of lateritic soil treated with lime and rice husk ash. Assumpt. Univ. J. Thailand **12**(2), 115–120 (2008)
31. Choobbasti, A.J., Ghodrat, H., Vahdatirad, M.J., Firouzian, S., Barari, A., Torabi, M., Bagherian, A.: Influence of using rice husk ash in soil stabilization method with lime. Front Earth Sci. China **4**(4), 471–480 (2010)

Study of Dry Granular Flow Behaviour with and Without Erodible Layer

S. Sureka, C. Kavinkumar, and Rakesh J. Pillai

1 Introduction

Rock and debris avalanches can travel extremely long distances along flat or almost flat surfaces. The collapse of a granular column is of great interest for studying transient granular flow conditions. Granular column collapse is similar to the well-known dam-break problem in fluid mechanics [1]. Landslides frequently occur along surfaces mantled by a shallow layer or thick deposits made of erodible materials. As a result, entrainment occurs increasing the volume of the failure mass, thereby changing the behaviour and mobility of the flowing mass. Considering these implications, it is hoped to infer the initiation and propagation mechanism of real debris flows with the help of the granular column model proposed by Lajeunesse et al. [2] and Lube et al. [3] in plane strain conditions along a smooth basal surface and an erodible surface.

2 Methodology

The configuration of the numerical model used in this research is based on a granular column collapse model as proposed by Lube et al. [4]. As shown in Fig. 1, a removable gate is placed to control the collapse of the granular column. The walls are provided with the same friction coefficient as that given for the particles. In this way, every particle experiences the same amount of friction. The horizontal base is with and

S. Sureka (✉)
Department of Civil Engineering, NIT Warangal, Warangal 506004, India

C. Kavinkumar
Department of Civil Engineering, NIT Warangal, Warangal 506004, India

R. J. Pillai
Civil Engineering Department, IIT Palakkad, Kozhipara 678557, India

C. N. V. Satyanarayana Reddy et al. (eds.), *Stability of Slopes and Underground Excavations*, Lecture Notes in Civil Engineering 185,
https://doi.org/10.1007/978-981-16-5601-9_11

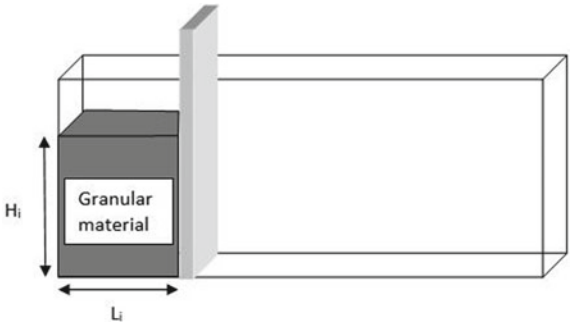

Fig. 1 Granular column collapse model without erodible bed

without an erodible bed, where the non-erodible ones have the same roughness as the flowing material (see Figs. 1 and 2). The space enclosed by the removable gate and the nearest wall is packed with granular materials.

A loose granular column is generated within the parallelepiped prism of initial column height (H_i) and initial column width (L_i). After the generation of the particles with specified size, gravity is applied to the particles which make the particles settle down by gravity and form a dense granular column similar to the natural deposit. Once the particles are settled down attaining a static state, the gate is released to initiate the collapse. The granular column collapses by flowing along the erodible and non-erodible horizontal floor following both vertical and horizontal movement. When the particles come to rest, the final run-out distance (L_f) covered by the granular deposit and final granular height (H_f) is found for both erodible and non-erodible base conditions. As proposed by Zenit [5], the outermost edge of the deposit is the point where the majority of the flowing materials are in contact with each other. This idea neglects the position of loose materials that are jumping out of the flow.

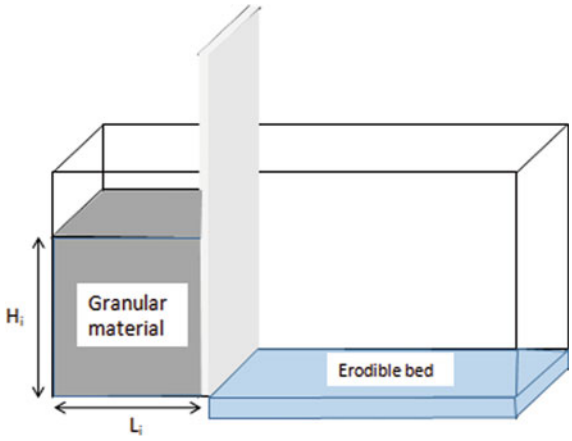

Fig. 2 Granular column collapse model with erodible bed

3 Results and Discussion

In the DEM model, it is necessary to select a representative elementary volume (REV) (Modenese et al. [6]) so that the size of the granular column or the number of grains present in it has a negligible effect on the numerical results obtained. From the implications of Zhao [7], the influence of model size ratio for granular flows is negligible for values greater than 40. By considering this into account, granular columns of model size ratio greater than 40 are taken in this study.

The input parameters involved in this study are given as follows:

1. Initial column height (H_i), m = varies
2. Initial column length (L_i), m = 0.5
3. Aspect ratio ($a = H_i/L_i$) = varies
4. Young's modulus (E), $N/m^2 = 5 \times 10^7$
5. Poisson ratio = 0.4
6. Friction coefficient = 0.6
7. Particle diameter (D), mm = 3
8. Packing porosity (n) = 0.43
9. Particle density (ρ), $kg/m^3 = 2650$
10. Damping coefficient = 0.0
11. Gravity (g), $m/s^2 = -9.81$
12. Time step (Δt), $s = 10^{-5}$

The main controlling factors are the column geometry described in terms of aspect ratio a, between initial column length (L_i) and height (H_i). Simulations are done for four different aspect ratios, each for both erodible and non-erodible conditions. Figures 3 and 4 show the evolution of bulk coordination number with and without erodible beds, respectively. The higher the bulk coordination number, the lower the average velocity of particles in the system and vice versa. This is due to the fact that the bulk coordination number is related to the density of particles in the system.

For the columns of aspect ratio lesser than 3, the evolution of bulk coordination number with respect to the normalized time is gradual for both the erodible and non-erodible conditions. The bulk coordination number values are maintained low in non-erodible cases than that of the erodible condition.

For the columns of aspect ratio greater than 3, the values of bulk coordination number change rapidly in reference to the normalized time for both erodible and non-erodible conditions. Bulk coordination number values in non-erodible bed condition shoot up above the values in erodible bed condition.

In both erodible and non-erodible conditions, a minimum value of bulk coordination number is attained after the removal of the confining gate which symbolizes the occurrence of the maximum kinetic energy of the system. At a normalized time [T] = 0.5, the maximum kinetic energy is attained. For smaller aspect ratio columns, this value is attained after gradual increment, whereas a sharp change is noted in the larger aspect ratio columns. It is due to the fact that the movement of granular particles in smaller aspect ratio columns are governed by the interparticle friction,

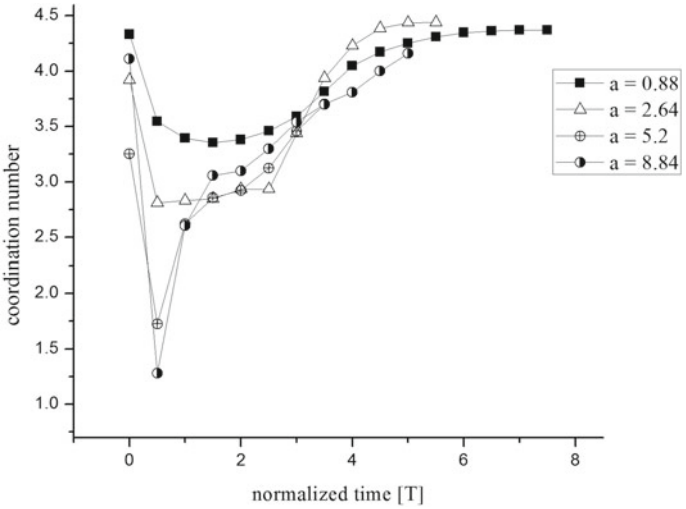

Fig. 3 Bulk coordination number variation in the presence of erodible bed

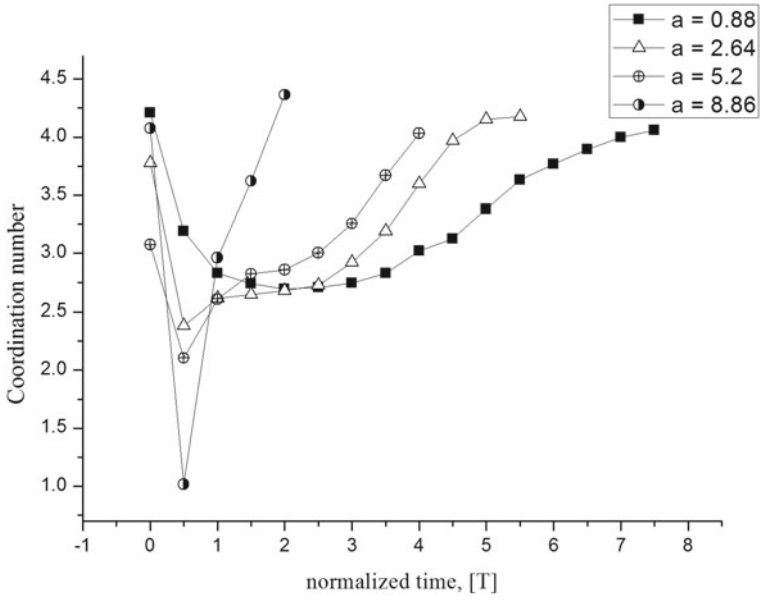

Fig. 4 Bulk coordination number variation without erodible bed

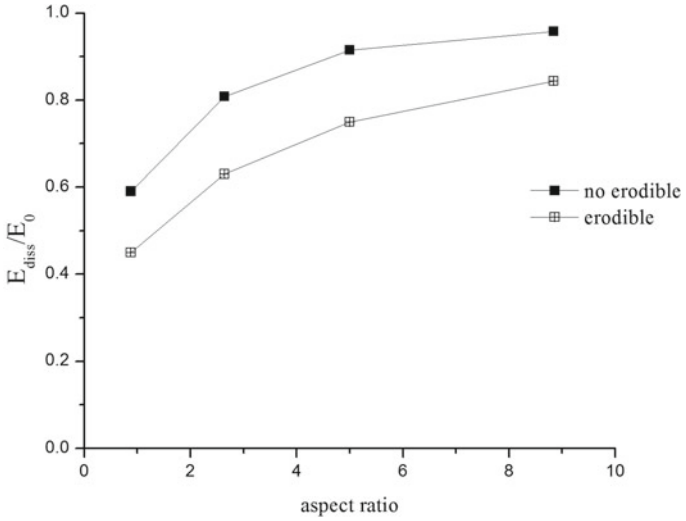

Fig. 5 Variation of dissipation energy

whereas the inertial property of the particles comes into effect in the case of larger aspect ratio columns. This also confirms the lesser velocity of particles in smaller aspect ratio columns with a greater velocity witnessed in the particles of larger aspect ratio columns.

Figure 5 shows the variation of dissipation energy normalized with the total energy of the system for both erodible and non-erodible bed conditions. The dissipation energy witnessed in non-erodible bed condition is greater than that of the erodible bed condition. Hence, it can be inferred that the majority of the total energy is converted into kinetic energy rather than getting dissipated, thereby causing the final run-out length to increase in erodible bed condition. This also supports the occurrence of maximum kinetic energy in erodible bed condition.

4 Conclusions

From the studies carried out numerically, it has been found that the presence of an erodible layer in the path of the granular flow affects its behaviour, especially for the failure mass originating from the granular columns of larger aspect ratios. The final run-out length of the failure mass changes, due to the increased kinetic energy in response to the presence of an erodible bed.

References

1. Ritter, A.: Die fortpflanzung der wasserwellen. Zeitschrift des Vereines Deutscher Ingenieure **36**(33), 947–954 (1892)
2. Lajeunesse, E., Monnier, J.B., Homs, G.M.: Granular slumping on a horizontal surface. Phys. Fluids **17**(10), 1–16 (2005)
3. Lube, G., Hippert, H.E., Sparks, R.S.J., Hallworth, M.A.: Axisymmetric collapses of granular columns. J. Fluid Mech. **508**, 175–199 (2004)
4. Lube, G., Huppert, H.E., Stephen, R., Sparks, J., Freundt, A.: Collapses of two-dimensional granular columns. Phys. Rev. E–Statist. Nonlinear Soft Matter Phys. **72**(4), (2005)
5. Zenit, R.: Computer simulations of the collapse of a granular column. Phys. Fluids **17**(3), (2005)
6. Modenese, C., Utili, S., Houlsby, G.T.: A numerical investigation of quasi-static conditions for granular media. Int. Symp. Discrete Element Model. Particul. Media Edit. 187–195, (2012)
7. Zhao, T.: Coupled DEM-CFD Analyses of Landslide-Induced Debris Flows. Springer Nature, Singapore (2017)
8. Shi, B., Zhang, Y., Zhang, W.: Analysis of the entire failure process of the rotational slide using the material point method. Int. J. Geomech. **18**(8), 04018092 (2018)

Numerical Analysis of Buried Pipelines Located in Slopes

Rishi Ranjan, Anil Kumar Choudhary, and Awdhesh Kumar Choudhary

1 Introduction

Transportation of fluids all over the world is extensively executed by long-distance pipelines, since an early stage of civilization. But due to high rate of urbanization and living standards, a problem regarding scarcity of land is rising rapidly. So, engineers and practitioners are continuously trying to invent some alternatives such as underground infrastructure. Subsequently, the concept of buried pipes was innovated as a reliable approach for transporting drinking water, wastewater, natural gas, oil, etc. Because of the long distance between the extraction sites and the utility point, buried pipelines need to be passed through different geological and topographical areas. Consequently, various kinds of difficulties occur during installation of pipelines as well as during the whole service life. The stability of buried pipelines is mainly affected by soil motion or large ground movements or by slope failure.

The first analysis of the buried pipe was developed on the basis of Terzaghi's theory to determine the loads acting on the crown of the pipe [1]. It is noteworthy that pipe failures may occur during their service life due to corrosion, external forces, or accidental pipe defects so a pipe should possess enough strength and stiffness. Meanwhile, the pipe should have enough resistance to withstand against loads come from soils, loads exerted by foundation, internal pressure, differential settlement, longitudinal bending, etc. [2]. The stiffness of pipes and soil properties are very important parameters for calculating the flexible pipe deformation in lateral direction under loading conditions [3]. Furthermore, a new elastic solution for the deflection

R. Ranjan (✉) · A. K. Choudhary · A. K. Choudhary
National Institute of Technology, Jamshedpur 831014, India

A. K. Choudhary
e-mail: akchoudhary.ce@nitjsr.ac.in

A. K. Choudhary
e-mail: awdhesh.ce@nitjsr.ac.in

C. N. V. Satyanarayana Reddy et al. (eds.), *Stability of Slopes and Underground Excavations*, Lecture Notes in Civil Engineering 185,
https://doi.org/10.1007/978-981-16-5601-9_12

of an elastic pipe in an infinite elastic medium was introduced [4]. Deformation of pipe generally gets influenced by pipe flexibility factor and is not proportional to the diameter of the pipe, which was observed from the field test done on polyurethane pipes [5]. The strain of pipe in horizontal direction is smaller than strain of pipe in vertical direction for short-term loading [6]. Throughout this study, the behavior of pipes embedded in sand slope and subjected to loads governed by strip footing was investigated by numerical analysis, i.e. finite element method in PLAXIS-3D.

2 Methodology

2.1 Numerical Analysis

The evaluation of complex problems using numerical modeling can be done by differential calculation consists of two methods, i.e. finite element method and finite difference method. The concept of the finite element method is based on splitting the complex structure into large number of finite element, which can be interrelated using nodes. The elements describing the local coordinate system are calculated and summarized in global coordinate system to get the uncertain result present in the complex structure. One of the commercial available programs based on the finite element method is PLAXIS 3D, which is used in the study for evaluation of deformation, stress, strain and failure aspect of the given problems.

Overview of PLAXIS-3D

PLAXIS 3D is a software, based on the finite element method, which is developed for geotechnical engineering for the analysis of condition prevailing in geotechnical activities in three-dimensional approach. The conditions such as deformation, underground movement of water, stability can form complex equation of differential equation, which leads to arise the needs of finite element method. Thus, PLAXIS 3D can solve the problem of forming mesh of different elements. In geotechnical applications, extra constituent models are required for simulating time-dependent, non-linear, anisotropic soil and rock in multiple layers of materials. Generally, the geotechnical projects are based on soil–structure interaction. The complex problem is based on two nodes, i.e. displacement (deformation) nodes, which are at the corner of every element in the nodes present in mesh, and the other is stress nodes, which locate at the center area of the element in the nodes. Each element generated in mesh in PLAXIS 2D is in triangular shape and in PLAXIS 3D is in tetrahedron shape.

2.2 Materials to Be Modeled

To find out the stability of buried pipes under the influence of slope and structural load such as strip footing, a model has been interpreted in PLAXIS 3D. The geometry of the model has been created by providing the footing (simulated by steel plate) nearer to the summit of the slope or to the face of the slope. The model's dimensions were selected in such a way that the 0.1q stress contour of footing (q is the stress transmitted by the footing) will never be intersected by the side and bottom edges of the model.

For numerical analysis in this context, the hardening soil model (HS) has been used in PLAXIS 3D for simulating soil layer. The properties of the soil layer have been shown in Table 1. Along with soil layer, the plate has been also modeled to simulate strip footing and buried pipe.

In PLAXIS 3D, the plate has been modeled as a linear elastic material and plate elements are allowed to behave as an orthotropic material.

(a) To simulate as a strip footing, the linear elastic steel plate was installed at the ground surface nearer to the slope and subjected to a load of 100 kN. The properties of steel plate when simulated as strip footing are shown in Table 2.

(b) To simulate as a buried pipe, the plate was embedded under the ground, i.e. below structural load and nearer to the slope. The position of pipe has been changed vertically and horizontally to find out the safest position of pipe, where

Table 1 Values of hardening soil parameters for 85% relative density of soil used in PLAXIS-3D analyses

Parameters	Value	Parameters	Value
γ_{unsat}	18.20 kN/m^3	e_{init}	0.5000
γ_{sat}	21.02 kN/m^3	c'_{ref}	1.000 kN/m^2
e_{init}	0.5000	φ phi	38°
e_{min}	0.000	ψ psi	10°
e_{max}	999.0	υ'_{ur}	0.3000
E_{50}^{ref}	60.00E3 kN/m^2	p_{ref}	100.0 kN/m^2
E_{oed}^{ref}	60.00E3 kN/m^2	K_0^{nc}	0.3845
E_{ur}^{ref}	180.0E3 kN/m^2	c'_{inc}	0.000 kN/m^2/m
C_c	5.750E-3	z_{ref}	0.000 m
C_s	1.424E-3	R_f	0.900

Table 2 Properties of steel plate as footing in model tank

Parameters	Value	Parameters	Value
D	0.2000 m	υ_{12}	0.3000
Y	78.50 kN/m^3	G_{12}	80.77E6 kN/m^2
E_1	210.0E6 kN/m^2	G_{13}	80.77E6 kN/m^2
E_2	210.0E6 kN/m^2	G_{23}	80.77E6 kN/m^2

Table 3 Properties of pipe

Parameters	Value	Parameters	Value
d	0.5000E−3 m	υ_{12}	0.3100
Y	13.83 kN/m^3	G_{12}	356.1E3 kN/m^2
E_1	933.0E3 kN/m^2	G_{13}	356.1E3 kN/m^2
E_2	933.0E3 kN/m^2	G_{23}	356.1E3 kN/m^2

the influence of slope and structural load is minimum. The properties of steel plate as a pipe are shown in Table 3.

2.3 Details of Numerical Model

The test tank used by Lee and Manjunath [7] during experimental analysis is modeled in PLAXIS-3D. Since the size of the test tank is kept the same as that of experimental analysis, therefore model domain having dimensions 1.8 m × 0.9 m × 1 m is provided to build the model tank within it. The reason behind selecting the HS model in spite of the availability of other soil models in PLAXIS-3D is because the magnitude of soil deformations can be modeled more precisely by assigning three input stiffness parameters corresponding to the triaxial loading stiffness (E_{50}), the triaxial unloading–reloading stiffness (E_{ur}), and the Oedometer loading stiffness (E_{oed}). Plate elements are used to simulate footing and pipe in the model. Pipe of diameter 75 mm is placed in this model at a certain depth from footing. Pipe depth is varied to locate the safest position of pipe. The present model consists of 7944 triangular soil elements and 13,287 nodes. The generated mesh of this model is presented in Fig. 1.

3 Results and Discussion

3.1 Validation of Finite Element Analysis Against Experimental Result

A typical load–deformation response of strip footing in slope obtained from finite element analysis has been compared with experimental results conducted by Lee and Manjunath [7] as shown in Fig. 2. Similar model dimensions and properties for each material are considered in the numerical analysis as mentioned in literature by Lee and Manjunath [7]. From Fig. 2, it is seen that the result of numerical analysis is almost the same as experimental study. Hence it can be said that the present numerical model can accurately simulate footing behavior in slope.

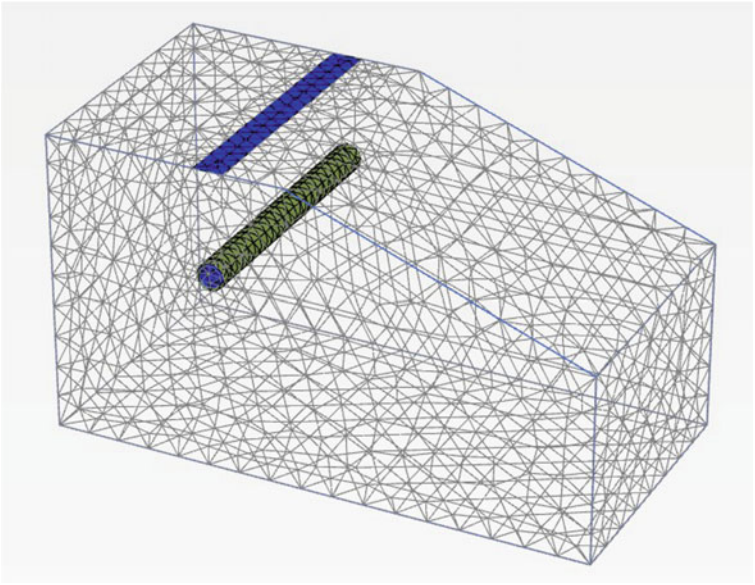

Fig. 1 Finite element mesh for model

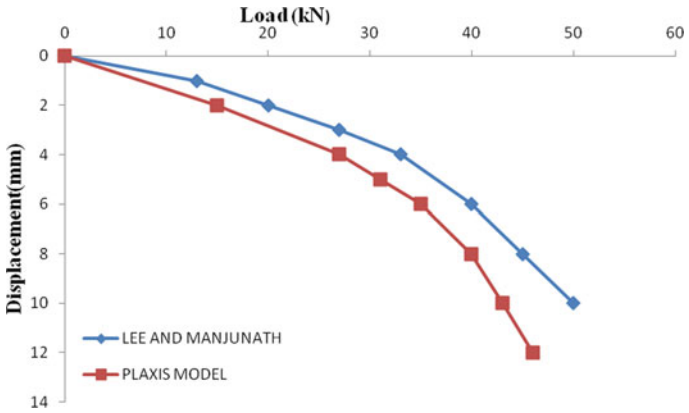

Fig. 2 Validation with experimental results [7]

3.2 Influence of Footing Distance from the Slope Crest on Bearing Capacity of Footing

A series of numerical models were carried out on strip footing by keeping the setback to footing's width ratio (b/B) as 0, 1, 2, 3, 4, 5 and 6 on a sandy slope in order to investigate the impact of the footing distance with respect to the slope crest (b/B). In

these test series, the angle of slope β has been adopted as 20°, the R.D of sand was 85% and the footing width was $B = 100$ mm.

A non-dimensional factor, bearing capacity reduction factor (i_β) is introduced in the study to analyze the ultimate bearing capacity of footing with or without soil slope before inserting pipe in the slope. Bearing capacity reduction factor (i_β) of footing is defined as the ratio of the ultimate bearing capacity of footing resting on soil slope (q_{slope}) to the ultimate bearing capacity of footing resting on the flat ground surface (q_u) without any pipe. The bearing capacity reduction factor for different setback distances obtained in PLAXIS 3D has been shown in Fig. 3 and tabulated in Table 4.

When the footing position is shifted away from the slope crest, the bearing capacity is increased. It is found that about 31% increase in bearing capacity when setback distance increases from b/B = 0 to the b/B = 1. In a similar manner, 22% and 20% increase in bearing capacity is observed for change in setback distance from b/B = 1

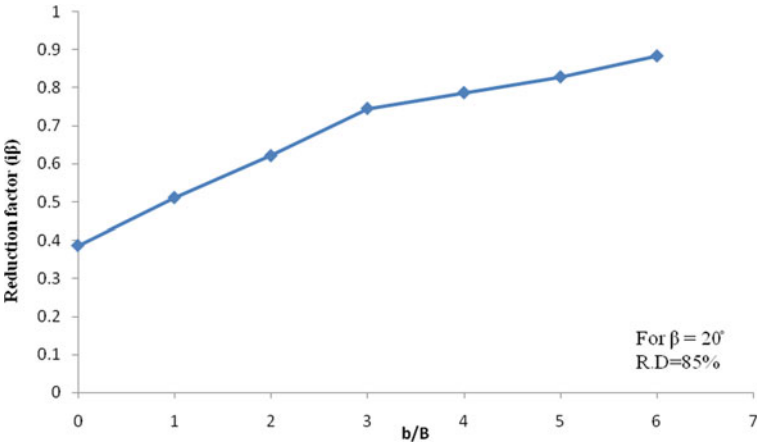

Fig. 3 Variations of reduction factor (i_β) with b/B

Table 4 Summarized the results of footing located at seven different positions from the slope crest ($\beta = 20°$, R.D = 85%, $B = 100$ mm)

b/B	Bearing capacity of footing on slope (q_{slope})	Non-dimensional reduction factor (i_β)
0	560	0.39
1	740	0.51
2	900	0.62
3	1080	0.75
4	1140	0.79
5	1200	0.83
6	1280	0.88
Level ground	1450	1

to b/B = 2 and b/B = 2 to b/B = 3. Beyond b/B = 3, the rate of increase in footing's bearing capacity gets reduced. The ultimate bearing capacity of the footing on soil slope beyond the b/B value of 6 approaches to footing's bearing capacity on ground or flat level. The increase in the bearing capacity of footing with increase in distance from slope crest is due to effect of the resistance offer by passive zone of soil from the slope surface side toward the footing base.

3.3 Influence on Bearing Capacity After Installation of Pipe in Soil Slope

Influence of Vertical Position of Pipe on Bearing Capacity

The influence of the embedment ratio (H/B) of the pipe in soil slope on the bearing capacity of footing was computed by model test series in PLAXIS-3D. Throughout the analysis, the diameter of embedded pipe (D) and widths of the footing (B) have been kept as 75 and 100 mm, respectively. Slope angle (β) of 20°, R.D 85% and setback distance to the width of footing ratio (b/B) 2.0 were adopted for analysis. The model test analysis is performed for seven different H/B ratios such as 0.5, 1.0, 1.5, 2.0, 2.5, 3.0 and 3.5. Load-settlement curves for seven different embedment (H/B) ratios are presented in Fig. 4 and have been tabulated in Table 5. Additionally, the result of bearing capacity of footing in soil slope without any pipe was also represented in Fig. 4, for comparison.

A significant increase in the bearing capacity of footing was found when the embedded pipe position changes from H/B = 0.5 to H/B = 2.5. The increase rate in bearing capacity decreases after H/B value 2.5 and ultimately reaches near about

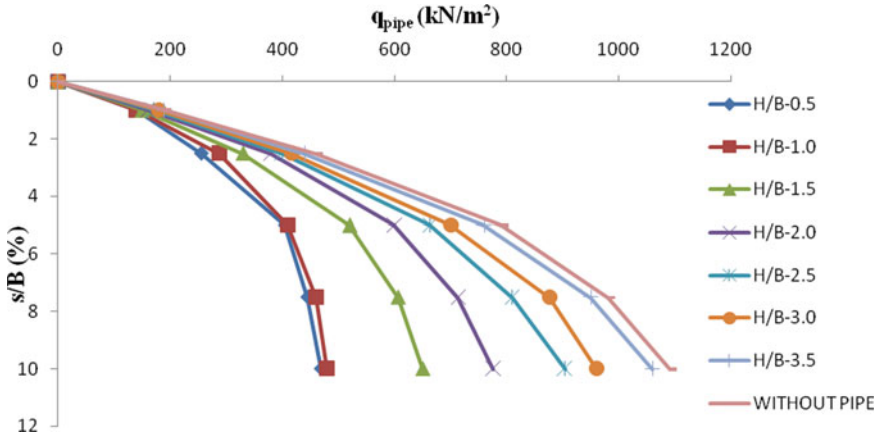

Fig. 4 Variations of load intensity (q_{pipe}) with s/B (%) for vertical position of pipe in different ratios of embedment (H/B)

Table 5 Test results for different embedment ratios (H/B)

H/B	q_{pipe}
0.5	330
1.0	370
1.5	520
2.0	710
2.5	780
3.0	800
3.5	890
No pipe in slope	920

97% of case of without pipe. The footing's bearing capacity is directly get affected by a pipe installation within the stress bulb of footing. In this case, the footing's bearing capacity gets increased as the pipe position going away from the stress bulb (stress bulb generated beneath of footing) in a downward direction. This observation can be discussed using vertical displacement contour. The displacement contour of model with and without pipe is presented in Figs. 5 and 6. It is clearly observed from displacement contour that pipe position for H/B ratio 3.5 lies in between the contour of lesser value (i.e. 2–5 mm). This signifies safe position of pipe with respect to footing load. The pipe position in vertical direction to footing's width ratio (H/B) has been adopted as 3.5 for safety consideration.

Influence of Horizontal Distance of Pipe on Bearing Capacity

The influence of the horizontal position of pipe to footing width (X/B) (i.e. the horizontal position X, taken from the nearest edge of the footing) on bearing capacity was investigated by the sequence of model analysis on the soil slope. Analysis for X/B ratios of 0.5, 1.0, 1.5, 2.0, 2.5 and 3.0 was performed at H/B value 3.5 and

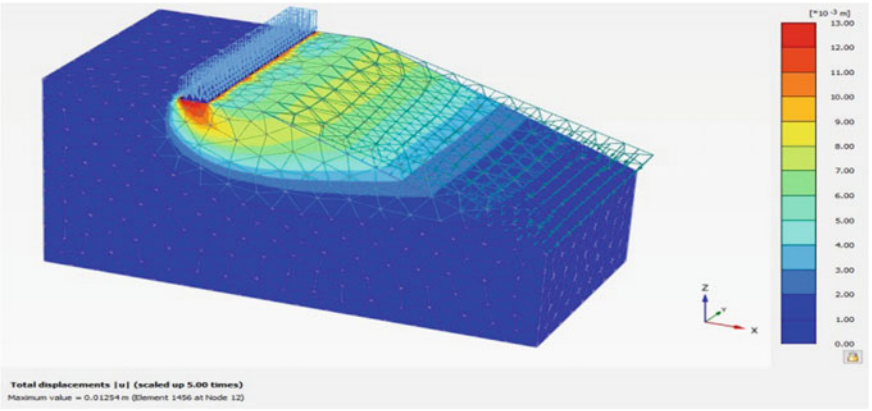

Fig. 5 Displacement contour without pipe

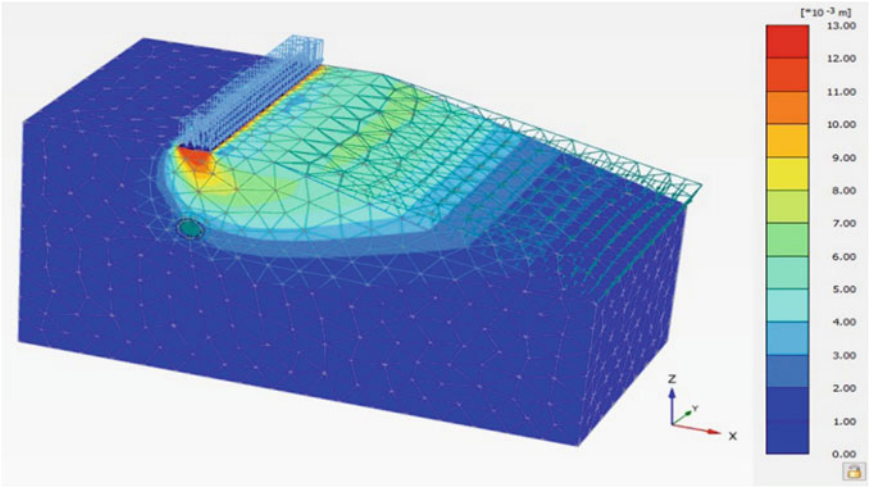

Fig. 6 Displacement contour with pipe: H/B = 3.5

represented by load settlement curves in Fig. 7 and tabulated in Table 6. There was a considerable increase in bearing capacity of footing in soil slope with pipe (near about value of 92% of no pipe condition in slope) when the pipe is located at X/B = 1.0. The bearing capacity reached to 95% at X/B = 1.5 and become 100% in case of without pipe and at the location where X/B = 2.0. It means that when the pipe is placed at X/B = 2, the bearing capacity reaches the same value as in the case of without pipe in soil slope.

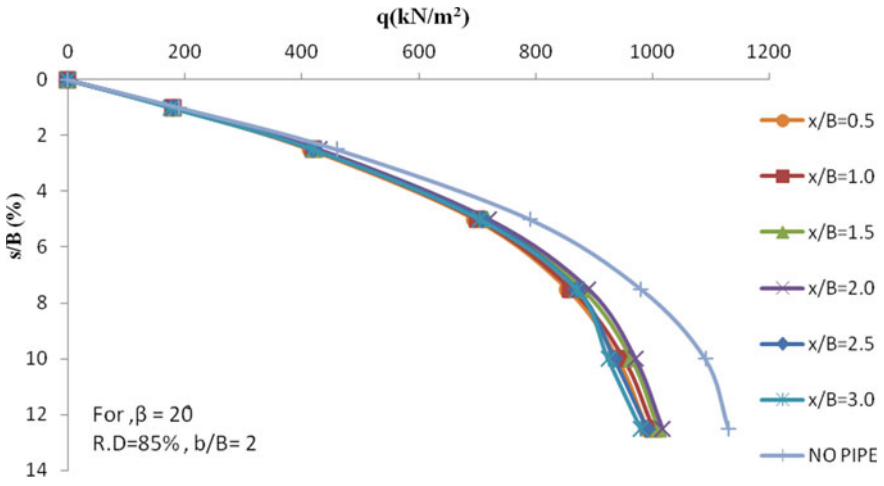

Fig. 7 Variations of load intensity (q) with settlement (s/B %) for different horizontal positions of pipe and no pipe conditions

Table 6 Test Results for X/B variations

X/B	q_{slope}
0.5	840
1.0	850
1.5	876
2.0	920
2.5	780
3.0	760
Without pipe in slope	920

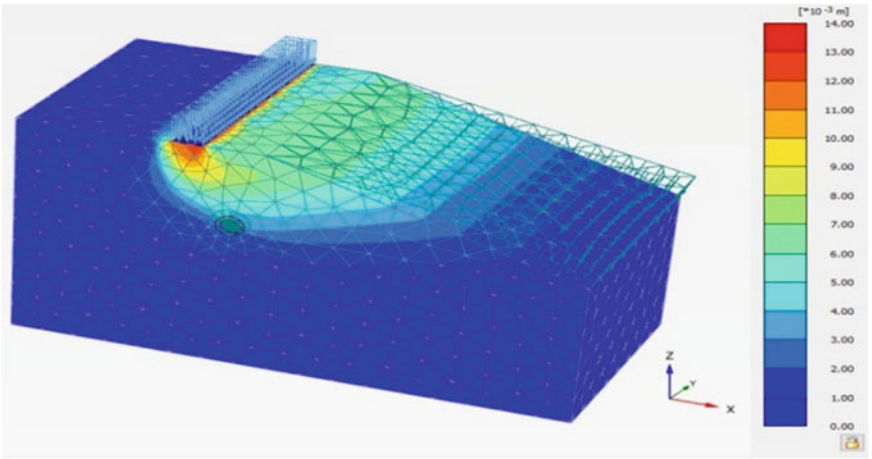

Fig. 8 Displacement contour with pipe: H/B = 3.5 and X/B = 2

Vertical displacement contour for this position is presented in Fig. 8. It is also found that pipe position lies between lesser value (i.e. 2–5 mm). This also indicates the safe position of the pipe.

4 Conclusions

1. The result indicated that, with increasing the setback distance (b), the bearing capacity of soil slope also increased up to b/B = 6, after that slope behaves like a level ground and the corresponding bearing capacity is nearly equal to the bearing capacity on level ground. When footing at setback distance b = 2B, they achieve 62% of bearing capacity at level ground, which was adopted for economy consideration.

2. It was also concluded that when the pipe depth was increased with respect to the lower surface of the strip footing, then the bearing capacity of the footing also get increased which signifies lesser effect on pipe.
3. Increasing the H/B ratio of pipe leads the way to an increase in the percentage rate of increment in bearing capacity after a certain H/B ratio, the change in the bearing capacity of soil on the slope is negligible. Moreover, if the pipe is placed at H/B = 3.5, the bearing capacity tends to nearly equal to the same bearing capacity that in the case of without embedded pipe in soil slope. On the basis of present observation, an optimum depth of pipe is fixed at H/B ratio 3.5.
4. The bearing capacity reached 95% at X/B = 1.5 and the bearing capacity reaches 100% in the case of without pipe in soil slope which is the same as in the case of X/B = 2. Further increase in the horizontal position of pipe tends to decrease in the bearing capacity of the soil slope with an embedded pipe.
5. Based on observation, the optimum position of pipe with respect to footing is fixed at H/B ratio 3.5 and X/B ratio 2 from the point of view of safety and serviceability.

References

1. Marston, A, Anderson, A.O.: The theory of external loads on closed conduits in the Iight of the latest experiments, Iowa State College Bulletin, no. 96, Vol. XXVIII. Iowa Engineering Experimental Station, Iowa State College (1913)
2. Moser, A.P., Folkman, S.: Buried Pipe Design. McGraw-Hill, New York, NY, USA (2008)
3. Spangler, M.G.: Structural design of flexible pipe culverts. Bulletin, no. 153, Iowa Engineering Experiment Station, IA, USA (1941)
4. Hoeg, K.: Pressure distribution on underground structural cylinders. Technical Report No. AFWL TR 65-98, Kirtland Air Force Base, NM, USA (1966)
5. Hurd, J.O.: Field Performance of corrugated polyethylene pipe culverts in Ohio. J. Trans. Res. Board **1087**, 1–6 (1986)
6. Adams, D.N., Muindi, T., Selig, E.T.: Polyethylene pipe under high fill. Trans. Res. Rec. (1231), 88–95 (1989)
7. Lee, K.M., Manjunath, V.R.: Experimental and numerical studies of geosynthetic-reinforced sand slopes loaded with a footing. Can. Geotech. J. **37**(2000), 828–842 (2000)

Different Sets of Remediation for Mitigation of Landslides in Hilly Terrains of India

R. K. Panigrahi

1 Introduction

Landslides refer to the movement of mass of rock, debris, or earth down the slope, when the shear stress exceeds the shear strength of the material. It occurs when the consequence of a complex field of forces (stress is a force per unit area) active on a mass of rock or soil on the slope. It happens due to geological causes, morphological causes, physical causes, and human causes. There are two parameters that determine the landslides are as follows.

a. **Increase of Shear Stress**: It happens due to the removal of lateral and underlying support; the increase of lateral forces as well as load; transitory stresses like blasting, earthquakes, etc., and geological movement.

b. **Decrease of Material Strength**: It happens due to the weathering, pore water pressure, and changes in structure.

The incidents of landslides increasing day by day due to over urbanization, massive deforestation, construction, and development work in landslide-prone areas.

1.1 Falls

It happens due to the abrupt movements of masses of geologic materials, such as rocks and boulders that become detached from steep slopes or cliffs.

R. K. Panigrahi (✉)
Geotechnical Engineering Division, CSIR-Central Road Research Institute, New Delhi 110025, India

C. N. V. Satyanarayana Reddy et al. (eds.), *Stability of Slopes and Underground Excavations*, Lecture Notes in Civil Engineering 185,
https://doi.org/10.1007/978-981-16-5601-9_13

1.2 Topples

It happens due to the forward rotation of a unit or units about some pivotal point, below or low in the unit, under the actions of gravity and forces exerted by adjacent units or by fluids in cracks.

1.3 Slides

In these types, rocks, debris, or soil slide through slope forming material.

1.4 Spread

It usually occurs on very gentle slopes or flat terrain.

a. By restricting or even removing the population from landslides-prone areas.
b. By restricting certain types of land use where slopes are vulnerable.
c. By installing early warning systems based on the monitoring of ground conditions such as strain in rocks and soils, slope displacement, and groundwater levels.

2 Reinforced Earth Structure for Stabilization of Landslide

Reinforced earth is a composite medium. It consists of earth that is reinforced by layers of strips made of a material able to withstand large tensile stresses. The basic concept involves behind the earth reinforced structure is combining two materials of different strength characteristics to form a composite material of greater strength likewise reinforced soil structures combine the high tensile strength of steel with the high compressive, but the relatively low tensile strength of concrete. In earth-reinforced structures, the inclusion of materials (metallic strips, grids or meshes, and polymeric strips sheets) with high tensile strength in the soil results in improving the tensile strength of the soil. This mobilization of tensile strength is obtained by surface interaction between the soil and the reinforcement through friction and adhesion [1].

2.1 Components of Earth Reinforced Structure

(a) Soil or Fill Matrix-Backfill, (b) Reinforcement, (c) Strips, (d) Grids, (e) Sheet Reinforcement, and (f) Facing Elements.

The construction of a reinforced soil wall is carried out as given the following steps:

1. A reinforced soil structure is built in a series of successive steps, in each layer of facing elements, and the placing of corresponding earth fill, followed by a new layer of reinforcing strips/grids/sheets.
2. Temporary supports are installed to ensure stability while concrete or metal-facing elements are positioned and installed on the facing side of the wall. This is done in order to obtain a perfectly vertical wall facing.
3. The reinforcing strips/grids/sheets are placed perpendicular to the wall face, with the broad side of the strip resting on the previously placed layer of the compacted earth fill. The metal strips are attached to the facing elements by means of high-strength bolts which are of the same material as reinforcing strips.
4. The fill should be spread by the moving machinery parallel to the face of the wall in order to encounter the stresses that could be caused by earth moving equipment.
5. It is also advisable that the trucks and other earth-moving machinery do not go closer than 2 m to the face of the wall. The area closer to the facing should be compacted with light compacting equipment.

The reinforced earth structures for stabilization of hill slopes are a very useful technique. This technique results in many-sided advantages such as long-term durability, aesthetic value, ease of construction, suitability to various soil and hill slopes, large walls, ability to accept differential settlements, etc. Also, these walls are capable of supporting large live and dead loads of the structure and vehicles, etc. [2]. If proper specifications laid by BS 8006:1995 for out of water condition is followed up then the longevity and productivity of the structure can be increased. The cost of the earth-reinforced walls depends upon many variables such as need for cut and fill native soils, construction technique involves selection and use of material, etc. The length of reinforcement layers increases as the height of the wall increases. The design strength of reinforcement and vertical spacing between two reinforcements are also main factors. If the basic principles of the design of earth-reinforced structures are considered with due care, they can meet the mitigation and improvements of landslides and hill slopes in hilly terrains of India.

3 Soil Nailing Technique for Stabilization of Landslides

Soil nailing is one of the most efficient and widely used techniques for landslides prevention and mitigation. Soil nailing is the technique used in slope stabilization and excavation with the use of passive inclusions, usually steel bars, termed as soil nails. It consists of passive reinforcement which is encased in grout to provide corrosion protection and improved load transfer to the ground. Soil nailing mainly includes excavation which is done with conventional earthwork equipment which are started

at the ground surface and progressed downwards. It is done to accommodate the facing panels of soil nailing. Facing is done is to ensure local stability of the soil between the nails and to limit the decompression of the soil. Nailing involves the insertion of nails into the holes to develop a strong bond between the nail and the soil.

Soil nailing is one of the most effective methods of earth reinforcement for landslides prevention and mitigation, which involves reinforcing the soil with steel bars or other materials. The main purpose of soil nailing is to increase the tensile and shear strength of soil and restrain its displacement. The technique permits stabilization of both natural slopes and vertical or inclined excavations. Soil nails provide adequate tensile strength to the slope that helps in the effective stabilization of landslides. The design parameters involve calculations of various components including calculation of total earth pressure and moments, external stability, overturning, tilting/ bearing failure, global slope failure, internal stability, seismic stability, etc. The limitations of the soil nailing technique are not inevitable but the magnitude of limitations may be reduced to a certain extent by proper analysis and design [3].

3.1 Soil Nailing Technique

Soil nailing is a reinforcement technique in which closely spaced parallel steel bars are installed into the face of a slope or vertical cut to improve stability. The basic concept behind soil nailing consists of placing in the ground passive inclusions, closely spaced, to restrain displacements and limit decompression during and after excavation. The function of soil nailing is to strengthen or stabilize the existing steep slopes and excavations as construction proceeds from the top to the bottom. Soil nails develop their reinforcing action through soil–nail interaction due to the ground deformation, which results in the development of tensile forces in soil nail. The significant part of resistances comes from the development of axial force which is basically a tension force. Conventionally, shear and bending have been assumed to provide little contribution in providing resistance. The effect of soil nailing is to improve the stability of slope or excavation through

(a) Increasing the normal force on the shear plane and hence increase the shear resistance along the slip plane in friction soil.
(b) Reducing the driving force along slip plane both in friction and cohesive soil.

In soil nailing, the reinforcement is installed horizontally or gently inclined parallel to the direction of tensile strain so that it develops maximum tensile force develops. For a vertical cut slope with a horizontal back slope, the length of soil nails is usually 60–100% of wall height. Based on various soil types and ground conditions, the soil nails are placed 6 ft centers vertically and 5–8 ft centers horizontally. The most common installation method is to insert the steel bars into a drill hole and grout the bottom up by gravity or low pressure. This procedure is described in some detail in this paper. Other construction methods include jet grouting or driving nails into

the slope. The soil nailing is a top-down construction procedure and is suitable for temporary and permanent cut slopes and for shallow depth landslide remediation. Excavation to expose the steep cut face proceeds with a series of steps 3–6 feet high. After each step has been opened up, soil nails are installed in a row and the face is shotcrete to prevent collapse or erosion of the exposed face. The end of the nail which is projecting out of the slope face is then attached to the shotcrete facing by a metal plate and bolt. After the full depth of excavation has been reached, the second layer of shotcrete is further added to strengthen the wall and to protect the nails. Soil nails installed for permanent slopes require corrosion-resistant treatment for durability.

3.2 Design Procedure

Soil nailing method is an in situ soil reinforcement technique that is used at present to stabilize natural slopes, cuts or excavation, walls in stiff cliffs, granular soils, and also soft rocks. The procedure involves the insertion of steel rods (usually 20–30 mm in diameter) by simple driving or by grouting into the predrilled boreholes. The basic steps involved in construction are illustrated as below.

There are usually steel rods 20–30 mm in diameter, which are inserted into the soil either by simple driving or by grouting in the predrilled borehole. Standard construction steps for typical soil nailing method can be broadly divided into four steps and these steps are repeated in the cycle as outlined below.

The installation of soil reinforcement depends upon the construction method adopted either top-down or bottom-up. It is always desirable to place the soil nails simultaneously after the excavation to avoid the complication and cost of pretreatment. There is also a requirement of dewatering if water is present in the slope in order to ease the construction and durability of soil nailing. Otherwise, if water percolates through the face, the unreinforced soil will slump locally on the initial excavation. The nail length plays a vital role in the design of soil-nailed structures as both the economy and stability of the structure depend on it. The commonly used L/H ratio is in the range of 0.5–0.8. However, higher values of the L/H ratio indicate mainly the repairing of existing structures. L = Nail Length H = Overall structure height. The most commonly used nail inclination is between 10 and 20, with 15 being the most used inclination. This inclination is because of the ease of construction. Nail diameter is varied from 14 to 40 mm but the range of 20–30 mm is very common. Grouted hole diameter varied from 56 to 200 mm but the range 100–120 mm was more common. The basic behavior and mechanism of soil nailing have been explained with due regard to various failure modes of the nailed structure. The pullout strength of the nails has been explained with respect to its strength envelop. The effects of various parameters, namely analysis and design, potential failure modes of a soil nail wall, nail strength failure envelope and nail inclination on the nail behavior have been discussed.

4 Landslides Remedial Measures—Retaining Structures

4.1 Retaining Structures

Retaining walls can be constructed by either top-down or base-up methods. In the top-down method of construction, the wall is built starting from the ground surface of the landslide. The disturbed ground downslope of the wall is excavated after the wall support is in place. Top-down walls can provide some assurance that the landslide will remain stable during remediation work, which is beneficial to the safety and adjoining property owners.

Base-up retaining walls are conventional walls founded on firm ground and provide resistance due to gravity or cantilever action. In landslide situations, there is usually a need to excavate some of the landslide debris at the bottom of the slide before the retaining wall can be constructed. As this undermines the landslide, it may require dry weather conditions or dewatering to lower groundwater levels within the landslide before construction of the retaining wall can begin [4].

4.2 Retaining Wall System

a. **Masonry walls**

Masonry is the building of structures from individual units laid in and bound together by mortar. The common materials of masonry construction are brick, stone such as marble, granite, travertine, limestone; concrete block, glass block, and tile. Masonry is generally a highly durable form of construction.

b. **Sausage walls**

Apart from masonry or concrete retaining walls, crib walls, and sausage walls are also used as restraining structures. The crib wall is formed in a wooden crib/mesh, in which dry stone masonry is built. Sausage walls are made by forming sausage of steel wire netting of square or hexagonal holes and filling the sausages with hard local boulder/stones. The sausage walls have the advantage of being able to withstand large deformations without cracking. Further because of the open structure, sausage walls allow free drainage of water. One drawback that has been observed occasionally is that falling boulders may cut or break SWG mesh, thereby leading to the possibility of stones falling out of the sausage crates. Due to high humidity and other adverse climatic conditions, rusting of SWG may occur damaging the sausage casing. However, with adequate attention, such damages can be rectified and the integrity of sausage walls maintained.

c. **Concrete gravity retaining walls**

The concrete gravity walls are very expansive and advantageous for important structures and both urban and rural areas. Such walls require a foundation in bedrock or

good soil below the slip surface. The design of the stem of the wall and the stability of the whole body of the wall, are both considered in the design. The body of the wall is taken to include the mass of soil directly above the heel of the cantilevered wall and earth pressure. The formula for the safety factor may be used to estimate the resistance required to lateral thrust. The standard practice is to include weep holes in designing the wall. Concrete walls sometimes fail due to their inadequate ability to resist groundwater pressures. In these cases, analyzed routing of weep holes is recommended. These walls fail due to sliding along the base in such cases a thin layer of crushed sand or sand gravel should be placed between the native soil and wall base.

d. **Anchored walls**

The stability of the retaining wall can also be enhanced through ground anchors. Stabilization by deep, pre-stressed anchors is being applied to soil slope. Walls with pre-stressed anchors have a major advantage by actively opposing the movement of the soil mass, rather than behaving passively as in the case of unstressed anchors and gravity structures. These are employed either in conjunction with retaining structures or alone to reduce the driving forces of a landslide and to increase the normal effective stress on its slip surface. Tie back walls are used to transfer the imposed load to an area behind the slide mass where satisfactory resistance can be established. A tie-back sheet pile wall can be used to ensure adequate anchorage in the stiff clays. Stabilization by deep, pre-stressed anchors is being generally applied to soil slope. Walls with pre-stressed anchors have a major advantage by actively opposing the movement of the soil mass, rather than behaving passively as to unstressed anchors.

e. **Diaphragm wall**

A diaphragm wall is a structural element that transmits lateral loads to the vertical resisting elements of a structure. Diaphragms are typically horizontal but can be sloped. A diaphragm wall is constructed using a narrow trench excavated in the ground and supported by an engineered fluid (typically a bentonite mud) until the mud is replaced by the permanent material. Generally, diaphragm walls are made from reinforced concrete, though un-reinforced walls can also be used. Diaphragm walls are often used in congested areas or where the excavation depth is very deep which would otherwise require excavation of much greater soil volumes to provide stable battered slopes. They are well suited for deep basements, underground rail stations, rail car unloaders, tunnel approaches, pumping stations, and the like. Diaphragm walls can be installed close to existing structures and in restricted headroom. They are often used in “top-down” construction methods.

Despite having several advantages, diaphragm walls have limitations such as high cost of construction, special requirements of manpower and equipment which are not easily available in every part of the country [4].

5 Micro-piles or Root Piles for Slope Stabilization

Micro-piles (shown in Fig. 1.8) are essentially an outgrowth of the technology of the construction of ground anchors. They are small diameter bored piles in which steel reinforcement is grouted into a borehole to form the pile. The loads are carried by skin friction between the soil and grout, but load-bearing is provided by the steel; they can carry loads in either compression or tension. End bearing capabilities are ignored.

The piles can be designed for two broad uses:

- As a conventional pile of small diameter;
- As a composite soil/pile mass in which the piles reinforce the soil mass three-dimensionally into a gravity-type structure.

Micro-piles are typically 4–10 inches in diameter, 70–100 ft long, and carry loads of 35 to more than 100 tons in tension or compression. Their main attribute is the flexibility of use. The piles can be drilled into almost all ground conditions in any preselected direction. The construction equipment requires little headroom and can gain access to restricted spaces. They have been widely used for residential underpinning, seismic retrofit, and many other difficult circumstances Micro-piles for landslide stabilization typically are installed at various angles to the vertical (Fig. 1.8) to knit soils together into a composite mass of soil and piles. The individual piles are not directly loaded but provide a framework for achieving a coherent mass of soil. Such piles are frequently referred to as reticulated piles or root piles to provide an analogy to the roots of a tree.

5.1 Advantages of Micro-piles

The micro-piles have advantages that they can be constructed under the following conditions:

- Low headroom,
- Restricted access,
- Almost all soil conditions, including boulders, voids, etc.

6 Landslide Remedial Measures—Drainage

6.1 Drainage Remedial Measures—Surface Drainage

Surface drainage is the removal of water that collects on land. The control of surface water is most important in the stabilization of slopes. Drainage not only reduces the weight of the mass tending to slide out but also increases the strength of the slope

forming materials. Surface water can also cause erosion. Infiltration results in the development of excess pore water pressure within the slopes. Due to the absence of proper drainage facility, landslips occur. It is therefore natural that the improvement of the drainage facilities in the area is given high priority.

Control of surface water consists of two main parts:

1. The collection of run-off at the uphill boundary of any unstable area.
2. Maximum run-off from the unstable area and controlling and collecting this run-off.

Usually, any system of surface drainage should include investigating the need for other existing practices of hillside road construction such as slope treatment of the hillsides for erosion control, regarding the reshaping of the slope for promoting quick run-off. On the other hand, sealing of tension cracks by means of rodding in loamy earth will mitigate the susceptibility of the slope to a potential slide. Catch water or interceptor drains, side drains, and cross drains constitute some of the more important types of drains used in a system of surface drainage.

6.2 Catch Water Drains

Surface water flowing from the hill slope toward the potential unstable areas or the roadway is one of the main problems in the drainage of hill slope during heavy rains. In order to intercept and divert the water from the hill slope, catch water drains should be located very carefully, after the topography of the ground is studied in detail. It has been observed in practice that poor location of surface drains results in their serving no purpose since no water would be collected by them, and on the other hand, the run-off bypasses the drains and continues to damage the slopes.

Catch water drains should be lined and properly maintained and should be given a gradient of 1 in 50 to 1 in 33 to avoid high water velocity and possible wash out. A number of interconnecting lined catch water drains may need to be constructed on the slope to collect the surface run-off if the area of the slide is large. Water from the catch water drains should be diverted into a chute or a natural hillside drain or diverted by sloping drains and lead into culverts at a lower level finally to be led through chutes into the nearest natural watercourse.

6.3 Deep Trench Drains

Deep trench drains can also be used for the purpose of subsurface drainage. These are generally limited, by practical consideration, to those locations where water can be intercepted at a depth <5–8 m. Trench drains can also be used for the purpose of subsurface drainage when horizontal drilling is not possible because of site conditions or economic considerations. Deep subsurface trench drains, consisting of a number

of interconnected dug into the slope, and backfilled with well drainage rubble, can be highly effective in quickly draining a saturated slope. Maintenance is needed for the proper functioning of trench drains. Flow rate can be decreased during dry weather flow and erosion (if any) takes place should be repaired.

6.4 Scupper

It is an economical type of culvert or cross drain, where dry masonry retaining wall is provided for the road. The water collected through side drains, or nallah, is discharged to the valley side through small cross-drainage structures usually 0.85–1.2 m wide made of random rubble dry masonry abutments. The top of the abutments is corbelled with a few layers of stones and a stone slab is laid on the top. Hand-packed stones are placed on top about 0.35–0.60 m thick and also all around the scupper, retaining walls are provided on both ends of the scupper. Scuppers are provided approximately at every 150 m apart in full width of the road surface. Frequent maintenance is required in scuppers as they get choked due to the falling of boulders and materials into it resulting in very less or no drainage.

6.5 Subsurface Drainage

Subsurface drainage is concerned with removing water that percolates through or is contained in the underlying soil subgrade. Deep-seated landslides and slope failures are often caused by the presence of subsoil water in the slope area, and the resulting high water pressure on possible failure planes. Hence, successful methods for both prevention and correction of landslides have perforce to rely heavily on groundwater control by employing suitable deep drainage techniques. Subsurface drainage acts to modify the seepage pattern within the soil or rock mass and reduce the pore water pressures. The removal of water from within a slope by subsurface drainage is costlier than surface drainage. However, subsurface drainage is usually more effective because it leads to a decrease in pore water pressure directly at the failure plane.

Removal of subsurface water tends to produce a more stable condition in several ways such as

(a) Seepage forces are reduced,
(b) Shear strength,
(c) There is reduction in pore pressure, and
(d) Driving forces are reduced.

Seepage forces act together to increase the driving force on a landslide surface and hence attempts are generally made to intercept subsurface flows above the sliding

mass. Subsurface drainage is also useful in cut areas and under proposed embankments. Methods generally used to accomplish subsurface drainage are the installation of horizontal drains, vertical, drainage wells, deep trench drains, and drainage tunnels.

6.6 Horizontal Drains

Horizontal drains are defined as multiple holes drilled into a cut slope or embankment and cased with a perforated metal or slotted plastic liner. The purpose of using horizontal drains as part of landslide control work is to drain away groundwater, thus keeping the soil dry.

7 Bioengineering Measures for Stabilization of Landslides

Bioengineering techniques are useful approaches to prevent landslides as they improve the slope stability and maintain ecological balance. They are mostly suitable to be deployed in developing countries because of their cost-effectiveness and environmentally friendly nature [5].

The bioengineering techniques' contributions to the renewable energy sector will contribute to the sustainable development of the local community. Vegetation helps in sustaining biodiversity and giving a positive influence on the ground structure by creating a balance between the soil and water. It is very important to understand the root–soil relationship for a successful implementation of bioengineering techniques [6].

8 Conclusions

It is often very difficult to design an effective, economically feasible, and long-lasting remedial measures for landslides. Different types of remedial measures are discussed in this paper by representing the advantages and limitations of the same. Based on the investigation of landslide, the failure mechanism of landslides and stability analysis of slope a set of appropriate remedial measures are evolved. This paper will be beneficial for all the researchers and implementing agencies to refer to major landslides' remedial measures from one document. The important remedial measures are illustrated in this precise paper, which can further be used for designing of innovative, cost-effective, and less complex remedial measures in the future. Critical reviews of remedial measures given in this paper can be referred by the executing agencies to provide effective solutions to encounter landslides problems.

References

1. Bang, S., Shen, C.K., Romsted, K.M.: Analysis of an earth reinforcing system for deep excavation. Transportation Research Record, No. 749, pp. 21–26 (1980)
2. Cornoforth D.H.: Landslides in practice. In: Earth Reinforcement Systems, Chapter 20, pp. 424–441 (2005)
3. Sabahit, N., Madhav, M.R., Basudhar, P.K.: Seismic analysis of nailed soil slopes. In: Proceedings of IS Kyushu International Symposium on Earth Reinforcement, Kyushu, Japan, pp. 347–352 (1996)
4. Arya, A.S., Gupta, V.P.: Retaining wall for hill roads. I.R.C J. **44–1** (1983)
5. Lammeranner, W., Rauch, H.P., Laaha, G.: Implementation and monitoring of soil bioengineering measures at a landslide in the Middle Mountains of Nepal. Plant Soil **278**(1–2), 159–170 (2005)
6. Raut, R., Gudmestad, O.T.: Int. J. Des. Nat. Ecodyn. **12**(4), 418–427 (2017)

Influence of Fines Content on Stability of Unsaturated Soil Slopes

Ammavajjala Sesha Sai Raghuram, B. Munwar Basha, and Arif Ali Baig Moghal

1 Introduction

Natural sands usually consist of considerable fines content (FC), the presence of which severely affects its structure and unsaturated behavior [1–4]. Various proportions of clay and/or silt exist along with the natural sands, which significantly changes the shape of the soil–water characteristic curve (SWCC) or water retention characteristic curve (WRCC) [4]. SWCC or WRCC relates to soil water and soil suction. "Though the usage of locally available soil is economical many a times, it may not be appropriate for satisfactory execution. Therefore, it is necessary to opt for reconstitution of the soil. However, the capability of reconstituted soil would be significantly influenced by the level of reconstitution with the FC". Hence, it is highly necessary to understand the unsaturated behavior of reconstituted soils (sand and fines). WRCC is one of the key tools to address the unsaturated behavior of the soil in terms of shear strength and hydraulic coefficient. WRCC can be obtained in two ways namely desorption and sorption. However, both methods yield continuous WRCCs but are not identical. It is well accepted that, for a given constant water content, soil suction is not unique. This is termed as hysteresis. Hence, soil exhibits different WRCC during the desorption and sorption process. Hysteresis is due to the dependency of soil water content and desorption or sorption process. Ink bottle effect, contact angle effect, entrapped air, and aging of soil are responsible for hysteresis. The hysteresis of WRCC is illustrated in Fig. 1. The WRCC from full saturation to

A. S. S. Raghuram (✉) · B. M. Basha
Department of Civil Engineering, IIT Hyderabad, Kandi 502285, India

B. M. Basha
e-mail: basha@ce.iith.ac.in

A. A. B. Moghal
Department of Civil Engineering, NIT Warangal, Warangal 506004, India
e-mail: baig@nitw.ac.in

C. N. V. Satyanarayana Reddy et al. (eds.), *Stability of Slopes and Underground Excavations*, Lecture Notes in Civil Engineering 185,
https://doi.org/10.1007/978-981-16-5601-9_14

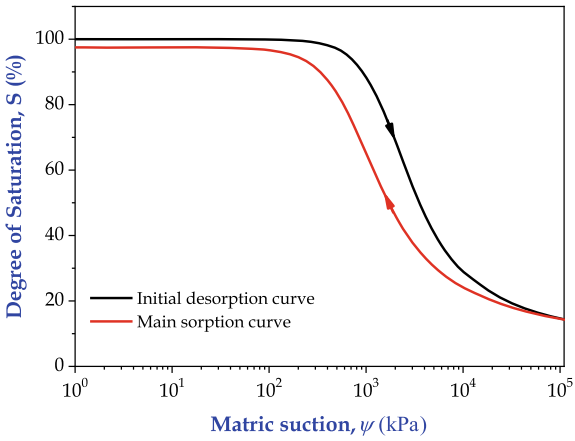

Fig. 1 Hysteretic water retention characteristic curve

residual zone represents the initial desorption curve. The main sorption curve is the WRCC from the residual zone to the completely saturated zone.

The change in depth of slip surface is very common in the natural and man-made slope due to seasonal variations. Most of the time, the failure slip surface lies in the unsaturated zone (i.e., above the water table). The change in soil suction in the unsaturated zone highly influences the stability of the slopes [5]. The assumption made in traditional soil mechanics is that the pore water pressures are either positive or zero along the failure plane. However, in the real field conditions, the pore pressures within the slope could be negative and even may change significantly. The earlier wealth of published research showed that there has been a clear understanding of the suction role in augmenting the shear strength and stability of the slopes. Recent developments have led to several devices that measure the soil suction accurately. Hence, it is highly appropriate to consider the effect of soil suction and hysteretic WRCC in the slope stability analysis. A simple procedure to obtain desorption and sorption WRCCs is presented by Raghuram et al. [6].

2 Literature on Hysteretic SWCC

Many researchers reported various techniques to predict the SWCC using a filter paper method [6–9], pressure plate apparatus [9–12], axis translation method [13], and dew point potentiometer [14]. Pham [15] used a pressure plate apparatus to find the hysteretic behavior of sands and loams and developed a simple method to estimate the SWCC scanning curves. Yang et al. [16] illustrated various parameters affecting the hysteretic SWCC of the sandy soil. A similar study was conducted by Ebrahimi-Birang et al. [17] to estimate the hysteretic SWCC at the high suction range. Li and Vanapalli [18] adopted an easy method to estimate the collapse behavior of soil under wet conditions. Recently Gapak and Tadikonda [19] investigated the

influence of desorption and sorption SWCCs of bentonites and developed a simple model to predict the boundary sorption SWCC. A study by Sun et al. [20] found that naturally deposited soils and most of the fine soils when compacted at the dry of optimum are prone to failure under wetting conditions. Xie and Chi [21] concluded that many slopes collapse under wetting conditions. A recent study by Raghuram et al. [6] demonstrated the effect of FC on the desorption and sorption of WRCC and concluded that the shape of WRCC changes significantly with change in FC. Likos et al. [22] and Raghuram and Basha [23] carried out the unsaturated slope stability analysis for three different soils and found that the factor of safety of the slope is significantly affected by the hysteretic SWCC.

The published studies highlight the importance of the influence of FC and hysteretic behavior of SWCC on unsaturated soils. However, to date, no studies are reported on the influence of FC and hysteresis of SWCC on the infinite slope stability and it has been undertaken in this work.

3 Soils Considered

Three different sand and red soil fines mixtures are used in this study from the Raghuram et al. [6]. Ennore sand of Grade—II quality was considered in this study. The specific gravity of the Ennore sand is 2.64. Ennore sand was reconstituted with 30, 40, and 50% red soil fines to obtain a desirable mixture of sand to fines ratio as 70: 30, 60: 40, and 50: 50, respectively. The basic and engineering soil properties of the three reconstituted samples are presented in Table. 1. The particle size distribution for Ennore sand and red soil fines is presented in Fig. 2. The shear strength parameters (cohesion and friction angle) and unit weight of the soil are maintained constant for all the three reconstituted soils to evaluate the effect of WRCC fitting parameters on the factor of safety (FS) of the unsaturated infinite slope.

Several models are available to estimate the WRCC. In the present study, the van Genuchten (VG) model is considered [24]. The VG model is popularly used and predicts the WRCC accurately and precisely. The VG WRCC model is given by

$$S = \frac{\theta_w}{\theta_s} = \frac{1}{\left[1 + (\alpha\psi)^n\right]^m} \tag{1}$$

where α is the fitting parameter of WRCC related to the inverse of air entry value (AEV), n is the fitting parameter of WRCC related to the slope of WRCC, and m is the fitting parameter of WRCC related to the symmetry of WRCC. The WRCC parameter m is directly related to the fitting parameter n as shown below.

$$m = \left(1 - \frac{1}{n}\right) \tag{2}$$

Table 1 Engineering properties of the reconstituted soils

Property	30% fines	40% fines	50% fines
Specific gravity	2.649	2.652	2.655
Maximum dry density	19.08	18.61	18.10
Plasticity index	–	7.78	11.01
Grain size distribution			
Sand (%)	70	60	50
Fines (%)	30	40	50
Unified soil classification system, USCS	SM	SC	SC-CL
Effective cohesion, c' (kPa)	10	10	10
Effective friction angle, ϕ' (deg.)	27	27	27
Drying saturated water content, θ_{sd}	0.266	0.285	0.306
Wetting saturated water content, θ_{sw}	0.262	0.281	0.302
VG fitting parameters			
α_d (kPa^{-1})	0.04292	0.02311	0.00484
α_w (kPa^{-1})	0.08145	0.04449	0.00937
n_d	12.74	10.19	5.76
n_w	10.99	10.04	5.32

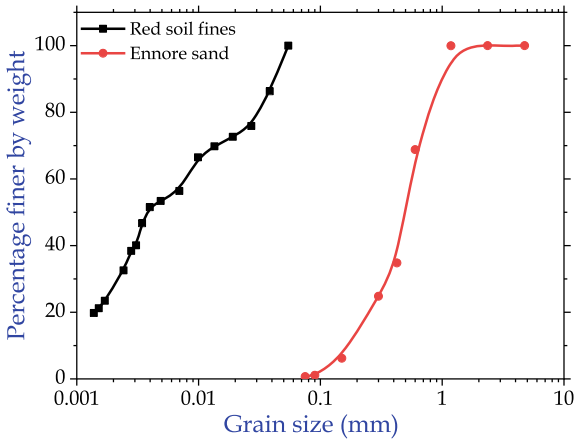

Fig. 2 Particle size distribution for Ennore sand and red soil fines

Substituting Eq. 2 into Eq. 1, it becomes

$$\theta_w = \frac{\theta_s}{\left[1 + (\alpha\psi)^n\right]^{\left(1-\frac{1}{n}\right)}} \tag{3}$$

4 Unsaturated Infinite Slope Stability

As shown in Fig. 3, an infinite slope with a slope angle "ω" is considered. The unsaturated shear strength (USS) model proposed by Fredlund et al. [25] is considered. The FS of the unsaturated slope is given in Eq. (4).

$$F = \frac{c'}{\gamma H \sin\omega \cos\omega} + \frac{\tan\phi'}{\tan\omega} + \frac{(\theta_w/\theta_s)^{\kappa} \tan\phi'(u_a - u_w)}{\gamma H \sin\omega \cos\omega} \tag{4}$$

where c' and ϕ' are the effective cohesion and effective internal friction angle, H = represents the depth of slip surface, γ is the unit weight of soil, $\psi = (u_a - u_w)$ is the matric suction, u_w and u_a are the pore water and pore air pressures, θ_w is the volumetric water content, and θ_s is the saturated water content. In atmospheric conditions, $u_a = 0$. Therefore, Eq. 4 becomes

$$F = \frac{c'}{\gamma H \sin\omega \cos\omega} + \frac{\tan\phi'}{\tan\omega} + \frac{(\theta_w/\theta_s)^{\kappa} \tan\phi'(-u_w)}{\gamma H \sin\omega \cos\omega} \tag{5}$$

Along the failure slip surface, the matric suction can be given as follows:

$$\psi = -u_w = -\left[\gamma_w(-H_w)\cos^2\omega\right] = \gamma_w H_w \cos^2\omega \tag{6}$$

where H_w represents the depth of the water table from the ground surface. The FS of the unsaturated infinite slope can be estimated using Eqs. 3, 5, and 6.

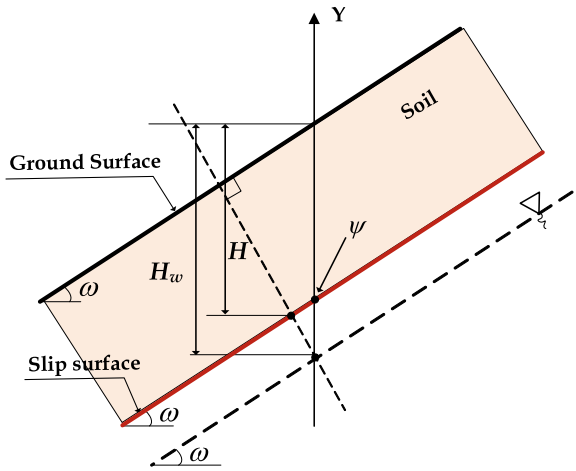

Fig. 3 The geometry of the unsaturated infinite slope

5 Results and Discussion

Figure 4a, b and c shows the hysteresis of WRCC for the three reconstituted soils with 30, 40, and 50% FC. It can be observed from Fig. 4a that the suction associated with desorption WRCC is greater than the suction associated with sorption WRCC because of hysteresis. The entrapped air in the soil is responsible for the higher degree of saturation for desorption WRCC when compared to sorption WRCC. Similarly, for given constant water content, the suction in desorption WRCC is greater than sorption WRCC. This could be attributed to the ink-bottle effect [1]. An interesting finding is that with an increase in the percentage of fines in the soil, the shape of WRCC significantly changes and shifts toward the higher suction range. This is because, as the FC increases, the macropores in the soil reduce, and therefore air requires more suction to enter the soil. Figure 4d shows the shift in WRRCs with respect to FC in the soil.

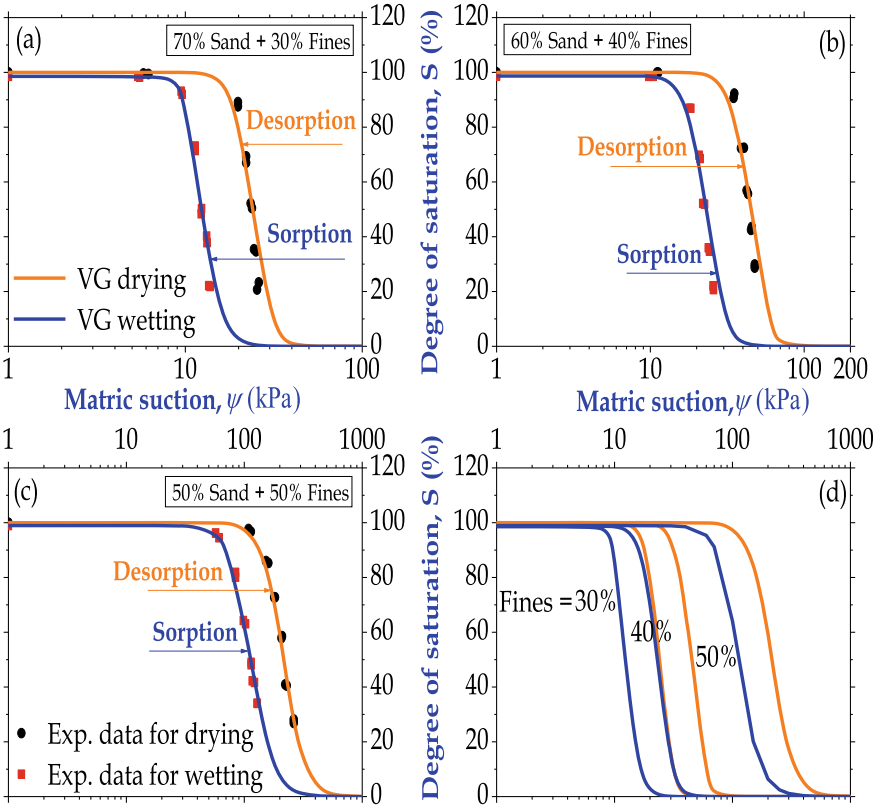

Fig. 4 Influence of FC on hysteretic WRCC, (**a**) 30% fines, (**b**) 40% fines, (**c**) 50% fines, (**d**) 30%, 40, and 50% together

The influence of FC and hysteretic WRCC on the factor of safety is shown in Fig. 5a, b and c. It can be noted from Fig. 5a that the effect of hysteresis on FS is insignificant for 30% fines. This is because suction in coarse-grained soil is less when compared to fine-grained soil. As the majority of the proportion is sand, the shear strength contribution by the suction is less. However, the difference in FS between desorption and sorption WRCC increases with an increase in depth of water table for 40 and 50% fines. As an example, the maximum difference in FS for desorption and sorption WRRC is 0.08 and 0.15 for 30 and 50%, respectively (Figs. 5a and c).

Additionally, it can be observed from Fig. 5a, b and c that the FS increases with an increase in the FC for both desorption and sorption cycles. This could be attributed to an increase in the shear strength due to matric suction with an increase in the FC. Furthermore, it can be observed that for a given depth of water table, the difference in FS between desorption and sorption WRCC follows the order for 30% fines > 40% fines > 50% fines. As an illustration for a given depth of water table at 7 m, the difference in FS between desorption and sorption WRCC is 0.08, 0.05, 0.03 for 30% fines, 40% fines, and 50% fines, respectively. The difference in FS between the desorption and sorption WRCC depends on the degree of hysteresis. As the degree of hysteresis is more, the more is the difference in FS between desorption and sorption WRCC.

5.1 Degree of Hysteresis

Lu and Khorshidi [26] and Raghuram et al. [6] proposed simple equations to estimate the degree of hysteresis. Figure 6a demonstrates the procedure to estimate the degree of hysteresis. The required number of slices to compute the D_h for the three reconstituted soils is shown in Fig. 6b. The difference between maximum and minimum suctions divided by the total number of slices gives the spacing between the slices ($\Delta\psi$). The suction value at the ith slice is given by

$$\psi_i = \psi_{\min} + (\Delta\psi \times i) \text{ Where } i = 1 \text{ to } N \tag{4}$$

The corresponding degree of saturation (S) can be estimated using the VG WRCC model. The local degree of hysteresis ($D_{h\_\psi_i}$) is given as

$$D_{h\_\psi_i} = \frac{S_{d\_\psi_i} - S_{w\_\psi_i}}{S_{m\_\psi_i}} \tag{3}$$

where $S_{d\_\psi_i}$ and $S_{w\_\psi_i}$ = degree of saturation on desorption and sorption WRCCs at the ith slice, and $S_{m\_\psi_i}$ = mean value of $S_{d\_\psi_i}$ and $S_{w\_\psi_i}$. The total degree of hysteresis (D_h) for the complete hysteresis is given by

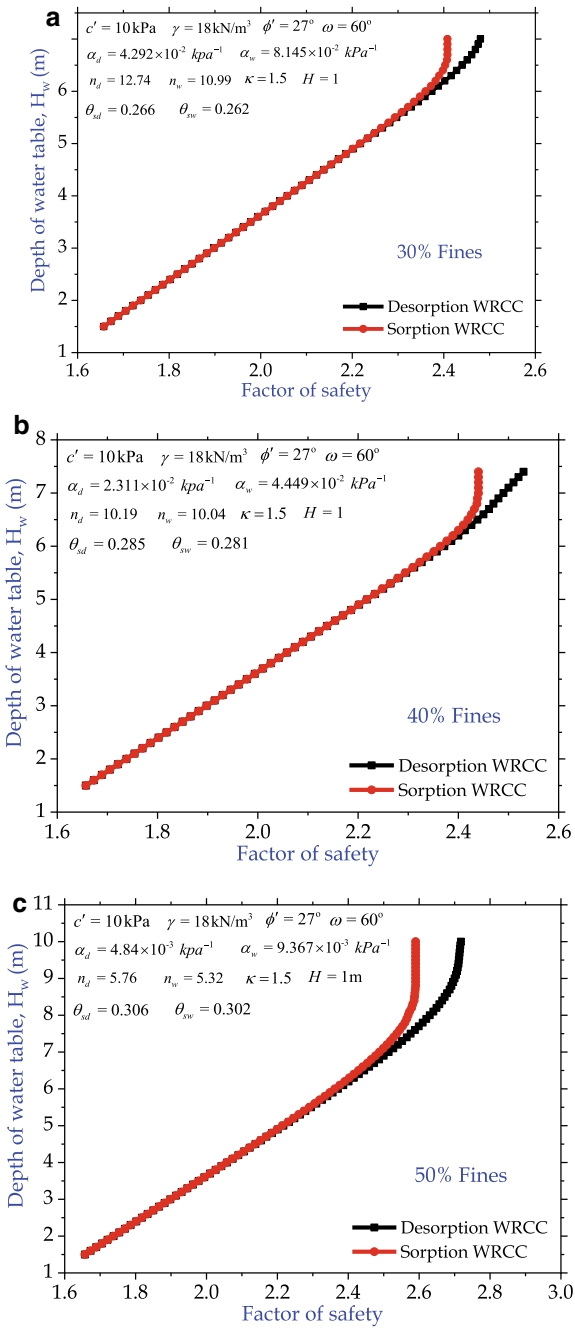

Fig. 5 (**a**) Effect of hysteresis on the FS for 30% fines in the soil. (**b**) Effect of hysteresis on the FS for 40% fines in the soil. (**c**). Effect of hysteresis on the FS for 50% fines in the soil

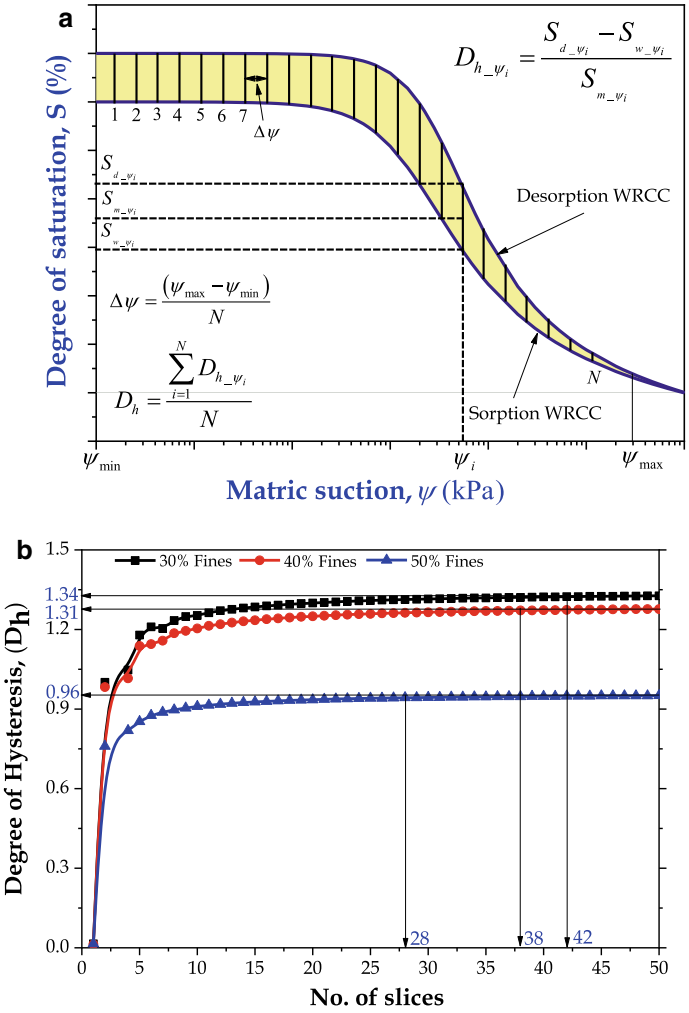

Fig. 6 (**a**) Degree of hysteresis for the WRCC and (**b**) Effect of FC and slice number on the degree of hysteresis

$$D_h = \frac{\sum_{i=1}^{N} D_{h\_\psi_i}}{N} \tag{4}$$

A D_h value of 0.4 represents the degree of saturation of 40% to its mean degree of saturation. Figure 6b shows that the required number of slices to compute the converged value of D_h reduces as the FC in the soil increases.

As an illustration, the number of slices decreases from 42 to 28 as the FC increases from 30 to 50%. This is because of the decrease in D_h from 1.34 to 0.96 as the FC

increase from 30 to 50%. The decrease in the degree of hysteresis with an increase in FC in the soil depends on the wet to dry ratio of the AEV value, which is highest for 30% fines.

6 Conclusions

The influence of fines content and hysteretic WRCC on the infinite slope stability is carried out at three different fines contents. The key findings from the study are:

1. The present study emphasizes the importance of the effect of fines content and hysteresis of WRCC on the infinite slope stability.
2. A considerable difference in the WRCC fitting parameters and FS is observed due to desorption and sorption WRCC.
3. The difference in FS between desorption and sorption WRCC depends on the degree of hysteresis which in turn depends on wet to dry ratio of the AEV value.
4. The difference in FS between desorption and sorption WRCC is maximum for 30% fines and minimum for 50% fines.

The results revealed that neglecting the effect of hysteretic WRCC overestimates the FS. The effect of FC has a substantial influence on the hysteretic WRCC and thereby on the FS of the slope. Therefore, due consideration must be given to sorption WRCC and FC to obtain realistic values of the FS of the unsaturated soil slope.

References

1. Fredlund, D.G., Rahardjo, A.: Soil mechanics for unsaturated soils. Wiley, New York (1993)
2. Gallage, C.P.K., Uchimura, T.: Effects of dry density and grain size distribution on soil–water characteristic curves of sandy soils. Soils Found. **50**(1), 161–172 (2010)
3. Benson, C.H., Chiang, I., Chalermyanont, T., Sawangsuriya, A.: Estimating van Genuchten parameters α and n for clean sands from particle size distribution data. In Proceedings of the Geo-Congress 2014: In From Soil Behavior Fundamentals to Innovations in Geotechnical Engineering: Honoring Roy E. Olson, 410–427. Reston, VA, ASCE. (2014)
4. Vanapalli, S.K., Fredlund, D.G., Pufahl, D.E.: The influence of soil structure and stress history on the soil-water characteristics of a compacted till. Géotechnique **49**(2), 143–159 (1999)
5. Godt, J.W., Baum, R.L., Lu, N.: Landsliding in partially saturated materials. Geophys. Res. Let. **36**, L02403 (2009)
6. Raghuram, A.S.S., Basha, B.M., Moghal, A.A.B.: Effect of fines content on the hysteretic behavior of water-retention characteristic curves of reconstituted soils. J. Mat. Civil Eng. **32**(4), 04020057 (2020)
7. ASTM Designation: D5298–16: standard test method for measurement of soil potential (suction) using filter paper. Am. Soc. Test. Mater. West Conshohocken, PA, (2016)
8. Puppala, A.J., Manosuthikij, T., Chittoori, B.C.S.: Swell and shrinkage characterizations of unsaturated expansive clays. Eng. Geol. **164**, 187–194 (2013)
9. Ahmed Al-Mahbashi, A., Al-Shamrani, M.A., Moghal, A.A.B.: Soil water characteristic curve response and one-dimensional deformation characteristics of fiber reinforced lime blended expansive soil. J. Mat. Civil Eng. **32**(6), 04020125 (2020).

10. Hoyos, L.R., Suescún-Florez, E.A., Puppala, A.J.: Stiffness of intermediate unsaturated soil from simultaneous suction-controlled resonant column and bender element testing. Eng. Geol. **188**(7), 10–28 (2015).
11. Rahardjo, H., Satyanaga, A., Leong, E.C.: Effects of flux boundary conditions on porewater pressure distribution in slope. Eng. Geol. **165**, 133–142 (2013)
12. Thakur, V.K.S., Sreedeep, S., Singh, D.N.: Parameters affecting soil-water characteristic curves of fine-grained soils. J. Geotech. Geoenviron. Eng. **131**(4), 521–524 (2005)
13. Vanapalli, S.K., Nicotera, M.V., Sharma, R.S.: Axis translation and negative water column techniques for suction control. Geotech. Geol. Eng. **26**(6), 645–660 (2008)
14. Leong, E.C., Tripathy, S., Rahardjo, H.: Total suction measurement of unsaturated soils with a device using chilled mirror dew-point technique. Geotechnique **53**(2), 173–182 (2003).
15. Pham, H.Q.: An engineering model of hysteresis for soil-water characteristic curves. M.Sc. thesis, University of Saskatchewan, Saskatoon, SK, Canada (2001)
16. Yang, H., Rahardjo, H., Leong, E.C., Fredlund, D.G.: Factors affecting drying and wetting soil-water characteristic curves of sandy soils. Can. Geotech. J. **41**(5), 908–920 (2004)
17. Ebrahimi-Birang, E., Fredlund, D.G., Samarasekera, L.: Hysteresis of the soil water characteristic curve in the high suction range. In: Proceedings of the Ottawa Geo Conference, pp. 1061–1068. Ottawa (2007)
18. Li, P., Vanapalli, S.K.: Simple method for prediction of the soil collapse behavior due to wetting. Int. J. Geomech. **18**(11), 06018026 (2018)
19. Gapak, Y., Tadikonda, V.B.: Hysteretic water-retention behavior of bentonites. J. Hazard. Toxic Radioactive Waste **22**(3), 04018008 (2018)
20. Sun, D.A., Sheng, D.C., Xu, Y.F.: Collapse behaviour of unsaturated compacted soil with different initial densities. Can. Geotech. J. **44**, 673–686 (2007).
21. Xie, Y., Chi, Y.: Geochemical investigation of dry- and wet-deposited dust during the same dust-storm event in Harbin, China: constraint on provenance and implications for formation of aeolian loess. J. Asian Earth Sci. **120**, 43–61 (2016)
22. Likos, W.J., Lu, N., Godt, J.W.: Hysteresis and uncertainty in soil water-retention curve parameters. J. Geotech. Geoenviron. Eng. **140**(4), 04013050 (2014)
23. Raghuram, A.S.S., Basha, B.M.: Effect of drying and wetting SWCCs on unsaturated soil slopes. In: Indian Geotechnical Conference 2019, GeoIND, December, SVNIT Surat, India. (2019)
24. van Genuchten, M.T.: A closed-form equation for predicting the hydraulic conductivity of unsaturated soil. Soil Sci. Soc. Am. J. **44**(5), 892–898 (1980)
25. Fredlund, D.G., Xing, A., Fredlund, M.D., Barbour, S.L.: The relationship of the unsaturated soil shear strength to the soil water characteristic curve. Can. Geotech. J. **32**(3), 440–448 (1996)
26. Lu, N., Khorshidi, M.: Mechanisms for soil-water retention and hysteresis at high suction range. J. Geotech. Geoenviron. Eng. **141**(8), 04015032 (2015)

Stability of Sloped Soil Embankment for Seismic and Tidal Load Combination

Amritansh Mishra and A. Trivedi

1 Introduction

Sloped soil embankment near the port faces fluctuation in water level due to tides in the sea, seismic action, dynamic vehicular load, and superstructure load. So the combined effect of these loading poses a threat to slope stability of soil embankment. In this study effect due to dynamic vehicle load and superstructure is not considered. In this paper, a sloped soil embankment is made with the help of Geoslope software. The stability of soil embankment is checked against seismic loading and a combination of seismic and tidal loading using M-C criteria. Fredlund and Krahn [1] explained various slope stability methods. However, in this paper, slope stability theories namely the Bishop method, Fellenius method, Spencer method, and Janbu method were considered to find a minimum factor of safety. Using Bishop's theory variation in the factor of safety with a surcharge is examined at horizontal seismic coefficients 0.225 and 0.16 (zone III cities) respectively for seismic loading and combination of seismic and tidal loading.

Duzceer [2] used the limit equilibrium method to test the stability of rock slope in Makkah, Saudi Arabia. Duzccer R used rock anchors to provide stability to the rock slope. Desai and Choudhury [3] studied the seismic ground response of different sites in Mumba using different peak horizontal acceleration. Misra et al. [4] simplified the analysis method for micro support pullout behavior.

A. Mishra
Geotechnical Engineering, Department of Civil Engineering, Delhi Technological University, Delhi 110042, India

A. Trivedi (✉)
Department of Civil Engineering, Delhi Technological University, Delhi 110042, India
e-mail: atrivedi@dce.ac.in

C. N. V. Satyanarayana Reddy et al. (eds.), *Stability of Slopes and Underground Excavations*, Lecture Notes in Civil Engineering 185,
https://doi.org/10.1007/978-981-16-5601-9_15

1.1 Equations Used to Find the Factor of Safety

Following equation are used to find the factor of safety,

$$F_{improved} = \acute{\eta}\ F_{original} \tag{1}$$

$$\acute{\eta} = F_{original} / F_{improved} \tag{2}$$

where $F_{improved}$ is a factor of safety after the application of micropiles. $\acute{\eta}$ is a non-dimensional improvement factor. $F_{original}$ is a factor of safety before providing any micropiles.

The equation to find $F_{original}$ [1] and $F_{improved}$ [as per Eqs. (3)–(8)] are presented as follows:

A. **Fellenius method**

$$F = \frac{\sum\{c'l\ R + (P - ul)R\ \tan\emptyset'\}}{\sum wx - \sum Pf + \sum kwe\ \pm Aa + Ld} \tag{3}$$

B. **Bishop Method**

$$P = \left(W - \frac{C'l \sin\alpha}{F} + \frac{ul \sin\alpha \tan\emptyset'}{F}\right) \times \frac{1}{m_\alpha} \tag{4}$$

$$m_\alpha = \frac{\cos\alpha + (\sin\alpha \tan\emptyset')}{F} \tag{5}$$

C. **Spencer method**

$$F_f = \frac{\sum\{c'l \cos\alpha + (P - ul)\cos\alpha \tan\emptyset'\}}{\sum P \sin\alpha + \sum kW \pm A - L\cos\omega} \tag{6}$$

D. **Janbu's Simplified Method**

$$F_O = \frac{\sum\{c'l \cos\alpha + (P - ul)\cos\alpha \tan\emptyset'\}}{\sum P \sin\alpha + \sum kW \pm A - L\cos\omega} \tag{7}$$

$$F = f_o \times F_o \tag{8}$$

2 Analysis of Sloped Soil Embankment

A sloped soil embankment is made using Geoslopes software. The height and slope of soil embankment are 8 m and 60° respectively. Necessary details for analysis are taken from Jawaharlal Nehru Port, Mumbai [5]. From bore log data each soil layer's depth and unit weight is calculated [3]. The cohesion and the friction angle value for each layer are determined as given in Table 1.

Two of the following cases are considered for analysis:

(a) Stability of sloped soil embankment against seismic loading
(b) Stability of sloped soil embankment against seismic and tidal load combination

The following combination of micropiles was used for the analysis of slope stability in both cases (Table 2).

To recommend a solution for slope stability it must satisfy the following conditions:

(a) It must ensure the safety of sloped soil embankment in both cases
(b) The factor of safety calculated from all considered slope stability theory must be 2 or more than 2 after the application of micropiles

Theoretically, a factor of safety more than 1 is considered safe but for all practical purposes, designers consider the factor of safety two or more than two. Hence we also set the bar at 2.

Table 1 Material Properties

S.no	Material	Unit weight (kN/m^3)	Cohesion (kPa)	Friction angle (°)
1	Sand embankment	12	12.26	2
2	Marine clay layer 1	12.26	12	2
3	Marine clay layer 2	12	12.26	2
4	Marine clay layer 3	12.2	12.26	2
5	Marine clay layer 4	12	12.26	2

Table 2 Combination of micropiles

Combination of micropiles	No of supports	Length (m)	Angle with horizontal (°)	Shear force [4] (kN)	Shear reduction factor
Set A	1	7	0	500	1
Set B	3	6	15	400	1
Set C	3	6.5	20	300	1
Set D	2	7	15	400	1
Set E	2	8	0	500	1
Set F	2	8.5	0	350	1

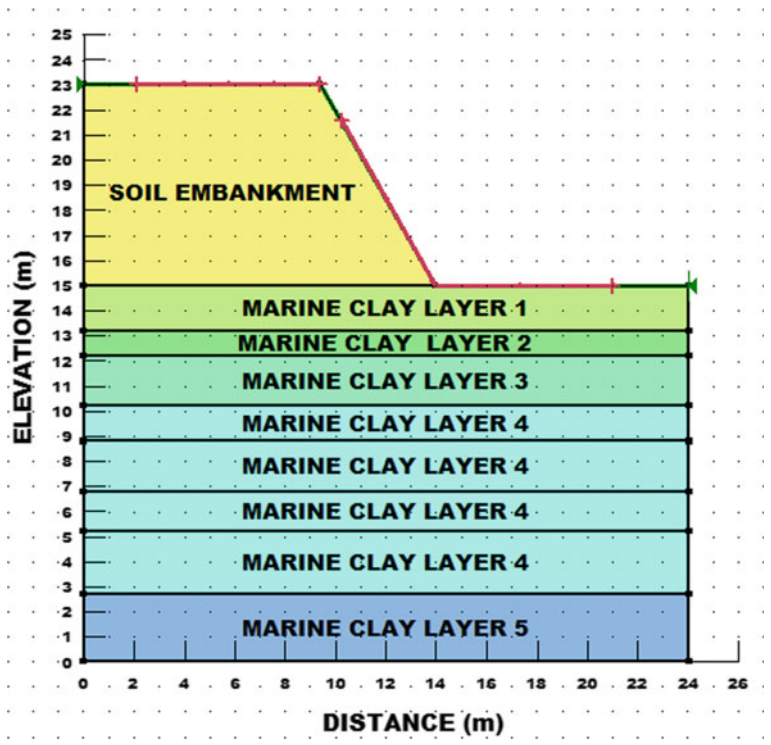

Fig. 1 Soil embankment of 8 m height and slope of 60° subjected to seismic loading with soil profile details up to 15 m depth

Table 3 The factor of safety for all considered combination of micropiles using slope stability theories

Description	Fellenius	Bishop	Janbu simplified	Spencer
No micropile provided	0.555	0.554	0.552	0.554
Set A[a]	0.555	0.554	0.552	0.554
Set B[a]	0.580	0.578	0.567	0.578
Set C[a]	0.611	1.680	1.566	1.677
Set D[a]	0.611	2.727	2.368	2.727
Set E[a]	0.611	2.768	2.582	2.767
Set F[a]	2.769	2.768	2.582	2.767

[a]Refer Table 2

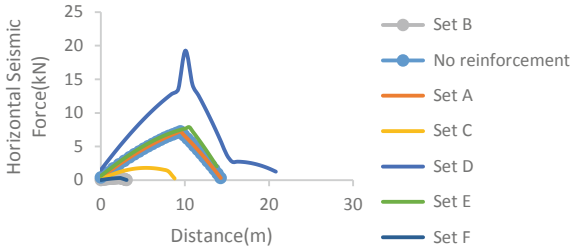

Fig. 2 Horizontal seismic force variation with distance for critical surface (Bishop method) when soil embankment subject to seismic loading

2.1 Sloped Soil Embankment Under Horizontal Seismic Loading

A sloped soil embankment is subject to seismic loading. The coefficient of horizontal seismic loading (k_h) is taken as 0.225 [3]. The factor of safety is calculated by Bishop method, Fellenius method, Janbu simplified method, and Spencer method using M-C criteria. All considered combinations of micropiles were tested by all four theories, and improvement in the factor of safety is recorded (Fig. 1 and Table 3).

Results for the considered combination of micropiles are as follows (Figs. 2, 3, 4, 5, 6, 7 and 8).

2.2 Sloped Soil Embankment Under Horizontal Seismic and Tidal Load Combination

A sloped soil embankment is subject to a combination of seismic and tidal loading. The coefficient of horizontal seismic loading (k_h) is taken as 0.225 [3], and the water level is taken as 5.8 m [5]. The factor of safety is calculated by Bishop method, Fellenius method, Janbu simplified method, and Spencer method using M-C criteria. All considered combinations of micropiles were tested by all four theories, and improvement in the factor of safety is recorded (Fig. 9 and Table 4).

Slope stability analysis is done for seismic and tidal load combination, and the result for the factor of safety is as follows (Figs. 10, 11, 12, 13, 14, 15 and 16).

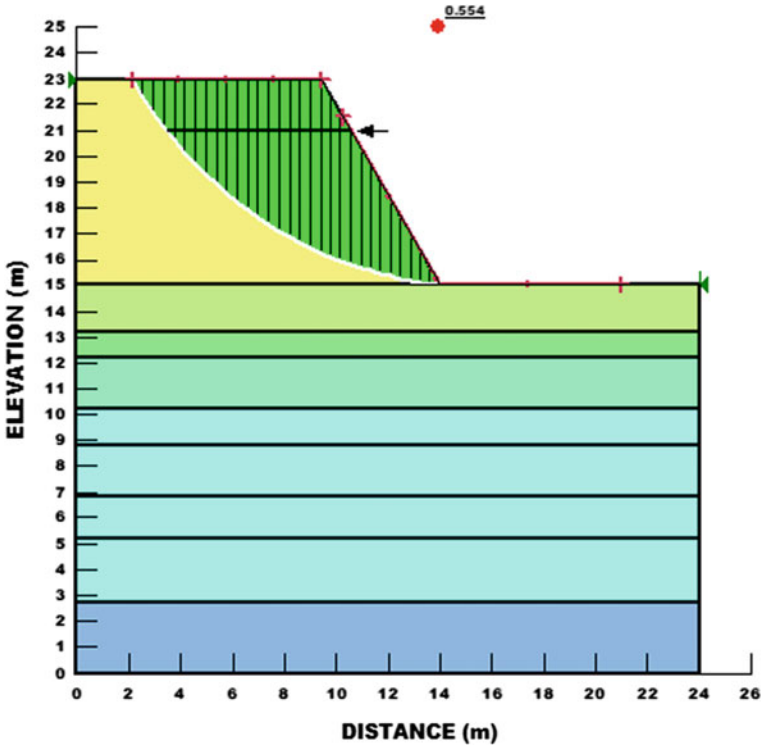

Fig. 3 Arrangement of micropile (set A) and corresponding critical surface (Bishop method) for seismic loading

3 Effect of Surcharge on the Factor of Safety

The effect of the surcharge load on the factor of safety is analyzed for the recommended solution when sloped soil embankment is subjected to seismic loading and a combination of seismic and tidal loading.

3.1 Sloped Soil Embankment Subjected to Seismic Loading

Once an adequate solution is prepared for slope stability, it is tested for surcharge loading. Surcharge load of 6 m length and 2 m height is applied to sloped soil embankment. Surcharge load density varies from 0 to 12 kN/m^3. The factor of safety is calculated for the horizontal seismic coefficient of 0.225 and 0.16 (for zone III cities) respectively at a different density (Figs. 17 and 18).

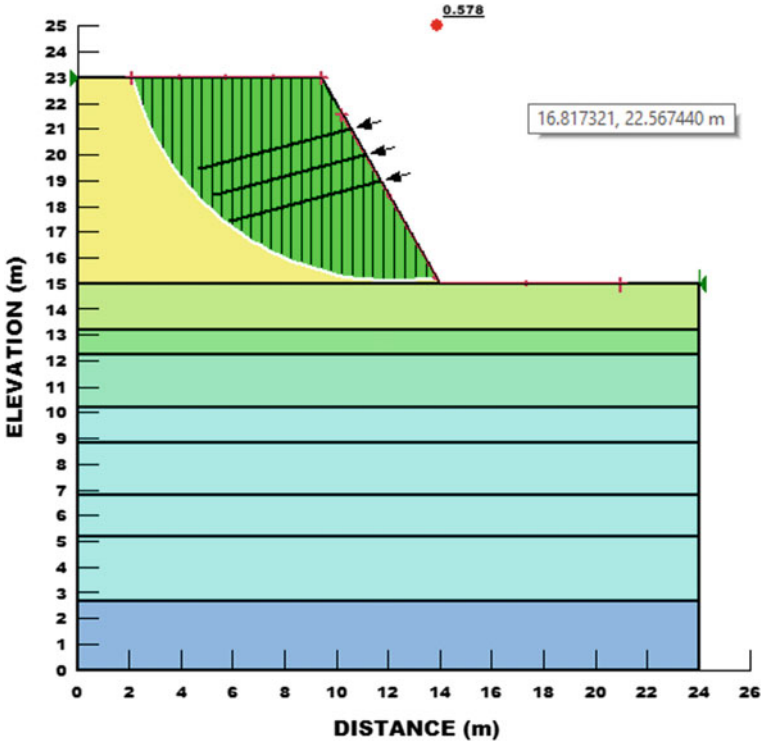

Fig. 4 Arrangement of micropile (set B) and corresponding critical surface (Bishop method) for seismic loading

For the recommended solution, sloped soil embankment subjected to seismic loading is analyzed for the surcharge load. When the horizontal seismic coefficient is 0.225 then the factor of safety is less than 1 for a surcharge load density of 6.2 kN/m^3. When the horizontal seismic coefficient is 0.16, then the factor of safety is less than 1 for a surcharge load density of 7 kN/m^3. But after 5.6 kN/m^3 difference between the factors of safety for both seismic coefficient is less; hence, 5.6 kN/m^3 should be the upper limit for surcharge loading.

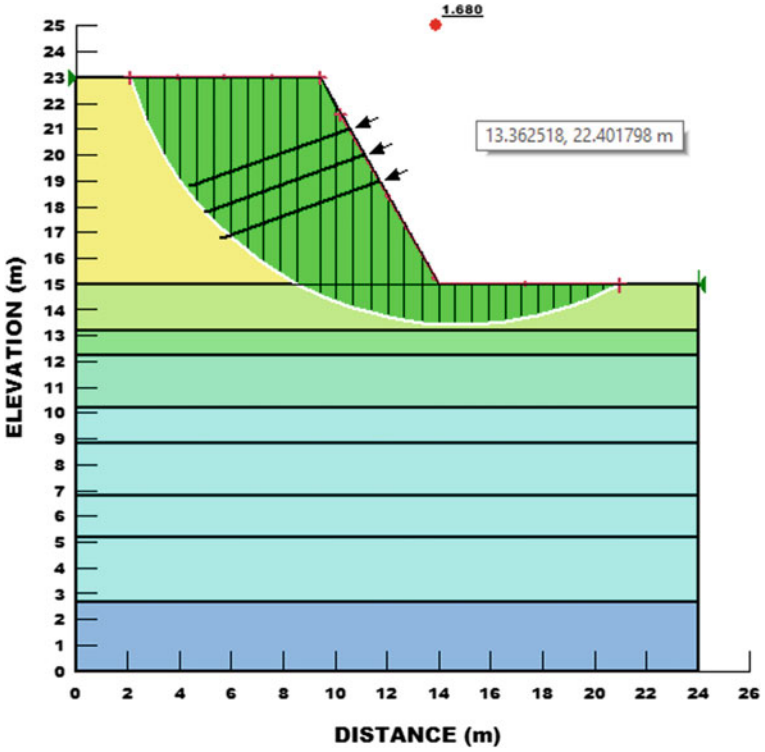

Fig. 5 Arrangement of micropile (set C) and corresponding critical surface (Bishop method) for seismic loading

3.2 Sloped Soil Embankment Subjected to a Combination of Seismic and Tidal Loading

Once an adequate solution is prepared for slope stability, it is tested for surcharge loading. Surcharge load of 6 m length and 2 m height is applied to sloped soil embankment. Surcharge load density varies from 0 to 12 kN/m^3. The factor of safety is calculated for the horizontal seismic coefficient of 0.225 and 0.16 (for zone III cities) respectively at a different density (Figs. 19 and 20).

For the recommended solution, sloped soil embankment subjected to a seismic and tidal load combination is analyzed for the surcharge load. When the horizontal seismic coefficient is 0.225, then the factor of safety is less than 1 for a surcharge load density of 6.2 kN/m^3. When the horizontal seismic coefficient is 0.16, then the factor of safety is less than 1 for a surcharge load density of 7 kN/m^3. But after 5.6 kN/m^3 difference between the factors of safety for both seismic coefficient is less; hence, 5.6 kN/m^3 should be the upper limit for surcharge loading.

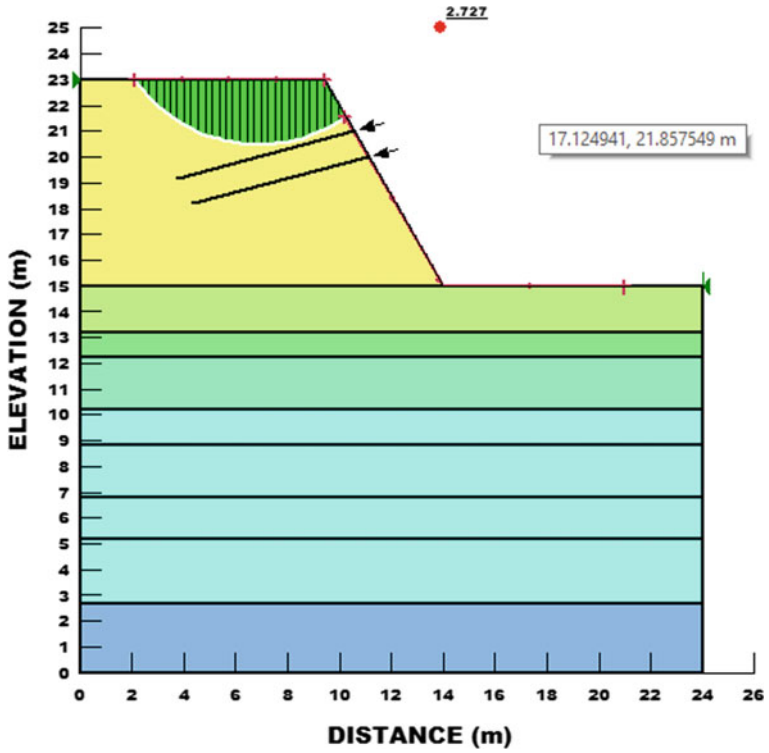

Fig. 6 Arrangement of micropile (set D) and corresponding critical surface (Bishop method) for seismic loading

4 Conclusions

1. It is recommended to use a set of micropile having 2 micropiles at 0° angle with horizontal. Length, shear force, and shear reduction factor is 8.5 m, 350 kN, and 1 respectively when slope embankment is subjected to either seismic loading or a combination of seismic and tidal loading.
2. The effect of surcharge on the factor of safety is as follows:

    (a) For the recommended solution, sloped soil embankment subjected to seismic loading is analyzed for the surcharge load. When the horizontal seismic coefficient is 0.225, then the factor of safety is less than 1 for a surcharge load density of 6.2 kN/m^3. When the horizontal seismic coefficient is 0.16, then the factor of safety is less than 1 for a surcharge load density of 7 kN/m^3. But after 5.6 kN/m^3 difference between the factors of safety for both seismic coefficient is less; hence, 5.6 kN/m^3 should be the upper limit for surcharge loading.

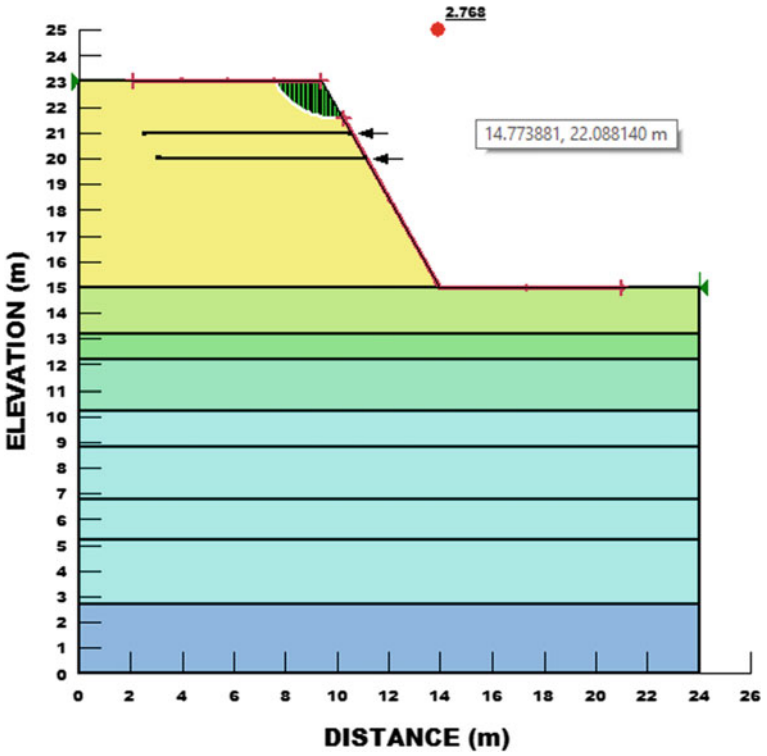

Fig. 7 Arrangement of micropile (set E) and corresponding critical surface (Bishop method) for seismic loading

(b) For the recommended solution, sloped soil embankment subjected to seismic loading is analyzed for the surcharge load. When the horizontal seismic coefficient is 0.225, then the factor of safety is less than 1 for a surcharge load density of 6.2 kN/m^3. When the horizontal seismic coefficient is 0.16, then the factor of safety is less than 1 for a surcharge load density of 7 kN/m^3. But after 5.6 kN/m^3 difference between the factors of safety for both seismic coefficient is less; hence, 5.6 kN/m^3 should be the upper limit for surcharge loading.

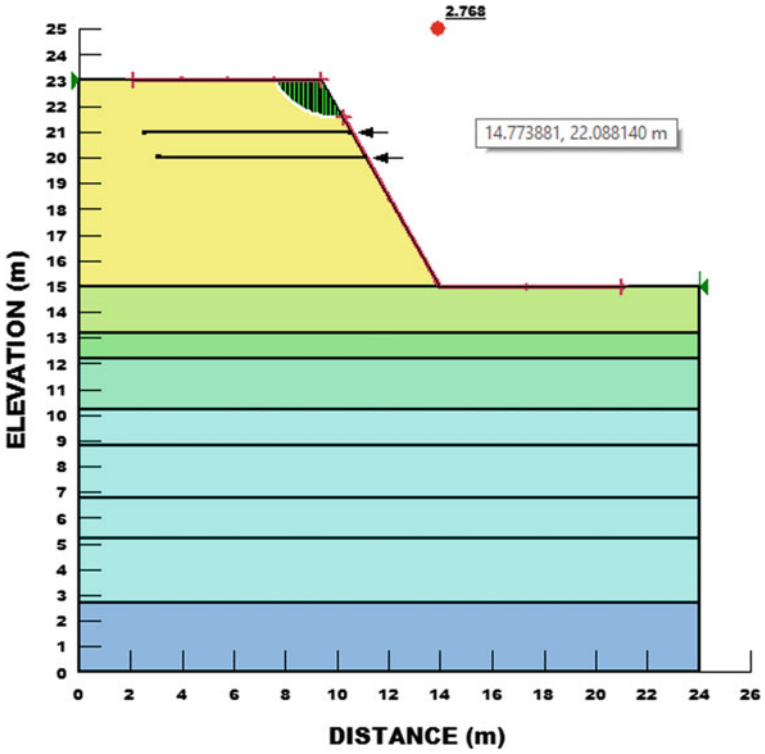

Fig. 8 Arrangement of micropile (set F) and corresponding critical surface (Bishop method) for seismic loading

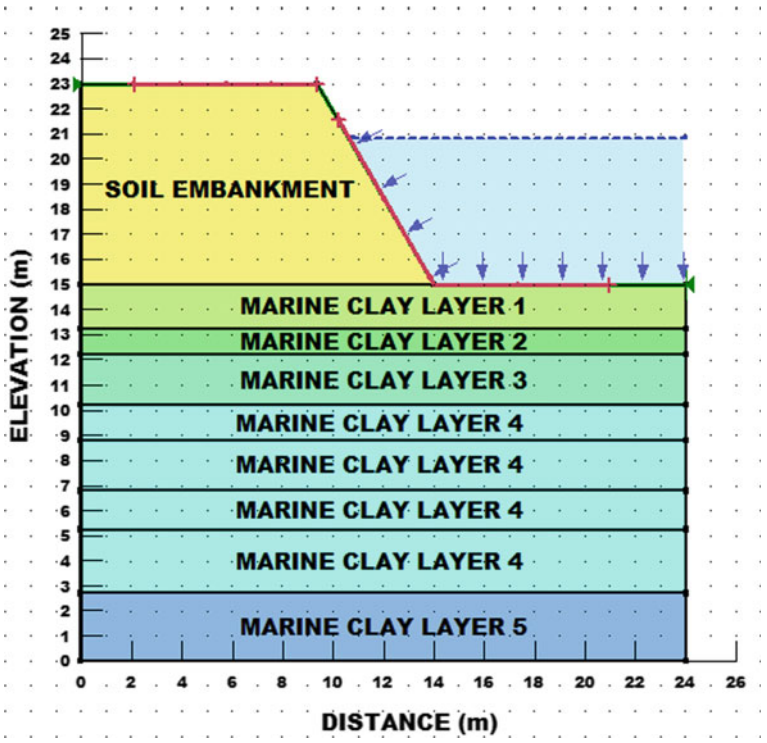

Fig. 9 Soil embankment of 8 mt height and slope of 60° subjected to a combination seismic and tidal loading with soil profile details up to 15 m depth

Table 4 The factor of safety under all considered combination of micropiles using slope stability theories

Description	Fellenius	Bishop	Janbu simplified	Spencer
No micropiles provided	0.855	0.862	0.818	0.861
Set A[a]	0.855	0.862	0.818	0.861
Set B[a]	0.891	0.905	0.858	1.053
Set C[a]	0.973	2.727	2.368	2.727
Set D[a]	0.973	2.727	2.368	2.727
Set E[a]	0.973	2.768	2.582	2.767
Set F[a]	2.769	2.768	2.582	2.767

[a]Refer table number 2

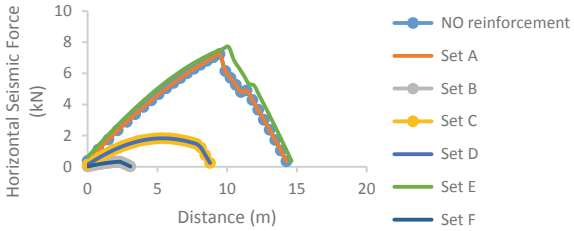

Fig. 10 Horizontal seismic force variation with distance for critical surface (Bishop method) when soil embankment subjected seismic and tidal load combination

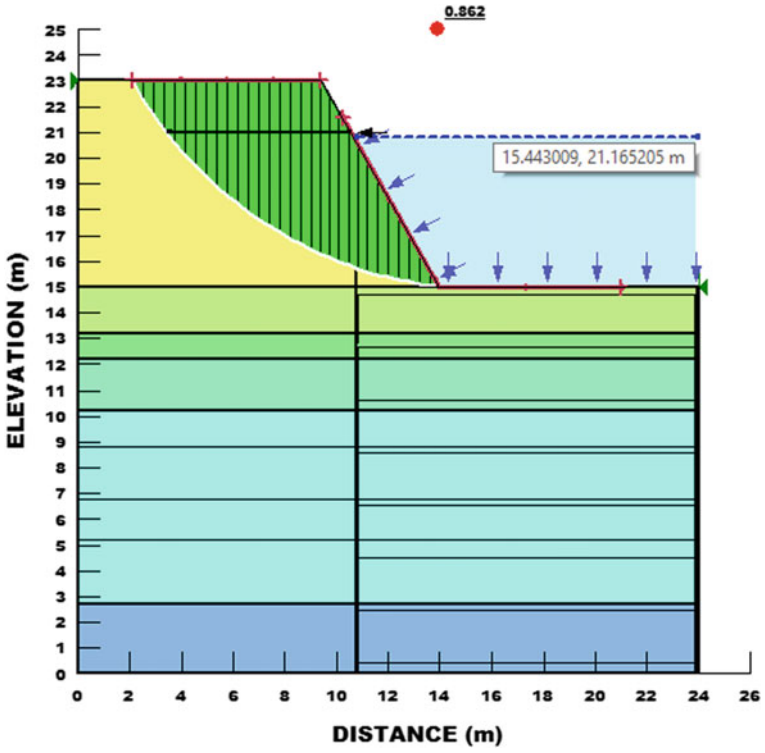

Fig. 11 Arrangement of micropile (set A) and corresponding critical surface (Bishop method) for seismic and tidal load combination

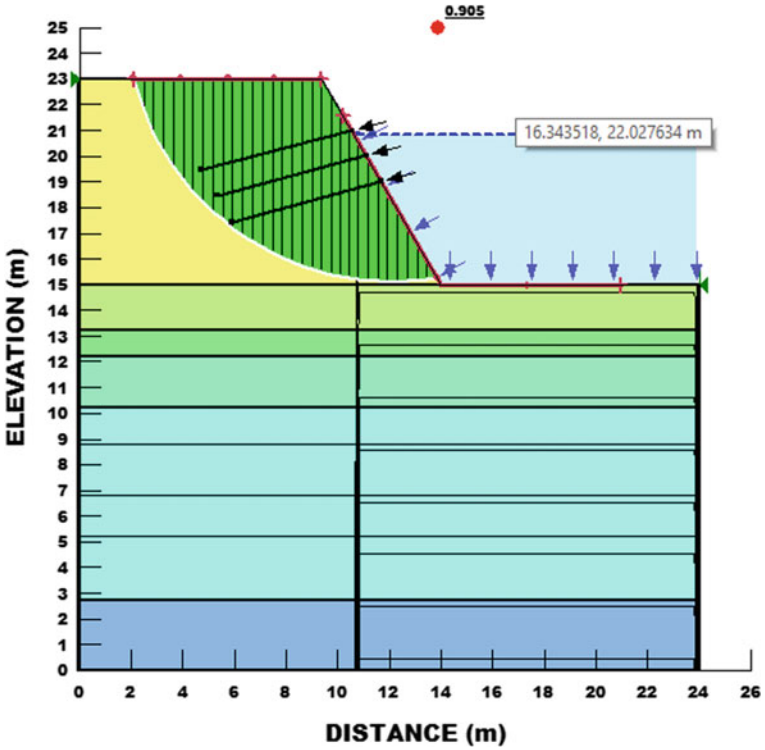

Fig. 12 Arrangement of micropile (set B) and corresponding critical surface (Bishop method) for seismic and tidal load combination

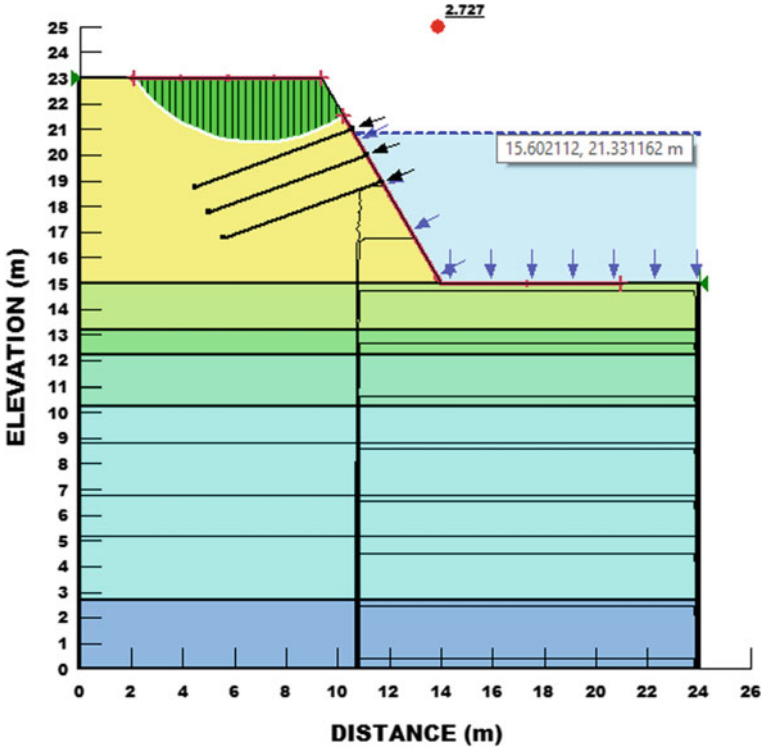

Fig. 13 Arrangement of micropile (set C) and corresponding critical surface (Bishop method) for seismic and tidal load combination

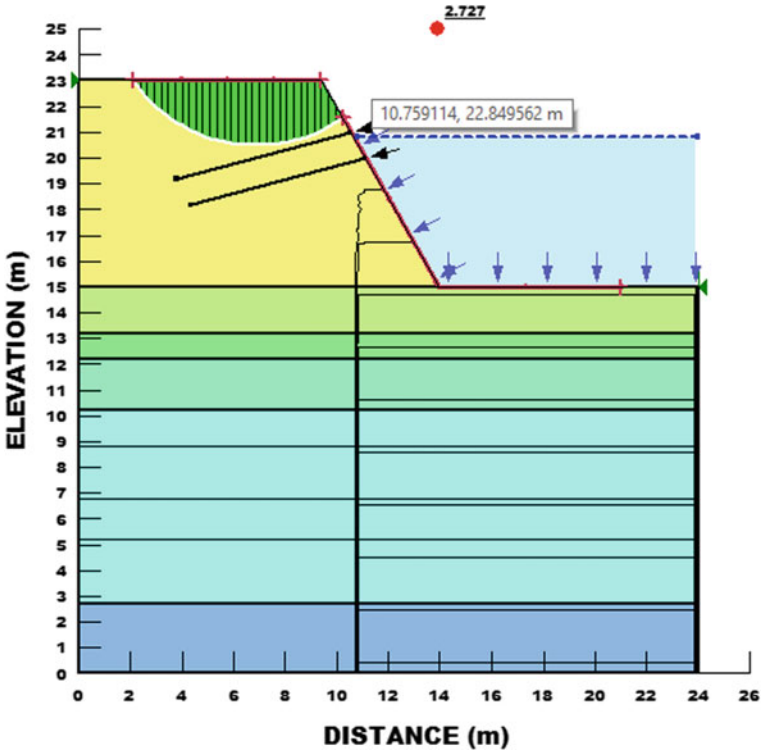

Fig. 14 Arrangement of micropile (set D) and corresponding critical surface (Bishop method) for seismic and tidal load combination

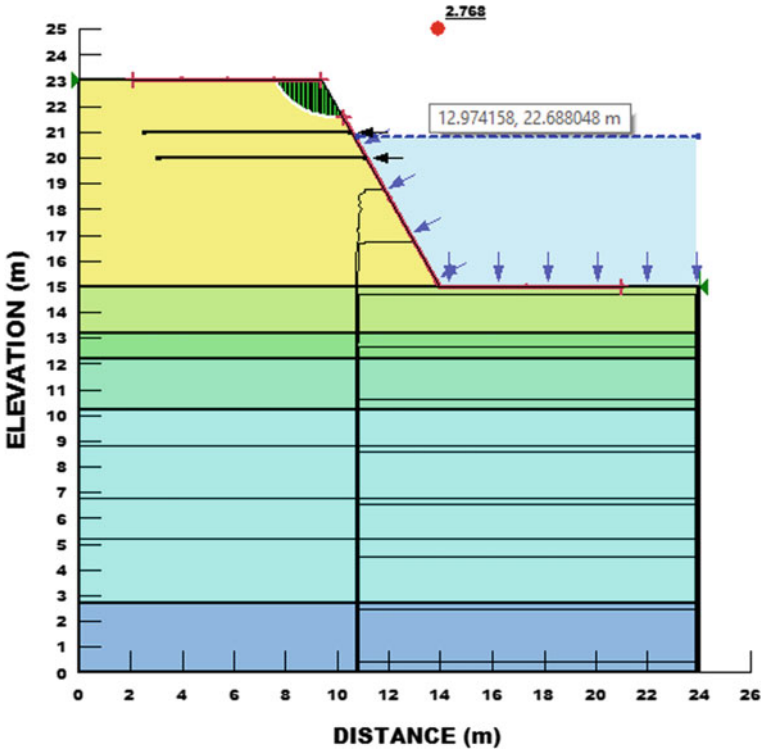

Fig. 15 Arrangement of micropile (set E) and corresponding critical surface (Bishop method) for seismic and tidal load combination

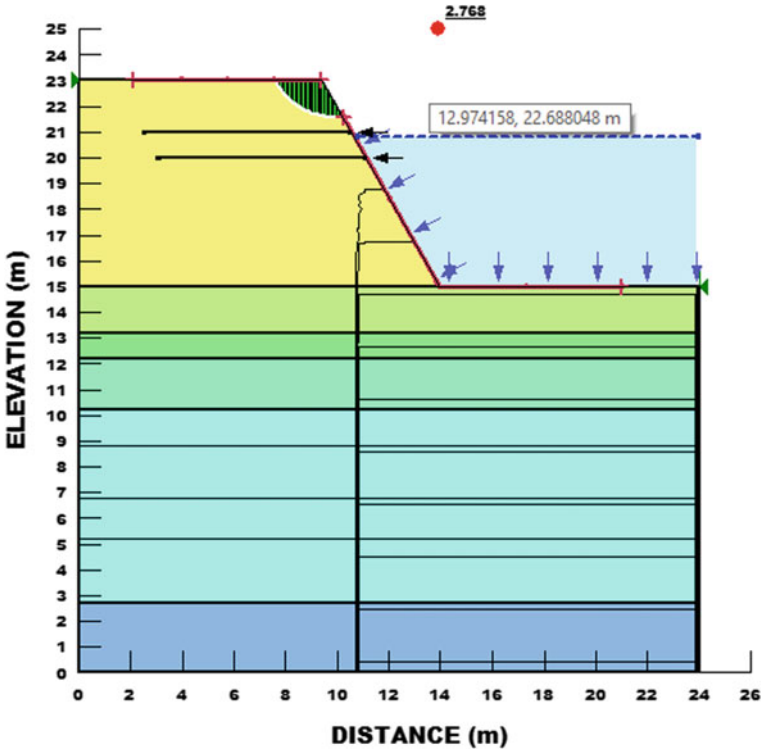

Fig. 16 Arrangement of micropile (set F) and corresponding critical surface (Bishop method) for seismic and tidal loading

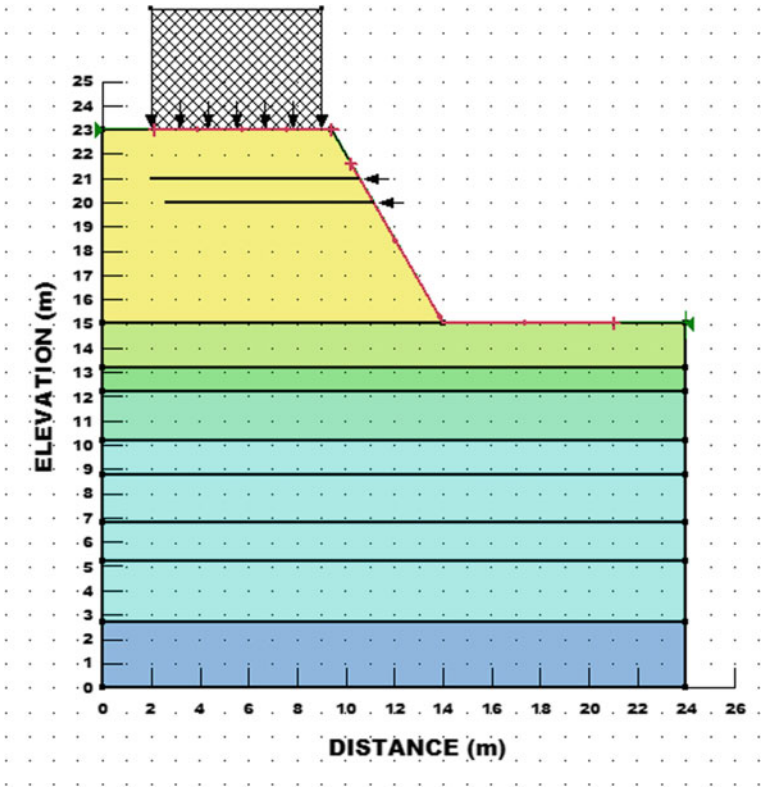

Fig. 17 Surcharge load on sloped soil embankment for recommended set F (Table 2) subject to the seismic loading

Fig. 18 Variation in the factor of safety with the surcharge when soil embankment subjected to seismic loading for set F (Table 2)

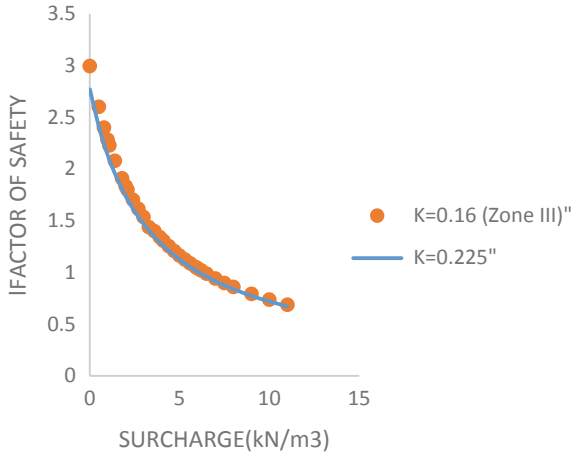

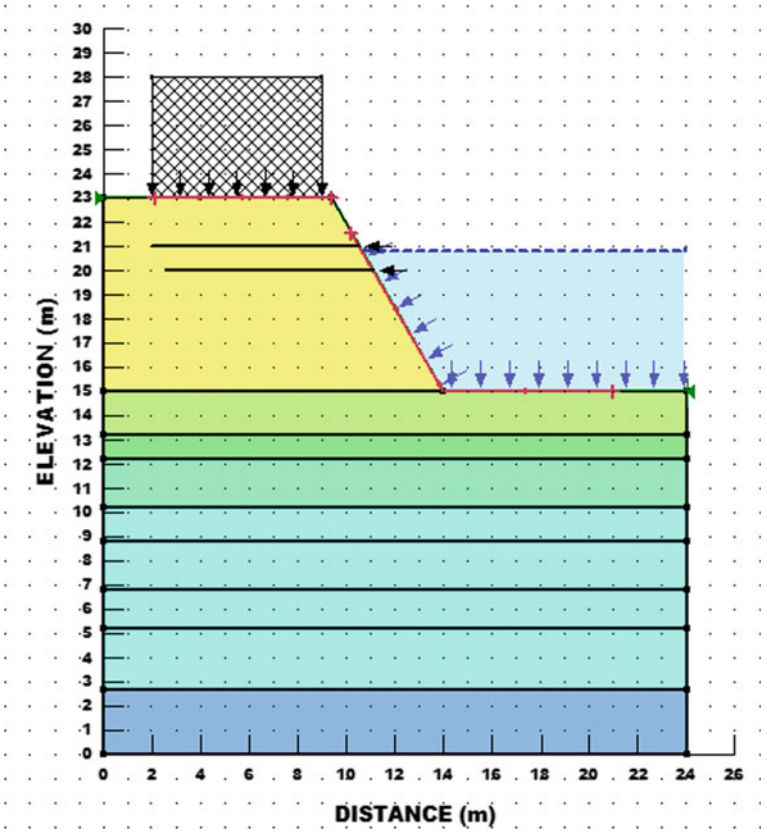

Fig. 19 Variation in the factor of safety with the surcharge when soil embankment subjected to seismic and tidal load combination for set F (Table 2)

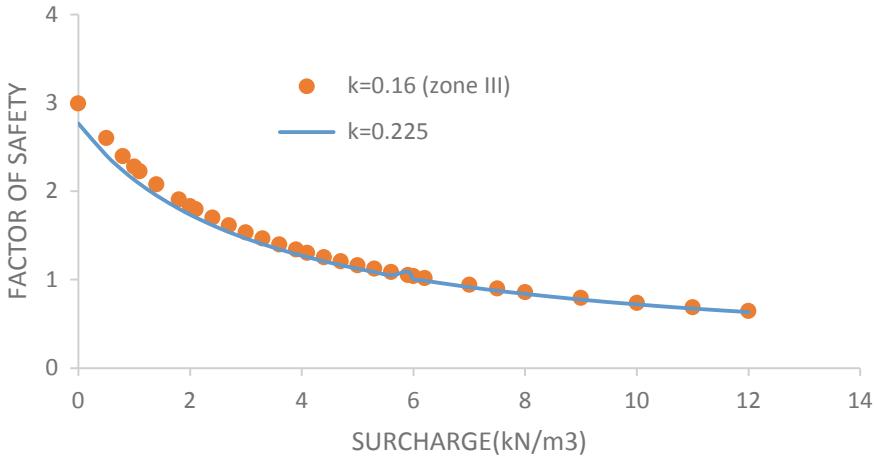

Fig. 20 Variation in the factor of safety with the surcharge when soil embankment subjected to seismic and tidal load combination for set F (Table 2)

References

1. Fredlund, D.G., Krahn, J.: Comparison of slope stability methods of analysis. ASCE J. Geotech. Geoenvironmental Eng. **14**, 429–439 (1977)
2. Duzceer, R.: Slope stability with permanent rock anchors. In: ASCE Advances in Analysis, Modeling & Design Proceeding in Geo-Florida Publication, no. 199, pp. 273–282 (2010)
3. Desai, S.S., Choudhury, D.: Site-specific seismic ground response study for nuclear power plants and ports in Mumbai. ASCE J. Nat. Hazards Rev. **04015002**(13) (2015)
4. Misra, A., Chen, C.H., Oberoi, R., Kleiber, A.: Simplified analysis method for micropile pullout behavior. ASCE J. Geotech. Geoenvironmental Eng. **130**(10), 1024–1033 (2004)
5. AECOM: Master Plan for Jawaharlal Nehru Port. Ministry of Shipping/Indian Ports Association New Delhi, India (2016) http://jnport.gov.in/jnpt_masterplan

Monitoring of Landslide in Heavy Rainfall Areas Using Low-Cost Microcontrollers

K. S. Beena, O. Varun Menon, and P. J. Rooma

1 Introduction

1.1 General

Among natural hazards, landslides occur virtually in every country in the world. Globally, it causes approximately 10,000 deaths a year along with property damage [1]. These slope failures have become a common geotechnical problem and are most common in many countries such as Hong Kong, Italy, Singapore, and India. In India, the Nilgiris region has frequently been confronted with the occurrence of slope failures and landslides. It poses a serious threat to human life and structures built in proximity. Early landslide warning is largely phenomenological, relying on surface measurements of displacements over time [2]. Landslides can be initiated in slopes already on the verge of movement by rainfall, snowmelt, changes in water level, stream erosion, and changes in groundwater, earthquakes, volcanic activity, disturbance by human activities, or any combination of these factors. Among these, rainfall is one of the most effective factors.

Rainfall-induced slope failures are due to a complex interaction between hydrological and geotechnical processes. Parameters of the slope that affect the stability of slope are slope angle, density of soil and its moisture content. Landslides usually occur during wet periods and the slope failures are induced by rainfall infiltration. During any rainfall period, negative pore-water pressures in an unsaturated soil slope are gradually reduced by rainfall infiltration and positive pressures start building up. This process may cause instability to soil slope. Rainfall intensity and duration play an important role in the extent and manner of slope failure. High-intensity short duration rainfall can easily trigger landslides.

K. S. Beena (✉) · O. V. Menon · P. J. Rooma
Division of Civil Engineering, School of Engineering, CUSAT, Cochin 682022, India
e-mail: beenavg@cusat.ac.in

C. N. V. Satyanarayana Reddy et al. (eds.), *Stability of Slopes and Underground Excavations*, Lecture Notes in Civil Engineering 185,
https://doi.org/10.1007/978-981-16-5601-9_16

Modeling of scaled embankments and monitoring of water contents within the soil, allow us to understand and to correlate the response of the soils due to the rainfall infiltration in the field. By conducting scaled model studies in the past, it has been inferred that the slope failure was induced by increasing the degree of saturation within the slope through seepage from the upslope section or by direct rainfall [3]. Water infiltration alone was not sufficient to induce instability. Rather, generation of pore-water pressure and increase in saturation ratios associated with the rise in the water level were necessary to create highly unstable zones. When most parts of the soil slope are almost fully saturated particularly those in the potential failure surface, a retrogressive type of failure is observed. The studies also demonstrated the possibility of predicting slope failure initiation by monitoring the changes in soil moisture content within the slope.

This clearly directs us to embark on a study with the help of monitoring devices to understand the phenomenon of landslide in a more perspective manner. In the past, such studies have been conducted [4] and it involves the installation of a real-time monitoring system to observe the physical property changes in soils in a valley during rainfall events. This monitoring included the measurement of volumetric water content, which was compared with the results of laboratory flume tests to identify landslide indicators in the soils. The results showed that there is a directly proportional relationship between the effective cumulative rainfall and the gradient of volumetric water content per unit time (t/t_{max}). Laboratory results showed that a high amount of rainfall and a high gradient of volumetric water content could induce slope failure.

This study involves the measurement of moisture content using sensors placed at various locations of the slope, thus in turn can be used as an early warning system for landslides. The effect of rainfall intensity on soils with different slope angles was investigated at constant density.

2 Laboratory Experiments

2.1 General

Many researchers work on theory, analysis, numerical simulation, and model tests. The rainfall simulator which can reproduce the rainfall intensity, drop size, drop energy, spatial and temporal distribution for the model test of landslide is very important [5]. Fabrication of a rainfall simulator was the first objective before conducting the model studies. With the available resources on the premises, we were able to assemble the simulator as seen in Fig. 1.

The study has been conducted with varying slopes of 30, 45, and 60° at a moisture content of 7.5% and filled by keeping 90% maximum dry density (1.53 g/cc). The water content is obtained from conducting a standard proctor test and interpolating the corresponding dry density. The main purpose of this study is to identify the point

Fig. 1 Rainfall simulator

at which the landslide triggers and let that point be the threshold in the upcoming proposal involving the early warning systems.

The soil has been collected from the geotechnical laboratory and basic properties have been found to maintain constant density throughout each iteration. The intensity of rainfall can be controlled by adjusting the inlet valves and the measurement is taken using a measuring jar.

2.2 Material Characteristics

The model studies have been conducted [7] with the facility available at Geotechnical laboratory, Cochin University of Science and Technology using red lateritic soil having the following material properties as given in Table 1. The soil comes under the classification of ML (low plasticity silt).

Table 1 Material properties

Property type	Value	Unit
Specific gravity	2.76	
Liquid limit	61	%
Plastic limit	28.30	%
Maximum dry density	1.70	g/cc
Optimum moisture content	14	%
D10	0.23	Mm
D30	0.70	Mm
D60	1.50	Mm
Cc	6.52	
Cu	1.42	
Soil classification	ML	

2.3 Sensor Characteristics

The experiments are conducted with the open-source platform called Arduino. To be precise, we have used the ATmega328P micro-controller-based Arduino Uno board for experimentation. This board can carry out small-scale processing with 32 kb internal memory. It can read both Analogue and digital data. We have used a SEN0114 analog output soil moisture sensor in locations A0 to A5 as given in Fig. 2. Figure 2 also consists of the image of the SEN0114.

Figure 2 gives the sensor locations corresponding to the 30° slope and there can be slight variations in the sensor locations for slopes of 45 and 60°. The sensors used in each location are the same for every individual testing to avoid any calibration errors.

Calibration of the sensors is the next important step in this study so that the medium between the man and the machine will become clearer to interpret. The ability of a system to communicate with the scientist is very important in the case of experimental study, so we must understand how the microcontroller responds with

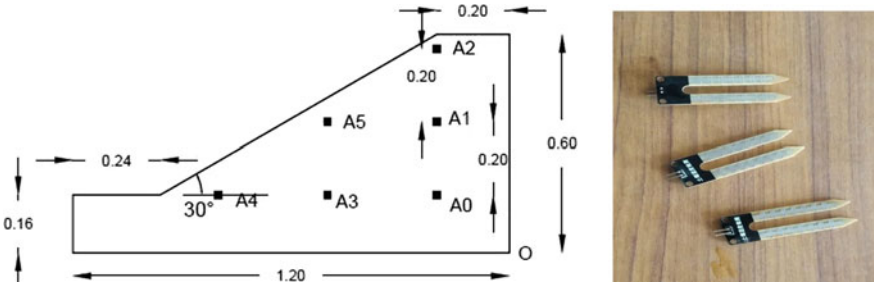

Fig. 2 Locations of the sensors in the model and the SEN0114 soil moisture sensor

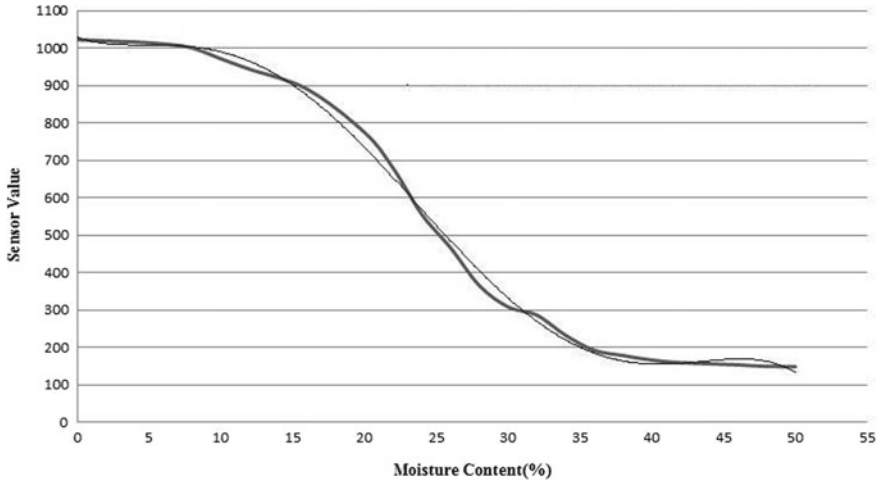

Fig. 3 Calibration chart of the SEN0114 sensors

the change in water content in the soil. For that, a dummy test has been conducted by filling 100 g of soil in a bowl and the water content has been changed by adding a known quantity of water from a dry state to the point up to which the sensor gives data. Figure 3 is the representative graph of the sensitivity of SEN0114 type moisture sensors.

This chart has been further used to relate between analog values of the sensors during experiments and the real-world moisture content of the soil.

By analyzing the data given in Fig. 3, it can also be observed that the sensors can be significantly sensitive during the regions of 10–40% moisture content in this soil.

According to the result of the experiment, moisture sensors located at different position shows a significant change in the values during the simulation of rainfall. These changes were in response to the infiltration of rainwater. The stage of increased moisture content was very prominent near the slope surface and with shallower sensors. The surface sensors respond earlier than those deeper within the slope profile.

Further to this, the sensors located closer to the slope recorded an increase in moisture content. In the next stage, the sensors placed at deeper depth show the increase in moisture content. Finally, the bottom sensors near the heel show higher moisture content than the top sensors because of the accumulation of water from top to bottom. But there is a slight variation in the duration of the sudden increase in moisture content at some locations of the slope due to the topographical characteristics (slope angle). The soil condition in the model slope is gradually changed from an unsaturated condition to a saturated condition by the infiltration of rainfall. When the water content reaches the maximum value in the saturated condition, it maintains the maximum value uniformly with further rainfall simulation. The water content at which embankment soil becomes fully saturated is theoretically obtained as 30% for a 90% relative density of this soil. A slope failure was observed for 60^0 slopes under

high-intensity rainfall conditions as seen in Fig. 4. In other slopes (i.e., 30^0 and 45^0) no failures were observed during the experimental study.

As per Fig. 5, the locations of the sensors in the failed model can be identified. The sensors are given in various locations to study the influence of water in the soil body with varying depth. The sensors A2, A4, and A5 are the most critical ones in the slope. The failure has occurred at the 600-s mark from the start of the simulation of the rain. The rainfall intensity was later calculated to be 48 mm/hr. Also, Fig. 6 shows the point of failure in each scenario, from this data we can come to an understanding that the limit of allowable water content just before failure can be set to 27 to 35% for this soil.

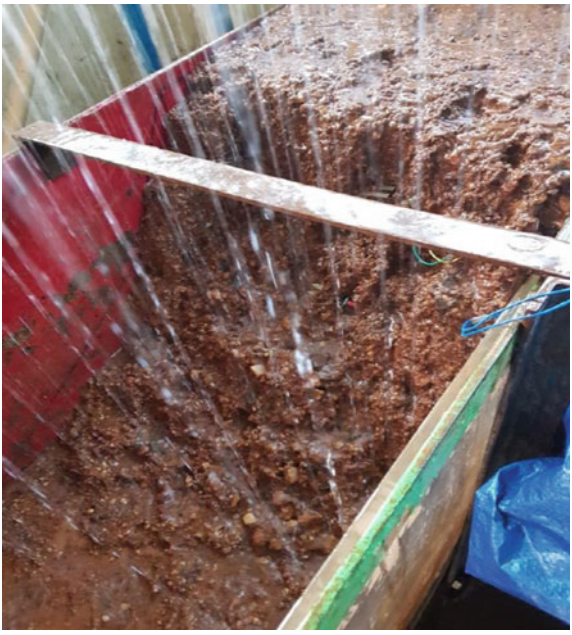

Fig. 4 Failure of 60° slope model

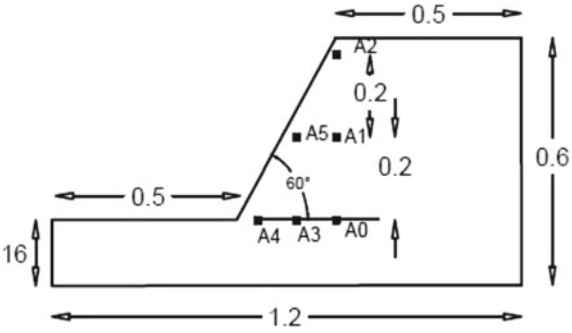

Fig. 5 Locations of the sensors (not to scale)

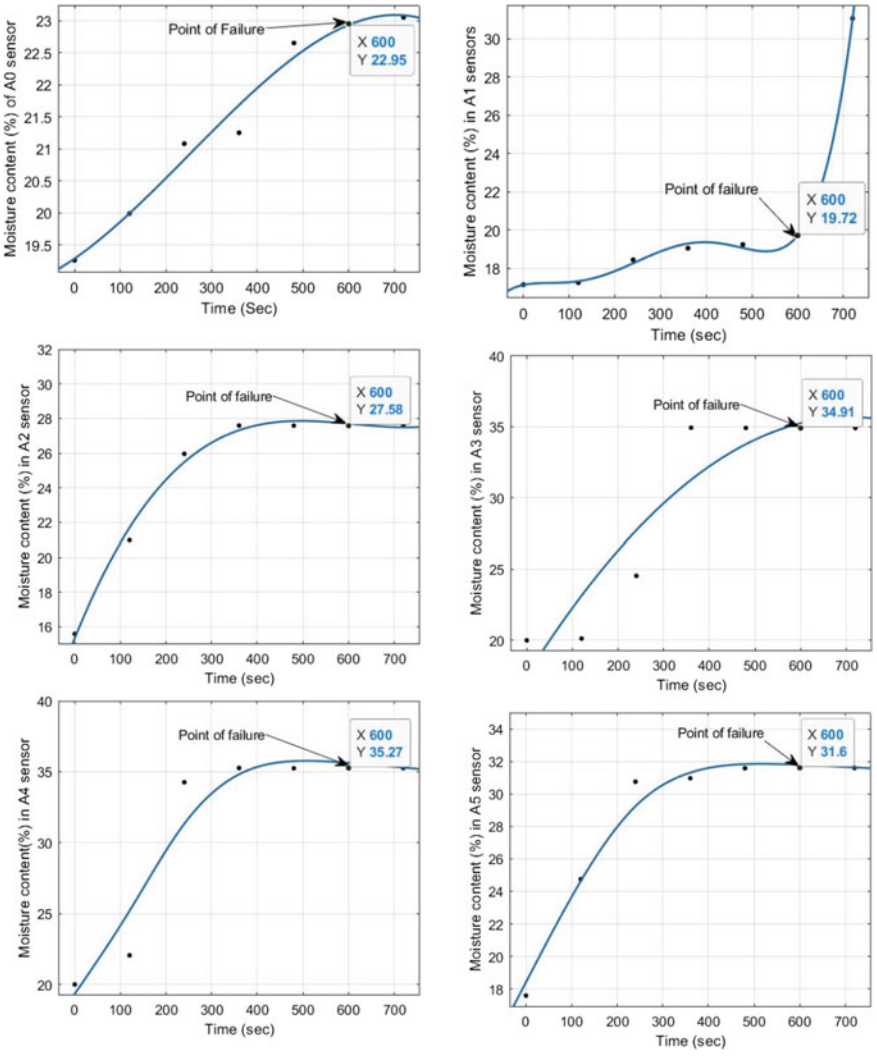

Fig. 6 Moisture content versus time graph of each sensor in the 60° slope model

The locations A2, A4, and A5 are very critical for the current study as this is closer to the upper layer soil. Landslide is a phenomenon, in which the upper layer of soil tends to lose its friction with the layer below it, causing large mass movement. The sensors at A0, A1, and A3 provide us with the moisture content deep under the top of the soil, these reading can be used for other studies like soil internal erosion. The current scope of study only focuses on landslides and early warning system design.

The data obtained was tabulated in MATLAB and Fig. 6 is plotted. This contains moisture content measured by each SEN0114 sensor versus time in seconds data.

The major implications of this graph in this study are the moisture content at the point of failure and the time it takes to reach this point. The development of an early warning system depends on these values as the point of failure data is given in the programming of the micro-controllers. There should be a suitable factor of safety that has to be considered to allow enough time to order an evacuation.

If the sensors read this threshold value and the rainfall intensity is greater than the one in the model study case, the failure is imminent. This is considered without taking the man-made factors that may accelerate the failure process. For that further investigative study is recommended.

From the obtained data, A2, A4, and A5 show similar values. The sensors reach the failure moisture content earlier than the failure point. It means there is a time gap between the failure point and the first presence of that moisture content value in the sensors. These can be easily spotted in Fig. 6 and the time gap can be approximated. This is a very useful data, and further study on unsaturated soil regions is recommended on why this delay occurred to lose the strength of the soil.

Figure 6 depicts the moisture content versus time graph plotted taking value every 120 s time interval. The lowest value measured by the sensor at the failure point as per the Fig. 6 is 19% although this value is of a deeper stratum than the surface soil, hence the values obtained from A2, A4, and A5 are only considered for the present study. From the data obtained as above, we are considering to give a factor of safety of 2 for this current soil and take 13.5% (half of 27% at which the failure triggered) as the threshold for our early warning. Because as per Fig. 6, the progression toward the failure point moisture content seems to be very rapid. The sensors also show that the value has already been reached at an earlier point of time and it tends to prolong that same moisture content for more than 300 s before failure. In the further sections of the study, we are only considering 13.5% moisture content as the threshold.

3 Future Developments Recommended

3.1 General

ESP32 belonging to Espressif systems is a multipurpose microcontroller with 2.4 GHz Wi-Fi and Bluetooth capability, it shows robustness and versatility with a wide variety of applications [6]. There are many models available in the market at an affordable price, from which we have selected ESP32-WROOM-32 as seen in Fig. 7. Using Microsoft Visual Studio Code software, we can code it to perform various tasks. The ability of ESP32 to access the internet plays a key role in the development of an early warning system. ESP 32 can be powered with a 9 V battery or AC to DC adapters.

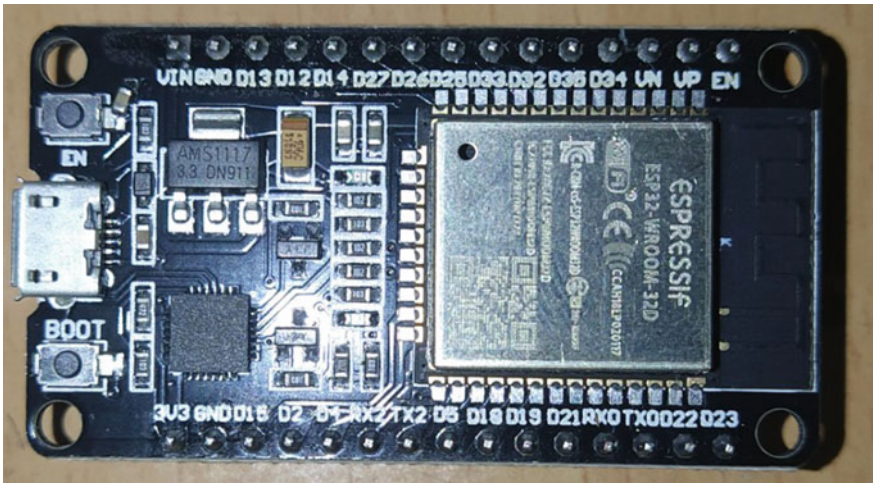

Fig. 7 ESP32-WROOM-32 microcontroller

3.2 Role of Web-Based Service Providers

There are many web-based freeware service providers in the world including IFTTT, Zapier, Huginn, etc., which play a key role in the development of this warning system. One of their function is to send short messages to provided mobile numbers when the moisture sensors read the threshold value of our soil, before failure. ESP32 microcontrollers can find the nearby internet provider and connect to the online service providers and give us the required message through mobile network. Hence, if the mobile number of every resident of the landslide-prone area is collected and made the recipient of such short messages, we can focus their attention towards evacuation and prevent major life-threatening situations. Figure 8 shows the working flowchart of the system developed.

Here, in this study, the ESP32 has been programmed to connect these web-based service providers to send short messages to the public when the point of threshold is reached. The system shows a response time of 4 s for an internet connection speed of

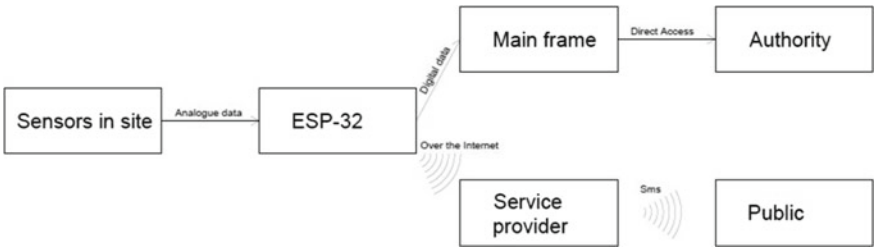

Fig. 8 Working flowchart of the system

10 mbps. The messages are delivered within 4 s from the point where the sensors read a moisture content of 13.5% moisture content. By considering the rainfall intensity, it seems to be a fair time for the evacuation process to start. The installation of sensors can be done by encasing the sensors to avoid outside interferences before embedding in into the ground.

This is one of the cheapest methods for an early warning system for landslides and can be used in any area, where there is a public internet facility is available.

4 Conclusions

To summarize, there are large-scale applications for multidisciplinary studies in civil engineering, rather than the conventional methods which can get us not that far. The methods given in this paper are very easy to learn for any civil engineer. The major conclusions that arise from this study are given below:

1. SEN0114 sensors can be effectively used to study the change in moisture content during rainfall.
2. The model study using locally available red lateritic soil, the slope failure occurred at 27% water content, when the rainfall intensity was 48 mm/hr and the slope is 60°.
3. There is a time gap between the occurrence of failure and the time at which the failure moisture content value was first observed.
4. Using ESP32 microcontrollers, a prototype web-based early warning system has been proposed.

This moisture content and the early warning system are applicable only for this soil at the given slope and rainfall parameters. It implies, where ever such a system is to be installed, a detailed model study using a rainfall simulator is very necessary.

References

1. Clague, J.J., Roberts, N.J.: Landslide hazard and risk. In: Landslides: Types, Mechanisms and Modeling published by Cambridge University Press, © Cambridge University Press (2012)
2. Eberhardt, E.: Landslide monitoring: the role of investigative monitoring to improve understanding and early warning of failure. In: Landslides: Types, Mechanisms and Modeling published by Cambridge University Press, © Cambridge University Press (2012)
3. Maeda, K., Orense, R., Shimoma, S., Towhata, I.: Instrumented model slope failure due to water seepage. J. Nat. Disaster Sci. **26**(1), 15–26 (2004)
4. Chae, B., Kim, M.: Suggestion of a method for landslide early warning using the change in the volumetric water content gradient due to rainfall infiltration. In: Environmental Earth Sciences (2012)

5. Hou, J.: Design of artificial rainfall simulator for model test of landslide. Appl. Mech. Mater. **220–223**(2012), 1491–1494 (2012)
6. ESP32 datasheet (PDF). Espressif systems, 2017-03-06. Retrieved 14 Mar 2017
7. IS 2720-part 8: methods of test for soils—determination of water content—dry density relation. Bureau of Indian Standards, New Delhi (1983)

An Experimental Study on the Influence of Water-Level Fluctuation on Stability of Slope of Model River Bank Composed of Cohesionless Material

Md. Firoz Ali, Supia Khatun, and Yasser Arafat

1 Introduction

The stability of a slope is utterly governed by soil properties, stress conditions, and slope geometries. Any change taking place of at least one of these factors, means slope stability conditions being potentially affected [1]. At a micro-scale, the inherent properties of a soil are governed by its history; no matter if the soil is processed (crushed, filled, etc.), or if it is naturally occurring; i.e., formed by weathering of rock, transported by erosive processes, and finally deposited from water, wind, or ice. Also, at a larger scale—considering the soil skeleton—many different processes are governing the properties of the soil; e.g., particle-size distribution, soil-profile homogeneity, denseness, etc. The properties of soil are continuously affected by long-term processes, including, e.g., transport and depositing (i.e., erosion and land-form development), and aging (i.e., weathering or other changed chemical or physical conditions). Any soil volume is continuously affected by the hydrological conditions prevailing; present water is either influencing or completely governing the actual soil properties. At the scale of bank slopes and embankment dams, the structures are influenced by external water loads, development of pore pressures, and hydrodynamic impact from internal and external water flow [2] (Fig. 1).

Md. F. Ali (✉)
Department of Civil Engineering, Dr. Sudhir Chandra Sur Degree Engineering College, Kolkata 700074, India

S. Khatun · Y. Arafat
Department of Civil Engineering, Aliah University, Kolkata, West Bengal 700156, India

C. N. V. Satyanarayana Reddy et al. (eds.), *Stability of Slopes and Underground Excavations*, Lecture Notes in Civil Engineering 185,
https://doi.org/10.1007/978-981-16-5601-9_17

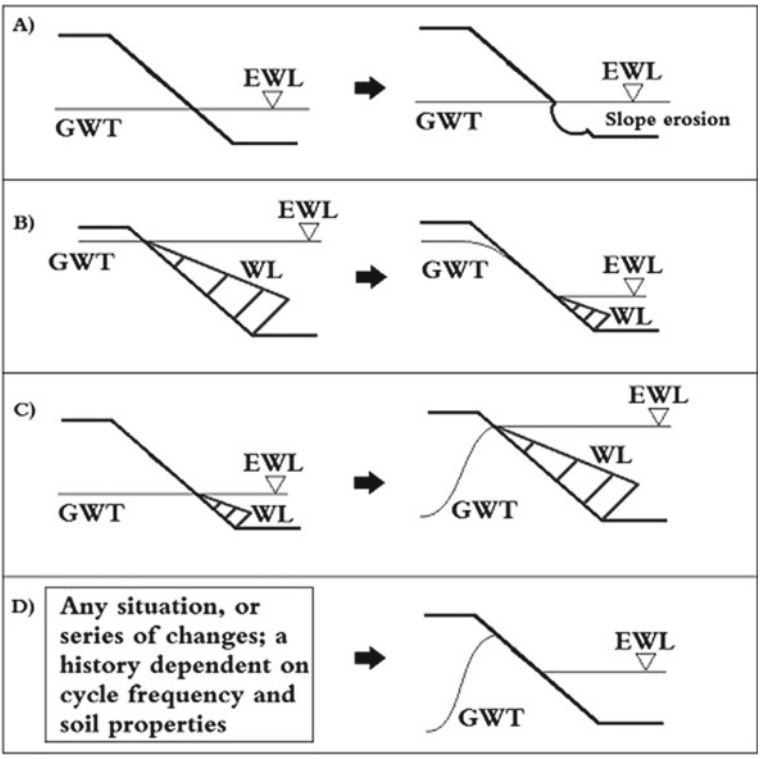

Fig. 1 Basic modes of water level change; streaming water (**A**), water level drawdown (**B**), raised water level (**C**), and fluctuating water level (**D**). Water loads (WL), positions of the ground-water table (GWT), and the external water level (EWL) are shown

2 Objective

2.1 Aim and Objectives

The aim of this study is to identify and enlighten the potential impacts on waterfront slopes subjected to water-level fluctuations, including evaluation of factor of safety by strength reduction method.

The summary of the objectives of this study is as follows:

1. Experimental model analysis of the stability of a bank simulating a river bank during post-flood condition.
2. Determination of factor of safety by strength reduction method.
3. Study of the influence of drawdown rate and ratios on the stability of a bank.
4. To study the variation of pore pressure with water level fluctuation and its effects on stability.

3 Literature Review

Mehmet M. Berilgen (2006): This paper presents an investigation of slope stability during drawdown depending on the soil permeability, drawdown rate, and drawdown ratio, considering the nonlinear material and loading conditions.

Jens Johansson, (June 2014): Water-level fluctuations have been reviewed; sources, geotechnical effects on slopes, and approaches used for modeling have been focused on. It has been found a predominance of research focused on coastal erosion, quantification of sediment production, bio-environmentally issues connected to flooding, and effects on embankment dams subjected to rapid drawdown.

Qin Rong, Pan HaiZe, Han LingFeng, Chen MengJie, (2014): Using SEEP/W, SIGMA/W and SLOPE/W Module of GEO-SLOPE software, we studied the slip mass change rule with the water level lifting, variation of the stress field and displacement fields of action under the reservoir water level lifting, and on the basis of the results of seepage and stress–strain calculation results, considering finite element method and limit equilibrium method to calculate the landslide stability analysis and comprehensive evaluation.

4 Experimental Programme and Methodology

4.1 Laboratory Model Study

The model river bank and hydro-fluvial conditions were defined simulating a river bank subjected to rapid drawdown based on the field condition of the bank of river Ganga at the upper region of Murshidabad district in West Bengal, India. The laboratory model study was done for the following reasons:

1. The socioeconomic losses are at alarming condition due to bank failure in West Bengal, India, which demands the scientific analysis of bank failure.
2. The bank consists of composite material, loamy sand in the lower layer, and thin silty clay at the top.
3. Most of the failure occurs during post-flood drawdown of water.

A series of trial experiments have been carried out to study the responses of model banks for varying bank geometries, different drawdown rates and ratios and hydrograph conditions. The slope of the model bank has not been perfectly represented as the actual bank slope as the site slope is not perfectly uniform. The slope of the model bank was chosen as 1 V:2H, 1 V:1.5H, respectively. This slope has been adopted in the field for protection work which has also failed experience.

4.2 Test Procedure and Program

A model river bank was built inside the tank with slope geometry as mentioned above. In each experiment, the initial bank slope 1 V:2H, LWL, and HFL have been kept constant. The model bank has been prepared by a uniform compaction energy of 0.209 kg/cm^2 to achieve 15.965 kN/m^3 unit weights of the bank materials. This density has been chosen based on pre-monsoon density obtained from the actual field. All the experiments have been recorded using a digital video camera. Three different hydrograph cases were undertaken by controlling two outlets of diameters 50.8 mm and 76.2 mm. Each run was continued for 3 h to record the observations. The water level in the model river course has been increased gradually from a low water level to a high flood level, i.e., 0.8H for this model study. The experimental program and variations of drawdown rate and ratios are presented in the following Table 1 (Fig. 2).

The pore pressure variations along the cross-section of the model river bank after each drawdown have been measured with the help of a tailored pressure measuring device (Fig. 3). It consists of eight numbers of transparent P.V.C. tubes (3 mm dia.); one end of which has been installed at different locations of the bank during the construction of the model river bank and other ends of the pipes are attached at the lower ends of the series of labeled manometers fixed on the Perspex wall of the model flume. The positions of the manometers inside the bank were shown in Fig. 3 and the planimetric and vertical positions of manometers are listed in Table 2.

The schematic diagram of the experimental setup has been presented in Fig. 4 (2.00 m long, 0.90 m wide, and 0.60 m deep). Two sets of pumps have been installed in the setup; 5L/s capacity pump has been assigned for maintaining the water level in the seepage tank. A 10L/s capacity pump was used to produce the required drawdown rates and ratios. The capacities of the pumps have been fixed after trial tests to achieve a drawdown rate from the high flood level to observe the failure condition. The high flood level (HFL, 0.8H cm) and low water level (LWL, 0.3 cm) for this particular research works have been selected based on the actual HFL at that particular site during monsoon and LWL during summer and adjusting with the model flume size.

4.3 Materials Used in the Study

It has been found that the major part of the river bank comprises a layer of sands which is vulnerable to failure. To represent the similar kind of bank material fine-grained local sand having similar grain size distribution has been used. The angle of internal friction and coefficient of permeability for horizontal flow for the three different unit weights are tabulated in Table 3.

Table 1 Summary of experimental program

Details of different geotechnical and fluvial conditions under which various runs of the experiment have been carried out:							Hydrograph cases	Initial bulk density (kN/m^3)	Bank slope 2 Types
Drawdown ratios	0.0	0.2	0.3	0.5	0.6	0.8	I (when the outlet pipe is 50.8 mm)	15.965	1:2 & 1:1.5
	0.0	0.2	0.3	0.5	0.6	0.8			
	0.0	0.2	0.3	0.5	0.6	0.8			
	0.0	0.2	0.3	0.5	0.6	0.8	II (when the outlet pipe is 76.2 mm)		
	0.0	0.2	0.3	0.5	0.6	0.8			
	0.0	0.2	0.3	0.5	0.6	0.8			
	0.0	0.2	0.3	0.5	0.6	0.8	III (when the outlet pipe is both 50.8 mm and 76.2 mm)		
	0.0	0.2	0.3	0.5	0.6	0.8			
	0.0	0.2	0.3	0.5	0.6	0.8			

Fig. 2 The gauging system to measure deformation in the profile

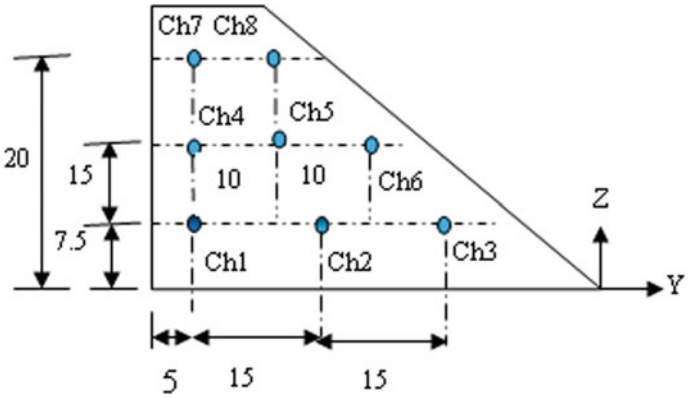

Fig. 3 Configuration of pressure monitoring manometers (Bank Slope 1 V:2H dimensions are in cm)

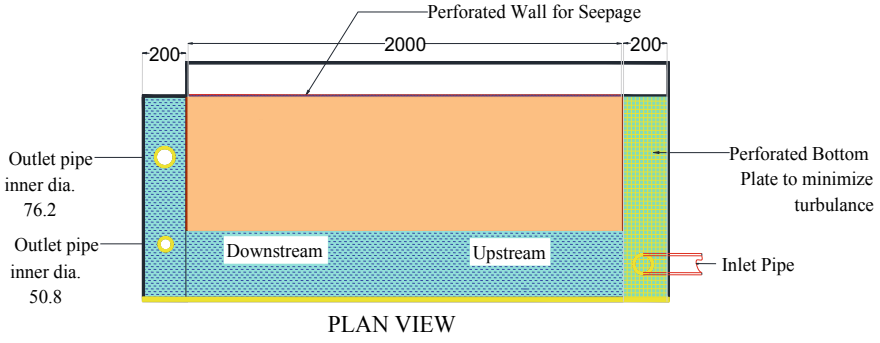

Fig. 4 Experimental setup plan view (all dimensions are in mm)

Table 2 Positions of pressure measuring channels, bank slope 1 V:2H

Manometer channels	Position in x-direction (along the length of bank (cm)	Position in y-direction (cm)	Position in z-direction (cm)
Ch1	48	5	7.5
Ch2	48	20	7.5
Ch3	48	35	7.5
Ch4	48	5	15
Ch5	48	15	15
Ch6	48	25	15
Ch7	48	5	20
Ch8	48	15	20

Table 3 Geotechnical Properties of bank material used in the experiment

Unit weight of bank material (γ) (kN/m^3)	Optimum moisture content (%)	Angle of internal friction ($\varphi°$)	Coefficient of horizontal Permeability
15.965	3	34.5	0.0675

4.4 Embankment Geometry

In this laboratory model study, a linear scale of 1:25 was selected to simulate the prototype bank geometry of river Ganga in Murshidabad District of West Bengal. The height of the bank was selected based on field observation and slope of bank 1 V: 2H and top width of the bank as 0.1 m as shown in Figs. 5 and 6 is the photographic view of the experimental setup along with the model bank.

5 Experimental Result and Discussion

As it is not possible to control the drawdown rate for each drawdown ratio manually, so the three average drawdown rates have been assigned that are named as Hydrograph case-I (2″ dia.), Hydrograph case-II (3″ dia.), and Hydrograph case-III (2″ + 3″ dia.). In case of results discussion, we prepared the tables and drew the curves of pore pressure variation with respect to time at different drawdown ratios and shear strength variation with respect to time at different drawdown ratios after drawdown. And at last, we prepared tables and draw curves on factor on safety variation with respect to drawdown rate and drawdown ratio on different hydrograph cases (Tables 4 and 5) (Figs.7, 8, 9, 10, 11 and 12).

Fig. 5 Model for the experiment in Lab

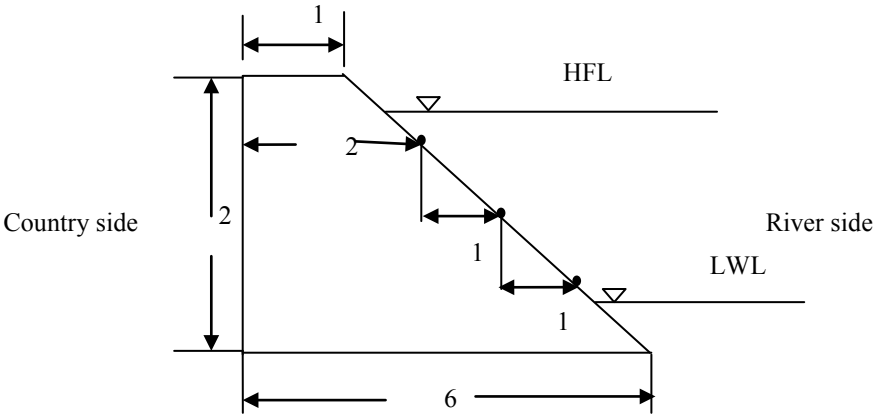

Fig. 6 Model geometry: Dimensions, Low water level (LWL), high flood level (HFL), and A, B, C are manometer positions (three rows as shown and six columns @280 mm c/c) are shown in the figure. (All dimensions are in mm)

Table 4 Experimental result of pore pressure variation at different times after drawdown from 0.3H to 0.0H (Bank Slope = 2H: 1 V)

Drawdown ratio = 0.3	Hydrograph Case: I	Pipe diameter: 2″	Date: 03–23-2019

Data measurement of pressure from manometers								
Time interval after drawdown (Sec)	Height of water in cm in pipe number							
	Ch.1	Ch.2	Ch.3	Ch.4	Ch.5	Ch.6	Ch.7	Ch.8
t = 0	6.0	5.5	7.0	5.6	8.2	5.9	0	0
t = 5	5.9	5.0	6.5	5.6	8.2	5.8	0	0
t = 10	5.7	4.0	6.4	5.4	8.0	4.8	0	0
t = 15	5.5	3.8	5.8	5.3	7.8	4.2	0	0

Table 5 Experimental result for the determination of shear strength at different times after drawdown from 0.3H to 0.0H (Bank Slope = 2H: 1 V)

Hydrograph case: I	Pipe diameter: 2″	Date: 03–23-19

Condition	Shear strength calculation				
	Initial reading of the vane	Final reading of Vane	Torque (kg-cm)	Shear strength (kPa)	Shear strength reduction (%)
Before flow (0.0H)	250	209	0.586	14.04	
After drawdown; t = 2 min	250	226	0.343	8.22	41.46
t = 4 min	250	224	0.371	8.91	-8.33
t = 6 min	250	223	0.386	9.25	-3.85
t = 10 min	250	220	0.429	10.28	-11.11

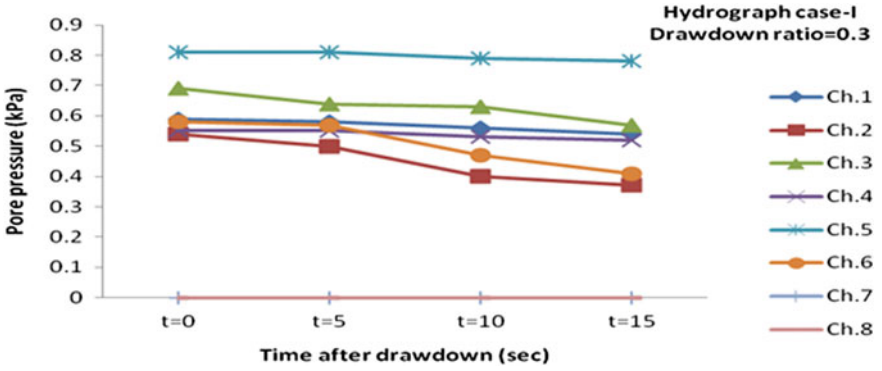

Fig. 7 Plot of pore pressure variation with time after drawdown from 0.3H to 0.0H (Bank Slope = 2H: 1 V)

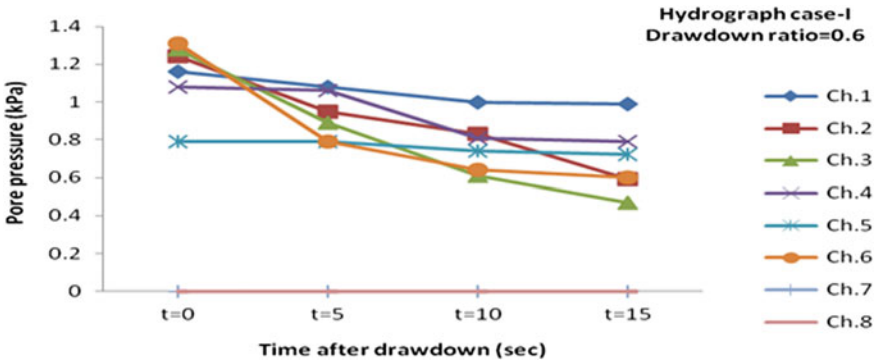

Fig. 8 Plot of pore pressure variation with time after drawdown from 0.6H to 0.0H (Bank Slope = 2H: 1 V).

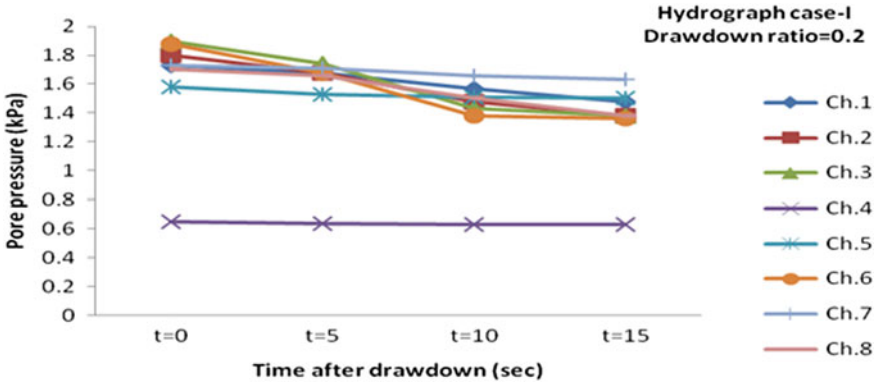

Fig. 9 Plot of pore pressure variation with time after drawdown from 0.8H to 0.6H (Bank Slope = 2H: 1 V).

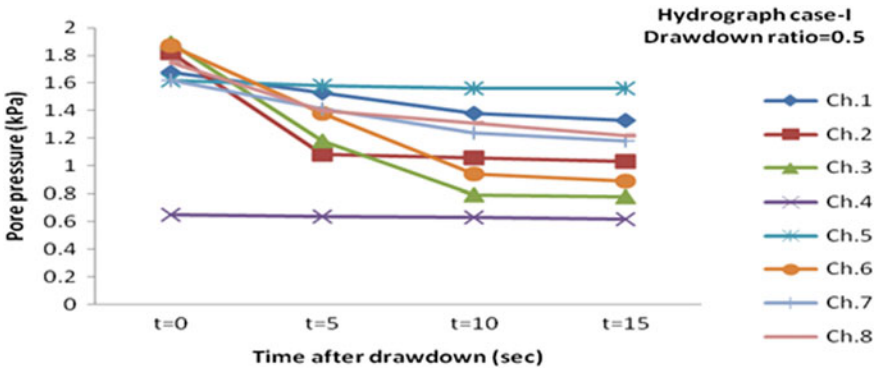

Fig. 10 Plot of pore pressure variation with time after drawdown from 0.8H to 0.3H (Bank Slope = 2H: 1 V)

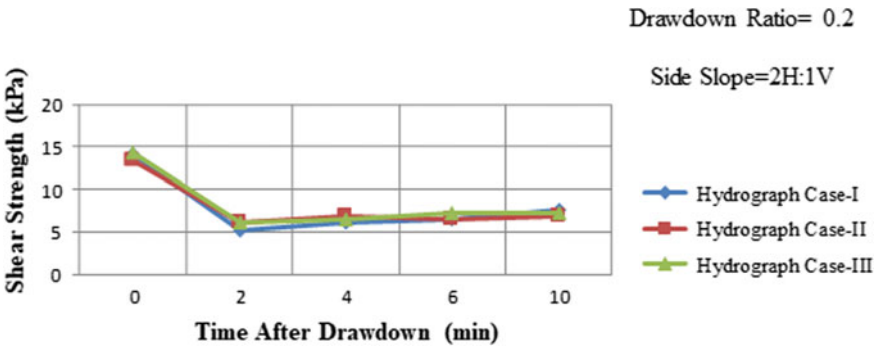

Fig. 11 Plot of Shear strength variation with time after drawdown for different hydrograph case conditions for drawdown ratio 0.2 (Bank Slope = 2H: 1 V)

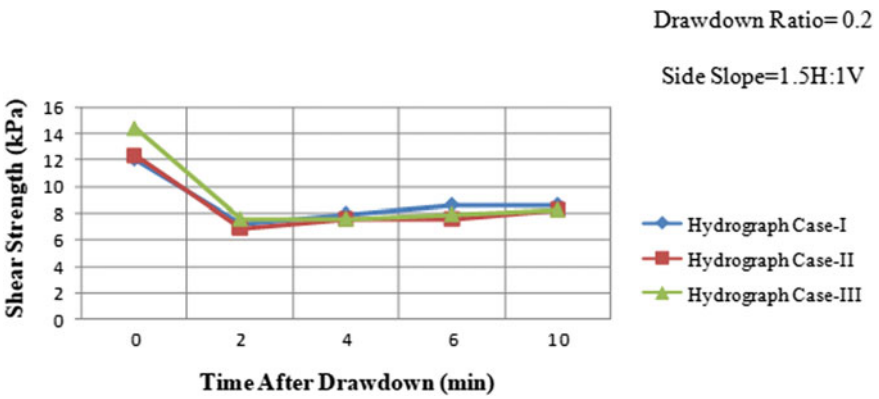

Fig. 12 Plot of Shear strength variation with time after drawdown for different hydrograph case conditions for drawdown ratio 0.2 (Bank Slope = 1.5H: 1 V)

5.1 Experimental Data of Pore Pressure and Shear Strength After Drawdown for Hydrograph Case-I

5.1.1 For Drawdown from 0.3H to 0.0H (Bank Slope = 2H: 1 V)

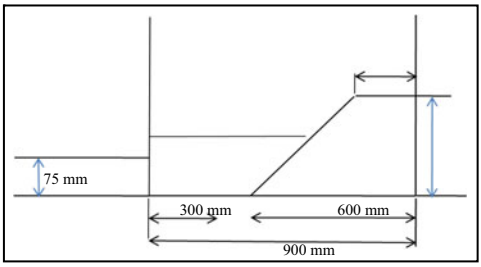

Initial water content = 3%

Bank Material: Homogeneous Sand

Bank Geometry

Side Slope = 2H: 1 V

Height of Bank = 250 mm

Base width = 600 mm

Top Width = 100 mm

Hydraulic Data

Height of bank up to which water level to be raised (a) = 0.3 H = 75 mm

Time required to fill up the tank up to desired level (b) = 84.00 s

Rate of filling of tank (a/b) = 0.90 mm/s

Volume of water collected (c) = 5.60 L

Time of collection (d) = 4.00 s

Flow rate (c/d) = 1.4 l/s

Area of Flow = 28,125 mm^2

Velocity of flow = (Flow rate*10^6)/Area of flow = 49.78 mm/s

Drawdown Data

Initial Height of water (L) = 0.3 H = 75 mm [Here, H = 250 mm]

Final Height of water after drawdown (F) = 0.0 H = 0 mm

Time required to drawdown from 0.3 H to 0.0 H (t) = 26.00 s

Drawdown Rate [(L–F)/t] = 2.88 mm/s Drawdown Ratio (L/H) = 0.3.

5.2 Calculation of Factor of Safety by Strength Reduction Method

5.2.1 Factor of Safety for Bank Slope 2H: 1 V

See Table 6 and Fig. 13

Table 6 Experimental results of factor of safety (FoS) after drawdown for different drawdown rates and drawdown ratios for hydrograph case-I

Hydrograph case: I		Pipe dia.: 2″			Side slope: 2 H:1 V			Date: 23-03-19		
Variation of shear strength with time and calculation of FoS										
DD ratio (L/H)	DD rate (R) mm/s	Time (min)	t = 0	2	4	6	10	Minimum shear strength or failure shear strength (kPa)	FoS	Failure condition
0.3	2.88	Shear Strength (kPa)	14.04	8.22	8.91	9.25	10.28	5.14	1.60	Minor mass failure
0.6	2.5		14.04	7.19	7.19	7.88	8.56		1.40	
0.2	2		14.04	5.14	6.17	6.51	7.54		1.00	
0.5	1.32		14.04	5.14	6.17	6.85	6.85		1.00	
0.8	3.28		14.04	6.17	6.85	6.85	7.19		1.20	

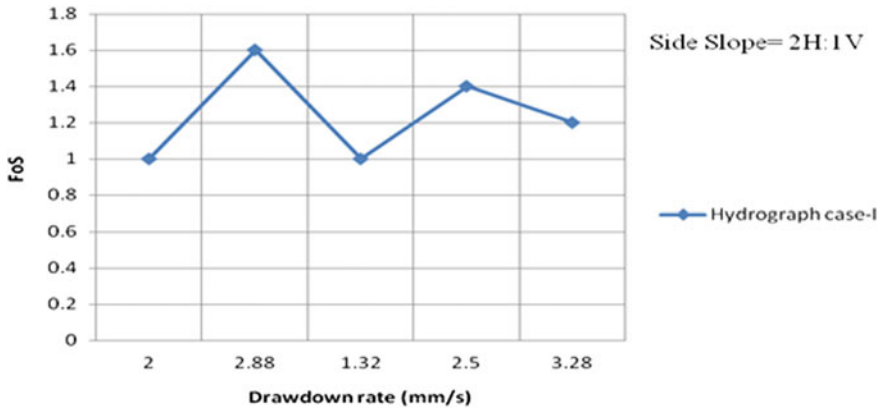

Fig. 13 Plot of FoS versus drawdown rate for bank slope 2H: 1 V and hydrograph case-I

5.2.2 Factor of Safety for Bank Slope 1.5H: 1 V

See Table 7 and Fig. 14

5.3 Results Discussion

It has been observed from the above data and the curve of pore pressure variations that immediately after drawdown the positive pore pressure is almost unchanged during the drawdown period, after that it is decreasing and becomes constant with respect to time. The change of pore pressure is maximum for maximum drawdown ratio and also it is varying for different hydrograph cases. Also, it is observed that after drawdown, the release of pore pressure is little bit slow in the case of 1:2 river bank slope compared to the 1:1.5 slope. In case of shear strength variation, it has been observed from the above data and the curve that immediately after drawdown the shear strength of the model river bank becomes minimum compared to the initial shear strength of the bank for different drawdown ratios, and after some time it is slowly increasing. It is also observed that the change of shear strength is maximums for maximum drawdown rate and also it is varying for different hydrograph case. At last, it has been observed from the above data and the curve of factor of safety (FoS) variation with respect to drawdown rate and drawdown ratio for different hydrograph cases that with the increase of drawdown rate and drawdown ratio, the factor of safety decreased and it became minimum for maximum drawdown rate and ratio. It is also observed that immediately after drawdown the factor of safety is minimum and it increases with respect to time (Figs. 15 and 16).

Table 7 Experimental results of factor of safety (FoS) after drawdown for different drawdown rates and drawdown ratios for hydrograph case-I

Hydrograph case: I		Pipe dia.: 2″			Side slope: 1.5 H:1 V			Date: 11-04-19		
Variation of shear strength with time and calculation of FoS										
DD ratio (L/H)	DD rate (R) mm/s	Time (min)	t = 0	2	4	6	10	Minimum shear strength or failure shear strength (kPa)	FoS	Failure condition
0.3	2.34	Shear strength (kPa)	11.99	6.51	6.85	7.54	7.88	651	1.00	Minor failure mass
0.6	1.90		11.99	7.54	7.88	8.22	8.56		1.16	
0.2	0.91		11.99	7.19	7.88	8.56	8.56		1.05	
0.5	0.83		11.99	6.85	7.54	7.54	7.88		1.05	
0.8	2.02		11.99	7.19	7.54	8.22	8.56		1.10	

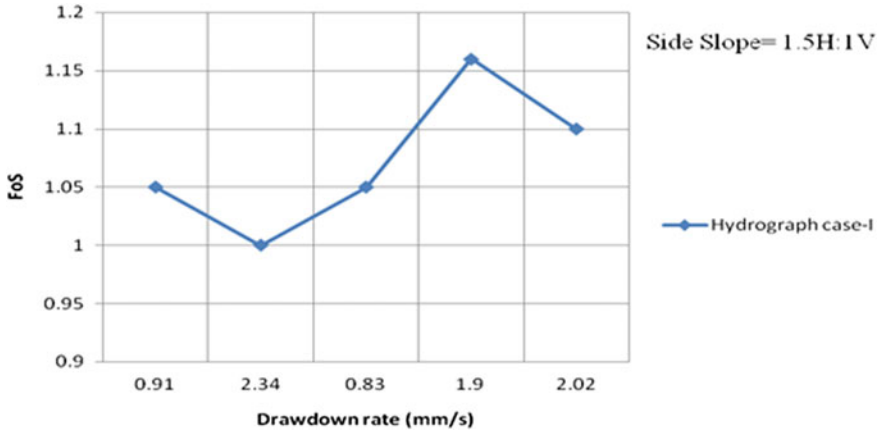

Fig. 14 Plot of factor of safety (FoS) versus drawdown rate for bank slope 1.5H: 1 V and hydrograph case-I

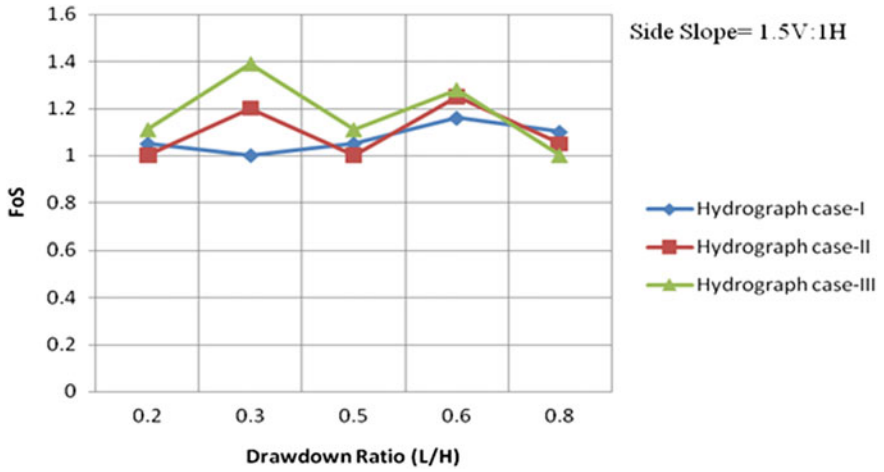

Fig. 15 Plot of factor of safety (FoS) versus drawdown ratios for bank slope 1.5H: 1 V and different hydrograph case conditions

6 Conclusions

After calculating the pore pressure variations with time after drawdown for different drawdown rates and drawdown ratios shows that the release rate of positive pore pressure increases with the increase of drawdown rate and ratios. And during major river bank failure, we observed that the release rate of positive pore pressure from the model river bank is minimum. In this model study of the stability of river bank, the effect of shear stress generated by the velocity of water flow has not been taken

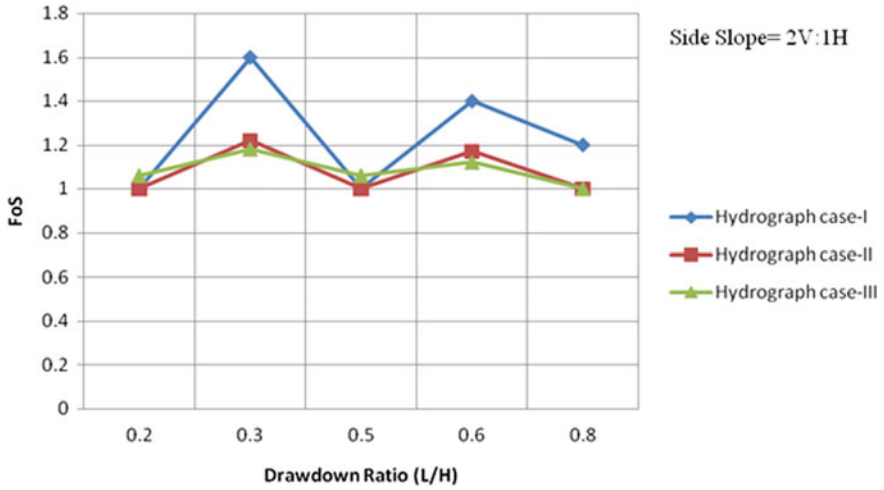

Fig. 16 Plot of factor of safety (FoS) versus drawdown ratios for bank slope 2H: 1 V and different hydrograph case conditions

into account, instead the river bank is subjected to rapid drawdown only, and from the experimental results, we may conclude that the water-level fluctuation is one of the dominating causes of bank failure for cohesionless soil. The factor of safety calculated for different drawdown rates and drawdown ratios shows that it decreases with an increase of drawdown rate and ratio, meeting the consequences of physical phenomenon associated with this condition. The effects of drawdown rate and drawdown ratio on the factor of safety reveals that it is rather than drawdown ratio which takes a leading role to make the river bank unstable in comparison to drawdown rate. And during major bank failure, we observed that the factor of safety of model river bank become minimum.

References

1. USACE, Engineering and Design: Slope Stability—Engineer Manual. US Army Corps of Engineers, EM 1110-2-1902 (2003)
2. Duncan, J.M., Wright, S.G.: Soil Strength and Slope Stability. John Wiley & Sons, New York, March (ISBN 0-471-69163-1) (2005)

Rock Mass Index (RMI) to Estimate the Shear Strength Parameters of the Rockmass: Case Study from Lesser Himalayas, Jammu & Kashmir, India

Pratap Chandra Dhang

1 Introduction

The rockmass incorporates the type of rock and discontinuities present within it, and these discontinuities have a significant impact on the stability of any engineering structures, like tunnels, foundation, or slope designs. The shear strength of the discontinuities in rockmass has a stronger influence on the mechanical behaviour of rockmass, and the structures often failed due to low shear strength. Even the deformation characteristics and stress distribution in rockmass depend upon the shear strength of the rockmass. Therefore, stability analysis of engineering structures requires assessment of shear strength parameters, i.e. cohesion (c) and angle of internal friction (Φ) of the rockmass [1]. Evaluation of shear strength parameters is mostly done by in situ shear tests [2, 3]. However, Palmstrom [4–6] have applied the Rock Mass index (RMI) system to assess the shear strength parameters of the rockmass. As RMI is based on the geological and geotechnical characterisation of rockmass directly on the ground, hence it has some inherent advantages over the use of in situ shear tests. RMI has been used to (a) determine the constants 's' and 'm' in the Hoek–Brown failure criterion for rockmasses to assess the shear strength parameters, (b) work out ground response curves using the same 's' and 'm' constants, (c) quantify the descriptive NATM classification and (d) estimate stability and rock support in underground openings.

The present work is an experiment carried out to determine the shear strength parameters by using the RMi of the Sirban Dolomitic Limestone at the vicinity of the major thrust zone in lesser Himalaya by following the method of Palmstrom [5]. The study area is located at Anji Khad (33°05′N/74°53′E) near Reasi, Jammu & Kashmir, India. The Reasi region of Jammu & Kashmir lies in a hilly terrain of the foreland zone of Himalaya and is drained by major two rivers, namely, Chenab and Anji

P. C. Dhang (✉)
Deputy General Manager, Ircon International Limited, Siliguri 734001, India

C. N. V. Satyanarayana Reddy et al. (eds.), *Stability of Slopes and Underground Excavations*, Lecture Notes in Civil Engineering 185,
https://doi.org/10.1007/978-981-16-5601-9_18

with their tributaries. Reasi Thrust is considered as equivalent to the Main Boundary Thrust (MBT) passes through this region. Massive bedded Sirban Dolomitic Limestone of Proterozoic age occurs as inliers fringed by Shale, Carbonaceous Shale and Limestone of Eocene Subathu Formation and Sandstone-Mudstone of Murree Group (Fig. 1). Siwalik Group of rocks occurs in the south of MBT. The region is under a high compressive stress regime, where maximum horizontal stress lies in the NE-SW direction. The rate of strain accumulation in the thrust blocks is very high, due to which frequent earthquakes are inevitable in this region. Singh and Sarwade [7] evaluated the shear strength parameters in jointed Sirban Dolomitic Limestone from this same area. They have conducted in situ shear tests on the left and right

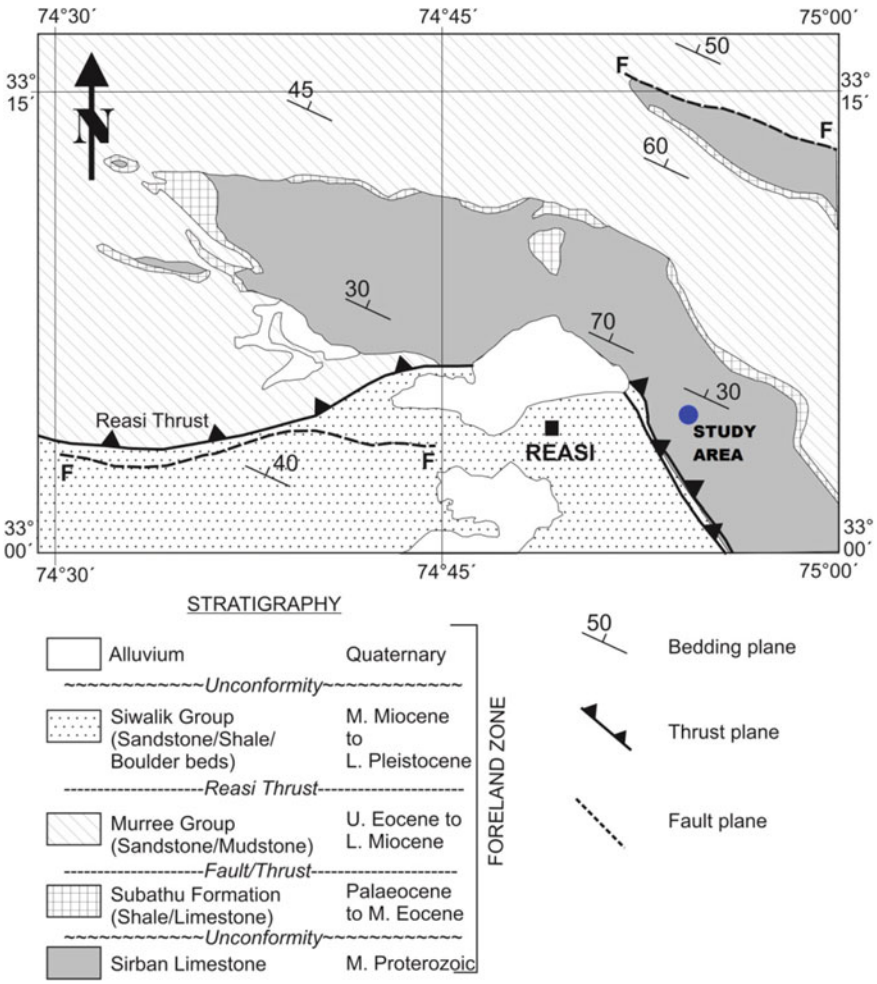

Fig. 1 Simplified geological map of Reasi area, Jammu & Kashmir, India (after GSI 1997 and 2005)

banks of the Anji River for the railway bridge to be constructed in this region. The present work centred on the same region and involves (a) geological mapping and geostructural scanline survey to characterise the discontinuities present within the rock and calculation of RMi, and (b) determination of shear strength parameters by application of RMi. The obtained results of both the present and earlier works of Singh and Sarwade [7] have been compared and analysed. Further, an attempt has also been made here to bring out the validity of this method in the application of slope design and/or tunnelling projects.

2 Methodologies

The exposures of the rock masses are excellent on both banks (right and left) of the Anji River. On the left bank, the bedded dolomitic limestone is exposed on the cliff, from which most of the geological data have been collected. At a few locations, especially along the small seasonal nallahs (rills and gullies), small cones of debris are present. On the right bank of the river, bedded dolomitic limestone is exposed on the much lower level of the hill. Detail geological mapping and geostructural surveys through the scanline method have been done on the left and right banks of the Anji River. The overview of the geological setup of the region has been obtained from (1) Poonch Quadrangle Sheet (degree sheet) of J&K State, No. 43 K (scale 1:250,000) published in 1997 by the Geological Survey of India; and (2) Geological Map of the Himalaya (Western Sector) on the scale of 1:1,000,000 published by Geological Survey of India, Kolkata in 2005. Universal Transverse Mercator (UTM) coordinate system has been used to locate and draw the geological features on the map as well as on scanline diagrams. ISRM methodologies have been adopted for characterisation of rockmass (degree of jointing, type of discontinuities, orientation, spacing, persistence, roughness, apertures, fillings, etc.) from the field for geological mapping and scanline survey [8]. The estimated unconfined compressive strength (UCS) of the rockmass (σ_c) ranges from 40 to 80 MPa, though around the sheared/faulted areas the UCS is around 20 MPa.

On the basis of degree and character of discontinuities from detail geostructural scanline surveys, five zones have been delineated: (I) moderately jointed zone (joint spacing 0.2–0.6 m), (II) closely jointed zone (joint spacing 0.06–0.2 m), (III) very closely jointed zone (joint spacing <0.06 m), (IV) open jointed zone and (V) sheared/faulted zones. Joint characterisation has been done on the basis of ratings of (i) joint roughness factor (jR), (ii) joint alteration factor (jA) and (iii) joint length and continuity factor (jL). RMI of the rockmass has been calculated by using the inherent parameters like compressive strength (σ_c) of intact rock and the jointing parameters (JP). Detail theoretical description of the methodology for the determination of shear strength parameters is beyond the scope of the present work. The RMI parameters, such as (i) scale factor of compressive strength (fσ), (ii) joint condition factor (jC) and (iii) jointing parameter (JP), have been calculated. These followed by the estimation of constants of Hoek–Brown (H-B) failure criterion ('s', m_b and

Table 1 The input data and calculation sheet for the determination of shear strength parameters from RMI

Input data		
1	Rock characteristics	Type of rock
I	Rock compressive strength (MPa)	Σ_c
II	H-B's m-factor for intact rock	m_i
2	Joint characteristics	
I	Joint roughness factor	jR
II	Joint alteration factor	jA
III	Joint length and continuity factor	jL
3	Block volume (m^3)	Vb
4	Effective normal stress (MPa)	σ'
Calculations		
5	RMI parameters	
I	Scale factor of compressive strength	Fσ
II	Joint condition factor	jC
III	Jointing parameter	JP
IV	Rock Mass Index	RMi
6	Shear strength parameters	
I	Instantaneous friction angle (°)	Φ
II	Shear stress (MPa)	T
III	Instantaneous cohesion (Mpa)	C

h) and shear strength parameters (friction angle (Φ_i), shear stress (τ_i) and cohesion (c_i) by following the methods of Palmstrom [5] (Table 1).

3 Results

Detail geological mapping reveals that the geological succession around this area comprises dolomitic limestone (stromatolitic) of Sirban Group (Fig. 2). The bedding plane is unidirectional, steeply oriented (50–70°) towards N-NE, with local variations along the faults. The other three prominent sets of joints with random joints occur (65/025, 70/280, 50/150). W-NW-ly (70/280) steeply dipping joint set is very persistent. It has been further inferred that the region is characterised by moderate jointing except at some locations, where the density of jointing is high to very high. There are numerous major and minor faults (oriented 65/300, 30/055, 45/160) and three major NNE-SSW trending sinistral faults sliced the region. They are identified by the variation of dip and strike of beds along the fault planes, scarps and the presence of calcite veins and slickensides. These faults are transverse to the MBT or Reasi Thrust. With these major faults, some minor faults NNW-SSE and NW–SE

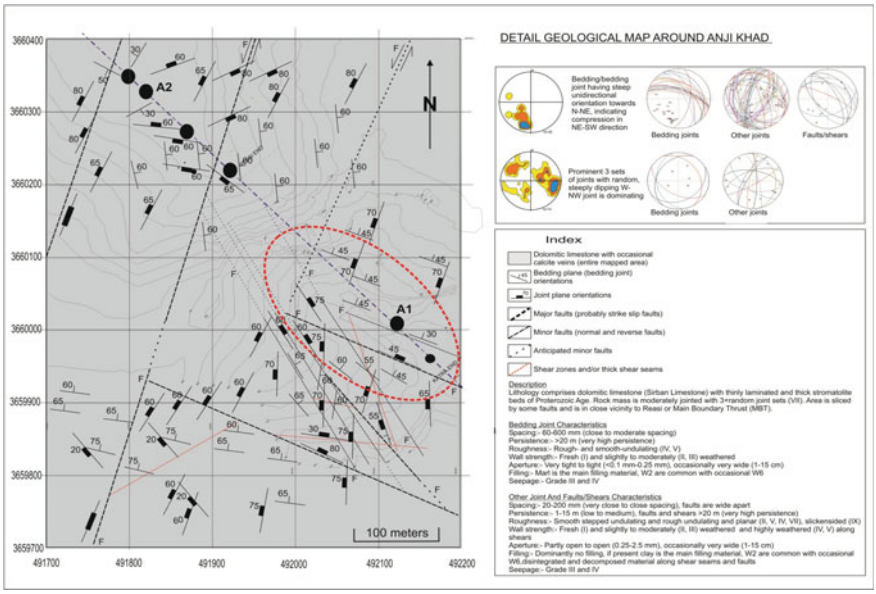

Fig. 2 Detail geological map around Anji Khad, Reasi, Jammu 7 Kashmir, India. A1 and A2 are the locations of in situ shear tests of Singh and Sarwade [7]

trending are also present; fault planes are defined by smooth polished and/or slickensided surfaces and are often associated with fault gouge and calcite veins. Some shear zones have also been delineated which have soft fillings.

The unconfined compressive strength (UCS) of the intact rock (σ_c) ranges from 40 to 80 MPa, though around the sheared/faulted areas the UCS is around 20 MPa. The discontinuities are bedding joints, tectonic joints, faults and shears. All the discontinuity planes are quite persistent and have different characteristic features (Figs. 3 and 4; Table 2). The block volumes (Vb) and diameter of blocks (Db) have also been estimated (Palmstrom [4]; Table 3). The scale factor for compressive strength (fσ) joint condition factor (jC), ratings of jointing parameter (JP) and Rock Mass Index (RMi) have been ascertained on the basis of block diameter (Db) and combination of three characteristic features of discontinuity planes, like joint roughness, joint alteration and joint length (Table 4). From the analysis, it has been inferred that the values of jC, JP and RMi decreases from Zone I to Zone V, whereas the fσ increases from Zone I to Zone V. The author here used the Hoek–Brown (H-B) failure criterion to determine the shear strength parameters of the rockmass, and for that, he used the RMi to estimate the constants, like, 's' and m_b in H-B failure criterion (Table 4). The results of residual shear strength parameters like, cohesion (c), friction angle (Φ) and shear strength obtained by Singh and Sarwade [7] are 0.38°–0.71 MPa, 48.97°–51.39° and 6.89°–7.59 MPa respectively. In comparison, it has been found that in the present work, the correlation coefficient (R^2) of each parameter is having strong

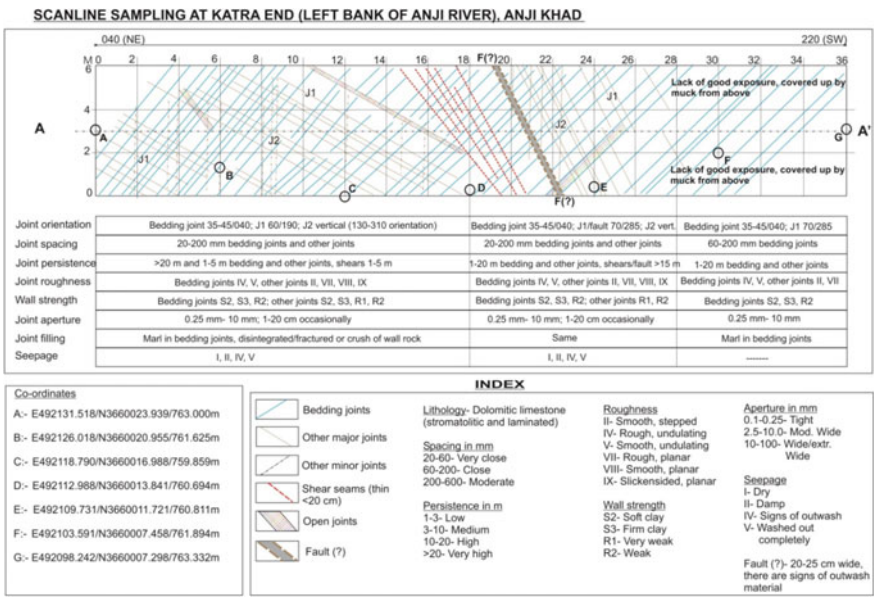

Joint orientation	Bedding joint 35-45/040; J1 60/190; J2 vertical (130-310 orientation)	Bedding joint 35-45/040; J1/fault 70/285; J2 vert.	Bedding joint 35-45/040; J1 70/285
Joint spacing	20-200 mm bedding joints and other joints	20-200 mm bedding joints and other joints	60-200 mm bedding joints
Joint persistence	>20 m and 1-5 m bedding and other joints, shears 1-5 m	1-20 m bedding and other joints, shears/fault >15 m	1-20 m bedding and other joints
Joint roughness	Bedding joints IV, V, other joints II, VII, VIII, IX	Bedding joints IV, V, other joints II, VII, VIII, IX	Bedding joints IV, V, other joints II, VII
Wall strength	Bedding joints S2, S3, R2; other joints S2, S3, R1, R2	Bedding joints S2, S3, R2; other joints R1, R2	Bedding joints S2, S3, R2
Joint aperture	0.25 mm- 10 mm; 1-20 cm occasionally	0.25 mm- 10 mm; 1-20 cm occasionally	0.25 mm- 10 mm
Joint filling	Marl in bedding joints, disintegrated/fractured or crush of wall rock	Same	Marl in bedding joints
Seepage	I, II, IV, V	I, II, IV, V	------

Fig. 3 Representative scanline survey from Anji Khad area

positive correlation ($\Phi/\tau = 0.984$, $\Phi/c = 0.962$ and $\tau/c = 0.995$) whereas correlation coefficient (R^2) of each parameter of Singh and Sarwade [7] is not having strong positive correlation ($\Phi/\tau = 0.793$, $\Phi/c = 0.032$ and $\tau/c = 0.368$).

4 Discussions

The study area is located at close vicinity of a major thrust, i.e. Reasi Thrust or Main Boundary Thrust (MBT), due to which the Sirban Dolomitic Limestone of Proterozoic age experienced significant tectonic deformation. High compressive stress in the region created tectonic joints and tilted the rock. The bed thickness of dolomitic limestone ranges from 10 to 50 cm, and the zones having lesser bed thickness have more closely spaced bedding joints as well as the tectonic joints. The degree of jointing has influenced the strength of the rock; relatively thinner beds are more prone to the effect of weathering also. Therefore, there are variations in the UCS of the intact rock (20–80 MPa) also. In addition to the UCS, the jointing parameters (JP) have been incorporated, which provided the Rock Mass Index (RMi) of the rockmass (cf. Palmstrom [9]).

Hoek–Brown (H-B) failure criterion [10–12] provides the means of estimating the strength of jointed rockmasses. RMi has been applied to determine the constants 's' and 'm' of the H-B failure criterion (Table 4). Earlier Hoek and Brown [10] and Hoek et al. [11] adapted the classification systems of RMR and Q system to determine the

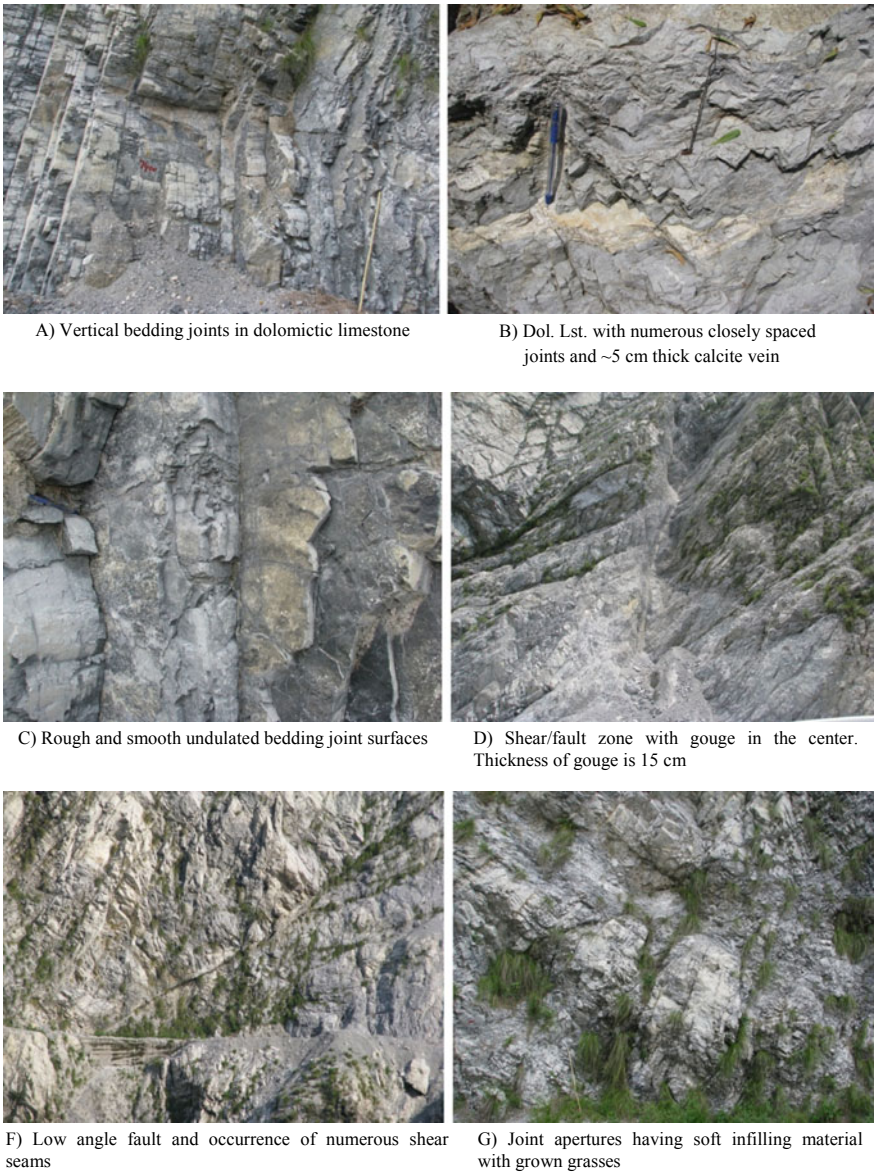

A) Vertical bedding joints in dolomictic limestone

B) Dol. Lst. with numerous closely spaced joints and ~5 cm thick calcite vein

C) Rough and smooth undulated bedding joint surfaces

D) Shear/fault zone with gouge in the center. Thickness of gouge is 15 cm

F) Low angle fault and occurrence of numerous shear seams

G) Joint apertures having soft infilling material with grown grasses

Fig. 4 Field photographs showing characteristic features of the rockmass. The stick in photographs is 1.5 m

Table 2 Characteristic features of the discontinuity surface with their ratings

Joint characteristics	Zones				
	Zone I	Zone II	Zone III	Zone IV	Zone V
Joint roughness (jR)	Rough slightly undulating	Rough planar	Rough planar	Smooth planar	Polished/ slicken sided
Rating	4	2	2	1	0.75
Joint alteration (jA)	Thin filling of clay	Thin filling of clay	Thin filling of clay	No joint wall contact, filling of soft clay	No joint wall contact, filling of soft clay
Rating	4	4	4	8	8
Joint length and continuity (jL)	10–30 m, continuous	10–30 m, continuous	10–30 m, continuous	10–30 m, continuous	>30 m, continuous
Rating	0.75	0.75	0.75	0.75	0.50

Table 3 Geomechanical properties of the rockmasses of different zones

Features	Zones				
	Zone I	Zone II	Zone III	Zone IV	Zone V
Discontinuity types and spacing	moderately jointed zone (Joint spacing 0.2–0.6 m)	Closely jointed zone (Joint spacing 0.06–0.2 m)	Very closely jointed zone (Joint spacing <0.06 m)	Open jointed zone	Fault/shear zone
UCS	80 MPa	60 MPa	40 Mpa	40 MPa	20 MPa
Vb (m^3)	0.0045	0.0015	0.0009	0.0007	0.0004
Db (m)	0.20	0.11	0.09	0.08	0.06

'm' and 's' constants, but these systems include external factors like groundwater and stresses. Subsequently, Hoek et al. [13] and Hoek [14] developed a GSI system and linked it for estimation of failure criterion. GSI is based on a good geological model of the area, emphasizing on geological structures and surface conditions, but does not fulfill the requirement of engineers who believe in numbers and not in a qualitative approach [15, 16]. As constants 'm' and 's' depend upon the properties of the rock, these values lower as the rockmass condition deteriorates from Zone I to Zone V in this present work (Table 4).

A positive correlation has been found as higher the spacing of the joints, higher the block volumes, diameter of the blocks, and also the UCS of the rockmass (Table 3) (cf. [17–21]). These have resulted in a gradual deterioration of shear strength parameters from Zone I to Zone V and thus have a strong positive correlation coefficient (R^2) among each parameter (Table 4). On comparison of results of the present study with that of earlier work [7], it has been found that the values of Φ, c and τ of present work are much less. Results obtained from Singh and Sarwade [7] do not show a strong positive correlation coefficient (R^2) among each parameter. These

Table 4 Estimation of shear strength parameters of rockmasses

	Zone I	Zone II	Zone III	Zone IV	Zone V
Type of rock	Dolomitic limestone				
σc (MPa)	80	60	40	40	20
Mi	8.4	8.4	8.4	8.4	8.4
jR	2	2	2	1	0.75
jA	1	4	4	8	12
jL	2	0.75	0.75	0.75	0.5
Vb (m^3)	0.0045	0.0015	0.0009	0.0007	0.0004
σ′ (MPa)	1	1	1	1	1
Fσ	0.8797	0.8448	0.889	0.9117	0.9641
jC	0.75	0.375	0.375	0.0937	0.0312
JP	0.0115	0.0065	0.0052	0.0008	0.0001
RMi	0.924	0.393	0.208	0.032	0.002
S	0.00013	0.00004	0.00002	0	0
Mb	0.4835	0.3365	0.2904	0.0888	0.0243
H	1.1409	1.2661	1.4607	2.5015	11.9634
Φ (°)	44.38	38.53	33.34	22.58	9.63
τ (MPa)	1.485	1.195	0.994	0.624	0.297
c (MPa)	0.507	0.399	0.336	0.208	0.128

variations are mainly due to (1) difference in methodology of determination of shear strength parameters, and (2) the present work conducted at the surface whereas Singh and Sarwade [7] conducted their test underneath the ground (in drifts having significant overburden), where weathering effect is minimal. Here characterisation of geological features disposed on the area as well as their quantitative analysis has been done and used as foremost criteria to classify each zona (Zone I–Zone V), therefore the determined shear strength parameters can be easily relatable with the geological features, e.g. moderately jointed zones (Zone I) have high Φ, c and τ, whereas faulted/sheared zones (Zone V) have very low Φ, c and τ (Table 4).

The analysis of physical and engineering properties (especially the shear strength parameters) of the rocks is important for the design of the structures. In practice, the rocks are invariably intersected by discontinuities, which govern the strength and deformational behavior. Therefore, the engineering properties assessed by laboratory tests on intact rocks are not suitable for use directly in analysis and design. Further in situ shear tests are too costly, time taking and usually done prior to the construction process. There are several models for the determination of shear strengths like RMR based Mohr–Coulomb failure criterion, Patton's Model, Q-index based Barton Model. However, Mehrotra [22] clarified that the shear strength is under-estimated or over-estimated by these methods. Later GSI-based Hoek–Brown failure criterion became the most widely used method for shear strength determination. But in this

case, also only geological features and disturbances to the rockmass are involved, and no measurements like joint mapping and quantitative analysis of joints, etc., are done in the field. Subsequently, Ramamurthy criterion [17, 18] and modified Mohr–Coulomb criterion Singh and Singh [7] has also came into existence. However, the most reliable method of shear strength determination is the Hoek–Brown failure criterion due to its extensive acceptability to the engineering geologists and engineers. Thus, the RMi system of Palmstrom [5] for classification of rockmass and application of the same for determination of constants 's' and 'm' in the Hoek–Brown (H-B) failure criterion for rockmasses to assess the shear strength parameters is quite useful. This method is cost-effective, not so time taking and can easily be done at any stage of design, construction, etc. Applications of RMi are manifold: (1) it can be used to work out ground response curves using the same 's' and 'm' constants, (2) also useful for quantification of the descriptive NATM classification and (3) to estimate stability and rock support in underground openings [23].

5 Conclusions

Five zones have been delineated (Zone I–V) on the basis of the discontinuity types and spacing of discontinuities in Sirban Dolomitic Limestone. The rockmass is poor with low UCS values throughout and intersected by numerous discontinuities, thus having low shear strength parameters (Φ, c and τ). The correlation coefficient (R^2) among each shear strength parameter having a strong positive correlation. When compared with the in situ tests done earlier in this area, the values of present obtained results are quite low. This may be due to the variation in methodology and location. In situ tests are often performed to get the shear strength parameters, but due to their operational difficulties, high cost and timing factors, are not performed regularly which often create information gap and constructional problems. Therefore, the method of estimation of shear strength parameters by RMi which is reliable and also cost- and time-effective can be used extensively. Therefore, there is ample scope for future studies on this aspect of RMi rockmass classification system.

References

1. Singh, B., Goel, R.K.: Engineering Rock Mass Classification, p. 384. Elsevier (2012)
2. IS 7746: Indian Standard Code of Practice for In-Situ Shear Test on Rock, Bureau of Indian Standards, New Delhi (1983)
3. ISRM: Suggested methods for determining shear strength, International Society for Rock Mechanics (ISRM) Commission on standardization of laboratory and field tests, In: Brown, E.T. (ed.) Rock Characterization Testing and Monitoring, pp. 131–140 (1981)
4. Palmstrom, A.: RMi-a system for characterizing rock massstrength for use in rock engineering. J. Rock Mech. & Tunnelling Tech. **1**, 69–108 (1995)
5. Palmstrom, A.: The Rock Mass Index (RMi) applied in rock mechanics and rock engineering. J. Rock Mech. Tunnelling Tech. **1**, 40 (1996)

6. Palmstrom, A.: The Rock Mass Index (RMi) applied in rock mechanics and rock engineering. J. Rock Mech. Tunnelling Tech. **11**, 1–40 (1996)
7. Singh, R., Sarwade, D.V.: Evaluation of shear strength parameters in jointed rock mass. J. Rock Mech. Tunnelling Tech. **22**, 21–36 (2015)
8. ISRM: Suggested methods for the quantitative description of discontinuities in rock masses, International Society for Rock Mechanics (ISRM) Commission on Standardization of Laboratory and Field Tests. Int. J. Rock Mech. Min. Sci. Geomech. Abstr. 15, 319–368 (1978).
9. Palmstrom, A.: Characterizing rockmasses by the RMi for use in practical rock engineering, Part 1: The development of the Rock Mass Index (RMi). Tunn. Undergr. Space Technol. **3**, 40 (1996)
10. Hoek, E., Brown, E.T.: Empirical strength criterion for rock masses. J. Geotech. Engng Div. ASCE **106**(GT9), 1013–1035 (1980)
11. Hoek, E., Wood, D., Shah, S.: A modified Hoek-Brown criterion for jointed rock masses. In: Hudson (ed.) Rock Characterization: Proceedings ISRM Symposium, Eurock '92, pp. 209–214. British Geotechnical Society, London (1992)
12. Hoek, E.: Strength of jointed rock masses. Geotechnique **33**, 187–223 (1983)
13. Hoek, E., Kaiser, P.K., Bawden, W.F.: Support of Underground Excavation in Hard Rock. A.A. Balkema, Rotterdam (1995)
14. Hoek, E.: Strength of rock and rockmasses. ISRM News J. **2**, 4–16 (1994)
15. Hoek, E., Brown, E.T.: The Hoek-Brown failure criterion and GSI- 2018 edition. J. Rock Mech. Geotech. Eng. **30**, 1–19 (2018)
16. Hoek, E., Marinos, P.G.: Predicting tunnel squeezing problems in weak heterogeneous rockmasses. Tunnels Tunneling Int **132**, 45–51 (2000)
17. Ramamurthy, T., Arora, V.K.: Strength predictions for jointed rocks in confined and unconfined states. Int. J. Rock Mech. Min. Sci. **31**, 9–22 (1994)
18. Ramamurthy, T.: Strength and modulus response of anisotropic rocks. In: Hudson, J.A. (ed.) Compressive Rock Engineering Principle Practice and Projects, vol. 1, pp. 313–329. Pergamon Press, Oxford (1993)
19. Singh, M., Rao, K.S., Ramamurthy, T.: Strength and deformational behavior of jointed rock mass. Rock Mech. & Rock Engng **35**, 45–64 (2002)
20. Singh, M., Rao, K.S.: Empirical methods to estimate the strength of jointed rock masses. Eng. Geol. **77**, 127–137 (2005)
21. Singh, M., Singh, B.: Modified Mohr-Coulomb criterion for non-linear triaxial and polyaxial strength of jointed rocks. Int. J. Rock Mech. Min. Sci. **51**, 43–52 (2012)
22. Mehrotra, V.K.: Estimation of engineering parameters of rock mass. Ph.D. thesis, University of Roorkee, Roorkee, India (1992)
23. Palmstrom, A.: Characterizing rockmasses by the RMi for use in practical rock engineering, Part 2: Some practical applications of the Rock Mass Index (RMi). Tunn. Undergr. Space Technol. **11**, 287–303 (1996)

The Light at the End of the Tunnel—The Sleemanabad Tunnel

Surendra Singh Pawar

1 Introduction

Mythologically, the two rivers originating from the ranges of Maikal, Narmada (f.) and Sonbhadra (m.), represented an estranged couple who went away in opposite directions. An attempt was made to reunite the two betrothed by constructing a 12 km long tunnel of 10 m diameter at Right Bank Canal of Bargi Project on River Narmada. This tunnel would be constructed between 104 and 116 km in Sleemnabad Carrier Canal, whose alignment was about 37 m high in mountainous terrain. In the project plan, the canal was proposed as an 'open cut'. This region is densely populated and is marked by passing-by NH-7 as well as the Howrah-Mumbai railway line. The Sleemanabad Carrier Canal is a part of the larger Bargi Diversion Project for the Narmada Valley Development Authority of Madhya Pradesh Government. Once completed, the major trans-valley canal will stretch across 194 km from the existing Bargi Dam on the Narmada River to arid areas of Katni, Rewa, Panna, Satana, and Jabalpur districts irrigating over 1,00,000 hectares of land, transferring 152 cubic meters of water per second.

2 Key Terms

a. **Clay Kicking**-Clay kicking is a specialized method developed in the United Kingdom for digging tunnels in strong clay-based soil structures. Military historian Peter Borton created clay-kicking, included a kicker with his kicking iron, a bagger, who passes lumps of clay back to a trimmer who passed it out of the tunnels.

S. S. Pawar (✉)
NVDA, Madhya Pradesh, India

C. N. V. Satyanarayana Reddy et al. (eds.), *Stability of Slopes and Underground Excavations*, Lecture Notes in Civil Engineering 185,
https://doi.org/10.1007/978-981-16-5601-9_19

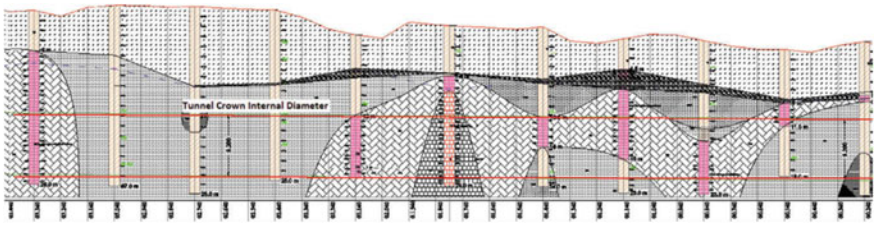

Fig. 1 Geological alignment of the tunnel

b. **Shotcrete**-Quick setting concrete is sprayed onto the bare rock immediately after excavation. It forms a preliminary tunnel liner.
c. **TBM**-A tunneling machine that has cutting teeth at its front. It creates the tunnel opening while passing the waste material through a rear.

3 Project Outline

On March 26, 2008, Narmada Valley Development Department, Bhopal, Madhya Pradesh, awarded the contract to build a tunnel in Sleemanabad Carrier Canal to M/S Patel Engineering (Senior Partner), SEW and Costal Project (Joint-Venture). The Executive Engineer, NDD DIV No-5, Katni was designated as the Project Owner and the date of completion was estimated to be on July 25, 2011. The design of the tunnel was vetted by Central Water Commission, New Delhi (Fig. 1 and Table 1).

4 Geotechnical Conditions

The geology along the tunnel alignment changes frequently. It consists of compact residual soils, silts, alluvium, highly weathered limestone and dolomite with stretches of slate, massive crystalline limestone and fresh marble. The strength of rock varies considerably with ultimate compressive strength values reaching as high as 180 M Pa. There is a highly permeable boulder horizon, which acts as a conduit for groundwater located 2–3 m above the tunnel for the initial 2.7 km of alignment.

In some instances, the transition zones extend between different geological conditions within 1.2 m, in some cases and in other cases the transition zone has extended for over 100 m. These lengthy transition zones result in different boring conditions due to the mixed-faced condition.

Table 1 Salient characteristics of the project

	Characteristic	Statistics
1	Cost of work	INR 799.00 Crores
2	Total length of canal under agreement	25.00 km (from 104 to 129 km)
3	Open + Cut and Cover portion	13 km (from 116 to 129 km)
4	Full supply discharge	152 cumecs
5	Canal bed width	12.2 km
6	Canal slopes-inner	1.5: 1
7	Canal slopes-outer	2: 1
8	Velocity	1.36 m/sec
9	Canal water depth	5.5 m
10	Tunnel-length	12 km (104–116 km)
11	Tunnel-diameter	10.00 m
12	Tunnel-cover	9.5–32.97 m
13	Tunnel invert level-at entry	387.95 m
14	Tunnel invert level-at exit	384.381 m
15	Tunnel slope	1:3352
16	Tunnel lining	Precast RCC M50-A20, Concrete mix designed from National Council for Cement and Building, Ballabhgarh
A	Cement	413 kg
B	Sand	728 kg
C	Metal	10 mm, 474 kg + 20 mm–710 kg
D	Flyash	75 kg
E	Gleshium	2.4 lit
F	Water	136 lit

5 TBM Selection

The geological report indicated that approximately 68% (8160 m) of the tunnel would be driven through residual soils, silts and highly weathered and decomposed rock with the remaining 32% (3840 m) being driven through competent rock. Bearing this in mind, a hybrid rock/EPB machine was considered for the project.

Approximately, 600 m of the anticipated 3840 m of competent rock was divided into numerous relatively short stretches. These short stretches would not have justified the downtime of one month required to remove the screw conveyor to install the belt conveyor and change from EPB into hard rock mode. However, over 3200 m of competent rock was made up of three stretches of 700, 1000, and 1500 m. The length of these stretches warranted the downtime required to convert from EPB to hard rock mode. Hence, a decision was taken to utilize a hybrid TBM. The construction

agency had drawn an agreement to take supply of EPB (TBM), Backup system, Cutting Tools, Spares, and Conveying system from Robbins.

5.1 Robbins

A reliable manufacturing company of the US, established in 1952, supplied the machines and technical assistance for Tunnel excavation of 1.0–19.2 m diameter.

Onsite assembly of TBM—The TBM was to be assembled at the location, rather than in a manufacturing facility. Critical subsystems, such as the electrical and hydraulic subsystem, were tested before being shipped to the jobsite. The work started on April 2, 2011 ().

6 TBM Technical Specifications

See Tables 2, 3, 4 and 5.

7 Project Launch

After the launch of the machine, the project suffered a multitude of commercial and technical problems. A comprehensive account of commercial problems is not in the scope of this paper. Nevertheless, it should be noted that it resulted in a number of

Table 2 Cutter head technical specifications [3]

	Characteristic	Specification
1	Nominal diameter	10.00 m with new cutter
2	Type	Mix face design
3	Number of disc cutter/knife bits	53

Table 3 Cutter head drive technical specifications

	Characteristic	Specification
1	Type	VFD Electric Motors (12 × 330 KW)
2	CHD Torque at 2.1 RPM	17,615 k Nm
3	CHD Torque at 5.4 RPM	6966 k Nm
4	Cutter head speed	0.54 RPM

Table 4 Main thrust technical specifications

	Characteristic	Specification
1	CHD thrust-EPB	23,731 kN
2	CHD thrust headwork	14,151 kN
3	Maximum propelling extension speed	100 mm/min

Table 5 Belt conveyor technical specifications

	Characteristic	Specification
1	Drive system	Hydraulic system
2	Capacity	1604 cubic m/min
3	Conveyor type	Screw conveyor
4	Screw diameter	1200 mm
5	Driven system	Hydraulic motors
6	Max torque	300 k Nm
7	Max speed	18 RPM

minor delays of up to a few weeks due to a shortage of spares, segments, consumables etc. They also resulted in the project being halted on two separate occasions for ten months and eight months, respectively (Fig. 2).

Fig. 2 Onsite assembly of TBM

7.1 Technical Problems

Failed Cutter head damage–Due to lack of cutter head interventions, the cutter head suffered wear damage to an extent that required repairs on three occasions. Because of low overburden and mix geological conditions, it was decided that excavation from the surface down to the TBM would be easier than creating a subsurface chamber to carry out the repairs. As neither shaft segment nor piling equipment was available at the site, heavy earth moving equipment was utilized for the canal work. The availability of this equipment made it possible to create an open-pit-type excavation.

The residual soils and alluvial material were relatively easy to excavate; however, their low cohesion called for a multi-level pit with several benches and involved the excavation of around 30,000 m^3 material. One of the problems faced during the excavation of the open pit was liquefaction caused by the saturated nature of the soil and vibration of the excavation equipment.

The three separate operations to repair the cutter head and backfilling of the pits resulted in a total delay of eight months.

Muck spillage–When boring in EPB mode, it is essential that a plug of material can be formed in the screw to the excavated material. The alignment of the tunnel up to 1600 m contained over 300 m of highly weathered or moderately weathered marble and slate, and 200 m of mixed face conditions where adequate quantities of fines along with the high water table and permeable geology caused problems in maintaining face pressure. This resulted in a relatively common issue of EPB. In this type of geology, due to the high pressure of water silt spills from the transfer point between the screw conveyor and TBM conveyor. The delays in manually cleaning the spillage amounted to almost 80% of working time.

Sink hole–A problem related to the failed cutter head interventions was sink holes appearing on the top portion of the machine. Several interventions were aborted up to 48 h. It became standard practice to reduce hyperbolic pressure to a min (approximately 0.9 bar) to reduce the amount of air losses, hence this also extended the duration of interventions. However, this sometimes resulted in water ingress steadily washing fines and silt into the cutter head chamber and around extrados of the TBM shields.

The section where sink holes occur is part of 95% of tunnel alignment that runs beneath agricultural land, so there was no risk to surface structures. Access to the land over the first 1.5 km of tunnel coat was relatively straightforward forward so earthmoving equipment was deployed to backfill the sink holes. Usually, after less than 24 h boring was able to continue.

Emission of Carbon Monoxide (CO)–The service team of cutter tools complained about the emission of CO. The Senior Scientist of Central Institute of Mines and Fuels, Dharwad, after site visit (07/01/2013) and testing of muck (strata available in contact of cutter head) and Chemical analysis of compressed air, denied the presence of CO. Although he advised to take general precautions during mining.

7.2 Project Back on Track

The technical paper '*Surang ki dusari taraf ujala*' by Pawar et al. [2] had the following recommendations to maximize tunnel activities, some of which were followed by the department:

1 Deploying another TBM at other ends (U/S side);
2 Construction of intermediate shaft;
3 Possibilities of cut-n-cover construction in patches of tunnel, where TBM is ineffective.

Deployment of another TBM–As a contingency measure, the construction agency did deploy another TBM (Herren Knecht [HK] Company Germany) at U/S end on 01/05/2016 and started tunneling from 21/06/2016. This HK TBM has completed 1893 m (1173 Ring) so far.

*Disposal plan of TBMs***-**An interim audit of diameter is proposed to be made at the place where both the TBMs would meet. The cutter heads would be pulled out by lift and backup systems would be returned back from subsequent ends.

Involvement of Robbins–The original scope for Robbins in the Sleemanabad Project included supply and commission of the TBM and tunnel conveyor, knowledge transfer as well as troubleshoot and resolve any technical problems with the equipment. In September 2017, due to the delayed progress of only 1600 m in 6.5 years, the project owner and senior JV partner decided to onboard Robbins fully as a subcontractor. Robbins' new scope of work covered all aspects of production operations including tunnel and surface works, supply of rails, pipes, cables, consumables, grout, electricity, and haulage of excavated material from the site. The supply of segments remained in the scope of the Senior JV partner.

A team was mobilized to begin refurbishment and testing of the TBM in September 2018. By the end of October 2018, the size of the team was increased to 180 people to enable the commencement of production operations.

Project Restart under supervision of Robbins–The measures taken to speed up the progress and mitigate frequent problems are listed below:

1. Reduction of air losses during interventions–Over the course of three interventions, weak-mix grout was pumped through the mixing chamber of the TBM and into the surrounding geology. On each occasion, air losses were minimized, and the interventions were completed. The grout mix design was modified as follows (Table 6).

   Rather than setting a limit, the actual volume of grout pressure was used to determine when sufficient grout has been pumped. The benchmark used was 0.3 bar above EPB pressure used during boring. Once this pressure was achieved, pumping was stopped for 15–20 min. If the pressure dropped by more than 0.2 bar over 20 minutes, grouting was recommenced until a steady pressure was achieved.

Table 6 Modified grout mix

	Element	Quantity
1	Design mix grout	Design mix /m^3
2	Cement	130 kg
3	Bentonite	50 kg
4	Water	820 lit
5	Retarder	2 lit
6	Sodium silicate	50 lit

2. Time consumed with weak-mix grouting methodology–The setting time for the weak mix is between 12 and 18 h depending on variables such as the amount of grout pumped, amount of groundwater present, temperature, etc. The time taken to pump the weak mix must also be reconsidered in the overall optima calculation. Additional time must also be factored in for cleaning the cutter head and changing cutters. There was no definite rule which was applied at Sleemnabad regarding whether or not to pump weak grout mix before an intervention because the geology changed too frequently. The Robbins staff decided to take an observational approach however, the overriding philosophy was 'If in doubt, pump weak-mix grout'. In the long term, this philosophy vastly reduced the overall average time spent in each intervention by reducing the amount of interventions that needed to be aborted. It also completely neglected the need for installing safe haven grout blocks from the surface.
3. Cutter tool and Cutter head damage–Reducing the amount of cutter changes automatically reduced the amount of downtime required for cutter head interventions and subsequently improved overall production rates. The total intervention time for replacing six cutters was at least 35 h, which equates to almost 6 h per cutter.

Identifying individual damaged cutters as soon as possible is essential. When one cutter gets blocked and stops rotating, it leads to a higher load on adjacent cutters, with a possibility of a cascading failure of all the cutters in the worst cases. Cascade wipe-outs can result in the damage to the cutter head and the damage can occur over the course of boring only after a couple of strokes. The problem with mix face excavation in constantly changing geology is that it is extremely difficult to predict cutter wear parameters. Robbins deployed the most experienced operators that were available to the project so that manual mistakes are avoided.

Another important factor in reducing cutter consumption was impact damage to the cutter discs in the mix face geology. Impact damage occurs when the cutter discs are rotating through relatively soft material before coming into contact with harder material. The magnitude of the impact is dependent on the speed of cutter head rotation and depth of penetration. The higher the percentage of soft material in mixed geology the higher the risk of damage to the cutter head. The maximum cutter travel speed is 30 m/min The depth of cutter penetration at the point of impact between soft and harder material is 8 mm.

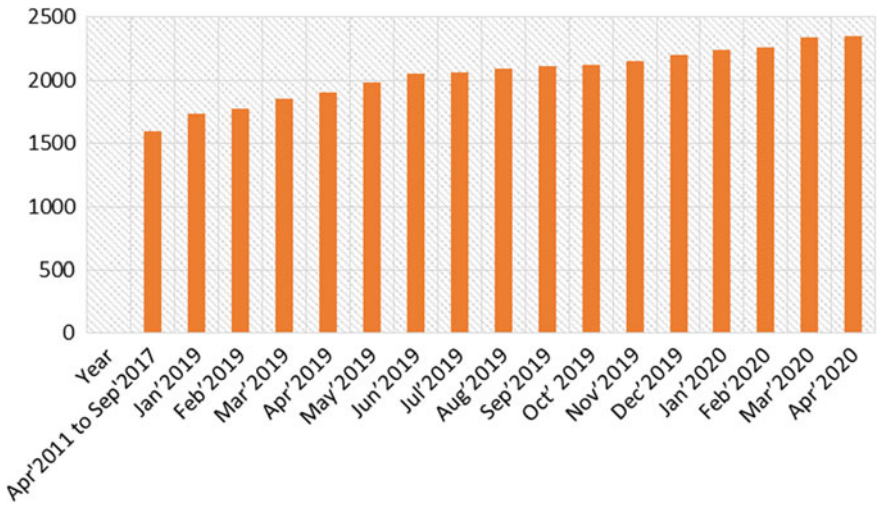

Fig. 3 Cumulative physical progress of work (in meters) at D/S end before and after Robins' involvement

In the Sleemanabad project, it had taken 6.5 years to complete just 1.6 km of tunnel. Even after deducting almost two years of stoppages due to commercial issues the average production rates in the remaining 4.5 years equate to less than 30 m/month. During the first six months after the restart, 463 m of boring was completed. Neither new technology nor additional equipment was deployed on the project. The principal reason for the improvement in production rates was the experience and skill set of the team that was mobilized (Fig. 3).

8 Diary of Tunnel Boring: Segment to Segment

Financial Progress during the agreement time period–114.72 crores (14.36%) (Fig. 4).

- First time extension for 29 months (26/03/2011 to 31/03/2013) granted.
- Work held up between 25/07/2011 to 31/07/2014 due to various technical and geotechnical issues.

Financial Progress during the first extension time period—60.71 crores (7.6%).

- Second time extension for 30 months (01/01/2014 to 30/06/2016) granted.
- 01/05/2016 Agency deployed another TBM (HK) at U/S.
- Robbins TBM breakdown from 06/08/2015 to 01/04/2017 due to commercial issues.

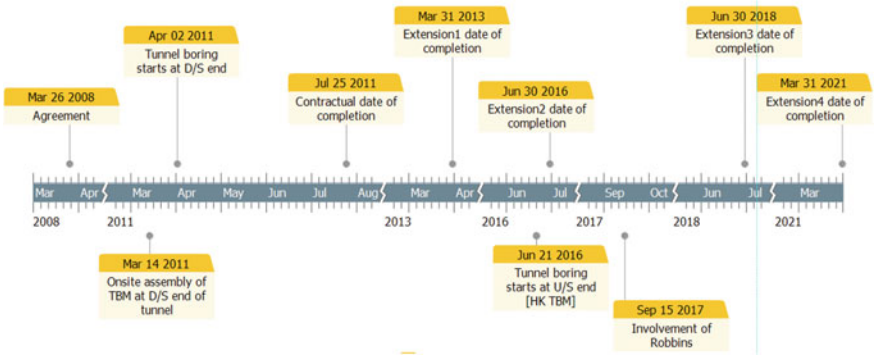

Fig. 4 High-level timeline of the work

Financial Progress during the second extension time period—18.62 crores (2.52%).

- Third time extension for 24 months (01/07/2016 to 30/06/2018) granted.
- 1/09/2018 Involvement of Robbins in supervision at D/S0.

  Financial Progress during the third extension time period—103.94 crores (13%).

- Fourth time extension for 30 months (01/07/2018 to 31/03/2021) granted.

  Financial Progress during 01/07/2018 to 30/06/2020—80.60 crores (10.08%).
  Overall Financial Progress since the beginning—78.59 crores (47.38%).
  Overall Physical Progress.
  At D/S (Robbins TBM) −3165 m.
  At U/S (HK TBM) −1893 m.
  Total Physical Progress −5058 m (42.31%).

9 Conclusion—Light at the End of a Dark Tunnel

In any project, a sufficient level of geological, geotechnical, and hydrogeological analysis of the terrain should be conducted before the work starts. In hindsight, it seems that the contractor had not performed the due diligence before betting with the Robbins TBM. Consequently, the contractor had to borrow experienced and skilled staff of Robbins as well as take drastic measures to deploy another [HK] TBM at the U/S side (Jabalpur end).

Treating the time to be the essence of the contract, the department (NVDA) has been regularly reviewing the progress and monitoring the delays, taking punitive actions such as issuing notices for the shortfall and imposing a penalty. There have been contingency measures as well such as extending the timeline till March 2021, and the department has also been mulling the proposal to go for cut-n-cover in virgin

patches of tunnel alignment at RD 106.700 km from where 152 cumecs water will be lifted to about 40 m. The proposal indicates that open-cut canal of length 5.5 km would be constructed at ground level. Water will be poured into this canal. Again water will be lowered to 27 m depth to join it with downstream side constructed tunnel. 59 MW power will be required for lifting out of which 27 MW will be generated from the canal itself. It is yet to be decided whether it would be done in the same agreement or new tender would be called after winding up the present contract.

The department and especially the state government has been hoping that the construction could be completed within the extended time period, else, the allotted quota of Narmada Water according to the Narmada Tribunal (up to the year 2024) will have to be forgone. The end goal is to serve the draught-prone area at the other end of the Sleemnabad tunnel and finally transfer water from Narmada Basin to Ganga Basin through Son Command.

That would also be a poetic closure to the story of Narmada (f.) and Son (m.), where the two estranged lovers would finally meet.

References

1. Katni, S.E.: Revised TEEP (pp. 1–5). Report No. 1, Narmada Valley Development Authority, Katni, Madhya Pradesh (2020)
2. Pawar, S.S.: Surang ki Dusari Taraf Ujala. Abhiyanta Bandhu, pp. 110–114. (2015)
3. Clark, J.: Challenging mixed face tunneling at India's Sleemanabad carrier canal. Retrieved from https://www.therobbinscompany.com/indias-sleemanabad-carrier-canal/ (2019). 16 July 2020

Static and Dynamic Assessment of Tunnel Rock Supports in Weak Rock

Jishnu Choudhury, Vineet Gajamer, Dhritilekha Deka, and S. Sreedeep

1 Introduction

Tunnel construction in rock is challenging as several factors, which are not readily visible comes into consideration for the design. Technological advancements along with empirical relations can help design safe and economic tunnel support. The unpredictable behavior in rocks due to the anisotropy and discontinuities requires an effective support system with reinforcements, lining, etc. to avoid huge losses and complexities [1]. The degree of anisotropy such as joints, faults, fissures, etc., strongly affects the mechanical performance of the rock mass [2]. The detection of rock mass disturbances near the tunnel face and the surrounding soil is compulsory to prepare a safe and reliable tunnel support design. The empirical relations obtained from the experience of several field experiments, establish the quantitative categories to classify these rock masses according to their properties such as RQD, RMR, GSI, RMi [3–5]. For an appropriate calculation with a more reliable result, numerical models can be utilized with various inputs from empirical relations to produce a meaningful knowledge about the ground conditions [6]. Both the methods are very much sensitive to the input parameters; hence they should be accurately and carefully measured [7].

Weak Rocks such as claystone, siltstone, coal, limestone, soft slate, shale have higher possibilities of squeezing and weathering as they are generally a transition between hard rocks and non-cohesive soils. A rock mass whose uniaxial compressive strength (generally less than 50 MPa) is less than one-third of the in-situ stress, is considered a weak rock [1].

Performance analysis of the support system in dynamic (seismic) loading in addition to static loading is necessary for a seismically vulnerable region. This paper

J. Choudhury (✉) · V. Gajamer · D. Deka · S. Sreedeep
Department of Civil Engineering, Indian Institute of Technology Guwahati, Guwahati 781039, India

C. N. V. Satyanarayana Reddy et al. (eds.), *Stability of Slopes and Underground Excavations*, Lecture Notes in Civil Engineering 185,
https://doi.org/10.1007/978-981-16-5601-9_20

aims to compare the performance tunnel for various support systems in weak rock concerning both static and dynamic loadings.

2 Empirical Approach

2.1 Rock Mass Classification

The purpose of rock mass classification is to develop a systematic way of describing and grouping rocks of similar behavior without any ambiguity and determine the support requirements for tunnels. The rock masses can be classified based on three major factors: (i) intact rock properties, (ii) discontinuity characteristics, (iii) boundary conditions. Several classification systems have been developed based on field investigations and experience. Some of the common classification systems are the Rock Mass Rating (RMR), Q-system, Geological Strength Index (GSI).

Barton et al. [8] proposed the Q-system of rock mass classification which can be calculated as follows:

$$Q = \frac{RQD}{Jn} * \frac{Jr}{Ja} * \frac{Jw}{SRF}$$

RQD = rock quality designation, J_n = joint set number, J_r = joint roughness number, J_a = joint alteration number, J_w = joint water reduction factor, and SRF = stress reduction factor.

The data reported in [9] is used for the analysis. As the detailed geotechnical study was not considered along tunnel alignment, the average Q value was obtained considering the minimum and maximum value of rock mass (Table 1).

From Fig. 1, support categories lie in the fourth region. Spacing of bolts = 1.5 m, Length of bolts = 3 m, Diameter of bolts = 1.9 cm, Thickness of shotcrete = 10 cm for Q = 0.785. For the given value of Q, rock mass lies in a very poor class [10].

Table 1 Estimation of average Q-value

Poor rock mass			Fair rock mass			Average Q
Parameter of Q	Rating	Q_{min}	Parameter of Q	Rating	Q_{max}	$(Q_{min} * Q_{max})^{1/2}$
RQD	35	0.38	RQD	65	1.625	0.785
J_n	91		J_n	4		
J_r	1		J_r	1		
J_a	2		J_a	2		
J_w	1		J_w	1		
SRF	5		SRF	5		

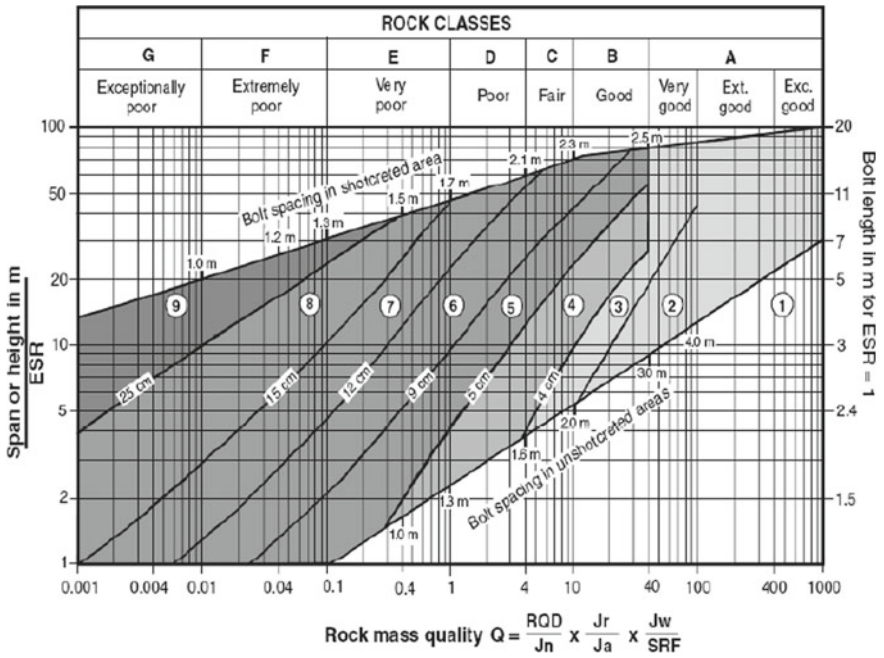

Fig. 1 Q chart for support requirement

3 Numerical Approach

The tunnel supports have been analyzed using Phase^2 9.0 [11], a 2D elasto-plastic finite element program capable of calculating stresses, displacements, yielded elements of the plastic zone in underground structures. Generally, the continuum model is utilized with a rock mass devoid of joints and equivalent Mohr–Coulomb failure criterion for such studies. But for this paper, analysis is performed on a discontinuum model with joints introduced by interface elements. Modeling of rock mass behavior is carried out considering it to be of a strain-softening case with the Generalized Hoek–Brown failure criteria. Half of the peak values of the strain-softening case are taken as residual parameters. Parameters used in the model are given in Tables 2 and 3 [9]. The mesh is discretized as 6-nodded triangular elements of 1413 number and it consists of 2991 nodes. Based on properties defined at each

Table 2 Details of rockbolt and shotcrete

Support system	Young's modulus (MPa)	Poisson's ratio	Tensile capacity residual (MN)
Shotcrete	30,000	0.2	–
Rockbolt	200,000	–	0.1

Table 3 Details of the rock mass properties

Type of rock	Sandstone
Unit weight (kN/m^3)	26.5
Young's modulus (MPa)	18,500
Poisson's ratio	0.14
Uniaxial compressive strength (MPa)	3.124
m_b	2.301
S	0.002
A	0.509
Residual m_b	1.1505
Residual s	0.001
Residual a	0.2545

node, Phase^2 solves the problem using the Gaussian elimination technique. Sigma 1 is the horizontal stress and Sigma 3 is the vertical stress for in-situ stress conditions. Stress field due to gravity exists in the in-situ stress condition. The proposed tunnel is inverted-D shaped of 3.5 * 3.5 m and located at 35 m depth. The set of joints at 60° inclination at 1 m spacing has been assumed. The geometry of the model is taken as 24.5 * 24.5 m. A comparative study among tunnel supports viz. unsupported, rock bolt, shotcrete, and combination of rockbolt and shotcrete are carried out for both static and dynamic loading. The stresses, total displacements, and yielded elements are obtained for the crown (A), walls (B & C), and invert (D) of the tunnel (Fig. 2).

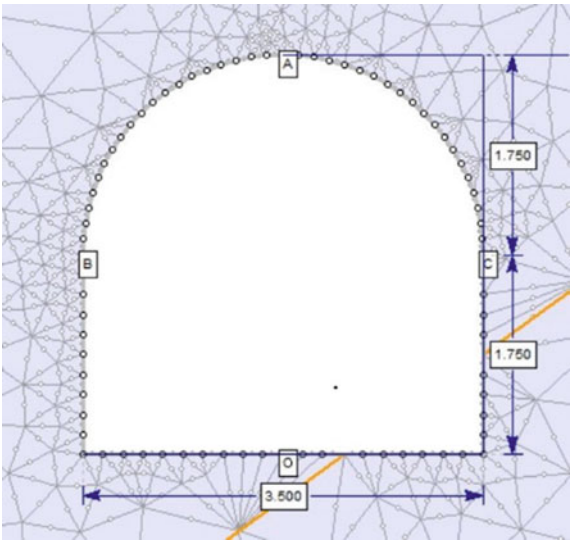

Fig. 2 Inverted-D shaped tunnel (all dimensions are in meters)

4 Static Analysis

For the static analysis using Phase^2, the stresses Sigma1, Sigma3, yielded elements, and the total displacements are mentioned in Table 4. Additionally, the results of the analysis are depicted in Figs. 3, 4, 5 and 6.

Induced stresses at invert are less than that of sidewalls and crown before and after support installation; however, total displacements at invert is higher. The negative minor principal stresses (tensile stresses) in unsupported condition has been corrected by the installation of supports. There has been a decrease in total displacement at all the concerned locations with the installation of supports, but no significant

Table 4 Summary of static analysis

Support system	σ_1 (MPa)		σ_3 (MPa)		Total displacement (mm)		Yielded elements
Unsupported	A	0.92	A	−0.04	A	0.7	508
	B	0.46	B	−0.04	B	0.98	
	C	0.23	C	−0.04	C	0.91	
	O	0	O	−0.11	O	1.33	
Rockbolt	A	0.61	A	0	A	0.63	502
	B	0.61	B	0	B	0.91	
	C	0.37	C	0	C	0.91	
	O	0.14	O	0	O	1.33	
Shotcrete	A	2.7	A	0.63	A	0.06	502
	B	0.74	B	0.1	B	0.72	
	C	0.46	C	−0.08	C	0.72	
	O	−0.1	O	−0.08	O	1.14	
Shotcrete + Rockbolt	A	2.75	A	0.55	A	0.06	443
	B	0.76	B	0.06	B	0.72	
	C	0.76	C	0.06	C	0.72	
	O	−0.1	O	−0.11	O	1.2	

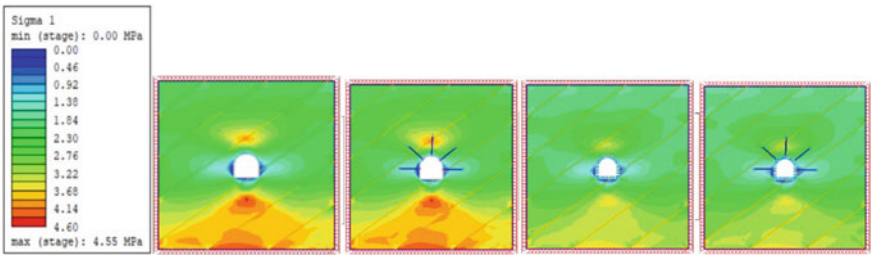

Fig. 3 Stress (σ_1) distribution before and after support installation

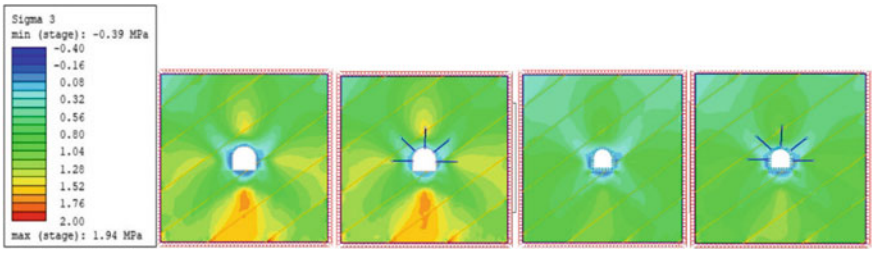

Fig. 4 Stress (σ_3) distribution before and after support installation

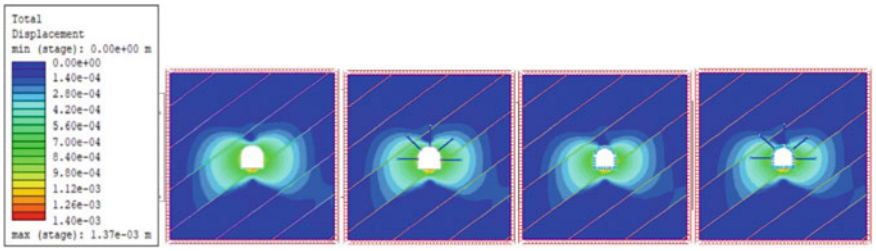

Fig. 5 Total displacement profile before and after support installation

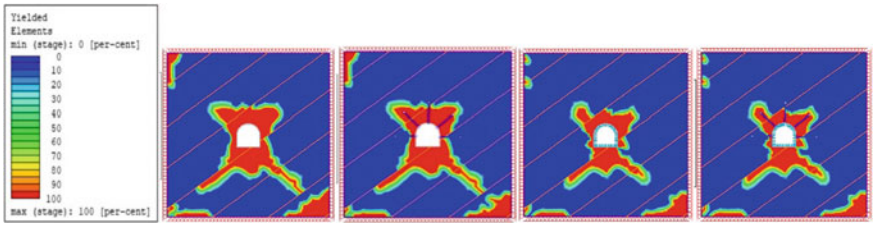

Fig. 6 Percentage of yielded mesh elements before and after support installation

change in displacement could be observed for support systems with shotcrete alone or combined shotcrete and rockbolt. The yielded elements have reduced from 508 to 443 on shotcrete application. The overall trend for the given gravity-induced stress conveys that the support from shotcrete alone can suffice for a weak rock for the mentioned properties.

5 Dynamic Analysis

5.1 Pseudo-Static Analysis

Pseudo static analysis has been performed considering horizontal seismic coefficient ($k_H = 0.3$) and downward vertical seismic coefficient ($k_V = 0.2$), which are within the typically exploited values. The vertical seismic coefficient is considered in the downward direction as it produces maximum stresses along the tunnel periphery when acting in the direction of gravity [12]. Seismic coefficients apply additional body force on each mesh. The stresses Sigma1, Sigma3, elements yielded from the plastic zone and the total displacements for the considered combination of supports and loading are extracted in Table 5 and are represented in Figs. 7, 8, 9 and 10.

Induced stresses at the crown are maximum before and after support installation. The total displacements on right side walls (C) are more as the direction of k_H is taken toward the right. There has been a decrease in total displacement at all the concerned locations with the installation of shotcrete or combined shotcrete and rockbolt. The yielded elements have reduced from 477 to 421 on shotcrete application. It has to be highlighted here similar to the previous case, shotcrete with given properties is sufficient to control displacements and yielded elements in the given weak rock exposed to pseudo-static loading.

Table 5 Summary of pseudo-static analysis

Support system	σ_1 (MPa)		σ_3 (MPa)		Total displacement (mm)		Yielded elements
Unsupported	A	1.7	A	0.38	A	0.315	477
	B	0.45	B	0	B	0.9	
	C	0.45	C	0	C	0.81	
	O	1.2	O	0.19	O	0.765	
Rockbolt	A	1.7	A	0.38	A	0.315	475
	B	0.45	B	0	B	0.855	
	C	0.45	C	0	C	0.81	
	O	1.2	O	0.19	O	0.765	
Shotcrete	A	3	A	0.76	A	0.08	421
	B	0.5	B	0	B	0.72	
	C	0.5	C	0	C	0.68	
	O	1.75	O	0.29	O	0.52	
Shotcrete + Rockbolt	A	2.75	A	0.67	A	0.08	440
	B	0.75	B	0	B	0.72	
	C	0.75	C	0	C	0.68	
	O	1.25	O	0.19	O	0.68	

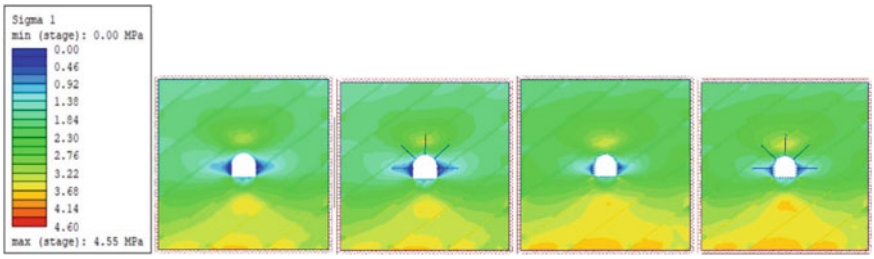

Fig. 7 Stress (σ_1) distribution before and after support installation

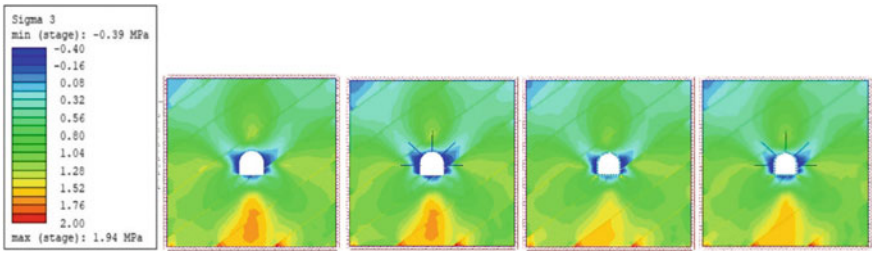

Fig. 8 Stress (σ_3) distribution before and after support installation

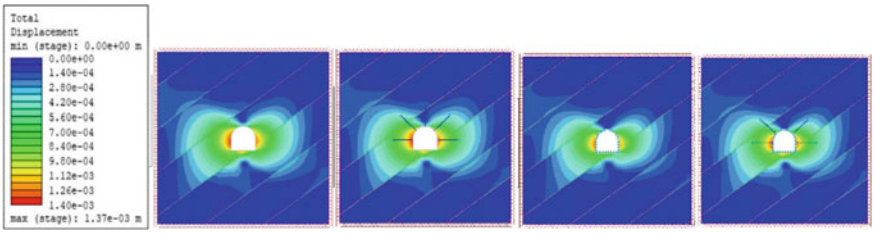

Fig. 9 Total displacement profile before and after support installation

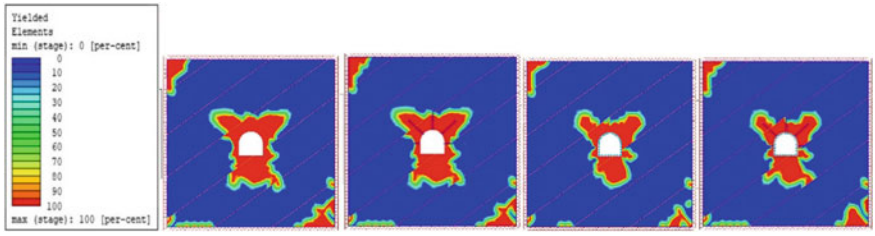

Fig. 10 Percentage of yielded mesh elements before and after support installation

5.2 Time Response Analysis

For the time response analysis, the data of the Nepal earthquake of the magnitude of Mw = 7.8 that occurred in the year 2015 is utilized. The acceleration time history has been shown in Figs. 11 and 12.

Dynamic analysis of the four different support systems has been done in two steps: undamped and damped. Earthquake loading is applied at the top of the model as time acceleration history. The viscous boundary condition at the base of the model is provided with an absorbent boundary such that the incoming pressure and shear waves effect is consumed. The vertical boundaries are set to transmit boundary conditions, ensuring no reflection of outgoing waves at these boundaries. After the completion of undamped dynamic analysis, the values of Rayleigh damping constants are adjusted to $\alpha_m = 0.0043$ and $\beta_k = 0.45$ to achieve a Rayleigh damping of 5%. Using the obtained values of the Rayleigh damping coefficient, damped dynamic analysis is performed again, the results of which are depicted in Figs. 13, 14, 15 and 16. The stresses Sigma1, Sigma3, yielded elements of the plastic zone, and the total

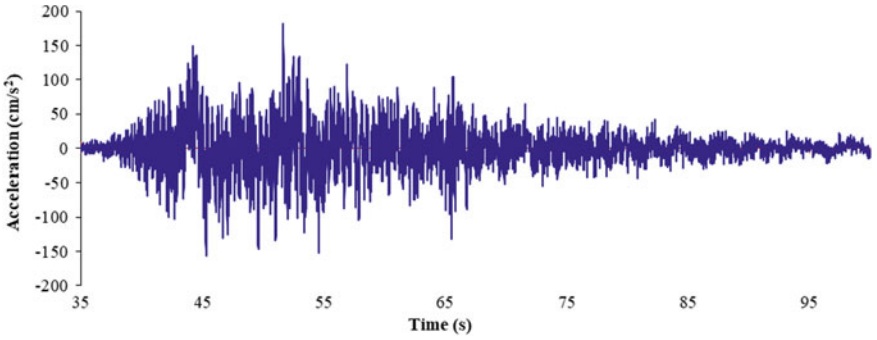

Fig. 11 The horizontal component of the acceleration time history of the Nepal earthquake, 2015 (*Source* USGS)

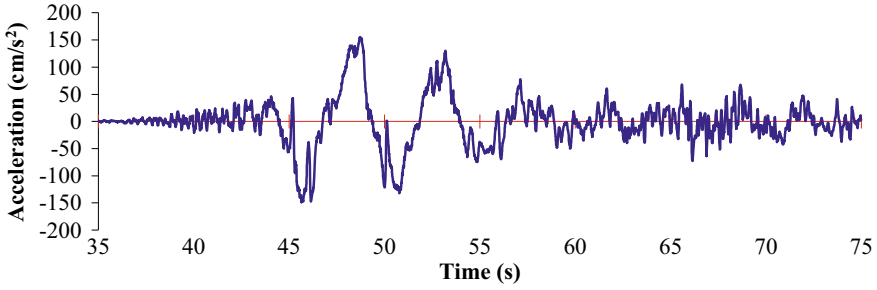

Fig. 12 The vertical component of the acceleration time history of the Nepal earthquake, 2015 (*Source* USGS)

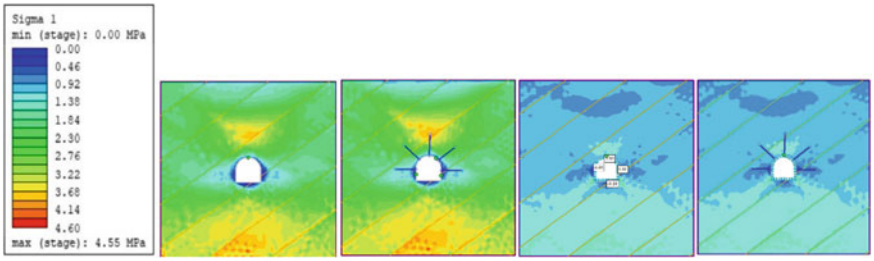

Fig. 13 Stress (σ_1) distribution before and after support installation

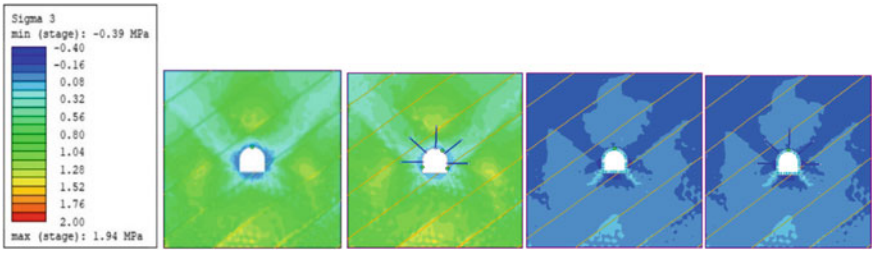

Fig. 14 Stress (σ_3) distribution before and after support installation

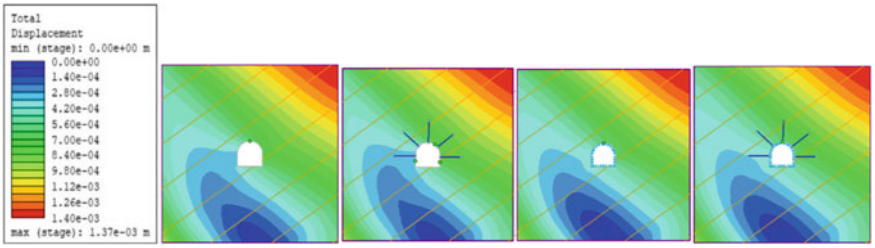

Fig. 15 Total displacement profile before and after support installation

displacements for the considered combination of supports and loading conditions are mentioned in Table 6.

Stresses at the crown have been maximum before and after support installation; however, displacements on the right-side walls (C) were more due to the nature of load application. The development of negative minor principal stresses is corrected on the installation of shotcrete alone, at the concerned locations. Displacements reported are considerably high in all the cases as all the elements of the model have yielded because of the strain accumulation due to dynamic loading. No specific trend in displacement could be observed before and after the installation of support. There has been a 100% yielding of plastic elements in all the cases. From the analysis

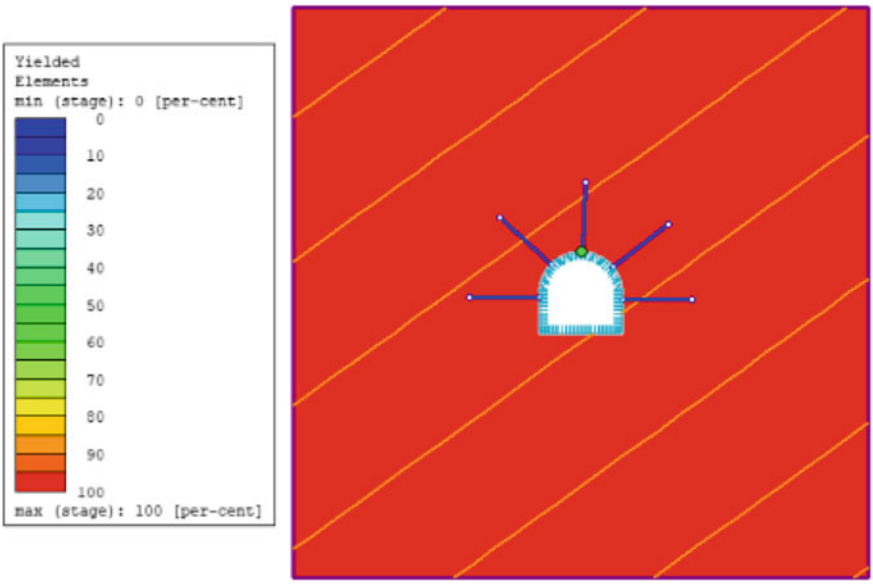

Fig. 16 Percentage of yielded mesh elements on rockbolt and shotcrete installation

Table 6 Summary of time response analysis

Support system	σ_1 (MPa)		σ_3 (MPa)		Total displacement (mm)		Yielded elements
Unsupported	A	0.77	A	−0.04	A	297	1305
	B	0.51	B	−0.04	B	165	
	C	0.51	C	−0.04	C	363	
	O	0.26	O	−0.04	O	231	
Rockbolt	A	0.68	A	−0.04	A	297	1305
	B	0.42	B	−0.04	B	165	
	C	0.42	C	−0.04	C	363	
	O	0.16	O	−0.04	O	231	
Shotcrete	A	3.8	A	1.6	A	306	1305
	B	2.2	B	0.95	B	204	
	C	0.6	C	0.3	C	306	
	O	−0.2	O	−0.35	O	204	
Shotcrete + Rockbolt	A	3.8	A	2.25	A	306	1305
	B	0.6	B	−0.35	B	204	
	C	0.6	C	−0.35	C	306	
	O	−0.2	O	−0.35	O	238	

below, it can be inferred that shotcrete can alone suffice as the optimum support condition for the given weak rock properties in time response analysis.

6 Conclusions

The weak rock mass was characterized by the geotechnical investigations reported in [9]. Based on values obtained from the empirical method (Q-system) of rock mass classification, numerical analysis using Phase^2 was performed for different loading conditions. The dis-continuum analysis provides a better insight into the rock mass behavior for any condition. The highly conservative results in the time response analysis are due to the high ground displacement amplitude considered for this model. Generally, the displacement variation is quite low in actual field conditions. Among the four support systems proposed in the paper for the loading conditions, shotcrete outperformed other support conditions in terms of stresses, displacements, and yielded elements. The analysis represents that, the safety of the structure is not directly related to the amount of support provided. The behavior of the rock mass, to any kind of support system, is entirely dependent on its properties. Therefore, a proper combination of the empirical and numerical methods can provide us with an estimation of the response of the rocks to the tunnel construction. Nevertheless, the validation of the observed results requires observational data from the field.

References

1. Hoek, E.: Tunnel support in weak rock. In: Proceedings of Reg. Keynote address, Symposium of Sedimentary Rock Engineering, pp. 20–22. Taipei, Taiwan (1998)
2. Cai, M., Horri, H.: A constitutive model of highly jointed rock mass. Mech. Mater. **13**(3), 217–246 (1992)
3. Koçkar, M.K., Akgün, H.: Methodology for tunnel and portal support design in mixed limestone, schist and phyllite conditions: a case study in Turkey. Int. J. Rock Mech. Min. Sci. **40**(2), 173–196 (2003)
4. Özsan, A., Başarır, H.: Support capacity estimation of a diversion tunnel in weak rock. Eng. Geol. **68**(3–4), 319–331 (2003)
5. Kaya, A., Bulut, F., Sayin, A.: Analysis of support requirements for a tunnel portal in weak rock: a case study from Turkey. Sci. Res. Essays **6**(31), 6566–6583 (2011)
6. Basarir, H., Ozsan, A., Karakus, M.: Analysis of support requirements for a shallow diversion tunnel at Guledar dam site Turkey. Eng. Geol. **81**(2), 131–145 (2005)
7. Basarir, H.: Engineering geological studies and tunnel support design at Sulakyurt dam site Turkey. Eng. Geol. **86**(4), 225–237 (2006)
8. Barton, N., Lien, R., Lunde, J.: Engineering classification of rock masses for the design of tunnel support. Rock Mech. **6**(4), 189–236 (1974)
9. Khadka, S.S., Maskey, R.K.: Stability analysis and design of rock support for tunnel and cavern of Kathmandu University Geo-Lab. J. Sci. Eng. Technol. **13**(I), 1–19 (2017)
10. Singh, B., Goel, R. K.: Tunneling in Weak Rocks, 5th edn. Elsevier Geo-Engineering Book Series (2006)

11. Phase2: A 2D finite element program for calculating stresses and estimating support around the underground excavations. In: Geomechanics Software and Research. RocScience Inc., Toronto, ON (2012)
12. Bhasin, R.: Effect of Earthquake on Rock Support in Tunnels. Tunneling Asia, New Delhi (2013)

Numerical Study on the Influence of In-Situ Stress Ratio on Stress and Deformation Characteristics of Rock Tunnel

T. Jegadeesh Kumar and M. Muttharam

1 Introduction

Rapid urbanization and economic development increase the usage of land. So, to reduce the traffic and for ease of transportation, tunnels are constructed nowadays. Tunneling in the rock is a complicated process. Rock at the depth was subjected to stress because of the weight of overlying strata, tectonic plate movements, soil erosion, construction of the building, etc., an excavation or opening in rock may disrupt the stress field new set of stresses are induced in the rock opening. The presence of joints or discontinuities also plays a significant role in the change of the in-situ stress ratio values. The presence of discontinuities may increase the risk of stability on the tunnel by creating more deformation [1, 2]. Knowledge and magnitude of in-situ stress and induced stress is an essential component in the rock tunneling. In-situ stress ratio is the ratio of the horizontal stress to the vertical stress. Stress values in the tunnel can be determined by various methods like Hydraulic fracturing, flat jack method, over coring, and under the coring method. The tunnel's size and shape also influence the tunnel's deformation characteristics, which with an increase in tunnel dimension, there is an increase in deformation of the tunnel [3]. Different shape of the tunnels is used based upon the needs. In this study, three different shapes of the tunnels are analyzed (circular, elliptical, and D shape [4]), and different in-situ stress ratios (0, 0.5, 1, 1.5, 2, 3) are considered. As it is difficult to perform an analytical study by creating models and applying stress values. Different methods can be adopted for analysis, they are the Coupled FEBEM method [5], Boundary Element Method [6] and displacement-based back analysis method [7] and some of the studies analyzed by using Finite Element Method. Among them, Finite Element method, analyzing the entire volume of the soil were as Boundary Element Method solves

T. Jegadeesh Kumar (✉) · M. Muttharam
Division of Soil Mechanics and Foundation Engineering, Civil Engineering Department, College of Engineering, Anna University, Guindy, Chennai 600025, India

C. N. V. Satyanarayana Reddy et al. (eds.), *Stability of Slopes and Underground Excavations*, Lecture Notes in Civil Engineering 185,
https://doi.org/10.1007/978-981-16-5601-9_21

only the unknowns of boundaries. So, this study has been performed numerically by using PLAXIS 3D finite element software. Two different models, Mohr–Coulomb and Hoek–Brown models are considered for the study. In Mohr–Coulomb, the soil parameters like cohesion and angle of internal friction are used. In Hoek–Brown, it incorporates both intact and discontinuities in rock, such as joints, Geological strength index, disturbance factor, etc.

2 Literature Review

Jha [8] analyzed the circular opening in which with the increase in in-situ stress ratio, deformation at the sidewall increases when $k > 1.5$ and also performed the analysis by increasing the size of the tunnel, with the increase in the size of excavation the deformation is large which varies linearly. **Zhang et al. [9]** studied the stress field distribution and deformation around the tunnel excavation in soft rock. The short bench construction method is used and shows that it effectively controls the deformation around the tunnel in the case of soft rock. **Meguid and Rowe** [10] analyzed the stability of D-shaped tunnel by using the Mohr–Coulomb model shows that at a high in-situ stress ratio, the deformation of the tunnel wall increases with the inward displacement of springline and upward displacement at the crown. **Zuo et al. [11]** undergone a case study in Baozhen tunnel Hubei china. The tunnel is analyzed using ADINA software. This shows that the tunnel's roof settlement becomes stable after a while due to the adjustment of stress and strain energy after the tunnel's excavation. **Srivastava** [12] analyzed single and interacting tunnel using the Finite Element method in which sequential excavation and simultaneous excavation have been undergone by considering rock as elastic and elastoplastic. Results obtained show that sequential excavation leads to more deformation when compared to simultaneous excavation. It may be because in sequential excavation tunnel bored on the left side influences the right side of the tunnel. The deformation at tunnel boundary at spring level on the pillar side is least for the elastic case compared to the elastoplastic case. Their difference is reflected more in the case of a smaller in-situ stress ratio 0.5. **Sing** [13] studied tunnel instability in the Bansagar region by using the Finite Element Method. Mohr–Coulomb's model is used for the analysis. The crown and bottom of the tunnel show more deformation compared to the tunnel's sidewall. Based on this study, the following methodology is adopted.

3 Methodology

The major part of the tunnel lies under the Earth as the tunneling work is done in different places for different stratigraphy for various purposes. The determination of stress and deformation around the tunnel is necessary. In this study, numerical analysis is performed using PLAXIS 3D, employing a 10-noded tetrahedral element.

Table 1 Dimensions for different shapes of the tunnel and model parameter

Shapes and Dimensions of the tunnel	Mohr–Coulomb model parameters	Hoek–Brown model parameters
Circular (8 m diameter)	Cohesion = 34.323 MPa Angle of internal friction = 50.57°	Intact Uniaxial Compressive Strength = 250 MPa Geological Strength Index = 95 Disturbance factor = 1 Intact modulus = 12000Mpa $m_i = 28$ $m_b = 19.591$ s = 0.4346 a = 0.5
Elliptical (8 m width and 6 m height)		
D shape (8 m width and 6 m height)		

In Chennai, the most abundantly present rock type is charnockite. So, charnockite rock is used for analysis. Rock considered here is intact, homogenous, and isotropic. The size for different shapes of the tunnel and model parameters are listed below (see Table 1). For which the mesh size is taken as 24 × 24 × 24 m. If the mesh size is two times the diameter, the stress and deformation overlapped up to the boundary. So, a mesh size of 3 times the diameter has been taken for analysis and tunnel is running toward the length of 24 m. Based on the literature study, the most commonly used model in literature is the Mohr–Coulomb model. In this study, Mohr–Coulomb and Hoek–Brown models are considered for analysis. The values are taken from the literature study done by Ademeso and Olaleye [14]. The Hoek–Brown criterion in a form that has been found practical in the field and that appears to provide the most reliable set of results for use as input for methods of analysis in current use in rock engineering.

Where m_b, s, and a are Hook and Brown constants. Different in-situ stress ratio values are considered for analysis by using two different models for each shape of the tunnel. The models are compared based on the stress and deformation values to understand which model shows more deformation and stress.

4 Results and Discussion

Deformation and stress values for different shapes and different in-situ stress ratio values are determined by considering two different models using PLAXIS 3D finite element software. A model of 24 × 24 × 24 m is created in the PLAXIS in which lining is not provided to get the exact deformation around the tunnel. The results obtained are plotted in the form of a graph to show the influence of the in-situ stress ratio in the rock tunnel's stress and deformation characteristics.

4.1 Mohr–Coulomb Model

Three different shapes of the tunnel are analyzed with different in-situ stress ratio values. The results obtained are discussed below with the graph for different shapes of the tunnel.

Circular Tunnel. A circular tunnel of 8 m diameter is simulated in the PLAXIS (see Fig. 1). The deformation and stress values for the different in-situ stress ratio values of the circular tunnel are plotted in the form of a graph to clearly show the influence of the in-situ stress ratio on stress and deformation characteristics of the tunnel. The graph plotted between displacement versus in-situ stress ratio shows that, for in-situ stress ratio values 0–1, the deformation in the vertical direction is more (i.e., displacement in the z-direction), and for in-situ stress ratio values 1–3, the deformation is more in horizontal direction (i.e., displacement in the x-direction) (see Fig. 2). When vertical stress is high, the deformation at the crown and bottom increases. But when horizontal stress increases, the deformation at the sidewall of the tunnel get increases.

When the in-situ stress ratio value is 0, a plastic zone is formed at the tunnel's sidewall, and with an increase in horizontal stress, the plastic zone moves toward the crown of the tunnel.

The graph plotted between radial stress and radial distance (from the center of the tunnel) shows that the radial stress is more in sidewall when the in-situ stress ratio is 0, and radial stress at the roof is more when the in-situ stress ratio is 3. It shows that radial stress increases with an increase in the radius of influence, but the radial stress at the tunnel boundary is zero (see Figs. 3 and 4). The graph plotted between

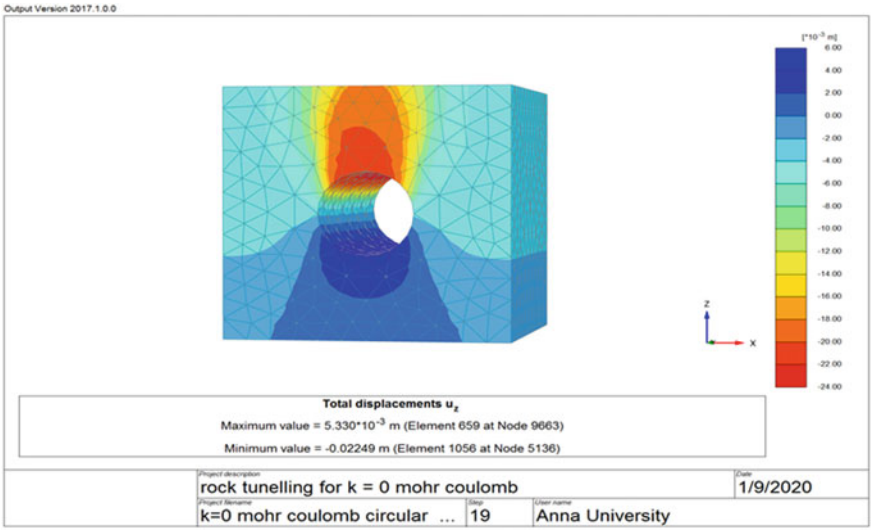

Fig. 1 Total displacement in the z-direction of the circular tunnel for $k = 0$

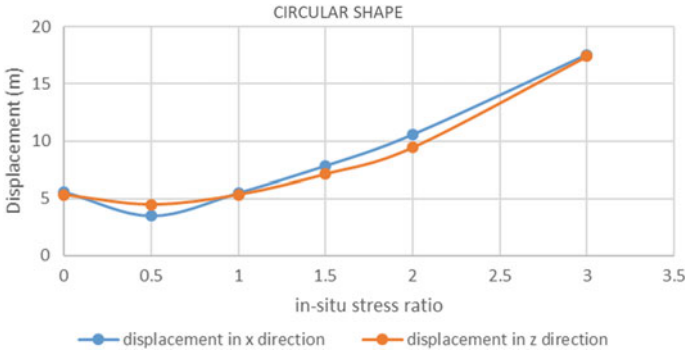

Fig. 2 Displacement versus in-situ stress ratio for circular tunnel

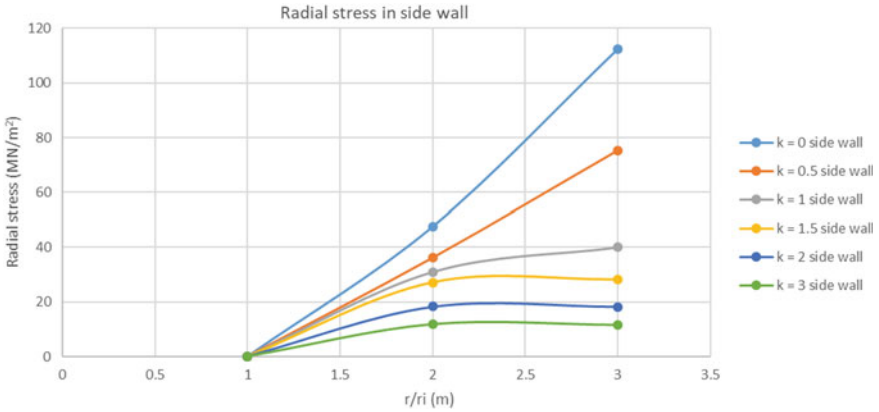

Fig. 3 Radial stress at side wall versus Radial distance (r/r_i) for the circular tunnel

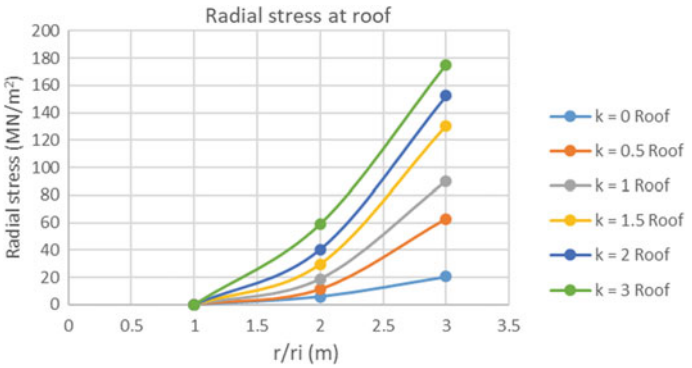

Fig. 4 Radial stress at roof versus Radial distance (r/r_i) for the circular tunnel

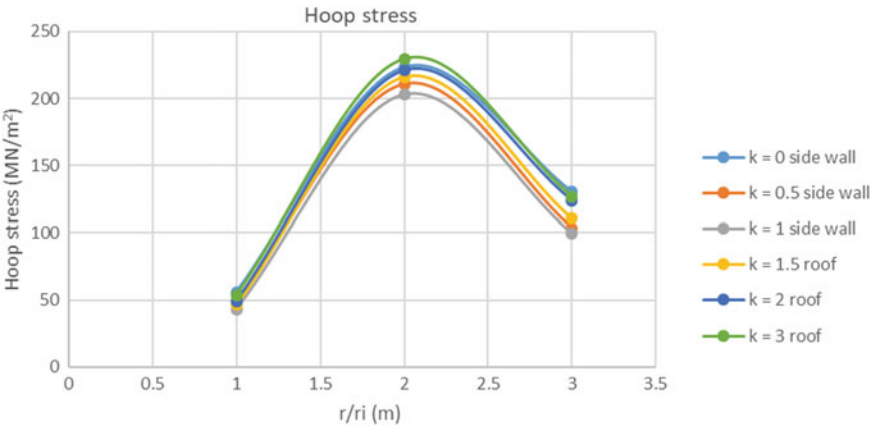

Fig. 5 Hoop stress versus Radial distance (r/r_i) for the circular tunnel in Mohr Coulomb

hoop stress and radial distance shows that hoop stress is maximum in sidewall when the in-situ stress ratio lies from 0 to 1, and it is maximum at the roof when the in-situ stress ratio value lies from 1.5 to 3. When comparing hoop stress and radial stress, hoop stress is a major stress that has high-stress values than radial stress.

The hoop stress rises to the distance of 2 times the diameter, and then it gets decreased (see Fig. 5). Where r is the radius of influence, r_i is the tunnel radius, and k is the in-situ stress ratio represented in the graph. Radial stress and hoop stress increase with the increase in the radius of influence because when the radius is equal to the plastic zone radius, the hoop stress reaches the maximum. As radial stress increases with an increase in radius, but the increase rate gradually decreases. Finally, both approach the value of in-situ stress.

Elliptical Tunnel. Elliptical tunnel of width 8 m and height 6 m is simulated in PLAXIS (see Fig. 6). The graph plotted between displacement, and in-situ stress ratio shows the same displacement pattern as that of the circular tunnel (see Fig. 7). But when compared to the circular shape, displacement is more in the case of elliptical shape because of the height to width ratio. As the tunnel (8 m) width is more than the height (6 m), the deformation is more vertical. Graphs plotted between radial stress versus radial distance (from the center of the tunnel) and hoop stress versus radial distance follow the same pattern as that of the circular tunnel. But the stress values are high when compared to the circular tunnel.

D-Shaped Tunnel. D-shaped tunnel of 8 m width and 6 m height is simulated in the PLAXIS (see Fig. 8). The graphs show the same variations as that of the circular and elliptical tunnel. But due to the corner effect, deformation in the x-direction is less than the deformation in the z-direction for an increase in the in-situ stress ratio (see Fig. 9). Graphs plotted between radial stress versus radial distance (from the center of the tunnel) and hoop stress versus radial distance show the same pattern as that of

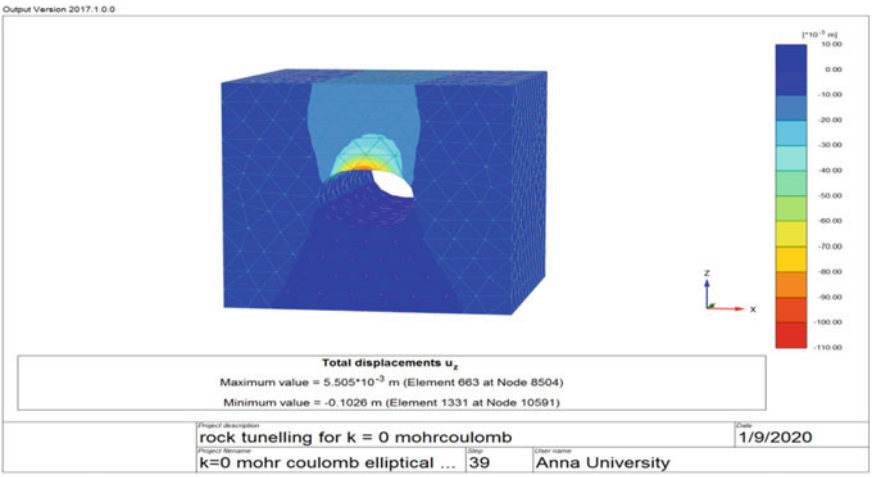

Fig. 6 Total displacement in the z-direction of the elliptical tunnel for $k = 0$

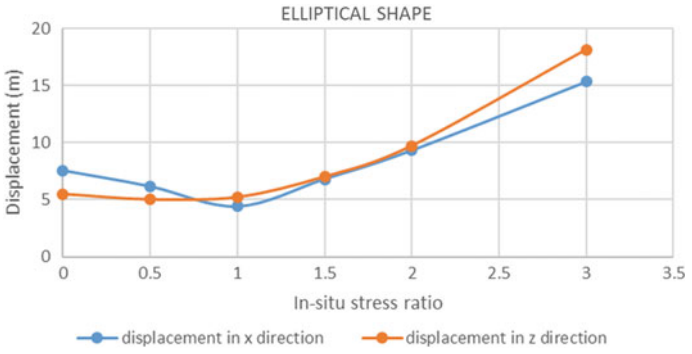

Fig. 7 Displacement versus in-situ stress ratio for the elliptical tunnel

the circular and elliptical tunnel. But the stress concentration at the sharp edge of the D shape is high, and with an increase in horizontal stress, the stress concentration effect also increases.

4.2 Hoek–Brown Model

In the Hoek–Brown model, the tunnel's size and shape are the same as that of the Mohr–Coulomb model, but parameters for analysis are different. Hoek–Brown criterion includes the rock mass properties like GSI, Disturbance factor, etc.

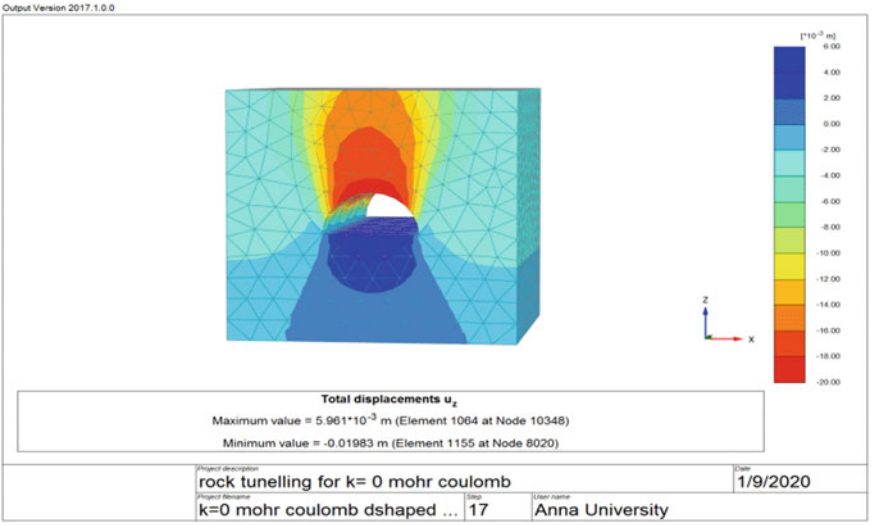

Fig. 8 Total displacement in the z-direction of the D-shaped tunnel for $k = 0$

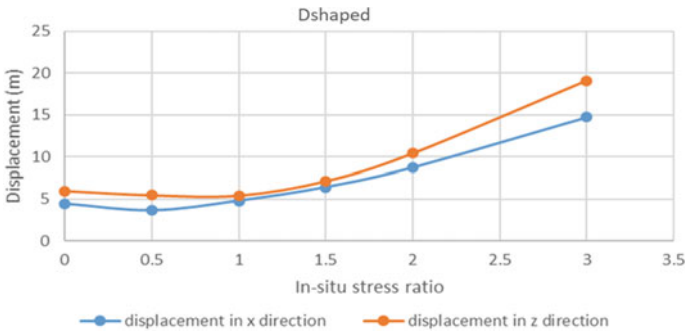

Fig. 9 Displacement versus in-situ stress ratio for the D-shaped tunnel

Circular Tunnel. A circular tunnel of 8 m diameter is simulated in PLAXIS. The graph plotted between displacement and in-situ stress ratio shows the same deformation pattern as that of the Mohr–Coulomb Circular tunnel. But the deformation values obtained are different. For the in-situ stress ratio value 0, the displacement in the vertical direction for Hoek–Brown is 65.9 mm, and for Mohr–Coulomb, it is 5.55 mm.

Mohr–Coulomb gives more conservative results because the strength envelope for the Hook–Brown model is not a straight line. It curves down. Whereas in Mohr–Coulomb, it is a straight line. The radial and hoop stress versus radial distance pattern for Hoek–Brown also shows the same way as that of the Mohr–Coulomb, but the stress values obtained are high in the case of Hoek–Brown. The graph plotted between radial stress and radial distance (from the center of the tunnel) shows the influence of stress in x and z-direction. The graph plotted between hoop stress and radial distance

shows that up to two times the tunnel's diameter, the hoop stress value increases, and then it decreases (see Figs. 10, 11 and 12). Where r is the radius of influence, r_i is the tunnel radius, and k is the in-situ stress ratio. Radial stress and hoop stress increase with the radius's increase. when the radius is equal to the plastic zone radius. The hoop stress reaches the maximum and then begins to decline as radial stress increases with an increase in radius, but the increase rate gradually decreases. Finally, both approach the value of in-situ stress.

Elliptical Tunnel. Elliptical tunnel of width 8 m and height 6 m is simulated in PLAXIS. The graph plotted between displacement and in-situ stress ratio shows the same deformation pattern as that of Mohr–Coulomb's deformation, and the values are different. The deformation or displacement in the Hoek–Brown and Mohr–Coulomb model's vertical direction is 78.07 mm and 5.88 mm, respectively, for in-situ stress ratio 0. The graph plotted between radial stress versus radial distance (from the center of the tunnel) and hoop stress versus radial distance follows the same pattern as that of Mohr–Coulomb but compared to the stress values of Mohr–Coulomb, Hoek–Brown stress values are higher.

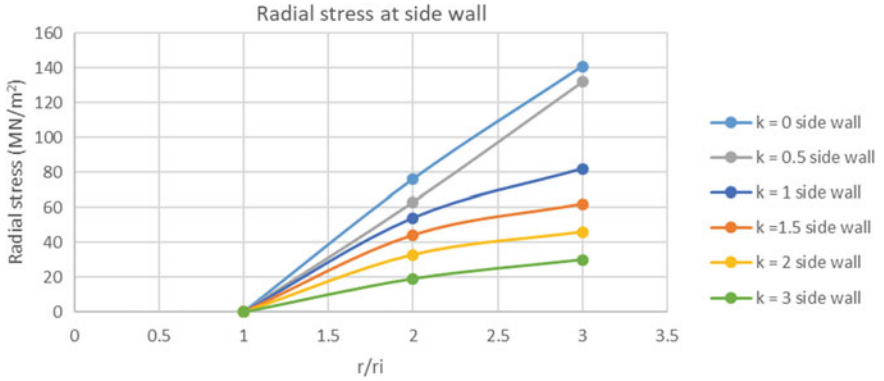

Fig. 10 Radial stress at side wall versus Radial distance (r/r_i) for the circular tunnel

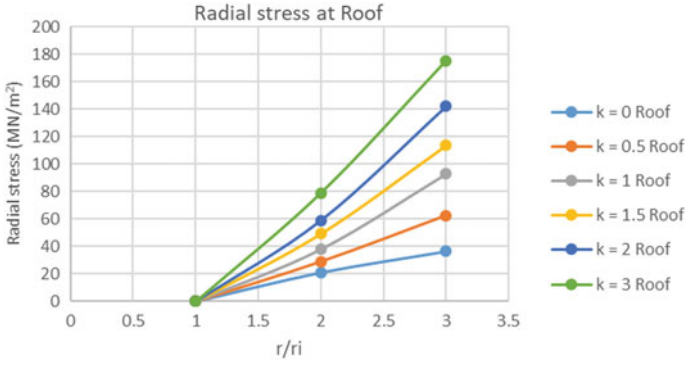

Fig. 11 Radial stress at roof versus Radial distance (r/r_i) for the circular tunnel

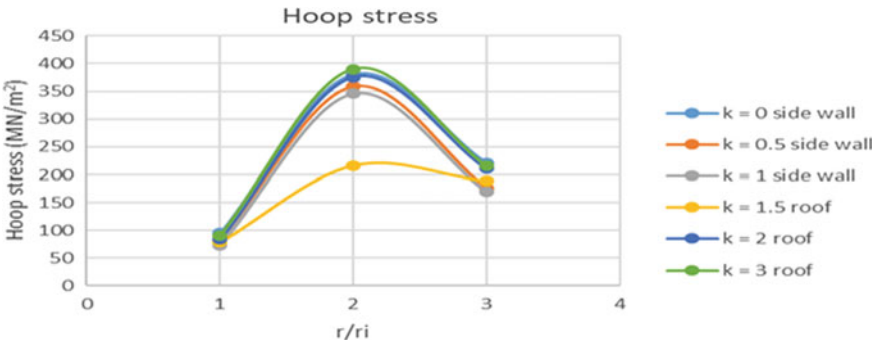

Fig. 12 Hoop stress versus Radial distance (r/r_i) for the circular tunnel in Hoek–Brown

D-Shaped Tunnel. D-shaped tunnel of width 8 m and height 6 m is simulated in PLAXIS. The graph plotted between displacement and in-situ stress ratio shows the same pattern as that of Mohr–Coulomb, but the deformation values are different. The displacement in the vertical direction for Mohr–Coulomb and Hoek–Brown is 6.24 mm and 75.20 mm, respectively. The graph plotted between radial stress versus radial distance (from the center of the tunnel) and hoop stress versus radial distance follows the same pattern as that of Mohr–Coulomb, but when compared to the stress values of Mohr–Coulomb, Hoek–Brown stress values are higher.

Total Displacement. For the in-situ stress ratio 0, the total displacement for the elliptical, circular, and D-shaped tunnel is 138.3 mm, 24.12 mm, and 21.35 mm, respectively shows that deformation is more for elliptical tunnel because of the width to height ratio of the tunnel. When comparing the total displacement of Mohr–Coulomb and Hoek–Brown, the total displacement is more in the case of Hoek–Brown. For the circular tunnel, the total displacement for in-situ stress ratio 0 for Mohr–Coulomb and Hoek–Brown is 24.12 and 76.81 mm. The difference in the displacement values is 68.5%. For elliptical shape, the displacement values of Mohr–Coulomb and Hoek–Brown for the in-situ stress ratio 0 are 138.3 mm and 150.3 mm, respectively. For the D-shaped tunnel, the displacement values for Mohr–Coulomb and Hoek–Brown for in-situ stress ratio value 0 are 21.3 mm and 105.3 mm, respectively. It is clear from the graph that the Hoek–Brown model shows more deformation than that of the Mohr–Coulomb model (see Fig. 13).

5 Conclusions

The following conclusions were made by analyzing the above variations like different in-situ stress ratio values for different tunnel shapes by using different models.

1. Mohr–Coulomb's results for deformation give conservative results when compared to Hoek–Brown results. Because the strength envelope is not a straight

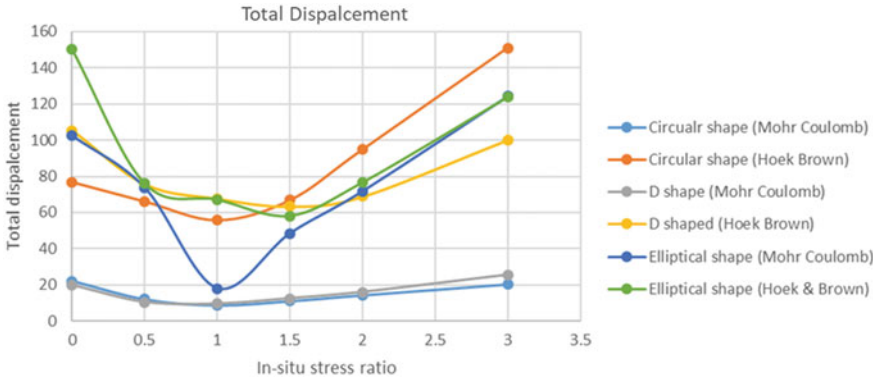

Fig. 13 Total displacement versus in-situ stress ratio

line in the case of the Hoek–Brown model. It curves down, so it gives a low strength estimate than the Mohr–Coulomb model.

2. The results obtained clearly show that with increased in-situ stress ratio, the deformation in vertical direction decreases, and horizontal direction increases. This is because, with an increase in horizontal stress, the deformation in vertical direction decreases.
3. The total displacement is maximum in the case of an elliptical tunnel. If there is a need to provide an elliptical tunnel, a proper support system like bolt grouting support can be provided. The elliptical shape shows more deformation due to height to width ratio as the tunnel's width is more when compared to the height, the deformation in the vertical direction is high when vertical stress is high.
4. D-shaped tunnel suffers high-stress concentration at their sharp bent edges, i.e., critical stress concentrations increase as the boundary's relative radius of curvature decreases. Openings with sharp corners should therefore be avoided.
5. The proper support system for the tunnel which has high deformation and stress values can also be determined with the help of the Ground Response Curve.

References

1. Keykha, H.A., Huat, B.B.K., Asadi, A., Moayedi, H.: The effect of discontinuities on stability of rock blocks in tunnel. Int. J. Phys. Sci. **6**(1) (2011)
2. Zhu, Z., Li, Y., Xie, J., Liu, B.: The Effect of Principal Stress Orientation on Tunnel Stability. Tunneling and Underground Space Technology, China (2015)
3. Lollino, G., Davie, C.T., Okogbue, C.O.: Numerical analysis of the influence of tunnel dimensions on stress and deformation around tunnels. In: Rocks Engineering Geology for Society and Territory, vol. 6 (2015)
4. Srivastava, R.K., Sharma. K.G., Varadarajan, A.: Elasto-plastic finite element analysis of Horse-Shoe Tunnels. Indian Geotech. J. **17**(2), 159–182 (1987)

5. Singh, R.B.: Coupled FEBEM analysis of underground openings. Ph.D. Thesis submitted to Indian Institute of Technology, Delhi, India (1985)
6. Varadarajan, A., Sharma, K.G., Singh, R.B.: Analysis of tunnels by boundary element method. Indian Geotech. J. 249–268 (1983)
7. Zhang, L.Q., Yue, Z.Q., Yang, Z.F., Qi, J.X., Liu, F.C.: A displacement based back-analysis method for rock mass modulus and horizontal in situ stress in tunneling—illustrated with a case study. In: Tunneling and Underground Space Technology, pp. 636–649 (2006)
8. Jha, A.K.: Elasto-plastic analysis of circular openings for underground excavation in Hoek–Brown and Mohr-Coulomb criteria. Thesis of Department of Geotechnical Engineering, Institute of Engineering, Pulchowk Campus, Tribhuvan University, Nepal (2013)
9. Zhang, H., Chen, L., Zhu, Y., Zhou, Z., Chen, S.: Stress field distribution and deformation law of large deformation tunnel excavation in soft rock mass. Thesis on Appl. Sci. (2019)
10. Meguid, M.A., Rowe, R.K.: Stability of D-shaped tunnels in a Mohr–Coulomb material under anisotropic stress conditions. Published on the NRC Research Press Website (2006)
11. Zuo, Q., Wu, L., Adoko, A.C., Lu, Z.: Analysis of surrounding rock mass deformation characteristics: case study of BaoZhen Tunnel, Hubei China. Art. Electron. J. Geotech. Eng. China (2012)
12. Srivastava, R.K.: Elasto-plastic finite element analysis of single and interacting tunnels. Ph.D. Thesis submitted to Indian Institute of Technology Delhi, India (1985)
13. Singh, T.N.: Assessment of tunnel instability—a numerical approach. Department of Earth Science, Indian Institute OF Technology, Bombay. Arab. J. Geosci. 181–192 (2009)
14. Ademeso, O.A., Olaleye, B.M.: Physicomechanical characteristics of charnockitic rock of Akure, Southwest Nigeria. Gen. Sci. Res. **2**(1), 31–37 (2014)

Active Earth Pressure Distribution Against Braced Wall Considering Arching Effects

Kingshuk Dan and Ramendu Bikash Sahu

1 Introduction

Adequate prediction of active earth pressure is major design consideration of retaining structure. Distribution of earth pressure is practically non-linear depending on mode of wall movement, friction mobilization between soil and wall, wall rigidity, spacing of lateral support, etc. Thus consideration of arching during estimation of earth pressure against retaining wall is necessary. Various researchers proposed formulations of earth pressure distribution behind wall considering translational or rotational movement of wall [1–4]. But very limited works have been done for braced excavation. In present study, a formulation for calculating active earth pressure on a braced wall is proposed considering arching effects where effect of cohesion, angle of wall friction, angle of shearing resistance are taken into account. In order to validate, results obtained from proposed method are compared with the existing field values of three case studies reported by Som [5], Goh et al. [6], Liu et al. [7].

In the present study, translation along with rotation of wall about top for above cut level is assumed while in below cut level it is taken that wall rotates about its base. Considering all these types of yielding a planar slip surface making an angle of $(45° + \phi/2)$ with horizontal is assumed. Movement of ground surfaced is assumed to be spandrel type which is because considerable amount of wall deflection occurs before installing strut. Below cut level maximum vertical ground movement is assumed to occur at some distance from wall (Fig. 1).

K. Dan (✉)
Coochbehar Government Engineering College, Coochbehar, West Bengal 736170, India

R. Bikash Sahu
Jadavpur University, Jadavpur, Kolkata, West Bengal 700032, India

C. N. V. Satyanarayana Reddy et al. (eds.), *Stability of Slopes and Underground Excavations*, Lecture Notes in Civil Engineering 185,
https://doi.org/10.1007/978-981-16-5601-9_22

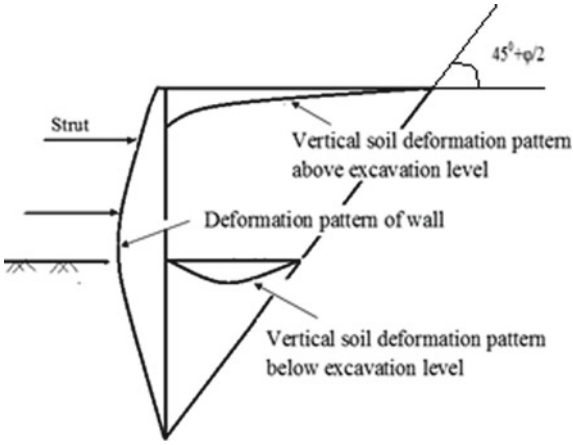

Fig. 1 Slip surface and soil deformation pattern

2 Theoretical Study

Above cut level an arc of a circle of convex type is taken into consideration. Here slip plane makes an angle of $(45° + \phi/2)$ with the minor principal stress at the right edge of the element. Major Principal Plane makes an angle of 'ψ' with horizontal, where, 'ψ' varies from 0 at right edge to 'θ' at left edge (Fig. 2).

From force equilibrium, at any point on arch it can be written as

$$\sigma_h = \sigma_3 \cos^2 \psi + \sigma_1 \sin^2 \psi \tag{1}$$

For calculation of 'θ', Mohr circle for stresses of soil element at edge of wall is considered (Fig. 3)

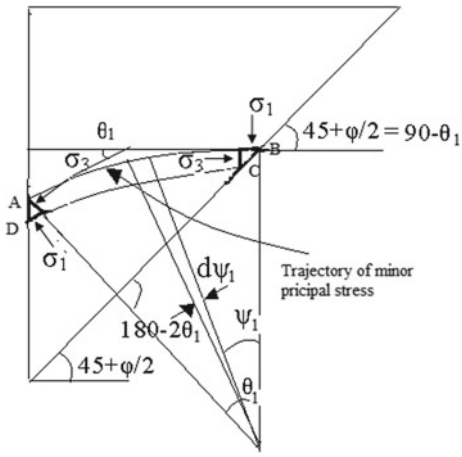

Fig. 2 Stress distribution on differential soil element

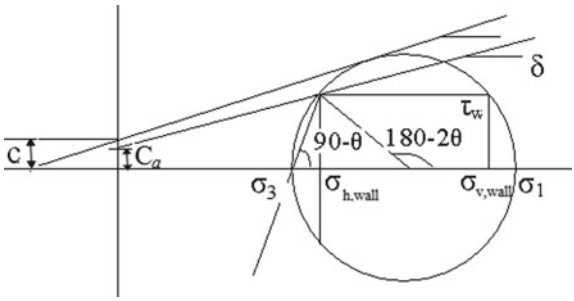

Fig. 3 Mohr circle for stresses at wall

$$\tau_w = C_a + \sigma_{h,\text{wall}} \tan\delta = \left(\sigma_{h,\text{wall}} - \sigma_3\right) \tan(90 - \theta) \tag{2}$$

Here '*Ca*' is adhesion of soil with wall which can be obtained from expression. Here, '*a*' is adhesion factor.

$$C_a = a \times c \tag{3}$$

Equation (2) can be further reduced as

$$\tan(90^\circ - \theta) = \frac{\left(\sigma_{h,\text{wall}}/\sigma_3\right) \tan\delta + (C_a/\sigma_3)}{\left(\sigma_{h,\text{wall}}/\sigma_3\right) - 1} \tag{4}$$

The expression of 'θ' can be written as

$$\theta = \tan^{-1}\left[\frac{(N-1) \pm \sqrt{\left[(N-1)^2 - 4(m + \tan\delta)(m + N\tan\delta\right]}}{2(m + N\tan\delta)}\right] \tag{5}$$

where, $m = \frac{C_a}{\sigma_3}$ and 'N' is the ratio of major and minor principal stress.

Average vertical stress over a differential element 'ABCD' at a depth 'Z' below ground surface as shown in Fig. 2 will be

$$\begin{aligned}\overline{\sigma}_v &= \frac{F}{B_Z} = \frac{1}{B_Z}\int_0^\theta dF = \frac{1}{B_Z}\int_0^\theta \sigma_v dA \\ &= \frac{1}{R\sin\theta}\int_0^\theta \sigma_1\left(\cos^2\psi + \frac{1}{N}\sin^2\psi\right) Rd\psi\cos\psi\end{aligned} \tag{6}$$

Integrating Eq. (6) yields

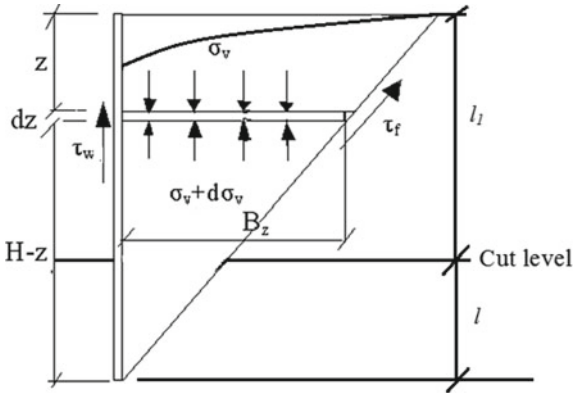

Fig. 4 Free body diagram of differential soil element

$$\overline{\sigma}_v = \sigma_1\left[\frac{3N+1}{4N} + \frac{N-1}{12N}\left(3 - 4\sin^2\theta\right)\right] \tag{7}$$

Active earth pressure co-efficient at the wall will be

$$K_{\text{wall}} = \frac{\sigma_{h,\text{wall}}}{\overline{\sigma}_v} = \frac{(1/N)\cos^2\theta + \sin^2\theta}{\left(\frac{3N+1}{4N}\right) + \frac{N-1}{12N}(3 - 4\sin^2\theta)} \tag{8}$$

From the stresses acting on differential element of 'dZ' behind braced wall (Fig. 4) force equilibrium is established in vertical direction.

$$d\overline{\sigma}_v B_Z = dZ(\gamma B_Z - (C_a + \overline{\sigma}_v K_{\text{wall}} \tan\delta)) \tag{9}$$

Solving Eq. (9) the expression of average vertical stress will be

$$\begin{aligned}\overline{\sigma}_v K_{\text{wall}} \tan\delta(\tan\alpha \tan\delta K_{\text{wall}} - 1) &= (aC_0 + aC_1H)(\tan\alpha \tan\delta K_{\text{wall}} - 1)\left[\left(1 - \frac{Z}{H}\right)^{\tan\alpha \tan\delta K_{\text{wall}}} - 1\right] \\ &+ (aC_1 \tan\alpha - \gamma)\tan\delta K_{\text{wall}}\left[H\left(1 - \frac{Z}{H}\right)^{\tan\alpha \tan\delta K_{\text{wall}}} - (H - Z)\right]\end{aligned} \tag{10}$$

where, $c = C_0 + C_1Z$, where, C_0 is initial cohesion at ground surface and C_1 is the rate of increase of cohesion with depth.

The active lateral stress at any depth 'Z' acting on the wall

$$\sigma_{h,\text{wall}} = \frac{(aC_0 + aC_1H)}{\tan\delta}\left[\left(1 - \frac{Z}{H}\right)^{\tan\alpha \tan\delta K_{\text{wall}}} - 1\right]$$

$$+\ \frac{(aC_1\tan\alpha-\gamma)K_{\text{wall}}}{(\tan\alpha\tan\delta K_{\text{wall}}-1)}\left[H\left(1-\frac{Z}{H}\right)^{\tan\alpha\tan\delta K_{\text{wall}}}-(H-Z)\right] \tag{11}$$

Similarly, analysis have been done for below cut level and lateral stress distribution

$$\begin{aligned}\sigma'_{h,\text{wall}} &= \frac{(aC'_0+aC_1l)}{\tan\delta'}\left[\left(1-\frac{Z'}{l}\right)^{\tan\alpha\tan\delta' K'_{\text{wall}}}-1\right]\\ &+\ \frac{(aC_1\tan\alpha-\gamma)K'_{\text{wall}}}{\left(\tan\alpha\tan\delta' K'_{\text{wall}}-1\right)}\left[l\left(1-\frac{Z'}{l}\right)^{\tan\alpha\tan\delta' K'_{\text{wall}}}-(l-Z')\right]\\ &+\ \left[\left(X\times K'_{wall}\right)\left(1-\frac{Z'}{l}\right)^{\tan\alpha\tan\delta' K'_{\text{wall}}}\right]\end{aligned} \tag{12}$$

where,

$$\begin{aligned}X &= \frac{(aC_0+aC_1H)}{\tan\delta}\left[\left(\frac{l}{H}\right)^{\tan\alpha\tan\delta K_{\text{wall}}}-1\right]\\ &+\ \frac{(aC_1\tan\alpha-\gamma)K_{\text{wall}}}{(\tan\alpha\tan\delta K_{\text{wall}}-1)}\left[H\left(\frac{l}{H}\right)^{\tan\alpha\tan\delta_1 K_{\text{wall1}}}-l\right]\end{aligned} \tag{13}$$

Total lateral active force on wall obtained as

$$P_h=\int_0^{l_1}\sigma_{h,\text{wall}}dZ+\int_{l_1}^{H}\sigma'_{h,\text{wall}}dZ' \tag{14}$$

Solving Eq. (14) we can get

$$\begin{aligned}P_h &= \frac{-(aC_0+aC_1H)H\tan\alpha K}{\tan\alpha\tan\delta K+1}\\ &+\ \frac{(aC_1\tan\alpha-\gamma)KH^2}{\tan\alpha\tan\delta K-1}\left[\frac{1}{\tan\alpha\tan\delta K+1}-\frac{1}{2}\right]\end{aligned} \tag{15}$$

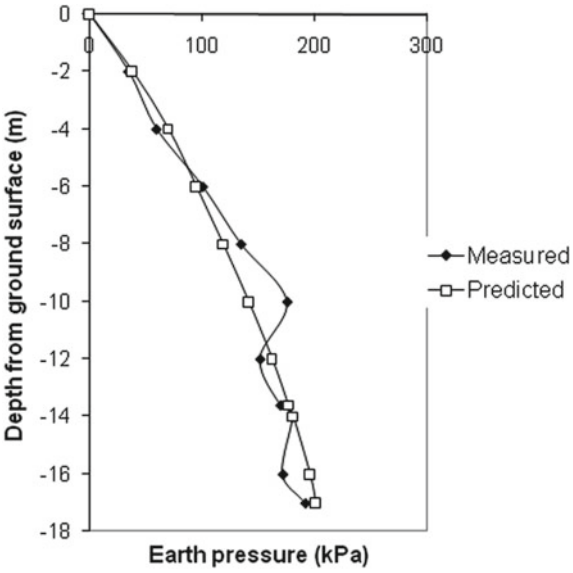

Fig. 5 Earth pressure distribution at Kolkata Metro Construction

3 Case Study

3.1 Kolkata Metro Construction [5]

Braced excavation varied in depth from 9 to 14 m was made with 600 mm RCC diaphragm wall propped by steel struts. The soil stratification at the site consists of desiccated brownish silty clay (upto 14 m) with cohesion value of 25 kN/m^2 and soil unit weight of 18 kN/m^3 followed by stiff clay ($c = 60$ kN/m^2). Predicted values are plotted with measured active earth pressure (Fig. 5).

3.2 An Idealized Deep Excavation [6]

An idealized 18 m deep braced excavation was analyzed by continuous beam method where idealized soil profile of sand layer with uniform friction angle of $\phi = 30°$ and unit weight of 19 kN/m^3 were assumed. Five stages of excavation were considered where final stage was done at a depth of 60 m with wall embedment depth of 6 m. The computed earth pressure at final stage of excavation by the use of continuous beam method is compared with the results obtained from proposed method (Fig. 6).

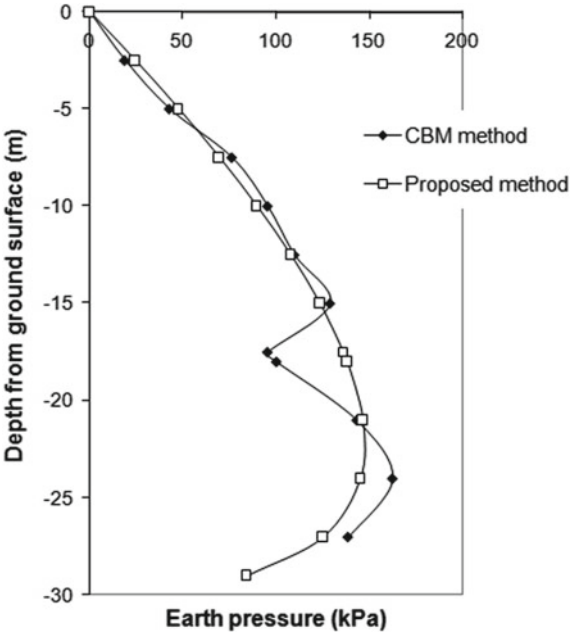

Fig. 6 Active earth pressure distribution for an idealized 18 m deep excavation

3.3 Excavation in Shanghai Soft Clay [7]

The excavation was supported by a 0.6 m thick, 28 m deep concrete diaphragm wall with final excavation depth was 15.5 m. Five levels of bracings were installed before reaching final stage of excavation. The uppermost clay layer appeared to be desiccated and it has higher shear strength than underlain marine deposits of soft silty and medium clay. Here active earth pressure along wall is predicted considering measured cohesion value simulating the clayey nature of soil. The result is shown in Fig. 7.

4 Conclusions

In present study, a new method is proposed for estimation of earth pressure distribution against diaphragm wall, both translating and rotating, considering arching effects assuming shape of arches as arc of circles for above and below excavation. This proposed formulation can be used for both cohesive and cohesionless soil as the expressions consist of cohesion and angle of internal friction. From the comparison with the published results of previous investigators and measured values, it is observed that formulation produces satisfactory prediction of earth pressure distributions in any kind of soil.

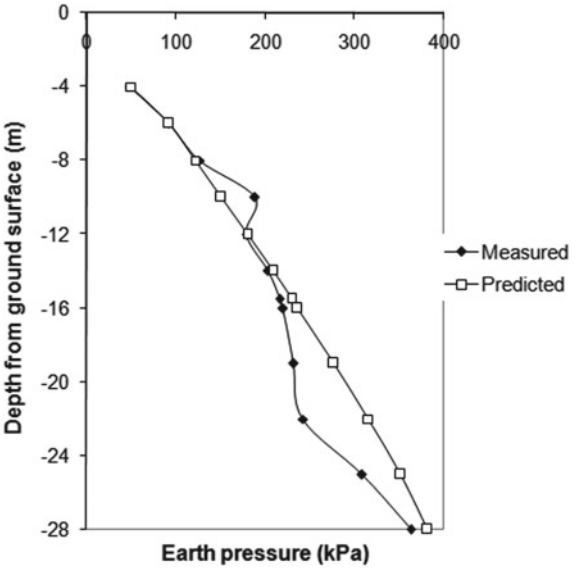

Fig. 7 Active earth pressure distribution at final stage of Shanghai Metro Station

References

1. Handy, R.L.: The arch in soil arching. J. Geotech. Eng. ASCE **111**(3), 302–318 (1985)
2. Goel, S., Patra, N.R.: Effect of arching on active earth pressure for rigid retaining walls considering translation mode. Int. J. Geomech. ASCE **8**(2), 123–133 (2008)
3. Paik, K.H., Salgado, R.: Estimation of active earth pressure against rigid retaining walls considering arching effects. Geotech. **53**(7), 643–653 (2003)
4. Rao, P., Chen, Q., Zhou, Y., Nimbalkar, S., Chiaro, G.: Determination of active earth pressure on rigid retaining wall considering arching effect in cohesive backfill soil. Int. J. Geomech. ASCE **16**(3), 1–9 (2016)
5. Som, N.N.: Performance study of braced cuts for calcutta metro construction. In: Proceedings of 9th Asian Regional Conference on SMFE, pp 387–394. Bangkok, Thailand (1991)
6. Goh, S.H., Semple, R.M., Tamaro, G.J.: Comparison of finite element and continuous beam methods for excavation support design. In: Structures Congress 2005: Metropolis and Beyond, ASCE, New York, USA (2005)
7. Liu, G.B., Ng, C.W.W., Wang, Z.W.: Observed performance of a deep multistrutted excavation in shanghai soft clays. J. Geotech. Geoenviron. Eng. ASCE **131**(8), 1004–1013 (2005)

Investigation on Axial Response of Pile Due to Staged Tunnelling: A Numerical Approach

Manojit Samanta, R. R. Abishek, and V. A. Sawant

1 Introduction

The distress on the substructure ultimately influences the response and stability of superstructures. The vulnerability of the pile foundation to tunnelling is more than other foundations as it extends up to a larger depth than a shallow foundation. The larger depth of the pile foundation possesses a greater possibility of extending into the influence zone of the tunnel. The length and location of piles are key parameters for the estimation of tunnelling-induced settlement. Therefore, the response estimation of pile foundations due to staged tunnelling is essential for preliminary hazards analysis of structures situated on or adjacent to the alignment of the tunnel.

A large number of numerical, analytical, and experimental studies in 1 g and centrifuge contributed to a greater understanding of tunnel–pile interaction. Experimental studies in the scaled-down model in 1 g and centrifuge are mostly conducted. Model studies on tunnel–pile interaction are primarily conducted in plane strain conditions. Usually, controlled volume loss within the soil mass has been adopted to simulate the tunnel construction procedure. Instrumentation like earth pressure cell, strain gauge, and pore pressure transducer is employed to measure the bending and axial response of pile, change in earth and pore water pressure within soil medium [1–6]. The deformation patterns of ground and pile, delineation of the zone of influence, and pile response are the main focus of these studies. The result shows that the

M. Samanta (✉)
Geotechnical Engineering Group, CSIR-Central Building Research Institute (CSIR – CBRI), Roorkee 247667, India
e-mail: manojit@cbri.res.in

R. R. Abishek
CSIR- Central Building Research Institute, Roorkee 247667, India

V. A. Sawant
Civil Engineering Department, IIT Roorkee, Roorkee 247667, India

C. N. V. Satyanarayana Reddy et al. (eds.), *Stability of Slopes and Underground Excavations*, Lecture Notes in Civil Engineering 185,
https://doi.org/10.1007/978-981-16-5601-9_23

pile settles more when located exactly above the tunnel. Higher deformation occurs at the centerline of the tunnel. The end bearing capacity of the pile significantly reduces, leading to stability issues in the foundation.

Evaluation of tunnel–pile interaction numerically is done in two ways. First, greenfield settlement due to tunnelling is estimated, and subsequently, in the second stage, estimated settlement are superposed to pile foundation to obtain the pile response due to tunnelling. Also, a combined analysis involving tunnel construction stages and existing piles are simulated to obtain the response of piles due to tunnelling. Finite element method (FEM), Boundary element method (BEM) or a combination of FEM and BEM are used for numerical analysis of pile–tunnel interaction [7–13] (Nematollahi and Daniel 14). Observations from the field studies also contributed to understanding the different aspects of the soil–tunnel, and soil–pile–tunnel interaction [13, 15–20]. Existing piles are usually in-service piles and are subjected to the working load. It is necessary to investigate the loaded piles response due to tunnelling to a realistic framework for estimating the tunnelling–induced hazards to existing adjacent structures. The undrained response of cohesive soil mainly governed the short-term behavior of the pile foundation during tunnel construction. Dilatancy is a major factor controlling the cohesionless soil behavior and soil–tunnel and soil–pile–tunnel interaction.

In the present study, the axial response of free head single pile has been investigated through three-dimensional finite element analyses in the cohesionless medium. Different pile and tunnel parameters, i.e., volume loss of tunnel and offset distance on the axial response, are investigated and reported. Particular attention has been paid to the influence of the working load of a pile on the axial response. Results of the present study are useful for preliminary hazards analysis of pile foundation situated adjacent and/or alignment of tunnel construction.

2 Materials and Methods

An extensive three-dimensional numerical analysis has been conducted using Plaxis 3D. Tunnel construction procedures, numerical analysis stages, geometric domain, and discretization of soil, tunnel, and pile have been discussed here.

2.1 Validation of Numerical Model

The present numerical model has been validated with a 1g experimental study conducted at the institute and published results from the literature. A scaled-down laboratory experimental study has been carried out in 1g conditions to investigate the tunnel–pile interaction. Model studies have been conducted in a mild steel tank of size 2 m $\times$ 2 m $\times$ 1.5 m. A hollow cylindrical pipe of 114 mm inside diameter has been used as a model tunnel. A staged fluid extraction technique has been used

to simulate the staged tunneling construction. A hollow circular aluminum pipe of 19 mm outside diameter and 1 mm wall thickens has been used as a model pile foundation. The response of the pile foundation has been studied for a volume loss in the range of 0.5 to 10%. All the model studies are conducted in a cohesionless soil medium. Properties of the soil medium are evaluated through a drained triaxial test. Details of the experimental procedure, sample bed preparation are out of the scope of the present paper. The same has been modeled numerically through Plaxis 3D. Results of the vertical settlement of the pile from experimental and numerical analysis match quite well with a variation of 4–6%.

Another benchmarking of the present numerical model has been done with the published results by Chen et al. [21]. Authors introduced a three-dimensional numerical model to simulate the Double O-tube staged tunnel construction procedure and estimate the surface settlement. The numerical model has been created adopting material properties and layering systems, as mentioned in the paper. The present numerical model shows a maximum surface settlement adopting a small strain hardening soil model for the monitoring section of 24.77 mm. The reported surface settlement from field measurement is 22.5 mm, respectively. This close resembles of the present results, with the reported numerical results established the accuracy of the present numerical model.

2.2 Soil and Tunnel Parameters

This section describes different soil and tunnel parameters employed in the present numerical study. Soil parameters of the present numerical model are evaluated from a series of drained triaxial tests on cohesionless soil medium at a relative density of 84%. The test small strain hardening soil parameters are evaluated and employed in the numerical analysis. Table 1 shows the different soil parameters. The embedded pile option available in the Plaxis library has been used to simulate the pile in the present study. Table 2 shows the different properties of the pile. Maximum skin resistance and base resistance are calculated from soil parameters following IS procedure [22], and the same are employed in the numerical analysis. Tunnel lining has been model as plate element. Table 3 shows the lining properties used in the present study.

2.3 Numerical Modelling

The numerical modelling is done using the finite element software Plaxis 3D. The borehole option available in the library is utilized in creating the soil medium. From the initial trial analysis, the size of the numerical domain has been fixed as 150 m $\times$ 52 m $\times$ 48 m. Ten noded tetrahedral elements with three translational degrees

Table 1 Small Strain hardening soil parameters

Soil parameters	Value
Cohesion, C (kN/m^2)	9.0
Angle of internal friction, θ (°)	35.8
Minimum unit weight (kN/m^3)	16.6
Maximum unit weight (kN/m^3)	17.7
Secant stiffness in the standard drained triaxial test/tangent stiffness for primary oedometer loading, $E_{50}^{ref}/E_{ode}^{ref}$ (kN/m^2)	8.374E3
Unloading/reloading stiffness at engineering strains, E_{ur}^{ref} (kN/m^2)	25.122E3
Dilatancy angle, Ψ (°)	10.5
Poisson's ratio, μ	0.2
Shear strain at which Gs = 0.722Go; $\gamma_{0.7}$	0.65E-3
Reference shear modulus at very small strains, G_0^{ref} (kN/m^2)	106E3
Power for stress-level dependency of stiffness, m	0.6
Failure ratio, R_f	0.9
Earth pressure coefficient, K_0^{nc}	0.415

Table 2 Pile properties

Parameters	Value
Pile type	Circular
Pile diameter (m)	0.6
Unit weight (kN/m^3)	25
Young's modulus (kN/m^2)	2.5 E 10^7
Poisson's ratio, μ	0.15

Table 3 Tunnel liner properties

Parameters	Value
Unit weight (kN/m^3)	25
Young's modulus, (kN/m^2)	2.5 E10^7
Poisson's ratio, μ	0.25
Liner thickness (m)	0.12

of freedom have been used to discretize the soil domain. Six noded triangular plate elements with six degrees of freedom have been used to discretize the tunnel liner. Mesh convergence studies have also been carried out before actual analysis. In the numerical analysis, the number of elements varies in the range of 50,000–60,000 for the different parameters and geometric conditions used in the present study. The bottom of the numerical boundary is fixed in all directions. Side boundaries are free to move in the plane, but the perpendicular movement is restricted, i.e., roller boundary

conditions are applied at the side of the numerical model. The top surface is free to move in any direction. A 4 m diameter circular tunnel has been simulated in the present study. The volume loss control method has been used to simulate the tunnel construction procedure. Volume loss in the present study varies in the range of 0.5 to 2.5%. Staged excavation with each excavation length of 2.5 m is used in the present study. Linearly increasing face pressure with depth calculated from earth pressure at rest condition has been applied at the tunnel face during excavation. The crown of the tunnel is at a depth of 24 m from the top surface. Piles length of 8 m and 16 m is used in the present study.

The location of the pile varies laterally from 0D, i.e., crown, to 6D from tunnel longitudinal axis, D being the diameter of the tunnel. Pile is located at a longitudinal distance of 44 m from the tunnel face. Figure 1a–c shows different stages of numerical modeling of half of the numerical domain. Figure 2a–d shows the different lengths of the tunnel excavation. Stages of tunnel construction in a single step include deactivating soil volume for a length of 2.5 m within the tunnel and activating the tunnel liner material, subsequently applying specified volume loss at the surface of the tunnel. In the present case, one half of the full geometry has been numerically analyzed. Pile situated at other distance rather than crown represent two pile condition in the full model. No interference is expected as the minimum distance between the two piles is more than 25d, d is the diameter of the pile.

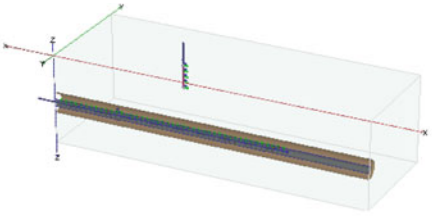

(a) Tunnel with pile

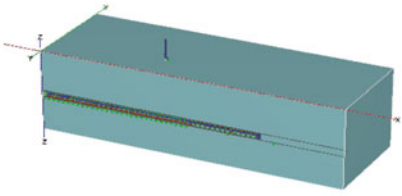

(b) Soil, tunnel and pile

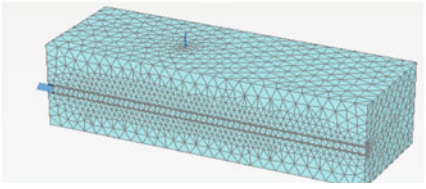

(c) Discretized model

Fig. 1 Different stages of numerical modeling

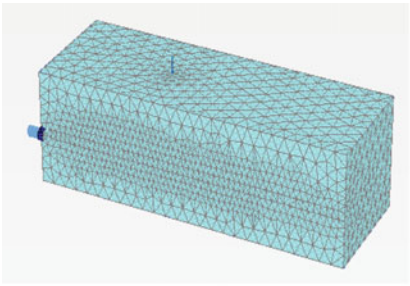

(a) 2.5 m

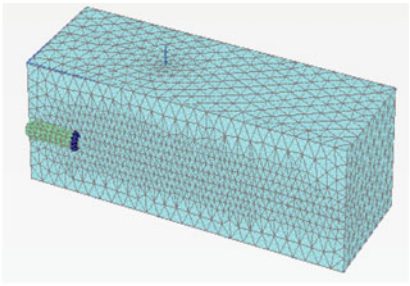

(b) 25 m

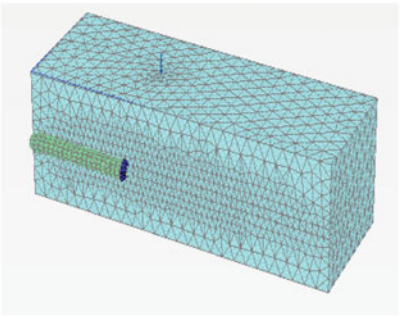

(c) 50 m

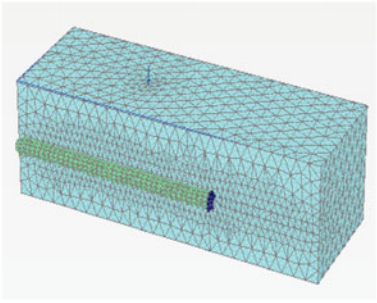

(d) 100 m

Fig. 2 Different length of tunnel excavation

3 Results and Discussions

3.1 Pile Head Settlement

Figure 3 shows the load–settlement relation of 8 m and 16 m pile. The load-settlement responses of piles are established from the separate analysis. The analysis aims to estimate the pile head load corresponding to equal settlement induced to pile due to tunnelling. Figure 4 shows the increase in pile head settlement with the lateral position of the pile from tunnel longitudinal axis for 1.5% volume loss and 16 m pile for different tunnel excavation length. Pile head settlement is expressed in the percentage of pile diameter, and tunnel excavation length is expressed in terms of tunnel diameter. Pile head settlement presented here is due to tunnelling only. The result shows that the pile suffers significant settlement depending on the location up to 6D lateral distance from tunnel longitudinal axis. Pile head settlement linearly decreases with an increase in lateral distance from the tunnel longitudinal axis.

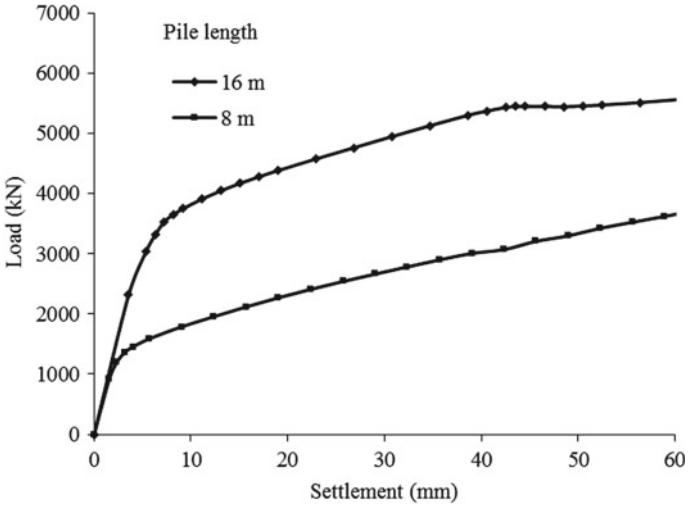

Fig. 3 Load–settlement relationship of pile

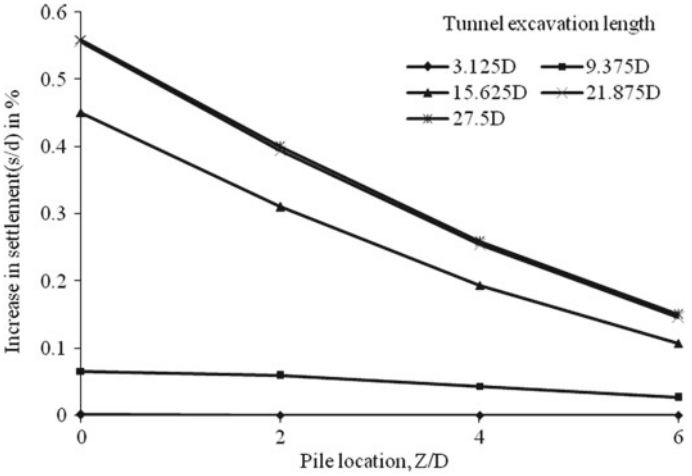

Fig. 4 Increase in settlement with position of pile for 1.5% volume loss

Figure 5a–d shows the increase in head settlement for the different lateral positions of the pile from tunnel axis for different volume loss of tunnel for no working load on the pile head. Pile head settlement decreases and increases with an increased lateral distance of pile from tunnel axis and tunnel volume loss, respectively. The maximum settlement of the pile head is 0.703% of pile diameter for pile located at the crown and tunnel volume loss of 2.5%. At a lateral distance of 6D, the pile head settlement is 0.182% of diameter for the same volume loss of tunnel. From the results, a clear zone of influence of tunnel excavation where pile suffers significant settlement

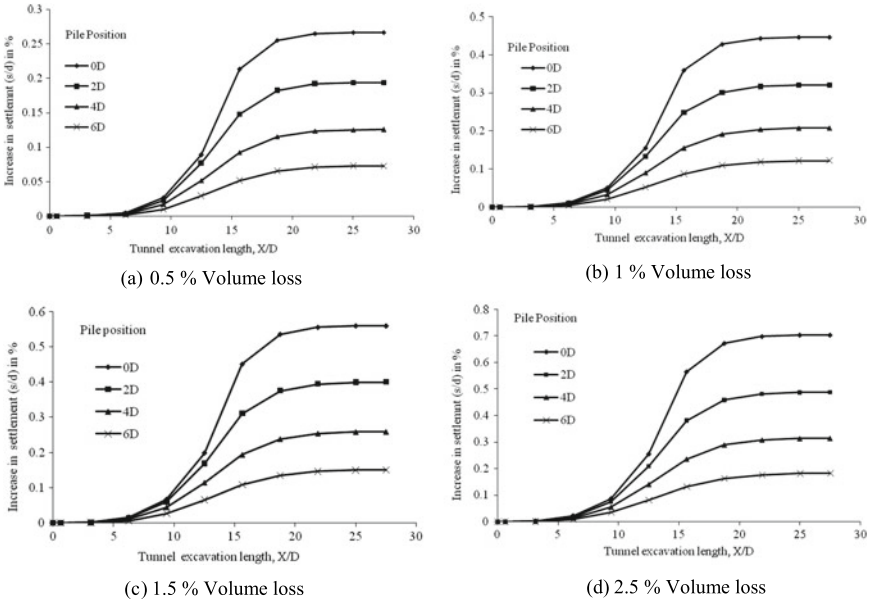

(a) 0.5 % Volume loss

(b) 1 % Volume loss

(c) 1.5 % Volume loss

(d) 2.5 % Volume loss

Fig. 5 Pile head settlement with progressive tunnelling for different volume loss

may also be identified. For all the analysis, the pile is located at a longitudinal distance of 11 times tunnel diameter from the tunnel face. The settlement of the pile started increasing rapidly when tunnel excavation length reached a distance of 6.25D from the tunnel face. Within a tunnel excavation length of 6.25D and 18.75D from the tunnel face, significant pile settlement occurs. Beyond 18.75D, pile settlement almost remains constant. From the present analysis, a zone of pile settlement of 5D distance ahead of pile location and 7.75D distance beyond of pile location may be identified. A similar result has been obtained for all the volumes loss of tunnel. For comparison purposes, settlement of pile due to tunneling has been compared with the pile load-displacement graph obtained from another set of numerical analyses employing the same soil material parameters. To obtain the same settlement of pile situated at the crown as induced by tunnel construction for 2.5% volume loss of tunnel, an equivalent load of 2600 kN is required. Equivalent load corresponding to the same pile settlement induced by tunnel construction varies in the range of 300 kN to 2600 kN for the parameters considered in the present study. It is to be noted here that the pile situated away from the center line may suffer rotational displacement also. This study mainly focuses on the axial response of pile, and rotational response is out of the scope of the present study.

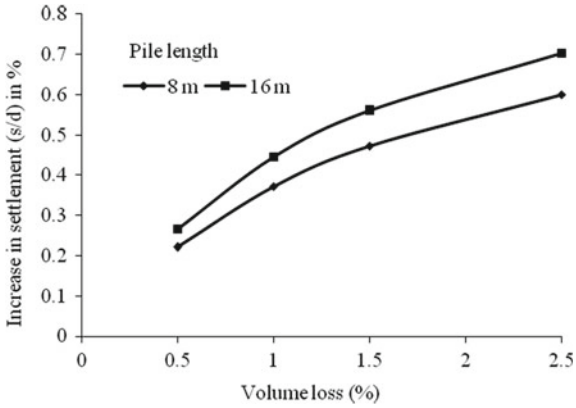

Fig. 6 Pile head settlement with volume loss

3.2 Effect of Length of the Pile

Pile head settlement for the pile length of 8 m and 16 m has been investigated in this section. Figure 6 shows the variation of pile head settlement for 8 m and 16 m pile situated at the crown with different volume loss of tunnel without any axial load on the pile head. Pile head settlement increases with an increase in pile length. The distance between the tip of the pile to tunnel crown is 16 m and 8 m for the 8 m and 16 m pile, respectively. Due to the volume loss of the tunnel, the soil around the tunnel undergoes volume contraction, resulting in a drag downforce along the pile shaft. Drag downforce is proportional to the surface area of the pile within the influence zone of tunnel excavation. A longer pile of the same diameter subjected to greater drag downforce, which results in a higher settlement for larger length of the pile. Results also clearly show the effect of volume loss on pile settlement. Settlement varies nonlinearly with volume loss of tunnel, and the settlement rate is observed to increase with volume loss of tunnel.

3.3 Effect of Working Load on Pile

In this section, the influence of working load on the pile head settlement due to progressive tunnel construction has been investigated for the16 m length of the pile. Axial vertical load on pile has been applied before the start of the construction of the tunnel. Different levels of the working load have been chosen from a load–settlement relationship of pile established beforehand for the same material properties (Fig. 3). Axial load is so determined to represent the different trends of load–settlement relationship of pile. A working load of 512 kN, 1778 kN, and 3537 kN have been applied at the pile head. While load–settlement relation remains linear for 512 kN and 1778 kN of axial load, nonlinearity starts from an axial load of 3537 kN and onward. Figure 7a, b shows the pile head settlement response at an axial load

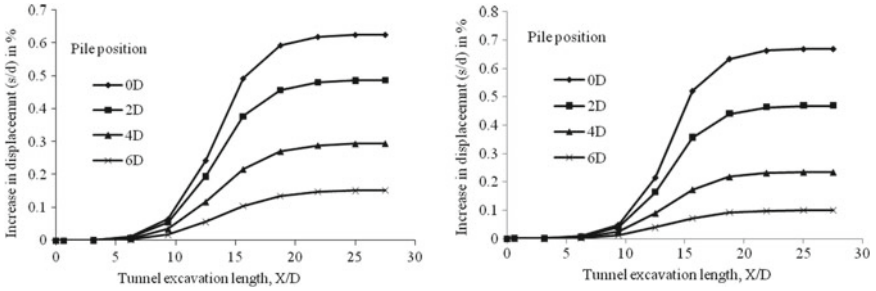

(a) Load 512 kN (b) Load 1778 kN

Fig. 7 Pile head settlement with progressive tunnelling for different axial load at 2.5% volume contraction

of 512 kN and 1778 kN for 2.5% volume loss. Figure 8a, b shows the pile head settlement response at 3537 kN at 0.5%, and 2.5% volume loss of tunnel. For pile situated at the crown, an increase in pile head settlement of 0.63%, 0.67%, and 0.8% has been observed for the above-mentioned working load for 2.5% volume loss. The equivalent load obtained from the load–displacement relationship is 2600 kN, 3500 kN, and 3900 kN for a settlement of 0.734%, 1.1%, and 1.84% of pile diameter, respectively. A load increment of approximately 2088 kN, 1722 kN, and 363 kN has been observed for different working loads applied on the pile foundation. Load level 1778 kN corresponds to a safety factor of 2.5 as determined from the isolated pile load–settlement relationship. The factor of safety after tunnel construction is 1.27. Results show that the level of working loads significantly influences the settlement of the pile foundations. For smaller working loads, the reserve capacity of the pile comes into effect during tunnel construction and prevents excessive pile settlement. If the working load is high or the safety margin of the pile at working conditions is minimal, an excessive settlement of pile during tunnelling is expected, and the pile may fail.

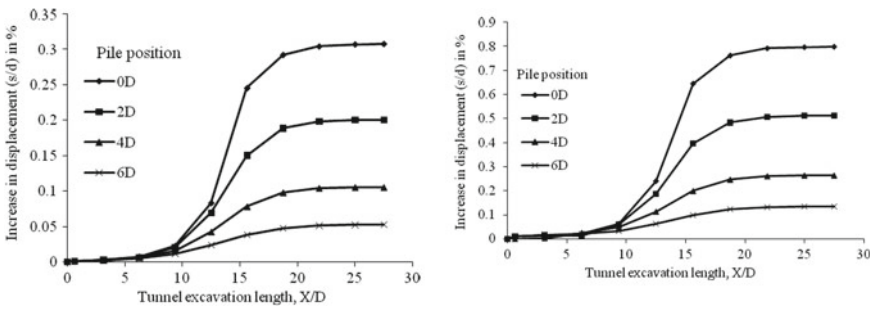

(a) 0.5 % Volume loss (b) 2.5 % Volume loss

Fig. 8 Pile head settlement with progressive tunnelling at 3537 kN axial load

4 Conclusions

The present study investigates the axial response of a free head single pile due to progressive tunnel construction. A three-dimensional numerical model of soil, tunnel, and pile has been adopted to investigate the axial pile response. First, a numerical model has been benchmarked against experimental and published results in the literature, and subsequently, a parametric study has been conducted. Different parameters, i.e., volume loss of tunnel, pile length, pile position, and working load on the pile on the axial response of the pile foundation, have been investigated and reported here. Following conclusions may be drawn from the present study

1. Tunnelling-induced volume loss significantly influences the pile head response. The settlement of pile increases with an increase in volume loss of tunnel. The rate of increase, increases with volume loss of the tunnel. In the present study, volume loss in the range of 0.5% to 2.5% has been considered.
2. A zone of influence where pile suffers excessive settlement has been identified. A zone, 5 times the diameter of the tunnel ahead and 7.75 times beyond pile location has been identified as the most vulnerable zone of pile settlement. Beyond a distance of 7.75D, pile settlement remains almost constant.
3. The level of working load plays a significant role in the pile head response. For smaller working loads, the reserve capacity of the pile comes into effect during tunnel construction and prevents excessive pile settlement. If the working load is high or the safety margin of the pile at working conditions is minimal, an excessive settlement of pile during tunneling is expected, and the pile may fail. A 50% reduction of safety factor has been observed for the adopted parameters in the present study.
4. The lateral influence zone of pile settlement has been extending up to 6 times of tunnel diameter from the tunnel longitudinal axis for the parameters and conditions adopted in the present study. Pile settlement varies linearly with a lateral distance of pile location from tunnel longitudinal axis.

References

1. Marshall, A.M.: Tunnel pile interaction analysis using cavity expansion methods. J. Geotechn. GeoEnviron. Eng. **138**(10), 1237–1246 (2012). https://doi.org/10.1061/(asce)gt.1943-5606.0000709
2. Jacobsz, S.W., Standing, J.R., Mair, R.J., Hagiwara, T., Sugiyama, T.: Centrifuge modelling of tunnelling near driven piles. Soils Found. **44**(1), 49–56 (2004). Japanese Geotechn. Soc. (2004)
3. Loganathan, N., Poulos, H.G., Stewart, D.P.: Centrifuge model testing of tunnelling-induced ground and pile deformations. Geotechnique **50**(3), 283–294 (2000)
4. Meguid, M.A., Mattar, J.: Investigation of tunnel-soil-pile interaction in cohesive soils. J. Geotechn. Environ. Eng., 973–979 (2009). https://doi.org/10.1061/_asce_gt.1943-5606.0000004

5. Lee, Y.J., Bassett, R.H.: A model test and numerical investigation on the shear deformation patterns of deep wall-soil tunnel interaction. Can. Geotech. J. **43**, 1306–1323 (2006). https://doi.org/10.1139/t06-088
6. Lee, Y.-J., Bassett, R.H.: Influence zones for 2D pile–soil-tunnelling interaction based on model test and numerical analysis. Tunnelling Underground Space Technol. **22**, 325–342 (2007). https://doi.org/10.1016/j.tust.2006.07.00
7. Cheng, C.Y., Dasari, G.R., Chow, Y.K., Leung, C.F.: Finite element analysis of tunnel–soil–pile interaction using displacement-controlled model. Tunnelling Underground Space Technol. **22**, 450–466 (2007). https://doi.org/10.1016/j.tust.2006.08.002
8. Chen, L.T., Poulos, H.G., Loganathan, N.: Pile Response caused by tunnelling. J. Geotechn. GeoEnviron. Eng. 1999, **125**(3), 207–215 (2000)
9. Mahmood, K., Kim, W.B., Yang, H.S.: A parametric study of Tunnel-Pile interaction using numerical analysis. Geosyst. Eng. **14**(4), 169–174 (2011)
10. Lee, C.J.: Numerical analysis of pile response to open face tunnelling in stiff clay. Comput. Geotechn. **51**, 116–127 (2013)
11. Mroueh, H., Shahrour, I.: Three-dimensional finite element analysis of the interaction between tunnelling and pile foundations. Int. J. Numer. Anal. Meth. Geomech. **26**, 217–230 (2000). https://doi.org/10.1002/nag.194. (2000)
12. Surjadinata, J., Carter, J.P., Hull T.S., Poulos, H.G.: Analysis of the effects of tunnelling on single piles. Geotechnical aspects of Underground construction in Soft ground- ISBN 0415391245 (2006)
13. Wan, M.S.P., Standing, J.R., Potts, D.M., Burland, J.B.: Measured short-term ground surface response to EPBM tunnelling in London Clay. Géotechnique **67**(5), 420–445 (2017). https://doi.org/10.1680/jgeot.16.P.099
14. Nematollahi, M., Daniel, D.: Three-dimensional numerical simulation of pile-twin tunnels interaction–Case of the Shiraz subway line, Tunnelling and Underground Space Technology. **86**,75–88 (2019). https://doi.org/10.1016/j.tust.2018.12.002
15. Standing, J.R., Selman, R.: The response to tunnelling of existing tunnels at Waterloo and Westminster. In Building response to tunnelling: case studies from construction of Jubilee Line Extension, vol. 2, case studies (eds J. B. Burland, J. R. Standing and F. M. Jardine), pp. 509–546. London, UK: Thomas Telford, (2001)
16. Jiang, X., Li, K.: Research on pull-out mechanical characteristics of pile foundation in submerged floating tunnel. Procedia Eng. **166**, 389–396 (2016). https://doi.org/10.1016/j.proeng.2016.11.570
17. Yu, J.B.Y.: Assessing ground interaction effects and potential damage on existing tunnels before and after new excavation works. Ph.D. Thesis, Imperial College London, London, UK (2014)
18. Khabbaz, H., Gibson, R., Fatahi, B.: Effect of constructing twin tunnels under a building supported by pile foundations in the Sydney central business district. Underground Space (2019). https://doi.org/10.1016/j.undsp.2019.03.008
19. Lee, G.T.K., Ng, C.W.W.: Fffects of advancing open face tunneling on an existing loaded pile. J. Geotechn. Environ. Eng., 193–201 (2005)
20. Sung, E., Shahin, H.M., Nakai, T., Hinokio, M., Yamamoto, M.: Ground behaviour due to tunnel excavation with existing foundation. Soil Foundat. Japanese Geotechn. Soc. **46**(2), 189–207 (2006)
21. Chen, S.L., Lee, S.C., Wei, S.Y.: Numerical analysis of ground surface settlement induced by double-O tube shield tunneling. J. Performance Constr. Facilit. (ASCE) **30**(5), 1–10 (2016)
22. Indian Standard 2911; Design and construction of pile foundations—code of practice; New Delhi (2010)

Comparison of Limiting Equilibrium and Finite Element Analysis for Embedded Retaining Walls

Tehseena Ali and K. M. Nazeeh

1 Introduction

Embedded retaining walls comprise of sheet pile walls, secant pile walls, diaphragm walls, etc., and for many civil structures are the most important part. The design of embedded retaining walls is a part of classic geotechnical engineering and 'limit equilibrium approach' is the most common approach for their design. Limiting earth pressures is the typical assumption of this approach and the wall should satisfy horizontal and moment equilibrium as well. The calculation of the embedment depth D and the prop force P for a typical propped cantilever wall shown in Fig. 1 uses two equations from two equilibrium equations. Subsequently, the bending moment (BM) distribution in the wall can be determined and the maximum value is taken as the design moment M. Earth pressure (EP) distribution acting on the wall is the critical matter in any method of limit equilibrium. Although the distribution depends on the mode of failure and for different modes of failure it may vary significantly, the linear variation of earth pressure with depth is assumed in most limit equilibrium applications. Earth pressure coefficients from classic earth pressure problem give the value of limiting active and passive EP's acting behind and in front of the wall. This variant of limit equilibrium is often referred to as the 'free earth support' method [1]. Nevertheless, several other EP distributions are possible to consider. A method provided by Brinch [2] is remarkable in this regard. Although the method has the same basic components, it is not regarded as limit equilibrium approach. This method allowing consideration of a larger range of EP distributions each corresponding to a mode of failure is the main difference from limit equilibrium approach. Though relatively complicated in terms of calculations, this method is not broadly used outside

T. Ali (✉) · K. M. Nazeeh
Department of Civil Engineering, IISc Bangalore, Bengaluru 560012, India

C. N. V. Satyanarayana Reddy et al. (eds.), *Stability of Slopes and Underground Excavations*, Lecture Notes in Civil Engineering 185,
https://doi.org/10.1007/978-981-16-5601-9_24

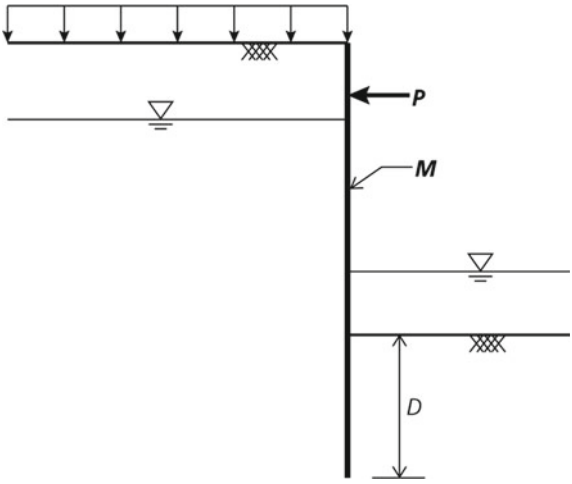

Fig. 1 A typical propped retaining wall

of Brinch Hansen's native Denmark. Simpson and Powrie [3] provide the additional details on historical developments for the design of embedded retaining walls using limit equilibrium and other approaches.

By means of computerized implementations, classic limit equilibrium approach continues to be used extensively. At the same time as finite-element method (FEM) provides several advantages, the tendency to use FEM is increasing. However, the practical application of FEM is not without complications and therefore is regarded as an analysis tool rather than a design tool. As such, an obvious approach to the task of determining, say, the three design parameters M, P, and D for a wall such as the one shown in Fig. 1 does not suggest itself readily. Furthermore, the way partial coefficients should be applied has been, and remains, the subject of some debate [4–6]. The most critical issue in the design is the determination of embedment depth by means of staged excavation analysis [7]. Once the minimum allowable embedment depth is determined, the maximum moment and prop force are used as a basis for the selection of the wall profile and design of the horizontal support system.

Limit equilibrium method was first introduced by Coulomb to calculate the force of a fill on a retaining wall. Later the theory was extended to infinite body by Rankine and earth pressure theories were developed. Subsequent developments were made by Fellenius, Terzaghi, and others that result in making the limit equilibrium method a well-utilized tool for stability calculations by practicing engineers. An arbitrary mechanism of collapse can be constructed with limit equilibrium method. Each element of mechanism should be in equilibrium, the whole mechanism is in equilibrium is the main assumption of the limit equilibrium approach. While in the implementation of Observational Method, finite element analysis has played a crucial role. An analytical tool is provided by FEM for making initial predictions and helps engineers to set "trigger" levels for ground movement during construction. FE model can

be calibrated by using the observed behavior during early stages and can be revised as necessary. If alternative construction strategies need to be examined, this can be done in a suitable manner.

This paper presents sample calculations by limit equilibrium method and comparison of the results with that of plaxis. Cantilever wall is analyzed limit equilibrium and compared with plaxis results. Similarly, limit equilibrium analysis of single propped wall (CMRL-Case study) is carried out and compared with plaxis results. Limit equilibrium analysis of multi-prop wall as given in CIRIA SP 95 for sheet pile cofferdams is compared with plaxis results.

2 Cantilever Wall Analysis

Cantilever wall analysis was carried out by means of limit equilibrium method. Problem setup for excavation of 3 m is shown in Fig. 2. The figure illustrates the cross-section of the embedded retaining wall with soil properties and the corresponding typical lateral earth pressure diagram. A homogeneous cohesionless soil layer of φ value 33° and γ value 20 kN/m^3 is considered for the analysis. The water table is at the ground level (GL). As per the analysis, an embedment of 6.1 m was required for the given soil parameters. The maximum BM was found at the level of zero shear at Limiting Equilibrium Condition (LEC). Consequently, the finite element analysis was carried out in plaxis with input parameters given in Table 1.

Figure 3 compares the (a) lateral earth pressure acting on the wall in active and passive conditions, and (b) bending moment (BM) obtained from plaxis and limit equilibrium calculation.

It can be observed that the active pressure as per plaxis is almost matching with the limit equilibrium pressure, which varies linearly with depth. The small variations toward the bottom can be because of the soil–structure interaction and wall deformations. But in the passive side, the plaxis and limit equilibrium values match in the beginning and the plaxis values reduce later. The limit equilibrium values are

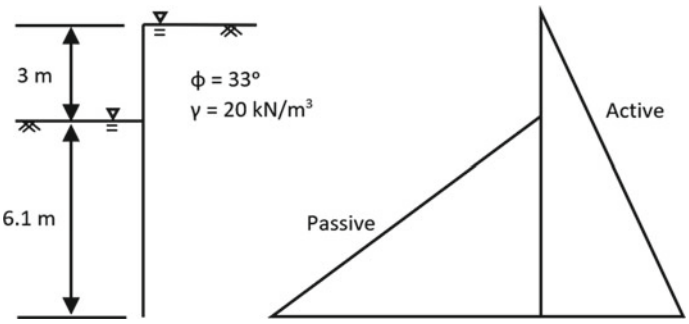

Fig. 2 Cross-section of embedded retaining wall with lateral earth pressure diagram

Table 1 Plaxis input parameters for cantilever wall analysis

Parameters	Units	Properties
Soil		
Identification		Sand and gravel
Saturated unit weight (γ_{sat})	kN/m^3	20
Young's modulus (E_{ref})	kN/m^2	$3.5*10^4$
Poisson's ratio (υ)		0.35
Cohesion/angel of internal friction (c/φ)	kN/m^2/deg	0/33
Plate		
Identification		D-Wall
Normal stiffness (EA)	kN/m	$5.5*10^6$
Flexural stiffness (EI)	kNm^2/m	$8.4*10^4$
Equivalent thickness (d)	m	0.42
Weight (w)	kN/m/m	12.5
Poisson's ratio (υ)	–	0.15

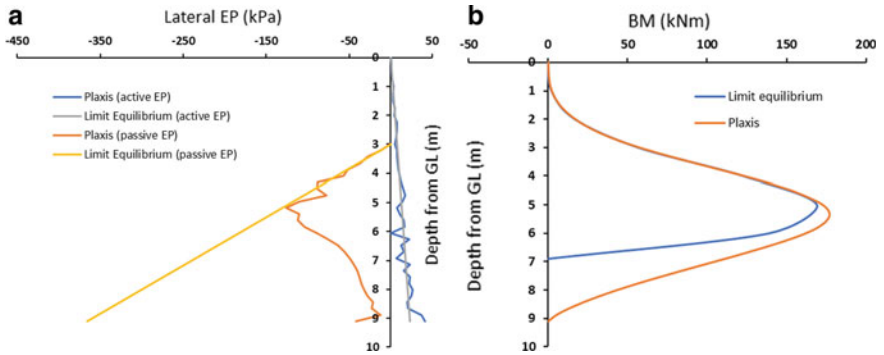

Fig. 3 Comparison between limit equilibrium and plaxis results: **a** Earth pressure diagram, and **b** Bending Moment diagram

at the ultimate condition, which requires larger wall movements toward the toe. It doesn't happen in the working conditions. So only a part of the passive resistance is mobilized. In case of BM, the values almost match. The limit equilibrium calculation gives a value of 169 kNm and plaxis gives a value of 176 kNm. The reduction in passive resistance in plaxis probably causes small increase in bending moment.

3 Analysis of Propped Walls

The analysis of single and multiple propped walls is discussed in this section. Single propped wall analysis is discussed considering the CMRL (Chennai Metro Railway) case history and multiple propped case is discussed considering the solved example from CIRIA SP 95 (Construction Industry Research and Information Association). The limit equilibrium analysis considering stage-by-stage method is compared with plaxis analysis.

3.1 Single Propped Wall (CMRL Case Study)

The multi-layered soil profile as per CMRL case history was used in the single propped wall analysis (see Fig. 4). The water table is at a depth of 4.71 m from the GL. For the excavation of 7.4 m an embedment of 4.4 m was provided for the retaining wall. The earth pressure diagrams were drawn, and the prop force, maximum BM, and overall FoS was determined by limit equilibrium method. The depth of embedment was determined at LEC, and the prop force was calculated taking the sum of horizontal forces equal to zero at LEC. Then the level of zero shear and the maximum BM was determined. The overall FoS for the given embedment was also determined based on gross pressure method. Consequently, the finite element analysis was carried out in plaxis with input parameters shown in Table 2.

A comparison of the limit equilibrium and plaxis pressure diagrams in active and passive condition is shown in Fig. 5. In case of plaxis, an increase in active pressure

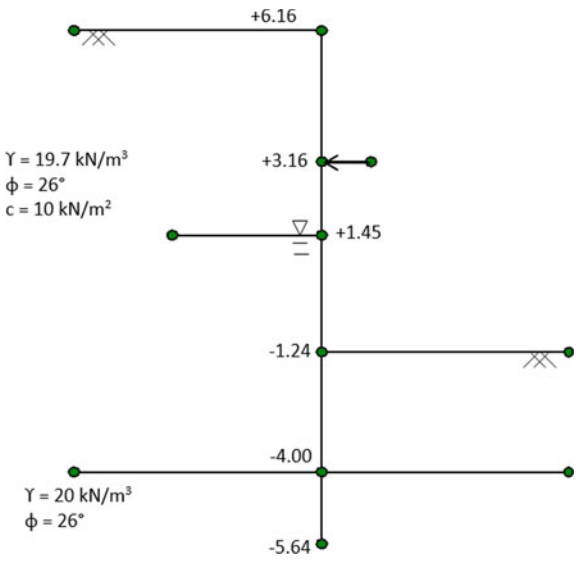

Fig. 4 Soil profile with level of excavation and prop

Table 2 Plaxis input parameters for single propped wall analysis

Parameters	Units	Value
Soil		
Identification		Sand and gravel
Dry unit weight(γ_{unsat})	kN/m^3	19.7
Saturated unit weight (γ_{sat})	kN/m^3	20
Young's modulus (E_{ref})	kN/m^2	2.29*10^4
Poisson's ratio (υ)		0.3
Cohesion/angel of internal friction (c/φ)	kN/m^2/deg	0/35
Plate		
Identification		D-Wall
Normal stiffness (EA)	kN/m	2.37*10^7
Flexural stiffness (EI)	kNm^2/m	1.26E + 06
Equivalent thickness (d)	m	0.80
Weight (w)	kN/m/m	2.00–10^1
Poisson's ratio (υ)	–	0.15
Struts		
Identification		Node to node Anchor
Normall stiffness (EA)	kN/m	2.38*10^5
Spacing (l_s)	m	1.5

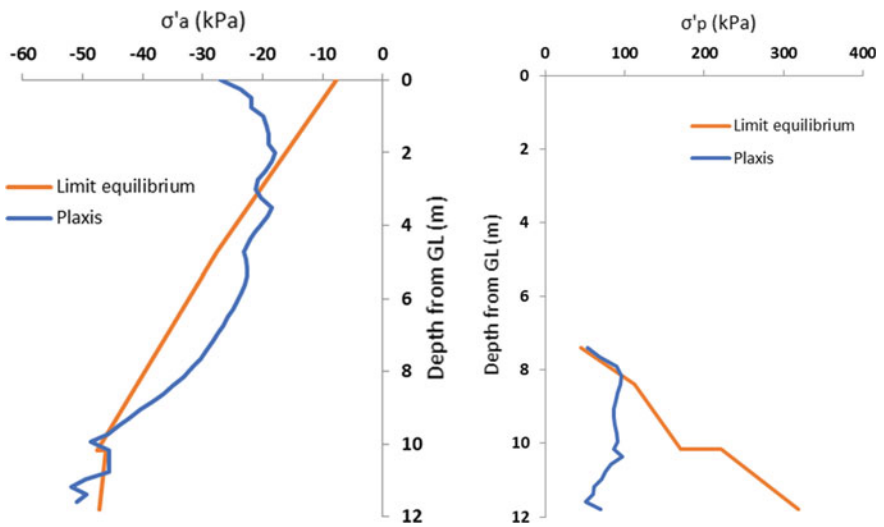

Fig. 5 Comparison of active and passive EP from limit equilibrium and plaxis results

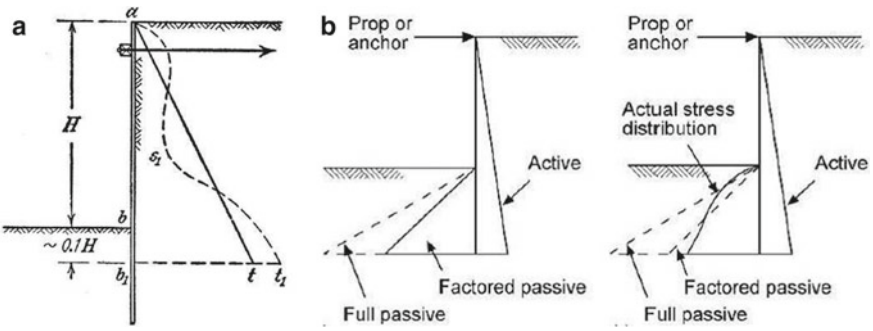

Fig. 6 Limit equilibrium and actual earth pressure diagrams **a** active (Terzaghi) **b** passive for rigid and flexible walls (Rowe)

at the top and a decrease in the pressure below the prop is observed. Finally, toward the toe the limit equilibrium and plaxis earth pressures almost match. In the passive state, the earth pressures are matching at the top, i.e., just below the excavated level. But the plaxis earth pressure decreases as it moves toward the toe.

The difference in EP distribution from the limit equilibrium method is explained by various researchers. The following EP diagrams (Fig. 6) clearly illustrate the real and limit equilibrium pressure distribution. The results obtained from the case study are similar to them, plaxis is almost showing the real pressure distribution.

In active case, the increase in the pressure at top is because of the inward movement of the wall due to prop. Due to the outward deformation of wall below the prop, the rigid prop results in arching of the soil. The arching of the soil increases the pressure on the prop and hence increases the prop load, as can be seen from the results. In the passive state (like in the cantilever case) large movement is required to develop the complete passive resistance. But the actual mobilized passive resistance will only be a part of the ultimate passive resistance. The arching of the soil and hence the decrease in active pressure reduces the bending moment of the wall. The reduction of passive resistance also reduces the overall FoS, compared to limit equilibrium result. Table 3 tabulates the results from limit equilibrium and plaxis analysis.

Table 3 Comparison of results from limit equilibrium and plaxis analysis

	LE analysis	Plaxis analysis
FOS	1.88	1.72
BM	125 kNm	95 kNm
Strut Force	1287 kN	1395 kN

3.2 *Multiple Propped Wall*

The multiple propped wall analysis in CIRIA SP 95 [8] is compared with plaxis analysis. The limit equilibrium analysis is carried out using stage-by-stage method, considering the construction sequence and analyzing the wall at each stage. For the soil profile provided (see Fig. 7), active and passive EP's were calculated. The wall was analyzed for the first stage of excavation with single prop, considering the level of zero net pressure as the point of contraflexure. The prop load and the maximum BM at the level of zero shear were determined at this stage. For stage 2, the wall between prop 1 and prop 2 was considered. A hinge is assumed at the level of prop 2 and the wall was analyzed for the load on prop 1 and the reaction on prop 2. Now for the wall below prop 2, the analysis was carried out as a single propped wall assuming a hinge at prop 2. The load on prop 2 and maximum BM at level of zero shear was determined at LEC. The adequacy of the embedment depth was also checked for the

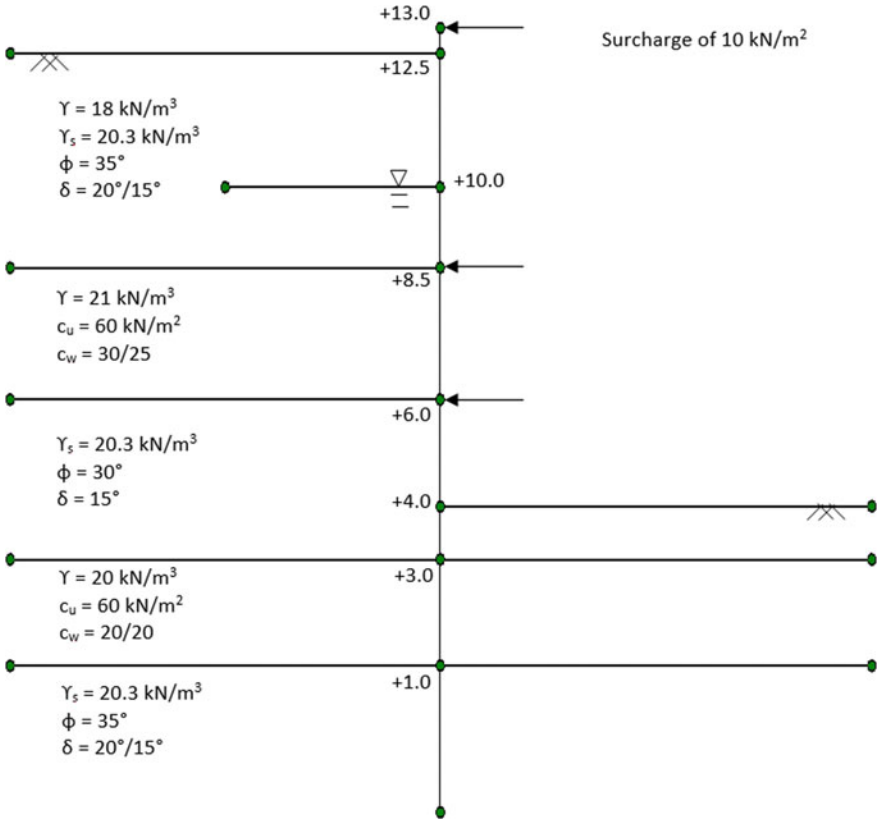

Fig. 7 Soil profile with levels of props and excavation

required FoS. Same procedure was repeated for stage 3 of the excavation. The above profile was modeled and analyzed in plaxis with input parameters given in Table 4.

The results obtained from the two analyses are tabulated in Table 5. Due to the soil–structure interaction and the wall deformations, redistribution of the pressure occurs. This results in a change in BM and prop loads. The horizontal stress distribution for rigid props on the retaining side of the wall is non-linear with load arching on to the relatively stiff prop [9]. Therefore, reduction in the bending moment occurs as lateral stress at the mid-section of the wall gets reduced. Because of the tendency of the upper part of the wall to rotate back into the retained ground, the rise in the lateral stress in the area of the prop may probably be noticeable in case if the wall is propped just below the [10].

In the pile, reduction in bending moment occurs due to redistribution of pressure. In front of the wall, the passive resistance close to the ground level may equal or

Table 4 Plaxis input parameters for multiple propped wall analysis (CIRIA SP 95)

Parameters	Units	Value				
Soil		Layer 1	Layer 2	Layer 3	Layer 4	Layer 5
Depth (m)		13–8.5	8.5–6	6–3	3–1	1 to top
Identification		Sand and gravel	Firm clay	Silty sand	Soft/firm clay	Medium sand
Dry unit weight (γ_{unsat})	kN/m^3	18	18	18	18	18
Saturated unit weight (γ_{sat})	kN/m^3	20.3	21	20.3	20	20.3
Young's modulus (E_{ref})	kN/m^2	4*10^4	5*10^4	5*10^4	5*10^4	5*10^4
Poisson's ratio (υ)	–	0.3	0.3	0.3	0.3	0.3
Cohesion/angel of internal friction (c/φ)	kN/m^2/deg	0/35	60	0/30	40	0/35
Plate						
Identification				D wall		
Normal stiffness (EA)	kN/m			3.79E + 06		
Flexural stiffness (EI)	kNm^2/m			4.18E + 04		
Equivalent thickness (d)	M			0.36		
Weight (w)	kN/m/m			7.00		
Poisson's ratio (υ)	–			0.25		
Struts						
Identification				Node to node anchor		
Normal stiffness (EA)	kN/m			6.37E + 06		
Spacing (l_s)	M			9		

Table 5 Limit equilibrium and plaxis results of the multiple propped wall (CIRIA SP 95)

Stage no	Prop load 1 (kN)	Prop load 2 (kN)	Prop load 3 (kN)	Max BM (kNm)
Limit equilibrium results				
1	25			58.3
2	14.9	166.8		268.7
3	14.9	68.1	203.8	171.7
Plaxis results				
1	22.6			42
2	25.3	291.3		133
3	26.4	295.23	122.68	163

surpass the limit equilibrium passive values and may decrease with depth toward the toe of the wall. The net result is a reduction in maximum bending moment compared with design based on a linear increase in limiting pressure with depth. This is however accompanied by an increase in the anchor loads [11] (BS 8002).

The EP diagrams based on the limit equilibrium calculations and plaxis are presented in Fig. 8. These diagrams are like that of the single propped case, the plaxis results showing some variation from the limit equilibrium EP. As discussed in the single propped case, the variations here also can be due to the arching effect onto the rigid prop and the wall deformations.

4 Conclusions

The analysis of cantilever wall, single propped wall (CMRL-Case study), and multi-prop wall as given in CIRIA SP 95 for sheet pile cofferdams is done using limit equilibrium approach and the results obtained are compared with those from the plaxis analysis.

In case of cantilever wall, it was observed that the active pressure as per plaxis is almost matching with the limit equilibrium pressure with small variations toward the bottom. But in the passive side, the plaxis and limit equilibrium values match in the beginning and the plaxis values reduce later. As for BM, the values almost match.

In case of single propped wall, an increase in active pressure at the top and a decrease in the pressure below the prop is observed for plaxis result. Finally, toward the toe the limit equilibrium and plaxis earth pressures almost match. In the passive state, the earth pressures are matching at the top, i.e., just below the excavated level. But the plaxis earth pressures decrease as it moves toward the toe.

In case of multi-propped wall, the earth pressure diagrams are similar to that of single propped wall. The plaxis results show some variation from limit equilibrium earth pressures which may be due to the arching effect onto the rigid prop and the wall deformations.

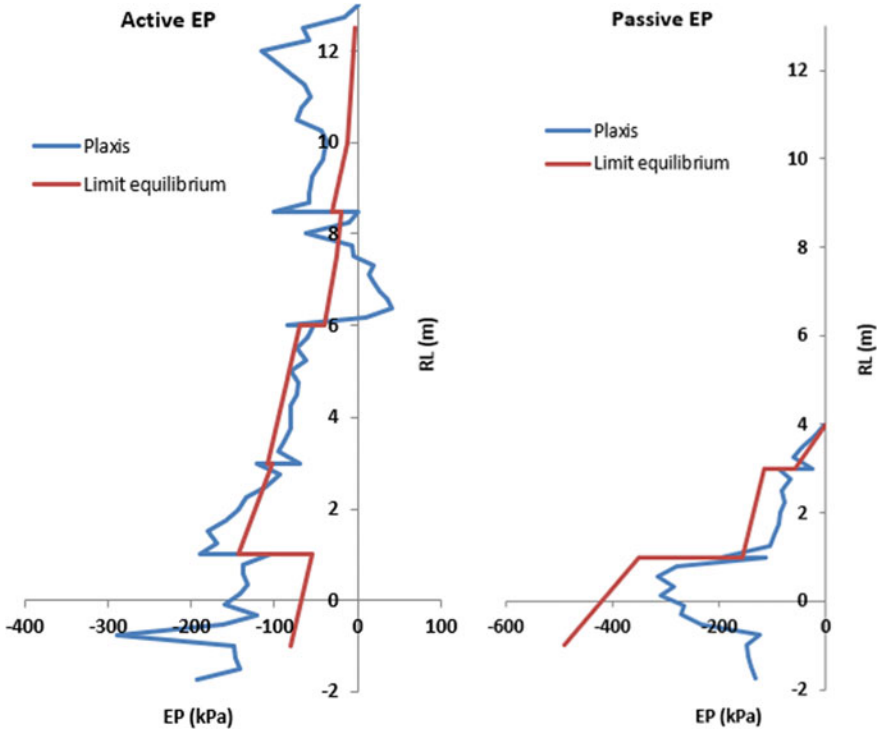

Fig. 8 Soil profile with levels of props and excavation

References

1. Budhu, M.: Soil Mechanics and Foundations. Wiley, Hoboken, NJ, USA (2000)
2. Brinch, H.J.: Earth Pressure Calculation. Teknisk Forlag, Copenhagen, Denmark (1953)
3. Simpson, B., Powrie, W.: Embedded retaining walls: theory, practice and understading. Proceedings of the 15th International Conference on Soil Mechanics and Geotechnical Engineering, Istanbul, Turkey (2001)
4. Bauduin, C., Devos, M., Simpson, B.: Accounting for partial material factors in numerical analysis. Proceedings of International Workshop on Limit State Design in Geotechnical Engineering (LSD2000), Melbourne, Australia (2000)
5. Schweiger, H. F.: Application of FEM to ULS design (Eurocodes) in surface and near surface geotechnical structures. Proceedings of the IACMAG, Turin, Italy (2005)
6. Potts, D.M., Zdravkovic, L.: Accounting for partial material factors in numerical analysis. Géotechnique **62**(12), 1053–1065 (2012). https://doi.org/10.1680/geot.11.P.057
7. Gaba, A.R., Hardy, S., Doughty, L., Powrie, W., Selemetas, D.: C760: guidance on embedded retaining wall design. Construction Industry Research and Information Association, London, UK (2017)
8. Williams, B.P.: The design and construction of sheet-piled cofferdams. Construction Industry Research and Information Association, London, UK (1993)
9. Rowe, P.W.: Anchored sheet pile walls. Proceedings Institution of Civil Engineers (London), 1, pp. 27–70 (1952)

10. Gaba, A.R., Simpson, B., Powrie, W., Beadman, D.R.: Embedded Retaining Walls: guidance for economic design. Construction Industry Research and Information Association, London, UK (2002)
11. BS 8002: Code of practice for earth retaining structures. British Standard Institute, London (2015)

Assessment of Effect of Deep Excavation on Adjacent Structures Using Finite Element Analysis

Anand M. Hulagabali, Pankaj Bariker, C. H. Solanki, and G. R. Dodagoudar

1 Introduction

In many of the metropolitan cities around the world are currently constructing residential houses, condominiums, high rise commercial buildings, transport facility, and other infrastructures. The daily extension of urban areas due to increased population has caused the majority of civil engineering projects in urban areas requires excavation. Deep excavations are becoming increasingly a common practice all over the world for the construction of high-rise structures, road tunnels, mass rapid transit systems, and other facilities in densely built-up areas within the city and suburban areas. Since excavation is the basic phase for construction of any foundations or basement of high-rise buildings and, underground structures in metropolitan areas, care must be taken for the safety of existing adjacent structures.

Many deep excavations have been carried out in a very poor subsoil conditions and in a very close proximity to the existing buildings and infrastructures. Therefore, deep excavations in urban areas generally may result in ground movements and excessive deformation that can induce significant damage to adjacent buildings and services. In such circumstance, the ability to predict ground deformation with certain accuracy and within an acceptable limit becomes an important and challenging task for geotechnical design. In order to reduce their impact, the excavations are supported

A. M. Hulagabali (✉)
National Institute of Engineering, NIE, Mysuru 570008, India
e-mail: anandmh@nie.ac.in

P. Bariker
National Institute of Technology Karnataka, Surathkal, India

C. H. Solanki
Civil Engineering Department, SVNIT, Surat 395007, India

G. R. Dodagoudar
Civil Engineering Department, IIT Madras, Chennai 600036, India

C. N. V. Satyanarayana Reddy et al. (eds.), *Stability of Slopes and Underground Excavations*, Lecture Notes in Civil Engineering 185,
https://doi.org/10.1007/978-981-16-5601-9_25

by retaining systems such as, stiff diaphragm walls, secant pile wall or contiguous pile wall and their supporting struts and anchors, which are installed as the excavation progresses.

In highly congested urban areas like there is a limitation for parking space and most of the vehicles park on the roadway. Such conditions will increase the traffic congestion in the city. Therefore, it's necessary to construct buildings having parking space at their basement level to minimize traffic congestion by providing parking lots. In addition to that, in weak subsoil conditions of shallower strata, excavation may proceed to greater depth in order to get firm foundation for high-rise structures. During the excavation and construction process, proper design and assessment of the effect of deep excavation on the nearby structures must be done. Detailed deformation and stability analysis of the retention system must be done in order to prevent damages of adjacent buildings and infrastructures around the excavation site.

The main objective of this study is to determine the parameters that affect buildings and infrastructures adjacent to deep excavation using Numerical modeling technique of Finite Element Method (FEM).

2 Literature Review

The construction of such tall buildings in metropolitan city increases the demand of using underground space, and deep excavations have been carried out for a greater depth for basements of the structure. Many deep excavations have been carried out to construct various types of underground infrastructures such as deep basements, subways, underground roads, and service tunnels. Excavations were considered shallow or deep depending on the ratio of their width to their depth. Simpson et al. [7] defines excavations with depths smaller than their widths as shallow excavations while excavations with depths larger than their widths as deep excavations. Terzaghi and Peck [9] described that excavations whose depths were less than 6 m could be defined as shallow excavations and those deeper than that as deep excavations.

Deep excavation is complex subject in geotechnical engineering and has been studied using various methods. Prediction of excavation-induced ground movement is an essential part in the design of deep excavation, because of the possible adverse effects on the nearby structures and other existing facilities. Soek et al. [6] describe that the assessment of deformation associated with deep excavation depends on the presence of buildings in the vicinity of excavation. Because the existence of buildings near the excavation modifies the induced deformation due to self-weight and stiffness of the building. Zuhair [11] identified an effective method of reducing deformations in the surrounding soil and damages of the adjacent structure by using advanced excavation techniques such as stiff diaphragm walls, secant pile walls, and support construction. It is important to establish practical solution to predict the displacement deformation around the excavation more accurately.

Empirical methods are based on the experience gathered by researchers in various parts of the world whereas numerical modeling utilizes computing power and, using various modeling techniques, can be a precise way of solving very complex problems [2]. The physical (Centrifuge) model relies on achieving the stress similarity between the model and prototype. This is achieved by an inertial accelerating a model to induce an inertial radial acceleration field N times greater than the gravitational field strength on Earth.

Theoretical method provides some basic understanding of the performance of deep excavation in a different way, but it has some limitation due to its simplicity and assumptions. The magnitude and distribution of induced deformation due to deep excavation depend on many factors such as soil and ground water condition, construction quality, excavation geometry, excavation sequence, duration of excavation, existence of adjacent buildings, wall stiffness, type, and installation of lateral support. The prediction of deformation based on theoretical method would be very complex to obtain the interaction between those mentioned factors. Some of the theoretical methods are reviewed in these sections.

The design of earth retaining walls requires the evaluation of active earth pressure which is largely based on the classic solutions of lateral earth pressure developed by Coulomb and Rankine. Coulomb [1] first studied the earth pressure problem using the limit equilibrium method to consider the stability of a wedge of soil between a retaining wall and the failure plane. Rankine [5] presented a solution for lateral earth pressures in retaining walls based on the plastic equilibrium. He assumed that there is no friction between the retaining wall and the soil, the soil is isotropic and homogenous, the friction resistance is uniform along the failure surface, and both the failure surface and the backfilled surface are planar. These theories are only applicable under certain conditions to estimate roughly the earth pressures on the wall. Moreover, they do not consider the construction process and give no indications on the wall deformations and ground movements in the more complex braced deep excavations.

Stability analysis is important in the design of retaining structures in clay, Terzaghi [10] suggested a mechanism consisting of a soil column outside the excavation which creates a bearing capacity failure. The failure is resisted by the weight of a corresponding soil column inside the excavation and also by adhesion acting along the vertical edges of the mechanism.

The wall deflections are normally measured with inclinometers, but the readings need to be adjusted to be consistent to the surface survey, because inclinometers usually only record the deflection pattern of the wall by assuming no displacement at the toe of the wall. In practice, however, a non-zero displacement at the toe of the wall is confirmed from both field measurements and numerical analyses [8].

Ou et al. [3] presented the building responses and ground movements induced by an excavation using the top-down construction method in Taipei. They concluded that the building performance during the excavation may be affected by factors such as the type and size of foundation, the geometry of the excavation, and the shape of the settlement profile. A building near a relatively short excavation side may experience smaller inclination than if it is near a long excavation side. They also suggested that

information regarding a building's location relative to the settlement influence zone is helpful in planning building protection measures during excavation.

3 Materials and Methodology

For the proper accomplishment of this work, it is required to review necessary and applicable materials, research findings, and data on soil parameters of the selected site used for the analysis of soil–structure interaction. The deformation of the supporting system and its influence on the existing adjacent structure has been studied using Finite Element based software. Material model is a set of mathematical equations that describes the relationship between stress and strains. In the Plaxis software, two constitutive models (MC &HS) have been selected for this study. Comparative analysis of the deformation of the supported soil and the contiguous pile wall deflection has been carried out. In addition to the deformation analysis, parametric study of supporting system has been performed. The soil and supporting wall parameters have been obtained from the geotechnical investigation report and from design of the shoring system. The derived soil parameters such as stiffness have been obtained from empirical correlations.

For carrying out of deep excavation analysis of the support system and its influence on existing nearby structures Plaxis 2D V8.6 software has been used. In this research, plane strain analysis and 15 node element have been selected. Drained effective stress analysis has been chosen as a drainage condition of constitutive model for both HS & MC model. Parametric studies of contiguous pile wall have been carried out to observe its effect on adjacent structure. The building load has been considered in the analysis of the pile wall deflection and analysis of settlement trough. The lateral ground deformation and maximum settlement have been obtained by varying the adjacent building load and corresponding distance from the face of excavation.

In this study, soil parameters were collected from geotechnical investigation report and the other parameters were taken as specified by ETG designers and Consultants ltd., and the same has been chosen for the analysis of deformation of supporting system and its influence on existing structures. Both Mohr–Coulomb (MC) and Hardening Soil (HS) model have been used to estimate the deflection of the Contiguous pile wall for comparative study of deformation of retained soil. With the absence of availability of appropriate test result for numerical modeling an empirical correlation with the SPT-N value can be used.

4 Modeling and Parametric Studies

4.1 Simulation of Deep Excavation in Plaxis 2D

For the numerical simulation of deep excavation, two dimensional finite element code of PLAXIS v8.6 has been used in this study, The general procedure for deep excavation analysis in numerical simulation include the creation of geometric model, generation of finite element mesh, execution of finite element calculation, and evaluation of output result. The analysis was carried out by assuming plane strain condition. In this deep excavation analysis, two soil constitutive models were selected for comparing support wall deflections and deformation analysis. The linear elastic-perfectly plastic Mohr–Coulomb model contains five parameters, and the advanced Hardening Soil model contains ten input parameters. The support system, contiguous pile wall has been modeled as plate element and the anchors as node-to-node anchor. The grouting body simulated as geo-grid element. The adjacent building can be considered as simple elastic beam as proposed by Potts and Addenbrooke [4] and modeling can be done as plate element in Plaxis.

4.2 Parametric Study of Contiguous Pile Wall

For the parametric study of retention system, the pile diameter (d), anchor spacing (L_s), and pre-stress force on settlement and lateral wall deflection have been considered for different loading condition.

4.2.1 The Effect of Pile Diameter on Settlement and Lateral Wall Deflection

The deflection of supporting system in deep excavation depends on its stiffness. As it's indicated in Fig. 1, the stiffness increase with increasing pile diameter for the model listed in Table 1. The deflections of pile support have been determined from Plaxis simulation for different pile diameter by assuming the pile as plate and elastic element using both HS and MC models.

For the parametric study, the loading condition (Li) and diameter of piles (d) both vary by fixing the building load distance (D). The neighboring building distance (D = 4 m) and different loading condition have been applied to determine the maximum lateral wall deflection. The relationship between maximum lateral wall deflection and support stiffness has been shown in Table 2 for different loading condition.

From this analysis, it has been noted that the maximum lateral wall deflection occurs at smaller values of pile stiffness in both MC and HS models. On the other hand, the bending moment increases with increasing support stiffness for both cases as indicated in Figs. 2 and 3. The maximum lateral wall deflection is expressed in terms of pile diameter in Table 2.

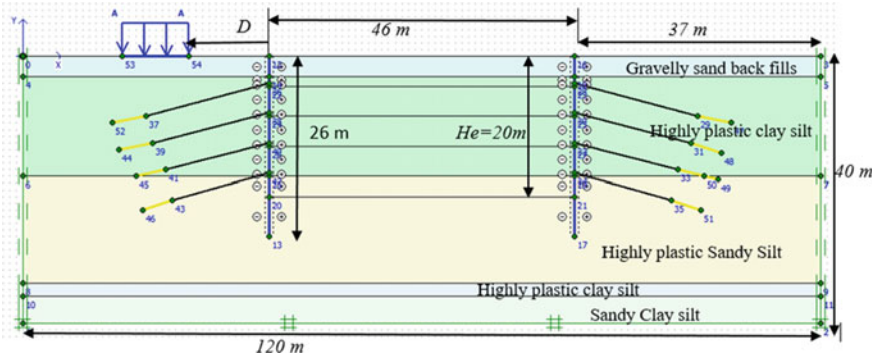

Fig. 1 Plaxis 2D modeling of deep excavation support system

Table 1 Stiffness parameter of contiguous pile wall for different diameter

Parameter	Name	Contiguous pile parameter			
Model no.		Pile-1	Pile-2	Pile3	Pile-4
Contiguous pile wall	(m)	0.4	0.6	0.8	1.0
Diameter	d, (m)	0.02	0.02	0.02	0.02
No. of reinforcement	No.	8	11	15	18
Area of reinforcement	A_s, (m^2)	0.00251	0.00346	0.00471	0.00565
Weight	W, kN/m	8.66	12.99	17.32	21.65

Table 2 maximum lateral wall deflection (δhm) with Pile diameter (d)

Load Type	Model	
	Mohr–Coulomb	Hardening Soil
L-1	$\delta_{hm} = 74.311e^{-0.138d}$	$\delta_{hm} = 66.705e^{-0.175d}$
L-2	$\delta_{hm} = 75.288e^{-0.149d}$	$\delta_{hm} = 66.318e^{-0.163d}$
L-3	$\delta_{hm} = 74.481e^{-0.133d}$	$\delta_{hm} = 66.885e^{-0.176d}$
L-4	$\delta_{hm} = 73.197e^{-0.105d}$	$\delta_{hm} = 67.202e^{-0.191d}$

4.2.2 Effect of Horizontal Anchor-Spacing (S) on Settlement and Lateral Wall Deflection

For the parametric study of contiguous pile walls, the horizontal anchor spacing is another important parameter for the study of wall deflection and maximum settlement in deep excavation. For the simulation process, five anchor spacing has been considered as shown in Table 3.

For this analysis, the neighboring-building distance (D_2) is assumed to be at 4 m from the face of excavation and the maximum lateral wall deflection is obtained by varying the anchor lateral spacing (S). The soil stratification is similar to the initial model. The contiguous pile walls diameter (d_3) is taken as 0.8 m for both MC and HS

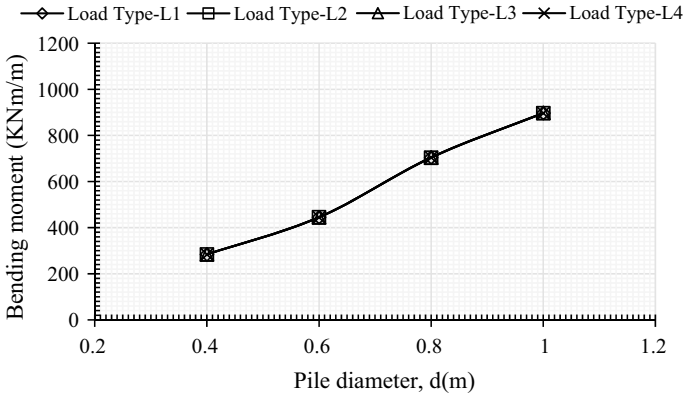

Fig. 2 Variation of maximum bending moment with support stiffness in MC model

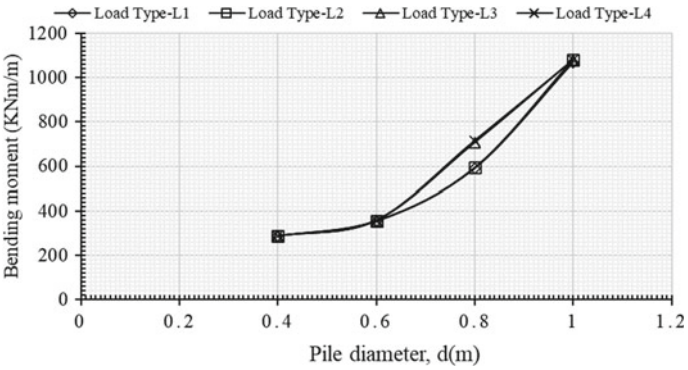

Fig. 3 Variation of maximum bending moment with support stiffnessin HS model

Table 3 Parameters for horizontal anchor spacing (S)

Anchor spacing, S(m)	S_1	S_2	S_3	S_4	S_5
	1.4	1.6	1.8	2.0	2.2

models. The variation of maximum wall deflection with horizontal anchor spacing is given by the equation as indicated in Table 4. It is observed that the maximum support wall deflection increases with increasing anchor spacing (S) and neighboring building load.

In the Mohr–Coulomb model for the loading condition L4, the maximum lateral wall deflection (δ_{hm}) is given by $\delta_{hm} = 68.97e^{0.0138S}$. From Table 4, for an anchor spacing of 1.8 m, the maximum lateral wall deflection calculated as δ_{hm} = 68.97e0.0138*1.8 = 70.70 mm. Similarly, for the same loading condition in HS model the maximum lateral wall deflection (δ_{hm}) is calculated as $\delta_{hm} = 40.76e^{0.0187*1.8}$

Table 4 Maximum lateral wall deflection (δhm) with horizontal anchor spacing (S)

Load type	Model	
	Mohr–coulomb	Hardening soil
L-1	$\delta_{hm} = 67.80e^{0.0171S}$	$\delta_{hm} = 38.20e^{0.0406S}$
L-2	$\delta_{hm} = 67.51e^{0.0215S}$	$\delta_{hm} = 39.25e^{0.0291S}$
L-3	$\delta_{hm} = 67.94e^{0.0207S}$	$\delta_{hm} = 39.95e^{0.0536S}$
L-4	$\delta_{hm} = 68.97e^{0.0138S}$	$\delta_{hm} = 40.76e^{0.0187S}$

= 42.15 mm. From this result, it has been observed that the maximum lateral wall deflection obtained using MC model is about 40.4% greater than those obtained from HS model.

As it has been indicated in Figs. 4 and 5, the wall bending moment increases gradually with increasing horizontal anchor spacing. The estimated bending moment

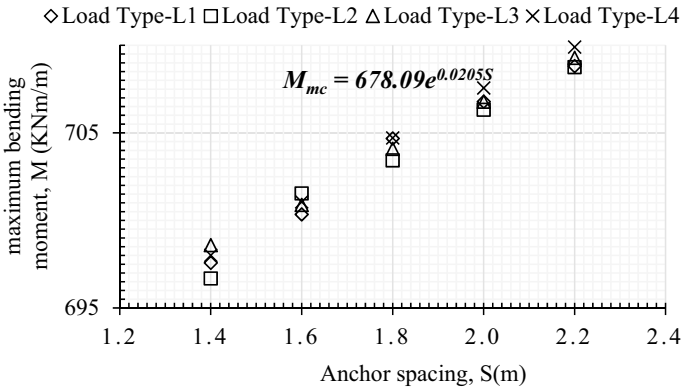

Fig. 4 Variation of maximum bending moment with anchor spacing in MC model

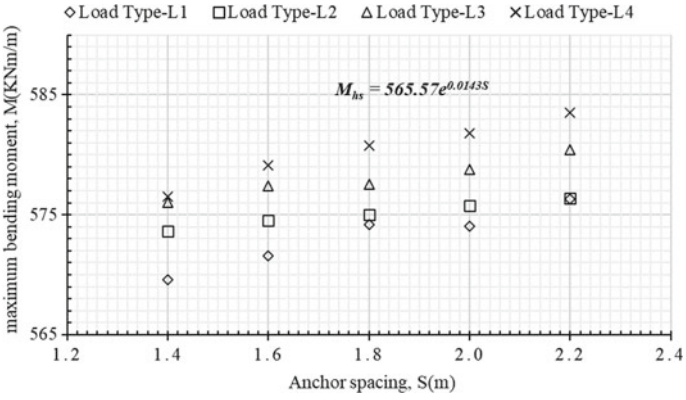

Fig. 5 Variation of maximum bending moment with anchor spacing in HS model

obtained in Mohr–Coulomb model is much higher than Hardening Soil model. This indicates that Mohr–Coulomb model overestimates the maximum lateral wall deflection as compared to Hardening Soil model. For loading condition L4 as the anchor spacing (S) increases by 0.2 m, the maximum bending moment increase with 0.29% and 0.41% in HS and MC model, respectively.

4.2.3 Effect of Anchor Pre-stress Force on Settlement and Lateral Wall Deflection

For this parametric study, the maximum lateral wall deflection and settlement were obtained by varying pre-stress force with depth of excavation. The neighboring building distance (D2), pile diameter (d3), depth of excavation (He), and loading condition L4 are assumed to be constant as shown in Table 5.

From this analysis, the maximum lateral wall deflection increase with decreasing the anchor pre-stress force in both MC and HS models. The lateral wall deflection decreases rapidly below the maximum depth of excavation for all pre-stressing condition in MC model.

Figures 6 and 7 shows the variation of horizontal wall deflection with depth and pre-stress force wrt MC and HS models respectively. Whereas, Figs. 8 and 9 shows variation of wall bending moment with depth and pre-stress force wrt MC and HS models, respectively. From this analysis result, the bending moment occurs for

Table 5 Pre-stress force of anchor system (p)

Anchor pre-stress force, P (kN/m)	P_1	P_2	P_3	P_4
	362	462	562	662

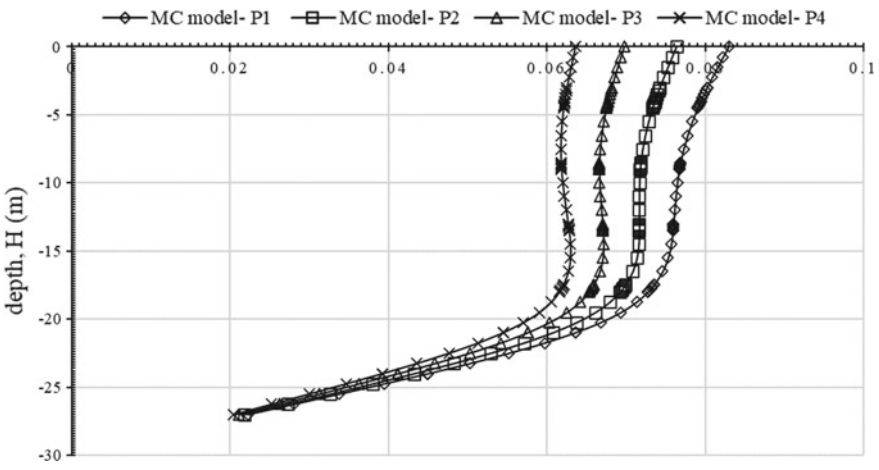

Fig. 6 Variation of horizontal wall deflection with depth and pre-stress force in MC model

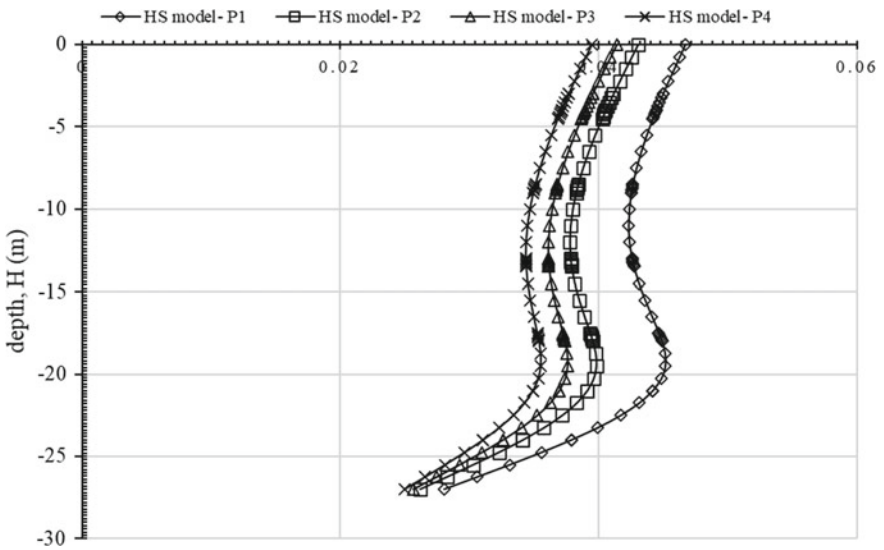

Fig. 7 Variation of horizontal wall deflection with depth and pre-stress force in HS model

higher values of pre-stress force to depth of about 10 m and then decreases within increasing the pre-stress force to depth of excavation (He). The maximum bending moment occurs at about a depth (He) of 20 m for all pre-stress force.

4.2.4 Effect of Depth of Excavation on Contiguous Pile Wall

For this parametric study, the pile diameter d3 = 0.8 m, neighboring building distance D2 = 4 m, and loading condition L1 considered. Lateral deflection of contiguous pile wall and bending moment determined by varying the depth of excavation. As the depth of excavation increases, the horizontal ground deformation increases to certain maximum value and then decreases as indicated in Fig. 10. The bending moment decreases at location of Anchor installation as indicated by sharp curve from Fig. 9 (Fig. 11).

5 Conclusions

1 Maximum lateral wall deflection occurs at smaller values of pile stiffness in both MC and HS models. Whereas, the bending moment increases with increasing support stiffness.
2 For horizontal anchor spacing, the maximum lateral wall deflection obtained using MC model is about 40.4% greater than those obtained from HS model.

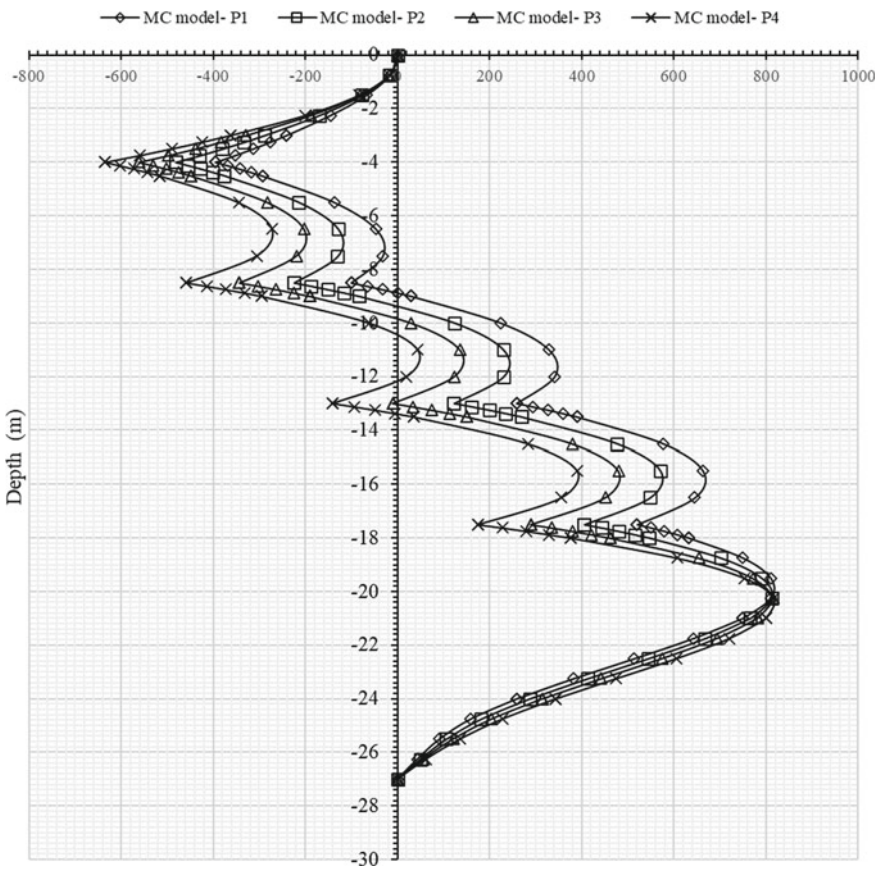

Fig. 8 Variation of wall bending moment with depth and pre-stress force in MC model

For loading condition L4 as the anchor spacing (S) increases by 0.2 m, the maximum bending moment increase with 0.29% and 0.41% in HS and MC model respectively.

3 The bending moment occurs for higher values of pre-stress force to depth of about 10 m and then decreases within increasing the pre-stress force to depth of excavation (He). The maximum bending moment occurs at about a depth (He) of 20 m for all pre-stress force.

4 As the depth of excavation increases, the horizontal ground deformation increases to certain maximum value and then decreases thereafter. The bending moment decreases at location of Anchor installation as indicated by sharp curve.

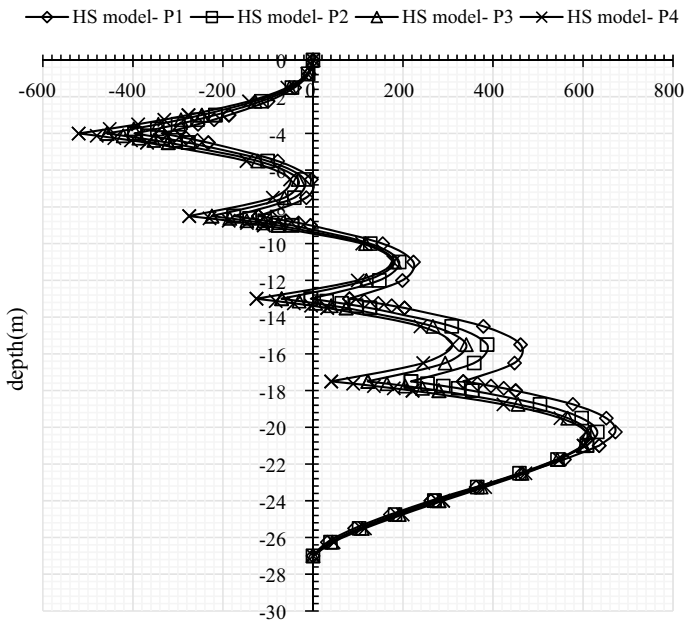

Fig. 9 Variation of wall bending moment with depth and pre-stress force in HS model

Fig. 10 Variation of bending moment with depth of excavation in both HS & MC model

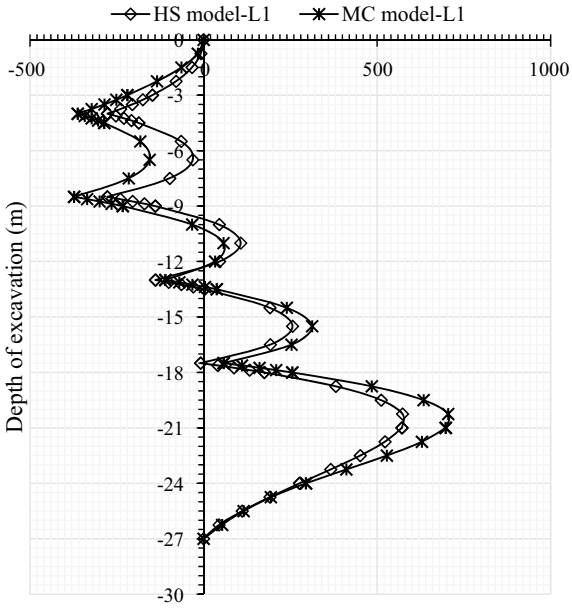

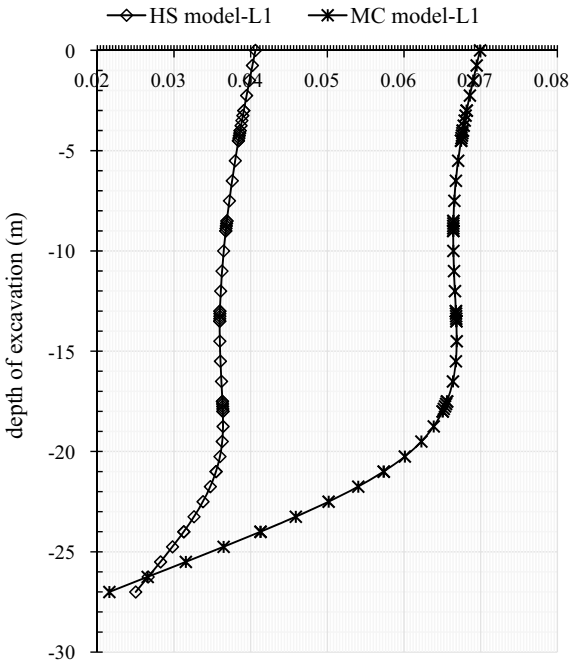

Fig. 11 Variation of lateral wall deflection with depth of excavation in both HS & MC model

References

1. Coulomb: Essai sur une application des regles des maximis et minimis a quelques problemes de statique relatifs a l'architecture. Memoires del'Academie Royale pres Divers Savants 7 (1776)
2. Niousha, R. et.al.: Comparison of empirical and numerical methods in tunnel stability analysis. Int. J. Mining Reclamation Environ. **26**(3), 261–270 (2011)
3. Ou, et al.: Three-dimensional deformation behavior of the Taipei National Enterprise Center (TNEC) excavation case history. Canadian Geotechn. J. **37**(2), 438–448 (2000)
4. Potts and Addenbrooke: A structures influence on tunneling induced ground movements. Proceedings of the Institution of the Civil Engineers, Geotechnical Eng. **125**(2), 109–125 (1997)
5. Rankine, W.: On the stability of loose earth. Philos. Trans. Royal Soc. London **147**, 9–27 (1857)
6. Seok et al.: Evaluation of ground and building settlement near braced excavation sites model testing. Can. Geotechn. J. **38**, 1127–1133 (2001)
7. Simpson, B.N. et al.: Collapse of the Nicoll Highway Excavation, Singapore. 4th International Conference on Forensic Engineering. London, UK, ICE (2008)
8. Simpson et al.: Collapse of the Nicoll Highway Excavation. London, UK, ICE (2008)
9. Terzaghi, K., Peck, R.: Soil Mechanics in Engineering Practice. Wiley, New York (1967)
10. Terzaghi, K.: Theoretical Soil Mechanics. Wiley, New York (1943)
11. Zuhair, A.H.: Simulation of deep excavation in sand by finite element using hardening soil model (HSM). J. Eng. Technol., University of AL- Mustansiriya /Baghdad **29**(15) (2011)

Performance Evaluation of Controlled Blasting and Prediction of Attenuation Relation for Charnockite Rocks

N. Nitheesh, G. Padmanabhan, Sudipta Chattopadhyaya, and B. P. C. Rao

1 Introduction

Foundations of nuclear power plant structures, dams, and other heavily loaded structures are often rest on competent rock strata which are moderate to slightly weathered rock. To reach this level, excavation in rock strata is required and is often carried out by mechanical chiseling, hydraulic splitting, expansive grouts, and blasting. However, the choice of hard rock excavation depends on the quantum of rock to be excavated, strength and type of the rock, and safety of adjacent structures. Controlled blasting is an advanced rock excavation technique which is employed for hard rock (like chanockite type) excavation, where in both production and safety of the existing structures are ensured.

Excavations using controlled blasting involves use of explosives and are detonated using non-electric detonators. These release shock waves and these shock waves exert pressure on the rock resulting into fragmentation of rock masses. In controlled blasting, the blasting is designed with suitable burden, spacing, and depth of blast holes, stemming, and delayed detonation to ensure the required fragmentation and safety of adjacent structures. Performance of controlled blasting is usually evaluated using a parameter Peak Particle Velocity (PPV) and this value is limited to that prescribed by Directorate General of Mines Safety (DGMS) [1] in India to minimize the damage of existing structure. By knowing the required PPV, the charge

N. Nitheesh (✉)
Scientific Officer (SO)-D, FRFCF, Indira Gandhi Centre for Atomic Research, Kalpakkam, India

G. Padmanabhan
SO-F, FRFCF, Indira Gandhi Centre for Atomic Research, Kalpakkam, India

S. Chattopadhyaya
SO-G, FRFCF, Indira Gandhi Centre for Atomic Research, Kalpakkam, India

B. P. C. Rao
Outstanding Scientist, FRFCF, Indira Gandhi Centre for Atomic Research, Kalpakkam, India

C. N. V. Satyanarayana Reddy et al. (eds.), *Stability of Slopes and Underground Excavations*, Lecture Notes in Civil Engineering 185,
https://doi.org/10.1007/978-981-16-5601-9_26

Table 1 Predictor relations for attenuation of blast waves

Proposers of attenuation relations	Equations
United States Bureau of Mines (USBM); DGMS (by Duvall and Fogelson) [5, 10]	$v = K\left(\frac{R}{\sqrt{Q}}\right)^{-B}$
Ambraseys-Hendron [6]	$v = K\left(\frac{R}{\sqrt[3]{Q}}\right)^{-B}$
Langerfors-Kihlstrom [7, 8]	$v = K\left(\frac{R^{1/3}}{\sqrt{Q}}\right)^{-B}$
Indian Standard (IS) predictor [9]	$v = K\left(\frac{R^{2/3}}{Q}\right)^{-B}$

per delay can be estimated by conducting a site-specific trial blast study. The PPV is usually expressed in terms of scaling distance and site-specific constants [3] and the expression is given in Eq. (1).

$$V = K \times SD^{-B} \tag{1}$$

where,

K, B; are site constants

V is the PPV in mm/s

SD is the scaling distance.

Scaling distance (SD) is defined as the ratio of distance at which PPV measured from source to the charge to the quantity of explosive, used per delay in blasting. There are various relations available in the literature for assessment of PPV in terms of SD. Most commonly used relations [4] are that proposed by United States Bureau of Mines (USBM), Langerfors&Kihlstrom, Ambraseys-Hendron, and Bureau of Indian Standard and are indicated in Table 1.

These predictive models are proposed based on size of explosive charges, shot to measurement distance, explosive types, method of initiation, geology of site, type of rock, etc.

2 Geology of the Site and Trial Blast Studies

The study area is located along East Cost of India, and the site consists of 8–10 m of course to medium-grained loose to dense sand. This layer is followed by 4–5 m of greenish Clayey/sandy layer. Subsequent to this clay layer, highly weathered, decomposed & disintegrated rock is observed and the foundation strata of Weathering grade III rock is available at a depth of 15–20 m, which is charckoite in nature. However, the slightly weathered to fresh and strong to very strong fractured rock is encountered at various places which required to be excavated through controlled blasting. The view

Fig. 1 View of the excavated pit

of the excavated pit is shown in Fig. 1. In situ compressive strength of exposed rock was determined by Schmidt rebound hammer (Fig. 2) and the rebound test report shows, in situ compressive strength range 38–63 MPa.

Subsequently, trial blast studies were conducted and Peak Particle velocity was monitored at four locations. From the observed data, a site-specific relation was established between PPV and charge per delay and the relation is given in Fig. 3.

The V_{max} (PPV) for 50% confidence is given in Eq. (2).

$$V_{max} = 178.6\left(D\sqrt{Q}\right)^{-1.19} R^2 = 0.79 \tag{2}$$

Fig. 2 Assessment of in situ strength of rock

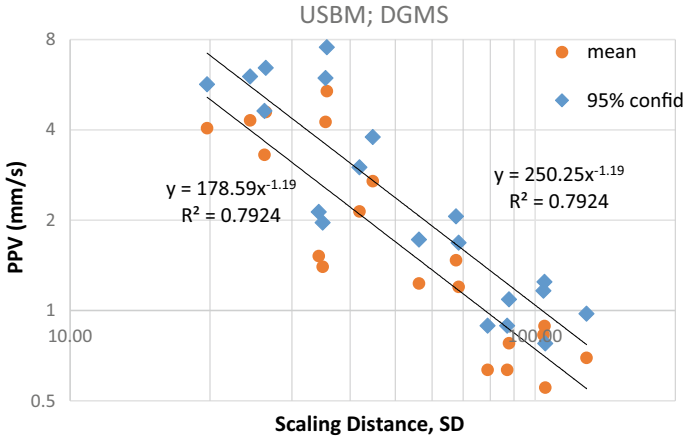

Fig. 3 Relation between PPV and Scaled Distance from trial blast studies

Table 2 Results of statistical analysis

Property	Value
Mean	0.208
SD, standard deviation	0.334
SE, standard error	0.075
Z (confidence coeff) for 95% confidence level	1.96
95% Confidence band upper level, ME = SE x Z	1.401

Statistical analysis of the trial blast data was carried out to determine the mean, standard deviation, and margin of error of all the data points and is shown in Table 2.

Using these values, PPV for 95% confidence was predicted and shown below in Eq. 3. The upper bound value for 95% confidence level is indicated in Fig. 3.

$$V_{max} = 250.24\left(D/\sqrt{Q}\right)^{-1.19} \text{mm/s}.R^2 = 0.79 \quad (3)$$

The dominant ground vibration frequencies in all the trial blast cases were more than 8–40 Hz. The permissible Vmax (Peak particle velocity) as per [2] for sensitive and critical structures is 5 mm/s for the frequency range of 8–25 Hz. The permissible peak particle velocity for various dominant frequency as per [2] is given in Table 3. As a conservative approach toward safety of sensitive structures located at farther distances, where the occurrence of low frequency waves cannot be negated, the frequency is considered lesser than 8 Hz, conservatively. Accordingly, the safe permissible limit of ground vibration has been considered as 2 mm/s for analysis and safe permissible maximum charge per delay was estimated.

Table 3 PPV limits in mm/s as per DGMS Guidelines

Sl no	Type of structure	Dominant frequency		
		<8 Hz	8–25 Hz	>25 Hz
1	Domestic houses	5	10	15
2	Industrial buildings	10	20	25
3	Buildings of historical importance	2	5	10
Building belonging to the owner				
1	Domestic House	10	15	25
2	Industrial Buildings	15	25	50

3 Analysis of Actual Blast

The actual blasts were monitored at different locations and PPV were observed for different specific charge. The observed PPV value was compared with the PPV value predicted from the site-specific attenuation relation Eq. (3) established from trial blast studies and indicated in Fig. 4. The comparison indicates that the PPV values observed are around 40% higher than those predicted from Eq. 3. The best fit line of PPV value for 50% confidence level is indicated in Eq. (4). The best fit line has a better correlation coefficient compared to that obtained from trial blast studies.

$$V_{max} = 356.96\left(D/\sqrt{Q}\right)^{-1.203} \text{mm/s } R^2 = 0.905 \tag{4}$$

Further, statistical analysis was carried out and 95% confidence level was estimated for PPV value and the relation is shown in Eq. (5) and Fig. 5.

$$V_{max} = 414.37\left(D/\sqrt{Q}\right)^{-1.203} \text{mm/s } R^2 = 0.905 \tag{5}$$

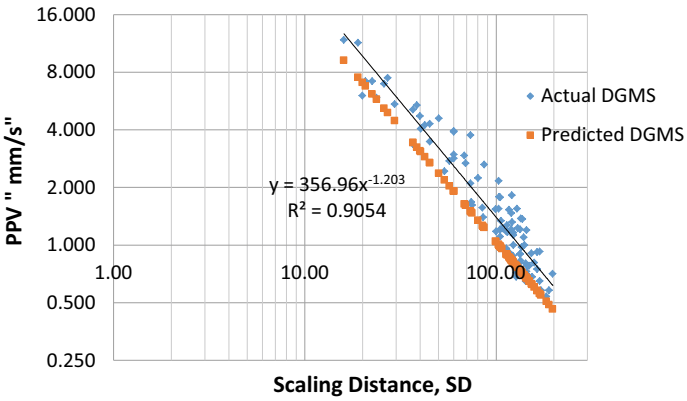

Fig. 4 Comparison of PPV monitored and predicted from site-specific relation

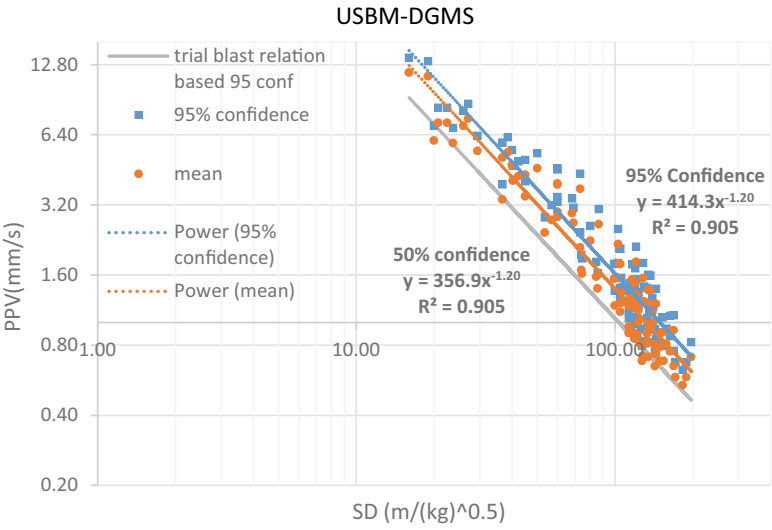

Fig. 5 Site-specific relation for PPV with 95% confidence

The empirical relations proposed by other researchers as indicated in Table 1 was used for prediction of PPV value and the predicted values were compared with the actual field data. The relations are indicated in Figs. 6 and 7. Statistical site-specific parameters obtained for these relations are shown in Table 4.

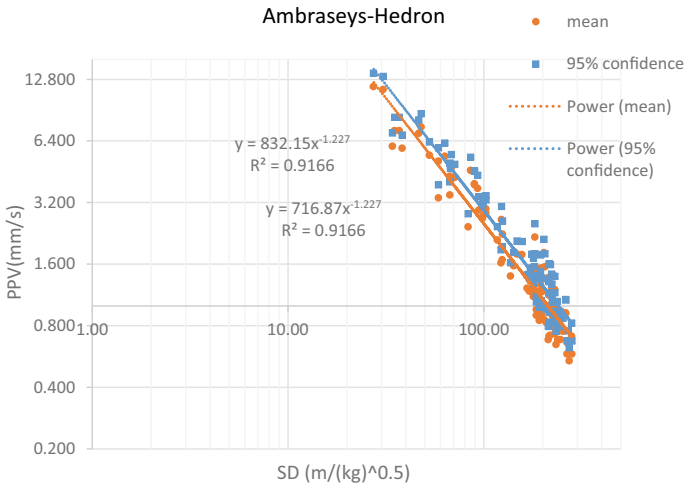

Fig. 6 Relationship between PPV and scaling distance for actual blast study based on Ambraseys-Hedron

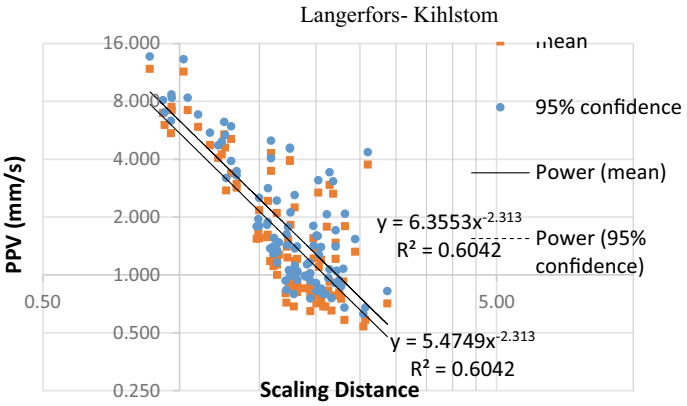

Fig. 7 Relationship between PPV and scaling distance for actual blast study based on Langerfors-Kihlstrom

Table 4 Comparison of site-specific parameters for various empirical relations

Predictor relation name	Site constants			Site constants	
	K	B	R^2	K95%	B95%
USBM (adopted by DGMS)	356.96	1.203	0.9054	414.37	1.203
Ambraseys-Hedron	716.87	1.227	0.9166	832.15	1.227
Langerfors-Kihlstrom	5.475	2.313	0.6042	6.3553	2.313
Trial Blast	178.67	1.19	0.7922	250.38	1.19

The PPV values predicted by Ambrasey's shows a better correlation compared to that predicted from Langerfors-Kihlstrom and are comparable to the actual PPV values. The analysis has indicated that the DGMS criteria provides lesser PPV values in comparison of with actual field monitored value, and hence the specific charges can be higher and hence not conservative. Considering this, charge per delay to limit the PPV to 2 mm/s is calculated for various empirical relations shown in Table 1 and the results are presented in Fig. 8.

It is evident from Fig. 8 that, Ambraseys-Herdon empirical formulation is conservative as the charge per delay required to limit the PPV is least among all the relations. Also this formulation shows better correlation coefficient compared to other relations. The site-specific relation obtained from trial blast studies is not conservative for distances beyond 200 m is also evident from Fig. 8. This can be attributable to the limited number of PPV observations beyond 200 m during trial blast studies. The site-specific relation developed using Ambraseys-Herdon relation can be used for assessment of charge per delay required for controlled blasting in sites of similar geology.

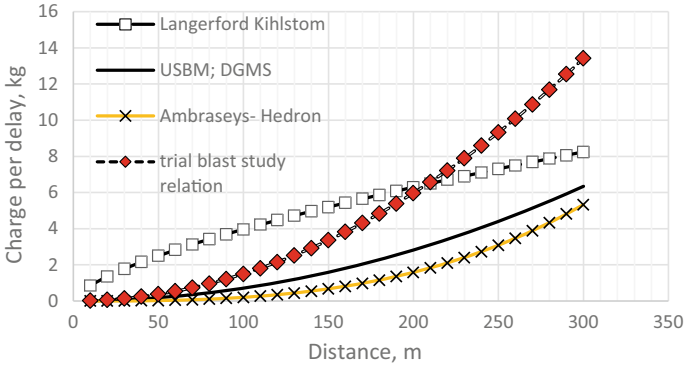

Fig. 8 Charge per delay for limiting PPV to 2 mm/s [2] for various empirical relation

4 Conclusions

The major conclusions, drawn from the study are

1. The PPV values observed during actual blast are higher than predicted using the site-specific relation established during trial blast employing DGMS relations.
2. Site-specific relation established from trial blast studies using DGMS correlations are not conservative for distance beyond 200 m and provides higher specific charge per delay in comparison with other relations.
3. Ambraseys-Hendron relation shows a better correlation and the predicted PPV values are comparable with the actual field values.
4. The site-specific relation established using Ambraseys-Hendron formulation provides least specific charge per delay and hence recommended for carrying out controlled blasting in the sites having similar geology of charnockite rocks.

References

1. Trial blast studies for design of safe blast patter for hard rock excavation at FRFCF project, A report on CSIR, CIMFR, Nagpur, 2014–2015
2. Circular on Damage of structures due to blast induced ground vibration in the mining areas, Director General of Mines Safety (DGMS Tech) (1997)
3. Silitonga, M: Prediction of ground vibration due to blasting, Ground movement and control related to coal mining symposium, pp. 74–81 (1986)
4. Parida, A., Mishra, M,K: Blast vibration analysis by different predictor approaches—a comparison. Procedia Earth Planetary Sci. **11**, 337–345, Elsevier (2015)
5. Duvall, W.I., Fogleson, D.E.: Review of criteria for estimating damage to residences from blasting vibration, USBM-I, 5968 (1962)
6. Ambraseys, N.R., Hendron, A.J.: Dynamic behaviour of rock masses. Rock mechanics in engineering practices. Wiley, London, pp. 203–207 (1968)

7. Langefors, U., Kihlstrom, B., Westerberg, H.: Ground vibrations in blasting. Water Power (1958)
8. Langefors, U., Kihlstrom, B.: The modern technique of rock blasting. Wiley, New York (1963)
9. Indian Standard Institute. Criteria for safety and design of structures subjected to underground blast. ISI Bull 1973; IS-6922
10. Nicholls, H.R,. Johnson, C.F., Duvall, W.I.: Blasting vibrations and their effect on structures, US Department of Interiors, Department of Mines

Embedded Retention Wall Design Practices Consequences and Measures

Govind Raj and Madan Kumar Annam

1 Introduction

The embedded retention walls systems offer constructive solutions for underground structures in crowded areas. The retaining wall analysis is influenced by the method of analysis used and parameters like drained/undrained analysis, wall flexibility, effects of groundwater table, over excavation and effects of surcharge.

Common analysis methods used for the design of the embedded retaining structures are limit equilibrium method, subgrade reaction method and finite element method. The purpose of the study is to identify the wall behavior by using these three approaches.

In addition to this, a comprehensive parametric study has been carried out to show the influence of various parameters as indicated above to understand the behavior of the retaining walls.

2 Method of Analysis and Its Influence

2.1 Method of Analysis

Common analysis methods used for the design of the embedded retaining structures are limit equilibrium method, subgrade reaction method and finite element method.

G. Raj (✉)
Keller Ground Engineering India Pvt Ltd., Mumbai 400059, India
e-mail: govind@kellerindia.com

M. Kumar Annam
Keller Ground Engineering India Pvt Ltd., Chennai 600024, India
e-mail: madankumar@kellerindia.com

C. N. V. Satyanarayana Reddy et al. (eds.), *Stability of Slopes and Underground Excavations*, Lecture Notes in Civil Engineering 185,
https://doi.org/10.1007/978-981-16-5601-9_27

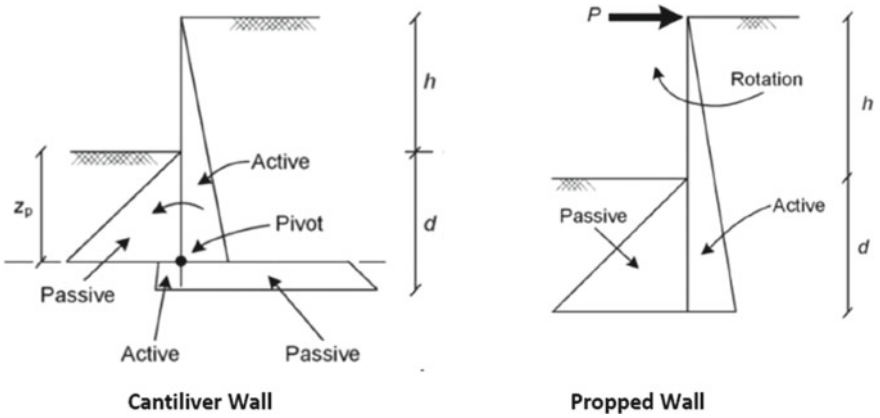

Fig. 1 Limit equilibrium analysis theories

2.1.1 Limit Equilibrium Method

Limit state equilibrium analysis is used to describe an analysis where the equilibrium of the wall is assessed under the action of linear, simple distributions of soil lateral pressures, usually calculated based on limiting (active and/or passive) lateral earth pressure coefficients. Cantilever/unpropped walls are assumed to rotate about a pivot at some depth below excavation level, whereas strutted/anchored walls rotate about the position of support. Cantilever walls rely on the support of ground to maintain horizontal and moment equilibrium whereas strutted/anchored wall relies on the support of ground and prop to maintain the equilibrium (Fig. 1).

2.1.2 Subgrade Modulus Method

The second approach is the subgrade reaction method in which the wall is modeled as a beam and the ground as a series of horizontal springs. This method considers the interaction between soil and structure which was ignored in the limit equilibrium approach. Wall displacements can be calculated by using this method (Fig. 2).

2.1.3 Numerical Modeling Method (FEM)

The third approach is the analysis using finite elements. It involves splitting the computational domain into smaller elements and finding solutions. It needs a good knowledge of soil behavior (Fig. 3).

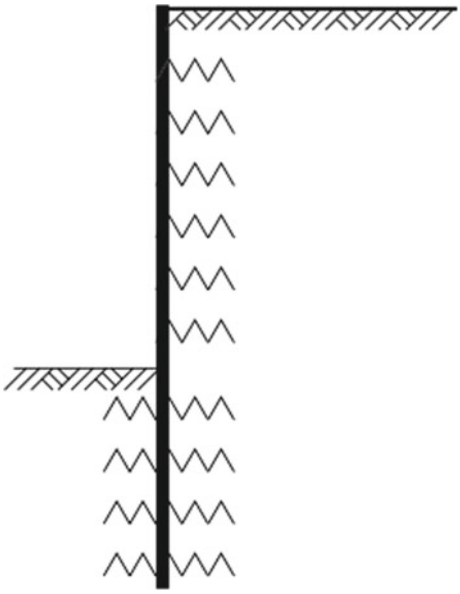

Fig. 2 Subgrade reaction methods

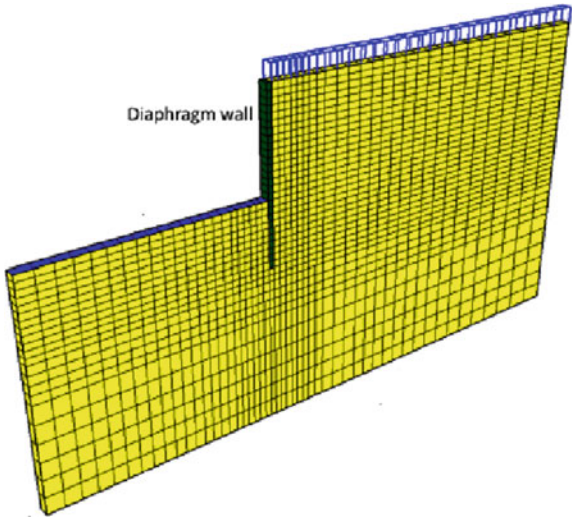

Fig. 3 Finite element method

2.2 Case Studies

Two examples are considered in this study to compare the results of three methods of analysis. The first case is a cantilever problem whereas the second case is a strutted wall. Wall forces, deflections and embedment are calculated and the results are discussed. Bending moments are computed based on the ULS combination of

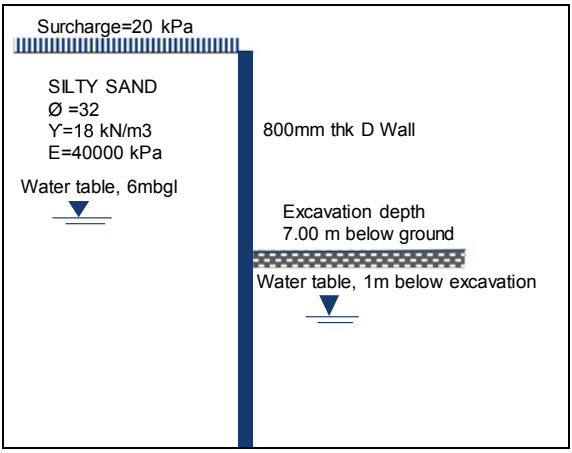

Fig. 4 Cantilever problem considered for the analysis

Table 1 Comparison of results for a cantilever wall

Item	Equilibrium method	Subgrade reaction method	Finite element method	% Variation in results
ULS bending moment (DA1C2), kNm/m [3]	1618	1545	1529	6%
Deflection at service condition (mm)	–	59	62	–

Eurocode 7 (DA1C2) [2] and at service conditions, whereas the deflections are checked at service conditions only. Wall friction of 0.67tan Ø and an effective stress approach are used.

Case 1: Cantiliver Example. A cantilever wall for 7 m excavation is considered for Case 1 (Fig. 4 and Table 1).

Case 2: Strutted Wall Example. Strutted walls for 7 m and 11 m excavation are considered for Case 2 (Fig. 5).

2.3 Observations

The results suggest that the bending moment in the ULS condition is comparable in all the methods for a cantilever case. However, there can be a considerable difference between the methods in the case of a strutted/anchored wall. This is due to the consideration of soil–structure interaction in the subgrade and finite element analysis, whereas limit equilibrium methods ignore soil–structure interaction (Table 2).

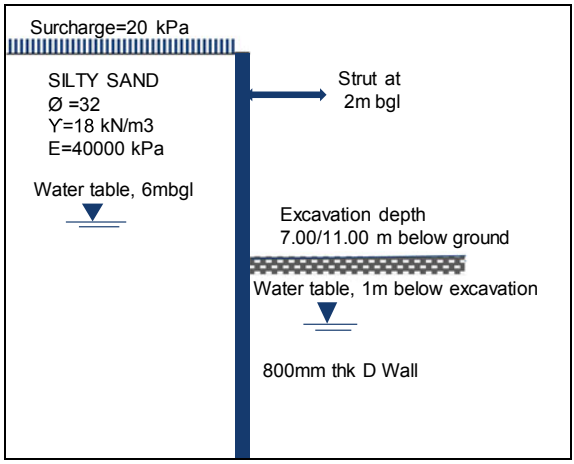

Fig. 5 Strutted wall considered for the analysis

It is found that for heavy loading cases, the difference in prop loads can be quite significant between the equilibrium method and subgrade/finite element approaches in the case of a strutted/anchored wall. The use of limit equilibrium methods can underestimate the prop loads in such a case, whereas FEM/subgrade reaction methods yield comparable results.

3 Parametric Study

Groundwater table variations, over excavation, surcharge, wall flexibility and stiffness of the soil affect the behavior of the retaining walls. The cantilever example shown in Sect. 2 is used to assess the influence of parameters on the retention wall design. The bending moments and factors of safety of embedment are computed based on the working conditions (SLS). Excavation depth of 7 m with a surcharge of 20 kPa for a 20 m deep wall is considered for the parametric study and Burlands Potts method is used to assess the factor of safety in the embedment. GWT assumed at 6 m below EGL (Fig. 6).

3.1 Effect of the Water Table

First, a parametric study is carried out by varying water table levels. It is found that water table levels are having a major impact on the behavior of the retention walls. The major reduction in the factor of safety and the sharp rise in the bending moment with the increase in water table explain the importance of consideration of water table variations for retention system (Fig. 7).

Table 2 Comparison of results for a strutted wall (7 m and 11 m excavations)

Item	7 m Excavation depth with strut (2mbgl)				11 m Excavation depth with strut (2mbgl)			
	Equilibrium method	Subgrade reaction method	Finite element methods	% Variation method	Equilibrium method	Subgrade reaction method	Finite element methods	% Variation method
Staged construction	No	Yes	Yes	–	No	Yes	Yes	–
ULS bending moment (kNm/m)	303	285	271	14%	1739	1637	1507	15%
ULS prop load (kN/m)	162	186	228	41%	393	530	508	35%
ULS shear force (kN/m)	134	137	144	8%	365	369	378	4%
Deflection at service condition (mm)	–	9	10	–	–	24	29	

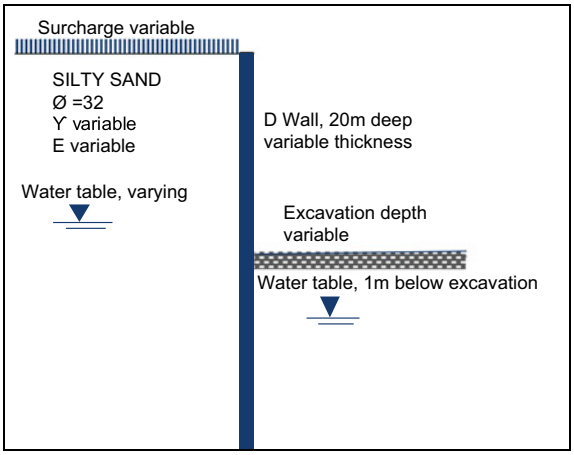

Fig. 6 Cantilever problem considered for the parametric studies

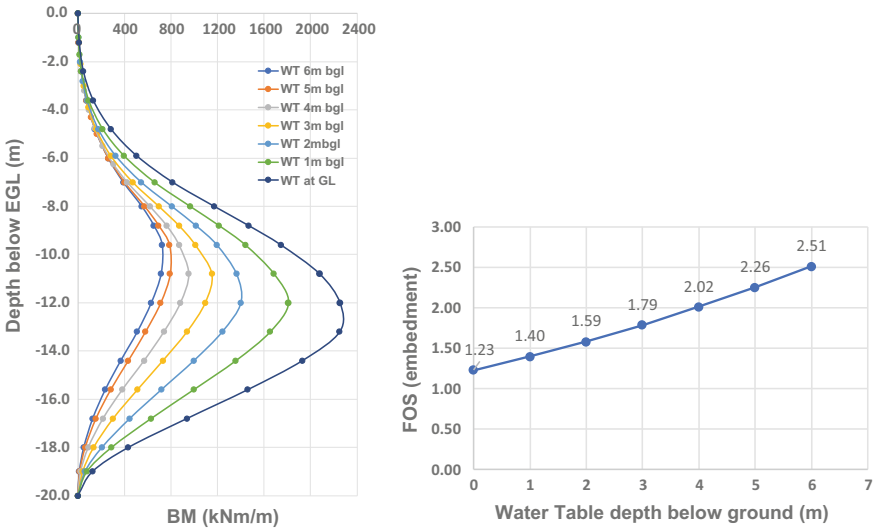

Fig. 7 Effect of water table variations on retaining walls

3.2 Effect of Over Excavations

Second, a parametric study is carried out by varying over excavation that can happen due to improper construction practices. Graphs below indicate the importance of consideration of over excavations in a retention wall design. Any increase in excavation depths is accompanied by a sharp increase in bending moments and a steep decline in the available factor of safety for embedment (Fig. 8).

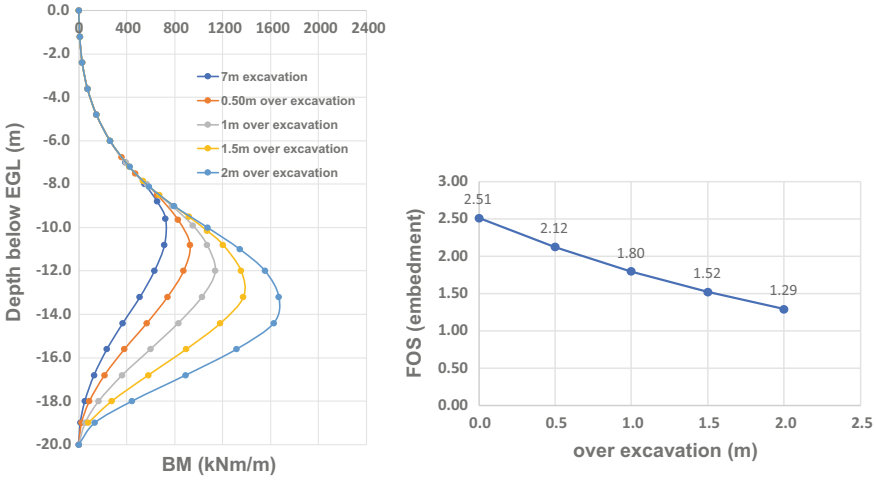

Fig. 8 Effect of over excavations on retaining walls

3.3 Effect of Surcharge

Third, a parametric study is carried out by varying surcharges. The bending moment is increased and the available factor of safety for embedment is reduced with an increase in a surcharge. Even though the variation is considerable, it is comparatively less as compared to variation in the water table and excavation depths (Fig. 9).

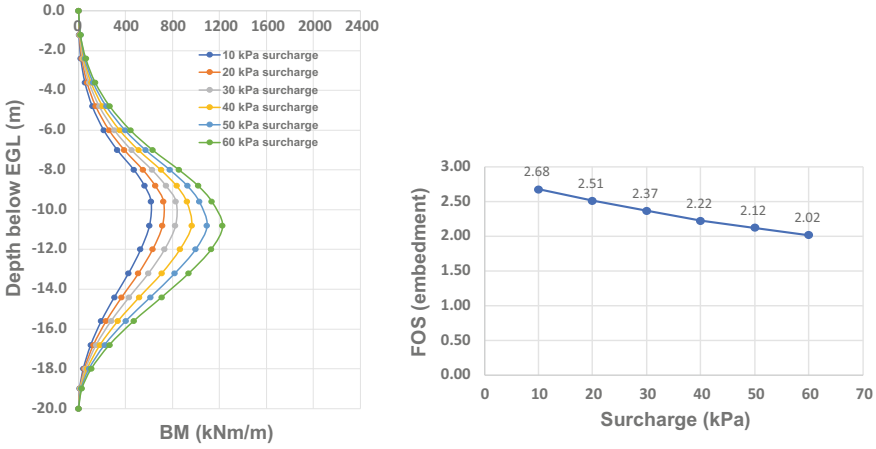

Fig. 9 Effect of surcharge on retaining walls

3.4 *Effect of Moment of Inertia of Wall*

Fourth, a parametric study is carried out by varying wall flexibility. The bending moments are increased, and deflections are reduced with an increase in diaphragm wall thickness. However, the influence of wall flexibility on the factor of safety of embedment is negligible (Fig. 10).

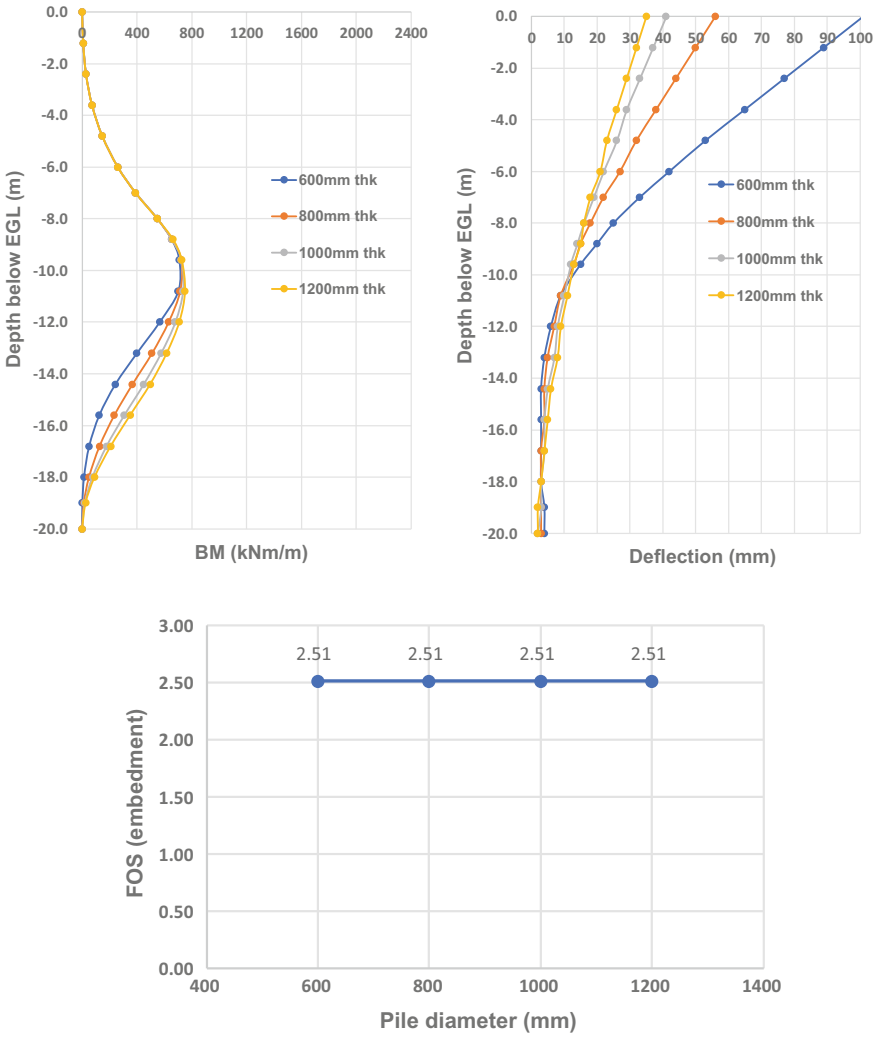

Fig. 10 Effect of wall flexibility on retaining wall performance

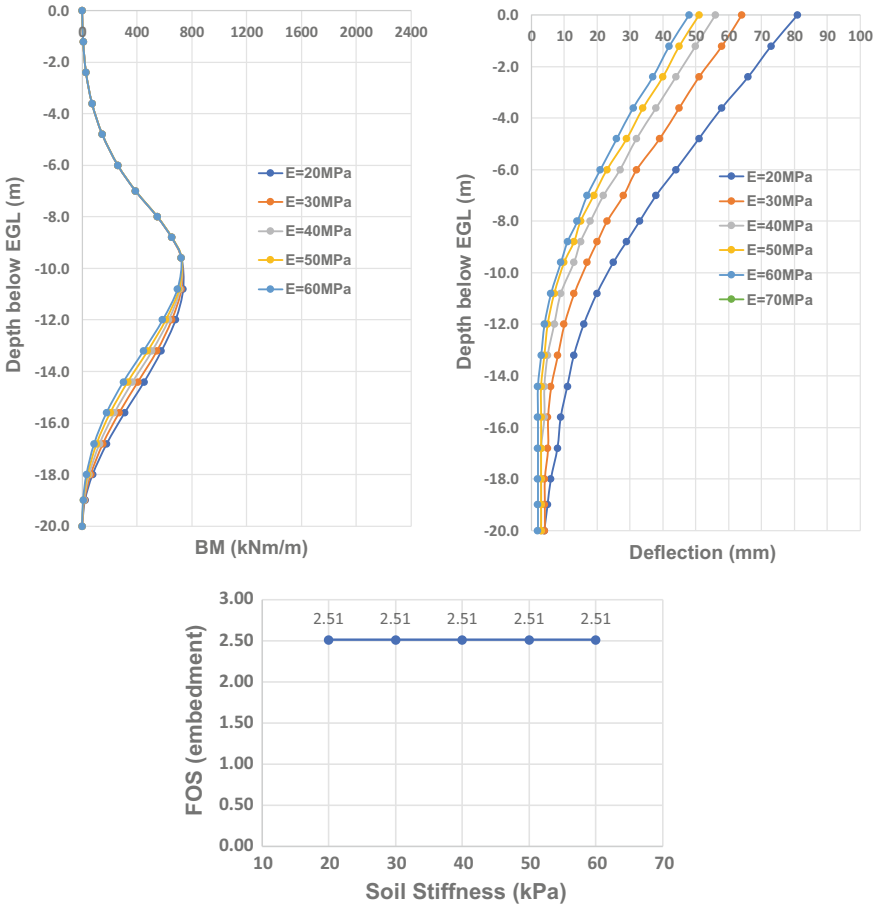

Fig. 11 Effect of soil stiffness on retaining walls

3.5 Effect of Soil Stiffness

Fifth, a parametric study is carried out by varying soil stiffness. There is a considerable impact on the wall deflections due to varying soil stiffness. However, the influence of soil stiffness on the factor of safety of embedment is negligible (Fig. 11).

4 Influence of Drained/Undrained Behavior of Soil

The distinction between drained (long-term)/undrained (short-term) analysis is very important in a retaining wall design. Any long-term exposure of the pit will eventually lead to the failure of the wall if it is designed only for undrained cases. The assessment

Table 3 Drained versus undrained applicability

	Undrained analysis (short-term)	Drained analysis (long-term)
Soft/very soft	Critical	–
Stiff/very stiff	–	Critical

Table 4 Drained analysis versus undrained analysis: results of case study

Item	Drained analysis	Undrained analysis
Required wall depth (m)	18.00	17.50
SLS bending moment (kNm/m)	735	415
Deflection at service condition (mm)	71	59

of which condition prevails depends on the in situ permeability of the soil. The following can be used as a guide to identifying which behavior prevails. The cantilever shown in Fig. 2 is used to find the influence of long-term and short-term effects. The bending moments and wall depths for the factor of safety of embedment (2.0) are computed based on the working conditions (SLS). The difference between the approaches can be found in Tables 3 and 4.

5 Discussions and Conclusion

This paper covers a study on the behavior of wall addressing method of analysis, i.e., limit equilibrium method, subgrade and finite element approaches. Further, a parametric study is carried out with the effect of the water table, over dig, surcharge, soil stiffness, wall flexibility and drained and undrained to understand the behavior of the wall.

This study suggests that the behavior of cantilever walls shows a similar trend for all three methods of analysis. On the contrary, a significant difference in behavior is seen for anchored/strutted walls (especially for heavily loaded cases), due to redistribution of stresses. A significant variation is observed especially for prop loads and bending moments among all three methods. The results of the study also confirm subgrade reaction or finite element methods are appropriate for analysis of deeper/anchored/strutted walls.

Retention system analysis using undrained parameters can create an unfavorable environment in excavation pits. Hence, it is suggested to check analysis for drained conditions addressing the long-term stability of the wall. Water table variations and over excavations have considerable influence on the retaining wall. The influence of surcharge has a moderate impact. Soil stiffness and wall flexibility have less impact on the embedment depth but significant influence on the wall movements.

References

1. CIRIA C760: Guidance on Embedded Retaining Wall Design (2017)
2. BS 8002: Code of Practice for earth retaining structures (1994)
3. BS EN 1997- Part 1: Eurocode 7. Geotechnical design (2004)

Effect of Overburden Pressure and Soil Parameters on Tunnel-Induced Ground Settlement

Chiranjib Sarkar, Sibapriya Mukherjee, and N. Kumar Pitchumani

1 Introduction

The underground tunneling is gaining popularity day by day in improving the surface space congestion problem of the urban transportation network. Every developing city is planning to construct underground structures, tunnels for metros, subways and other utilities. The construction of an underground tunnel usually leads to some disturbance on the surface of the soil, particularly settlement. Surface settlements due to underground tunneling are generally caused by stress relief and subsiding caused by support movement during excavation. Therefore, underground tunnel design requires a proper estimation of ground settlement for the safe and economically efficient construction of underground tunnel structures. The purpose of the present study is to review the current approaches of evaluating, measuring and preventing surface settlement as well as to develop a correlation between tunnel-induced ground settlement with overburden pressure and soil parameters. However, it is not to be denied that every project has its own uniqueness and it should be evaluated on a case-by-case basis by experts, as well as the available literature.

A cost-effective and safe design of tunnel structure should be in such a way that its impact on the adjacent structures should be as minimum as possible during construction and service. The main objective of calculating settlement by predictive methods is to propose a reasonable estimate of ground settlement. Peck and Schmidt (1969) assumed a geometric form of settlement profile, specifically the shape of

C. Sarkar (✉)
SAECOM India Pvt Ltd, New Town, Kolkata 700156, India

S. Mukherjee
Civil Engineering Department, Jadavpur University, Kolkata 700032, India

N. Kumar Pitchumani
AECOM India Pvt Ltd, T. Nagar, Chennai 600017, India

C. N. V. Satyanarayana Reddy et al. (eds.), *Stability of Slopes and Underground Excavations*, Lecture Notes in Civil Engineering 185,
https://doi.org/10.1007/978-981-16-5601-9_28

settlement trough above the tunnel which is represented by normal distribution curve (error function curve) [1]. This concept is well accepted as the very basic form of surface settlement profile. Settlement trough above the tunnel could be estimated by the error function curve shown in Fig. 1.

A more generalized form of normal distribution curve (error function curve) in three-dimensional space was derived by Attewell and Woodman (1982). However, New and Reilly (1991) discovered that the flexibility of the finite element model assists to understand the movements in a much better way. Ground movement and ground settlement depends on several factors, which include (i) geological and geotechnical conditions, (ii) tunnel depth and size, (iii) excavation methodology and (iv) the quality of work. It is known that a shallow-depth tunnel tends to have a relatively greater effect on the ground than the deeper one [2]. The ground settlement varies with the variation of subsurface deposits and various depths of the tunnel. The present paper covers a parametric study on a 6.3 m outer diameter typical circular tunnel structure having different depths of 9.7 m, 10.6 m, 12.8 m and 13.6 m, encountering varying soil layers of clayey silt, sandy silt and silty sand. With different tunnel

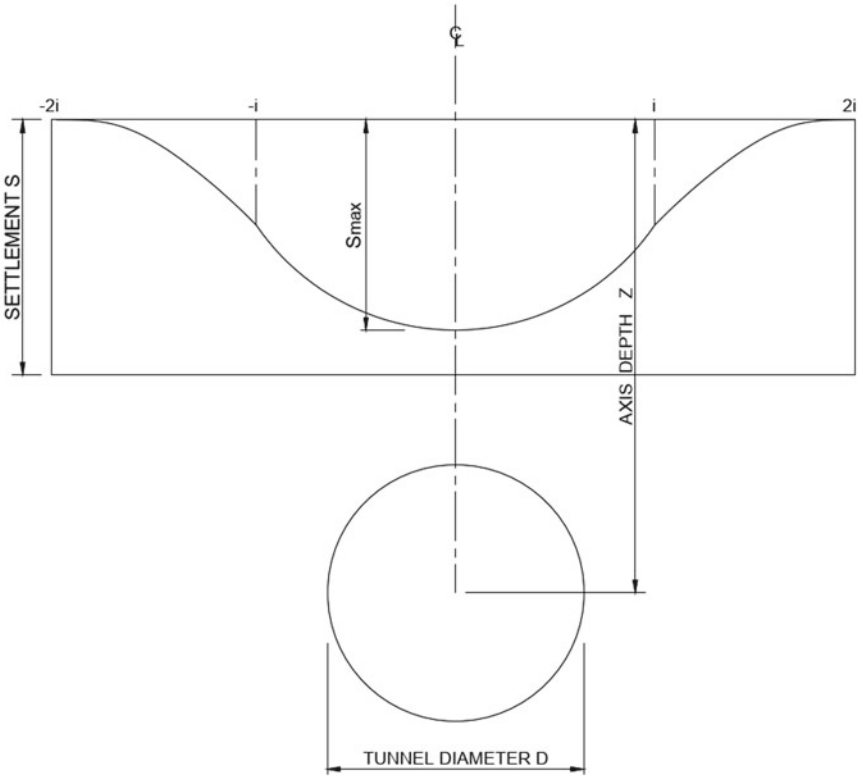

Fig. 1 Normal distribution curve (error function curve) to represent the cross-section of settlement trough

depths, the effects of various overburden pressures and difference in soil parameters on ground settlement have been logged to develop a correlation between ground settlement with tunnel depth and soil parameters. Also, a set of numerical models in the finite element method (FEM) has been developed to compare the results obtained from the analytical method as well as field data recorded at the project site.

2 Methodology

2.1 An Overview

The present paper discusses different approaches in predicting surface settlement associated with tunnel construction. In addition, this paper deals with different analytical, empirical and numerical methods to analyze the problem of tunnel-induced ground settlement. From various literature works, it has been observed that patterns of a settlement can be drawn with the help of different approaches mentioned below:

A. Analytical solution which includes (i) elasticity solution and (ii) Sagaseta's solution
B. Empirical solutions and
C. Numerical solutions

A. Analytical solutions. An analytical solution exists for a point load acting below the surface of an elastic half-plane (Poulos and Davis 1974). The strains and stresses due to the withdrawal of material inside a cavity are estimated with the stresses at infinity [3].

Elasticity solution. Chow (1994) used an elasticity solution to estimate settlement on shallow tunneling where the effect of the tunnel face is ignored, and the tunnel is assumed to have infinite length. The surface settlement of tunnel, S, is calculated as settlement relative to a distant point on the surface (Augard 1997):

$$S = \left(\gamma D^2 z^2\right) / \left\{8\mathrm{G}\left(\mathrm{x}^2 + \mathrm{z}^2\right)\right\} \tag{1}$$

where D is the tunnel's diameter, γ is the soil's unit weight, G is the shear modulus of soil, x is the horizontal distance from the center of the tunnel and z is the depth measured from the center of the tunnel. The elastic solution is also relevant for hard rock conditions.

Sagaseta's method. Sagaseta (1987) suggested a method to eliminate stresses from the equations and to work in terms of strain where the boundary condition is only in terms of displacement.

B. Empirical Solutions. The empirical solutions have been performed by several authors, such as Attewell and Woodman (1982), New and O'Reilly (1982, 1991),

etc. to predict the ground settlement induced by the bored tunnels for "green-field" site conditions. Peck (1969) described ground settlement based on data from more than 20 case histories.

In general practice, empirical solutions are most commonly used. These solutions are in many cases combined with analytical solutions or finite element computations, later calibrated with data from different case histories.

C. Numerical Solutions. Numerical solutions, mainly the finite element method (FEM), offer a flexible tool for predicting surface settlement. The finite element method could be performed in both two-dimensional plane (2D) and three-dimensional space (3D). New and Reilly (1991) estimated that the flexibility of FE models can assist in understanding the movements of the particular site by extending conventional design methods [1]. In short, the numerical solution (like FEM) is being used as a more reliable and powerful tool in computer technology. Numerical methods are not only applied for predicting ground settlement but for the entire design procedure of the tunnel, including excavation sequence, soil–tunnel lining interaction, consolidation etc.

2.2 Mathematical Background

The net volume of ground settlement trough is approximately equivalent to the volume loss (V_L) of the tunnel in most ground conditions. Volume loss (V_L) is generally expressed as a percentage ($V_L\%$) of the gross area of a finished tunnel. The magnitude of volume loss V_L is estimated based on case history data, site conditions and engineering appraisals. In the shield and EPB TBM tunneling method, V_L generally lies between 1% and 2% in a cohesive soil and 0.5–1% in a non-cohesive soil. The maximum surface settlement over the axis of tunnel S_{max} is expressed as:

$$S_{max} = 0.313V_L(\%)D^2/i \tag{2}$$

As per normal distribution curve (error function curve), theoretical surface settlement is expressed as:

$$S = S_{max}\exp\left(-x^2/2i^2\right) \tag{3}$$

where D is the equivalent excavation diameter of the tunnel, x is the transverse distance from the tunnel center and i is the width of the settlement trough which is the distance to the inflection point of the curve. Further, i can be calculated as a function of KZ_0, where Z_0 is tunnel axis depth and K is a dimensional constant that depends on soil type. Referring from various literature and study, the K value for loose to medium silty fine sand is generally considered as 0.3. The K values of 0.35 and 0.4 are generally considered for medium to dense silty sand and very stiff sandy clayey silt, respectively.

2.3 Numerical Analysis and Computational Method

A series of parametric studies for different ground conditions along with the different depths of the tunnel is carried out by developing a numerical model (FEM) compared to empirical/analytical solutions. The geotechnical software Phase2 (version: 8.009) and MIDAS GTX NX have been adopted which use the finite element method to calculate deformations and stresses. For all analyses, two-dimensional models have been applied using the Mohr–Coulomb criteria for ground and the elasticity theory for materials.

3 Model of the Study

A typical 6.3 m diameter circular tunnel section of the Delhi Metro Rail Corporation (DMRC) Dwarka–Najafgarh corridor has been considered for this study and analysis. The present section of the tunnel is located at Najafgarh area which has been constructed in DMRC Phase-III work. The double tube running tunnel has been excavated and supported by an earth pressure balanced tunnel boring machine (EPB-TBM). Ground conditions can be characterized according to one main stretch along the alignment, which coincides with the tunnel stretch within the project area. Geotechnical parameters which have been considered for the present study are presented in Table 1. Model view of the geotechnical profile from geotechnical software Phase2 (version: 8.009) and tunnel cross-section along with tunnel depth of 9.7 m is shown in Fig. 2.

Table 1 Depth-wise geotechnical parameters for tunnel stretch within the project area

Soil type	Depth m	SPT value (Avg.)	C′ (Avg.) kPa	Φ′ (Avg.)	Y (Avg.)	E′ (Avg.)	ν′ (Avg.)
				Deg	kN/m^3	kPa	
Filling material	0–1.5	10	–	26	18.0	10500	0.3
Loose to medium silty sand	1.5–7.5	15	–	28	19.0	21500	0.3
Medium to dense silty sand	7.5–10	36	–	30	19.0	36000	0.3
Very stiff sandy clayey silt	10–21	48	12	33	19.0	33600	0.3
Very dense silty sand	21–30	50	–	35	20.0	50000	0.3

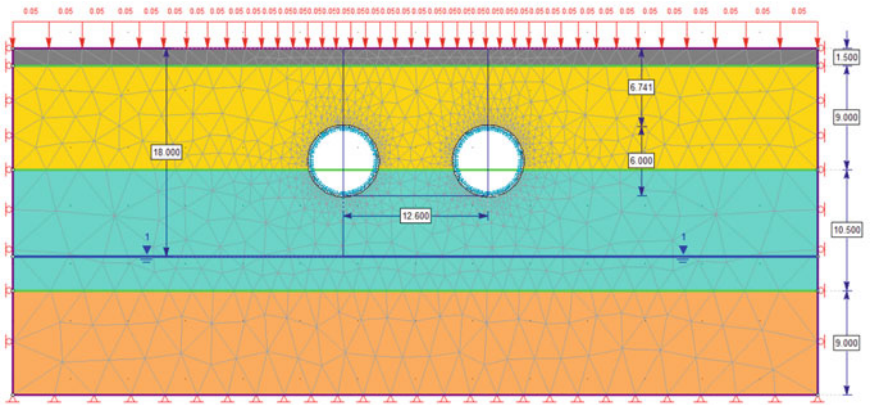

Fig. 2 Model view of geotechnical profile and tunnel cross-section along with tunnel depth of 9.7 m

The tunnel depth of the project area is not uniform. It varies from 9.7 m to 13.6 m depth below ground at different length sections of the project. Therefore, the surface settlement would vary due to change in tunnel depth as well as change in ground condition. An analytical method (elasticity solution) and empirical method have been proposed for estimating ground settlement at a depth of 9.7 m, 10.6 m, 12.8 m and 13.6 m. A two-dimensional numerical model (FEM) has been further developed with geotechnical software Phase2 for predicting ground settlement for tunnel depth of 9.7 m.

4 Presentation of Results

Surface settlement predicted by analytical method/elasticity solution with Eq. (1) for tunnel depth of 9.7 m, 10.6 m, 12.8 m and 13.6 m is shown in Fig. 3. Surface settlement predicted by empirical method with Eqs. (1) and (3) for tunnel depth of 9.7 m, 10.6 m, 12.8 m and 13.6 m is shown in Fig. 4. The ground settlement from geotechnical software Phase 2 (version: 8.009) for tunnel depth of 9.7 m is shown in Fig. 5.

The ground settlement results obtained from the predictive method have been further cross-checked with realistic ground settlement data recorded at the project site at Dwarka–Najafgarh corridor. A similarity in settlement behavior has been observed between results from the predictive settlement method with realistic ground settlement data recorded at the project site. Ground settlement at the project site during execution and post-construction has been recorded and monitored by ground settlement marker. Ground settlement data recorded at the project site for a similar location with a similar depth of tunnel (9.7 m from the ground) is shown in Fig. 6.

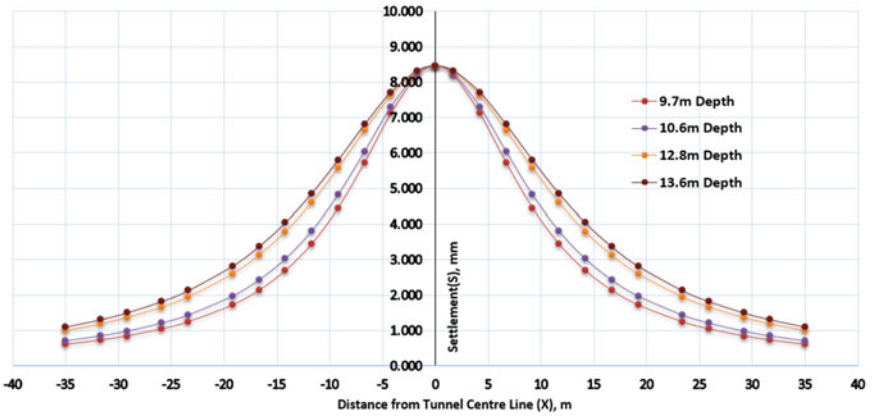

Fig. 3 Comparison of surface settlement predicted by analytical method (elasticity solution) for different tunnel depths

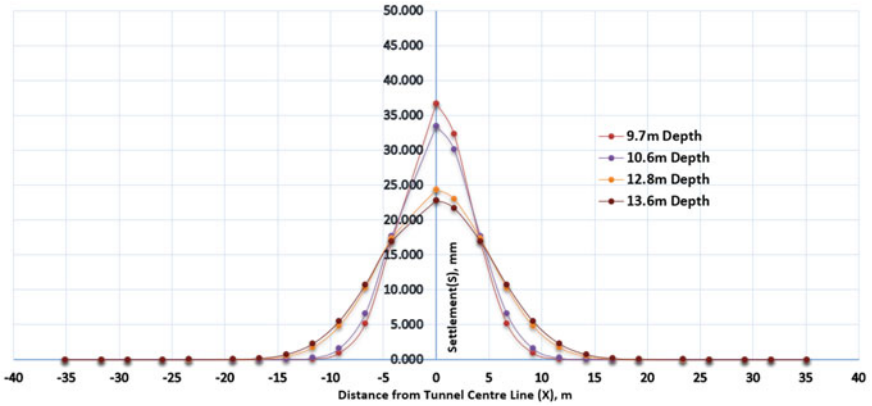

Fig. 4 Comparison of surface settlement predicted by empirical method for different tunnel depths

The present parametric study was initially conceptualized by comparing the ground settlement values obtained from different predictive methods along with realistic data recorded at the project site for a similar depth of tunnel on a similar ground condition. This study has been further elaborated for different tunnel depths (9.7 m, 10.6 m, 12.8 m and 13.6 m) with varying soil parameters, mostly from loose silty fine sand to medium dense silty sand and very stiff sandy clayey silt at different stretches of tunnel alignment of the study area at Najafgarh, Delhi. The entire investigation part of the parametric study has been conducted in 12 different cases for four different tunnel depths (9.7 m, 10.6 m, 12.8 m and 13.6 m) with three different ground conditions (loose to medium silty fine sand, medium to dense silty sand and very stiff sandy clayey silt). In the present investigation, along with conventional

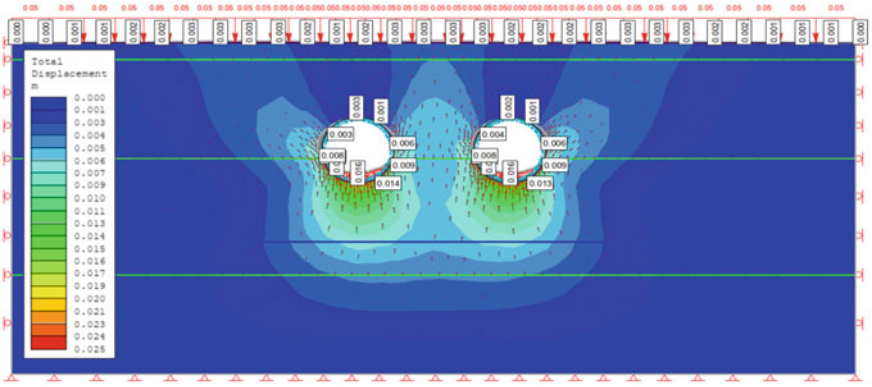

Fig. 5 Ground settlement from the numerical model (FEM) for tunnel depth of 9.7 m

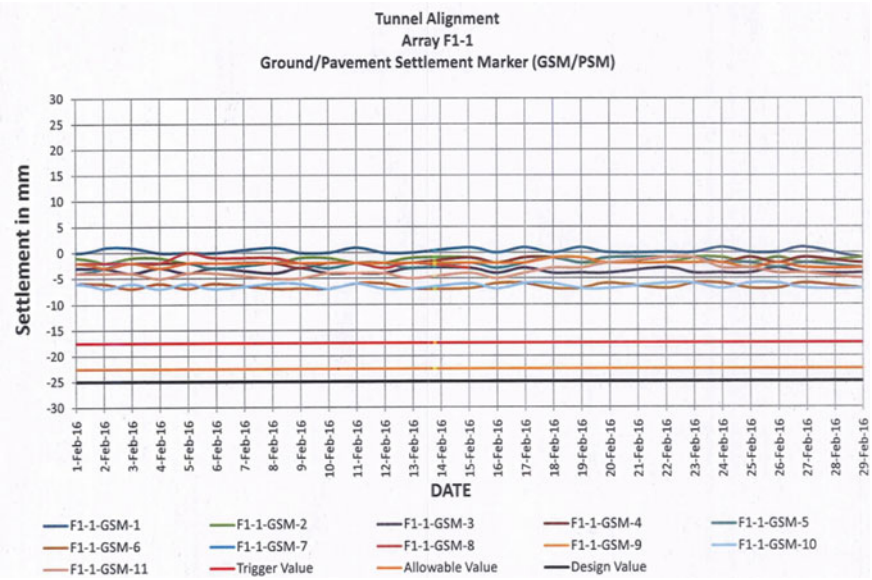

Fig. 6 Ground settlement data recorded at the project site

analytical and empirical methods, a set of numerical models has been further developed by FEM to identify the nonlinear behavior of tunnel depth, surrounding soil with the ground settlement. The ground settlement value obtained from the empirical method for 12 different situations of four different tunnel depths with three different ground conditions has been tabulated in Table 2.

Table 2 Surface settlement above the tunnel for different depths of a tunnel at different ground conditions

Depth of tunnel from the ground	Surface settlement above the tunnel at different ground conditions, mm		
	Loose to medium silty fine sand	Medium to dense silty sand	Very stiff sandy clayey silt
9.7 m	42.83	36.71	32.12
10.6 m	39.00	33.43	29.25
12.8 m	32.47	27.83	24.35
13.6 m	30.38	26.04	22.78

5 Discussions on Results

Based on the analyses done in the present study, an attempt has been made in this section to address the variation of ground settlement with varying ground conditions and tunnel depths, and also results obtained from different methods have been compared.

5.1 Surface Settlement for Different Tunnel Depths with the Same Ground Condition

Ground settlement for four different tunnel depths (9.7 m, 10.6 m, 12.8 m and 13.6 m) has been plotted for three different ground conditions (loose to medium silty fine sand, medium to dense silty sand and very stiff sandy clayey silt). Ground settlement for four different tunnel depths with the ground condition of *loose to medium silty fine sand* is shown in Fig. 7, *medium to dense silty sand* is shown in Fig. 8, and *very stiff sandy clayey silt* is shown in Fig. 9.

The results from the above-shown figures are clear that ground settlement gradually decreases with an increase in overburden pressure, and thereby the depth of the tunnel. It is observed from the above-shown figure that ground settlement value

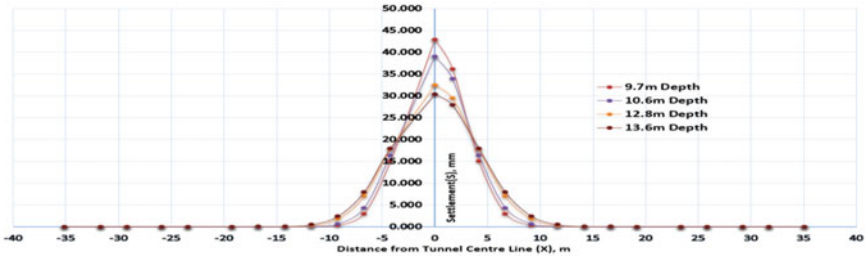

Fig. 7 Comparison of ground settlement for different tunnel depths at loose to medium silty fine sand

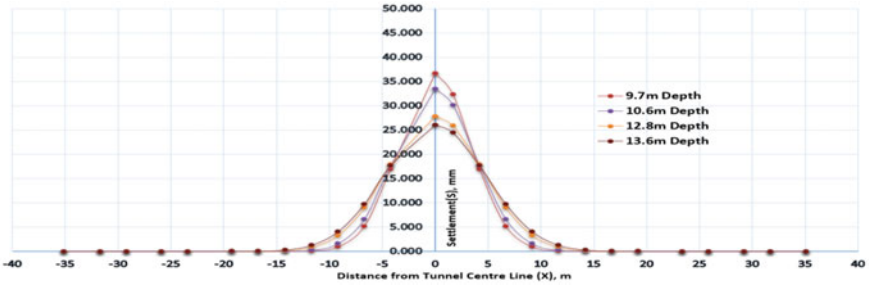

Fig. 8 Comparison of ground settlement for different tunnel depths at medium to dense silty sand

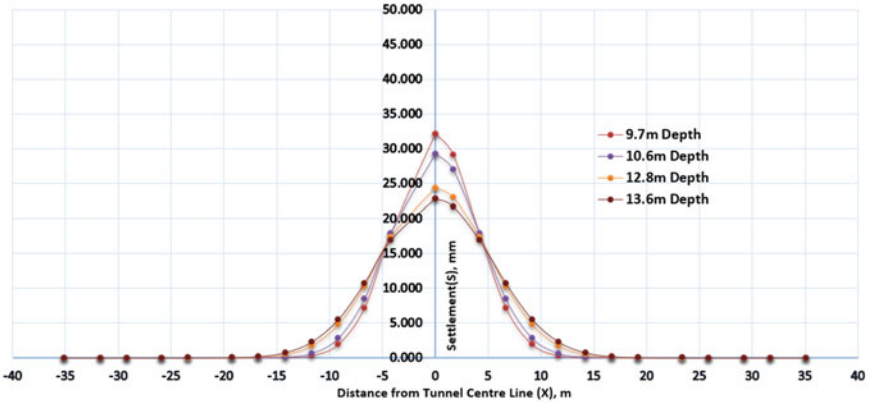

Fig. 9 Comparison of ground settlement for different tunnel depths at very stiff sandy clayey silt

decreases by 9%, 24% and 29% when overburden pressure as well as the depth of the tunnel increases by 10%, 32% and 41%, respectively, even when ground condition remains the same.

5.2 Surface Settlement for Same Tunnel Depth with Different Ground Conditions

Ground settlement for three different ground conditions (loose to medium silty fine sand, medium to dense silty sand and very stiff sandy clayey silt) has been further plotted for four different tunnel depths (9.7 m, 10.6 m, 12.8 m and 13.6 m). Ground settlements with three different ground conditions for 9.7 m tunnel depth are shown in Fig. 10, 10.6 m tunnel depth in Fig. 11, 12.8 m tunnel depth in Fig. 12 and 13.6 m tunnel depth in Fig. 13. Apart from the above empirical/analytical method, a set of

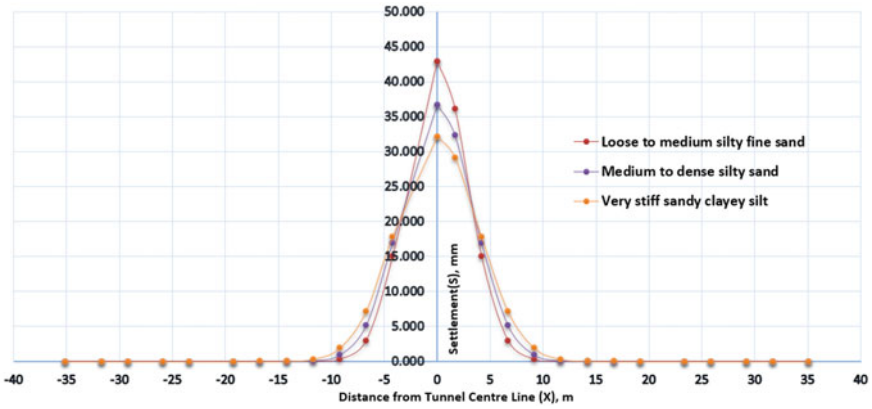

Fig. 10 Comparison of ground settlement for 9.7 m tunnel depth at three different ground conditions

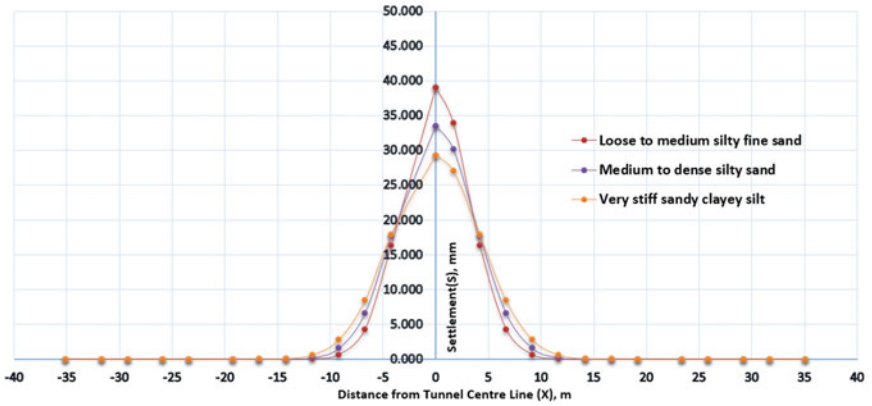

Fig. 11 Comparison of ground settlement for 10.6 m tunnel depth at three different ground

numerical models (FEM) analysis has been further performed for 9.7 m tunnel depth with two different ground conditions, i.e. silty fine sand and sandy clayey silt.

The results from the above-shown figures are clear that ground settlement gradually decreases with the change of soil layer from silty sand to clayey silt. It is observed that ground settlement value decreases by 14% when the ground condition is changed from the state of loose to medium silty fine sand to the state of medium to dense silty sand even at the same depth of the tunnel. Ground settlement value decreases by 25% when the ground condition is changed from the state of medium to dense silty sand to the state of very stiff sandy clayey silt, even when the ground condition remains the same.

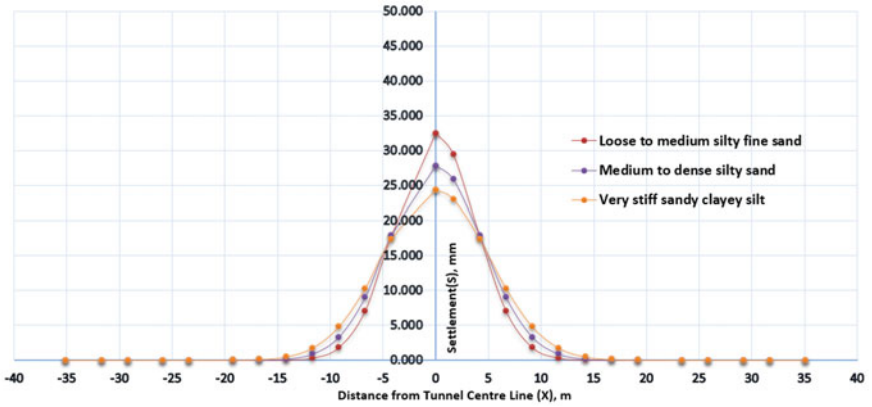

Fig. 12 Comparison of ground settlement for 12.8 m tunnel depth at three different ground conditions

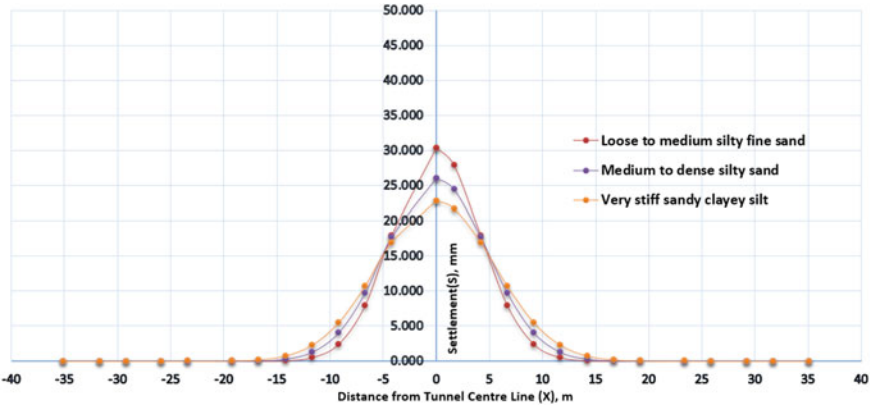

Fig. 13 Comparison of ground settlement for 13.6 m tunnel depth at three different ground conditions

Comparison of the ground settlement obtained from MIDAS GTX NX for 9.7 m tunnel depth at ground conditions of silty fine sand and sandy clayey silt is shown in Fig. 14.

From the above-shown figure of the numerical model is clear that surface settlement value decreases when the ground condition is changed from silty sand to the sandy clayey silt, even when the ground condition remains the same.

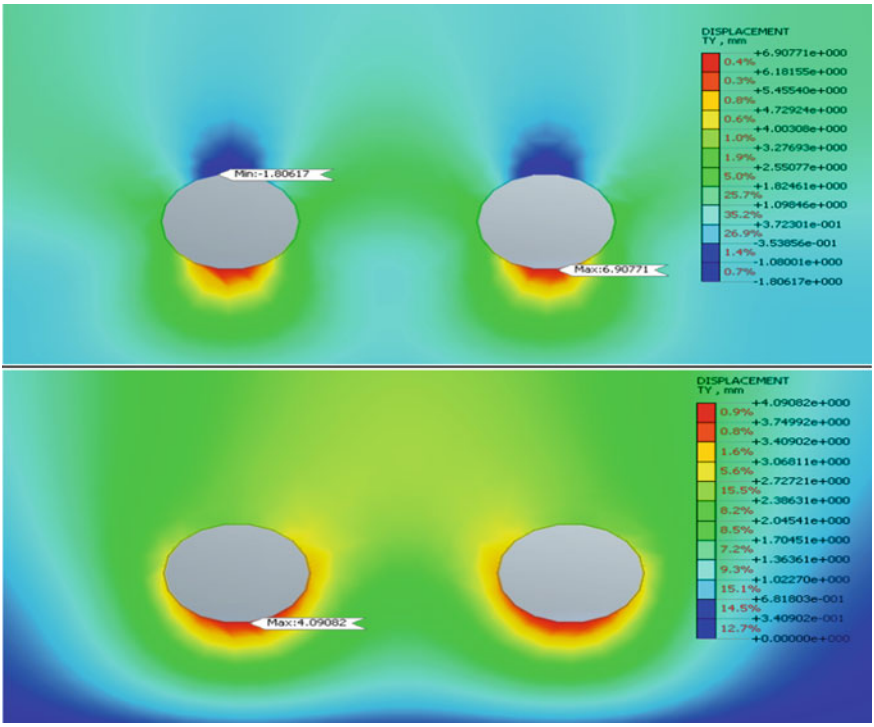

Fig. 14 Comparison of ground settlement from numerical models for 9.7 m tunnel depth at ground conditions of silty fine sand (top) and sandy clayey silt (bottom)

5.3 Comparison of Different Methods

After comparing ground settlement results from different predictive methods, i.e. analytical method (Fig. 3), empirical method (Fig. 4) and FEM method (Fig. 5) with actual settlement data recorded at the project site (Fig. 6), it is clear that surface settlement obtained from numerical models (FEM) gives more reliable results among all predictive method for obtaining surface settlement.

6 Conclusions

In the present study, the behavior of surface settlement above a tunnel placed on varying soil parameters at different depths has been studied by using analytical/empirical method and FE-based computer program. A series of parametric

studies has been further carried out to find out the interaction between soil and tunnel as well as to develop a relationship between tunnel-induced surface settlement with overburden pressure and soil parameters. The conclusions drawn from the current study and analysis are as follows:

1. Ground settlement results obtained from numerical models (FEM) are very close to actual ground settlement data recorded at the project site. Hence, it can be concluded that numerical models (FEM) give more reliable results among all other predictive methods for obtaining surface settlement. Analytical and empirical methods are suitable for preliminary estimations or assumptions.
2. The ground settlement varies with the variation of subsurface deposits and various depths of the tunnel. A shallow depth tunnel tends to have a relatively greater effect on the ground than the deeper one. Ground settlement decreases with the change of soil layer from silty sand to clayey silt.
3. The ground settlement gradually decreases with an increase in overburden pressure, i.e. depth of the tunnel. The ground settlement value reduces by 9–29% when overburden pressure as well as the depth of the tunnel increase by 10–41% even with the same ground condition. The ground settlement value decreases by 9%, 24% and 29% when overburden pressure as well as the depth of the tunnel increase by 10%, 32% and 41%, respectively, even when ground conditions remain the same.
4. With the change of ground conditions from silty sand to clayey silt, the ground settlement reduces significantly by 14–25%, even when the depth of the tunnel remains the same. When ground conditions are changed from the state of loose to medium silty fine sand to the state of medium to dense silty sand, ground settlement value reduces by 14% even at the same depth of the tunnel. When ground conditions are changed from the state of medium to dense silty sand to the state of very stiff sandy clayey silt, ground settlement value further reduces by 11%, even when the depth of the tunnel remains the same.

Acknowledgements The authors acknowledge the support from the entire team involved in the project of the Delhi Metro Rail Corporation Dwarka–Najafgarh corridor.

References

1. Moller, S.: Tunnel induced settlements and structural forces in linings. Mitteilung 54 des Instituts fur Geotechnik Herausgeber P.A. Vermeer (2006)
2. Leca, E.: Animateur Barry New, General Reporter: Settlements induced by tunneling in Soft Ground. Tunnelling and Underground Space Technology 22 (2007) 119–149, ITA/AITES Report (2006)
3. Fattah, M.Y., Shlash, K.T., Salim, N.M.: Settlement trough due to tunneling in cohesive ground. Indian Geotechn. J. **41**(2), 64–75 (2011)
4. Delhi Metro Railway Corporation, Technical Specification: DMRC Out line Design Specification for Underground Structure

5. Takahiro Aoyagi: Representing Settlement for Soft Ground Tunnelling. Massachusetts Institute of Technology (2005)
6. Toan, N.D.: TBM and Lining—Essential Interfaces. Politecnico di Torino, Turin, Italy (2006)

Seismic Analysis of Shallow Tunnels in Soil Medium

Abdullah Ansari, K. S. Rao, and A. K. Jain

1 Introduction

Natural disasters like earthquake and tsunamis have enough potential to affect the whole society and economical status of any nation [1]. Exponential growth in the population and infrastructure development in the last decade created the space problem on the Earth surface and pushed the human society to go underground [2, 3]. Most commonly constructed underground structures are tunnels, shafts and caverns. Tunnels are being constructed at an increasing rate in densely populated urban areas and metro cities to fulfill the expanding needs of space and passage. Tunnels may subjected to different types of dynamic loading conditions like impact load, blast load and seismic load. Tunnels constructed in earthquake prone areas must withstand both static load and seismic load. Sometimes, it becomes impossible to avoid construction of tunnels in the areas which have already suffered historical earthquakes in past due to infrastructural demand. There are strong probability of damage of these infrastructures, if not designed properly considering the seismic effects. Hence, a careful consideration of the seismic loading effect on the analysis, design, construction, operation and damage evaluation is of great importance. There are chances of damage of these infrastructures because of any kind of seismic activities in that area.

In the last decade, we have experienced several devastating earthquakes causing significant damages of tunnels in developed countries including China, Taiwan and

A. Ansari (✉) · K. S. Rao · A. K. Jain
Department of Civil Engineering, Indian Institute of Technology Delhi, New Delhi 110016, India
e-mail: cez188391@iitd.ac.in

K. S. Rao
e-mail: raoks@iitd.ac.in

A. K. Jain
e-mail: akjain@iitd.ac.in

C. N. V. Satyanarayana Reddy et al. (eds.), *Stability of Slopes and Underground Excavations*, Lecture Notes in Civil Engineering 185,
https://doi.org/10.1007/978-981-16-5601-9_29

Japan. The 1995 Hyogoken-Nambu earthquake in Kobe, Japan caused failure of underground Daikai station of railway tunnel of Kobe which shows that tunnels are vulnerable to seismic wave propagation if not designed properly. The combined effects of ground shaking and ground permanent deformation during the 1999 Kocaeli earthquake in Turkey caused collapse of the twin Bolu tunnel. Tunnel portals of Mizusawa tunnel and Longxi tunnel failed due to strong shaking during Chuetsu Earthquake (2004), Japan, and Wenchuan Earthquake (2008), China, respectively. From these historical events, it is clear that lack of understanding about the earthquake hazards in seismically vulnerable areas has increased the probability of failure of tunnel structures resulting into economical loss of the nation. Hence, the necessity has grown to study and evaluate the seismic hazard in earthquake prone areas and stability of tunnels to mitigate the damages of these infrastructures postured by such catastrophism.

To understand the seismic response of the tunnels, different approaches are adapted including closed form analytical solution, numerical modelling and physical modelling. To estimate the seismic internal forces of tunnels' linings, many researchers proposed the analytical solutions under certain assumptions and conditions, e.g. elastic response of the soil and the tunnel lining and simulation of seismic loading in quasi-static fashion. The analytical solutions are useful, relatively fast and easy to use for preliminary seismic design of tunnels. In the present study, analytical solutions suggested by Wang and Penzien were used to investigate the circular-shaped shallow tunnel located in earthquake prone area having soil media. For this purpose, classified soils including clay, silt, sand and gravel with different Poisson ratio and elastic modulus were considered. Effect of various soil parameters and maximum shear strain was evaluated using sensitivity analysis.

2 Tunnel Deformation Under Seismic Loading

It is assumed that tunnels can undergo three basic modes of deformation during seismic shaking: (1) longitudinal compression or extension; (2) longitudinal bending and (3) ovaling or racking. Type of deformation is decided depending on the mode in which seismic waves propagate, either longitudinal or transverse direction of the tunnel axis. Earthquake induced ground shaking along the longitudinal axis of a tunnel causes axial deformations and longitudinal bending, whereas for shaking in the transverse direction, the tunnel undergoes ovaling (for circular sections) or a combined racking-rocking distortion (for box-shaped sections), with racking prevailing [4] (Fig. 1).

The first seismic design basis for underground structures was proposed based on Newmark's pioneering work [5, 6]. The closed form solutions are based on slip between soil medium and tunnel. At the time, these solutions provided a very useful tool for practicing engineers to estimate the seismic behaviour of tunnels under ground shaking in both longitudinal and transversal directions. Free-field deformation approach was used to estimate the strains and curvature of the tunnel for ground

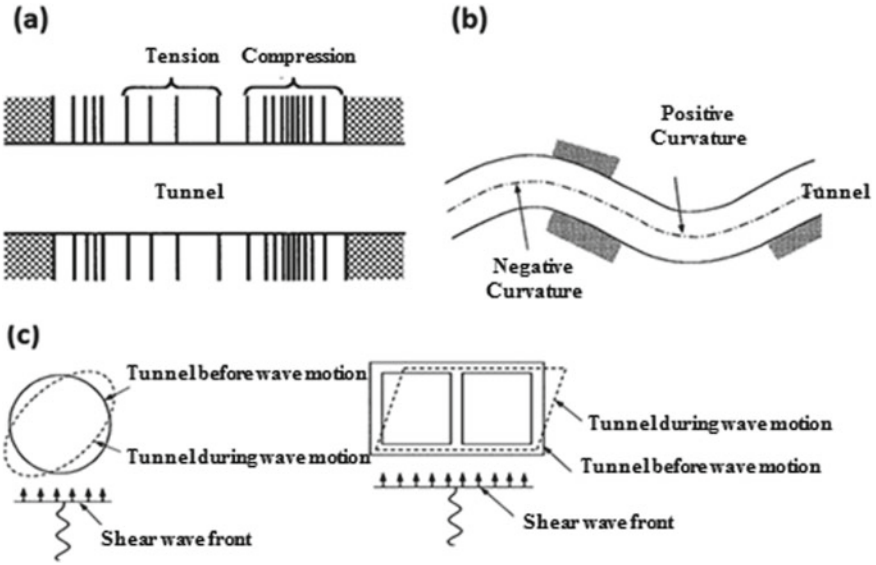

Fig. 1 Tunnel deformation: **a** axial compression and extension, **b** longitudinal bending, **c** Ovaling and racking [4]

motions propagating at an angle to the tunnel axis and furthermore proposed some modifications to account for soil-tunnel interaction effects. The soil-tunnel interaction effects examined and provided two solutions, one for full slip and another for no slip contact interface conditions [7]. Similar analytical solutions were developed for thrust, shear force and bending moment in the tunnel lining due to racking deformation [8]. Later, a complementary analytical procedure was provided for racking deformation evaluation of rectangular and circular tunnels [8]. For no slip condition, maximum thrust is much lower for Penzien's solution [9]. The response of tunnel lining depends on the factors like flexibility ratio and compressibility of the structure, and the in situ overburden pressure and coefficient of earth pressure (K_0) of soil at rest.

2.1 Wang's Analytical Solution

The closed form analytical solutions for the maximum thrust and bending moment in tunnel lining due to ovaling deformations due to earthquake loading were proposed for both full slip as well as no slip condition [7]. To calculate the maximum thrust (T_{max}) and moment (M_{max}) at the soil lining interface under seismic loading, following set of equations can be used, where $\frac{\Delta d}{d}$ represents the diametric strain.

$$\frac{\Delta d}{d} = \frac{\mp K_1 F}{3} \Upsilon_{max} \tag{1}$$

$$T_{max} = \mp \frac{K_1 E_m}{6(1+\nu_m)} r \Upsilon_{max} \tag{2}$$

$$M_{max} = \mp \frac{K_1 E_m}{6(1+\nu_m)} r^2 \tag{3}$$

$$K_1 = \frac{12(1-\nu_m)}{2F+5-6\nu_m)} \tag{4}$$

$$F = \frac{E_m\left(1-\nu_l^2\right)R^3}{6E_l I(1+\nu_m)} \tag{5}$$

$$C = \frac{E_m\left(1-\nu_l^2\right)r}{E_l t(1+\nu_m)(1-2\nu_m)} \tag{6}$$

where, E_m = modulus of elasticity of the soil medium; E_l = modulus of elasticity of the tunnel lining; I = moment of inertia of the tunnel lining (per unit width) for circular lining R; F = flexibility ratio; C = compressibility ratio; K_1 = full slip lining response coefficient; ν_m = Poisson's ratio of the soil medium; and ν_l = Poisson's ratio of the tunnel lining.

Full slip assumptions under simple shear may cause significant underestimation of the maximum thrust. Equation for maximum thrust for no slip assumption is given below:

$$T_{max} = \mp \frac{K_2 E_m}{2(1+\nu_m)} r \Upsilon_{max} \tag{7}$$

In the above equation, K_2 is no slip lining response coefficient, which can be estimated as follows.

$$K_2 = 1 + \frac{F\left[(1-2\nu_m) - (1-2\nu_m)C\right] - \frac{1}{2}(1-2\nu_m)^2 + 2}{F\left[(3-2\nu_m) + (1-2\nu_m)C\right] + C\left[\frac{5}{2} - 8\nu_m + 6\nu_m^2\right] + 6 - 8\nu_m} \tag{8}$$

2.2 Penzien's Analytical Solution

The closed form analytical solution was developed for racking deformation of rectangular-shaped tunnels [8]. An analytical solution to study deformation caused in circular- as well as rectangular-shaped tunnel was suggested for both no slip and full slip conditions under seismic loading [10]. The lining soil racking ratio can be calculated using below equation.

$$R^{n} = \frac{\mp 4(1-\nu_m)}{(\alpha_n + 1)} \tag{9}$$

$$\alpha_n = \frac{12E_lI(5-6\nu_m)}{d^3G_m\left(1-\nu_l^2\right)} \tag{10}$$

The analytical equations for thrust, bending moment and shear force in circular tunnel linings considering full slip condition under seismic activities is given below:

$$\mp \Delta d^{n}_{lining} = \mp R^{n} \Delta d_{free-field} \tag{11}$$

$$T(\theta) = -\frac{12E_lI\Delta d^{n}_{lining}}{d^3\left(1-v_l^2\right)}\cos 2\left(\theta + \frac{\pi}{4}\right) \tag{12}$$

$$M(\theta) = -\frac{6E_lI\Delta d^{n}_{lining}}{d^2\left(1-v_l^2\right)}\cos 2\left(\theta + \frac{\pi}{4}\right) \tag{13}$$

$$V(\theta) = -\frac{24E_lI\Delta d^{n}_{lining}}{d^3\left(1-v_l^2\right)}\sin 2\left(\theta + \frac{\pi}{4}\right) \tag{14}$$

For the case of no slip condition, the equations are presented as:

$$\mp \Delta d_{lining} = \mp R \Delta d_{free-field} \tag{15}$$

$$T(\theta) = -\frac{24E_lI\Delta d_{lining}}{d^3\left(1-v_l^2\right)}\cos 2\left(\theta + \frac{\pi}{4}\right) \tag{16}$$

$$M(\theta) = -\frac{6E_lI\Delta d_{lining}}{d^2\left(1-v_l^2\right)}\cos 2\left(\theta + \frac{\pi}{4}\right) \tag{17}$$

$$V(\theta) = -\frac{24E_lI\Delta d_{lining}}{d^3\left(1-v_l^2\right)}\sin 2\left(\theta + \frac{\pi}{4}\right) \tag{18}$$

Mathematical expression to calculate R and α is mentioned here.

$$R = \frac{\mp 4(1-v_m)}{(\alpha + 1)} \tag{19}$$

$$\alpha = \frac{24E_lI(3-4\nu_m)}{d^3G_m\left(1-\nu_l^2\right)} \tag{20}$$

3 Result of Analytical Solutions

Jammu and Kashmir region in northern part of India shows active seismic activities falling in Zone IV and V [11]. A reference tunnel in Jammu region is considered having 20 m depth from ground surface and 8 m diameter. Earthquake parameters are $M_w = 7.5$ and $a_{max} = 0.4$ g. Source to site distance is 120 km. To study the effect of soil strength parameters on shear force, thrust and bending moment, different soil models are considered having different values of modulus of elasticity and Poisson ratio. Different types of soils like clay, sand and gravel are considered, where Poisson ratio

Table 1 Earthquake and soil parameters for classified soil models

Soil type	Model		a_{max} (g)	C_m (m/s)	V_S (m/s)	γ_m (kN/m^3)	ν_m	E_m (kPa)
Very soft clay	S1		0.25	180	0.45	17	0.45	159732
Soft clay	S2		0.3	200	0.54	17.5	0.425	199500
Medium clay	S3		0.325	230	0.58	18	0.4	266616
Hard clay	S4	Upper	0.35	250	0.63	18.5	0.375	317968.8
Dense sand	S5	Limit	0.35	290	0.64	19.2	0.325	427900.8
Sand and gravel	S6		0.375	310	0.67	19.8	0.3	494722.8
Dense sand and gravel	S7		0.4	330	0.73	20	0.275	555390
Highly dense sand	S8		0.45	350	0.81	20.5	0.25	627812.5
Very soft clay	S1		0.2	170	0.36	16	0.45	134096
Soft clay	S2		0.25	190	0.43	16.5	0.425	169760.3
Medium clay	S3		0.275	210	0.49	17	0.4	209916
Hard clay	S4	Lower	0.3	230	0.54	17.5	0.35	249952.5
Dense sand	S5	Limit	0.325	250	0.58	18	0.3	292500
Sand and gravel	S6		0.35	270	0.63	18.5	0.275	343905.8
Dense sand and gravel	S7		0.375	290	0.67	19	0.25	399475
Highly dense sand	S8		0.4	300	0.72	19.5	0.2	421200

Table 2 Results of analytical solution based on Wang and Penzien methods

Method		Wang 1993			Penzien 2000				
Model		T_W (kN)	M_W (kN.m)	σ_W (kPa)	T_P (kN)	M_P (kN.m)	V_P (kN)	σ_P (kPa)	F
S1		29.98	119.94	7921.68	29.98	119.93	59.96	7921.69	19.16
S2		34.17	136.64	9012.11	34.17	136.63	68.23	9027.03	24.35
S3		33.95	135.11	8967.23	33.95	135.77	67.14	8967.89	33.12
S4	Upper	36.55	146.14	9655.31	35.03	140.81	70.21	9300.62	40.22
S5	Limit	34.18	136.71	9029.68	33.00	131.98	65.94	8718.53	56.17
S6		35.95	140.21	9402.78	34.40	137.62	68.33	9088.61	66.19
S7		36.11	147.32	9767.72	35.77	143.10	71.52	9451.27	75.75
S8		41.84	167.54	11066.07	39.33	157.74	78.67	10391.92	87.35
S1		25.13	100.50	6638.27	25.13	100.55	50.22	6638.63	16.08
S2		29.72	118.89	7852.54	29.72	118.89	59.45	7852.54	30.71
S3		31.15	124.56	8226.73	31.15	124.55	62.28	8226.98	26.07
S4	Lower	33.76	135.02	8918.27	33.75	135.03	67.52	8918.29	32.2
S5	Limit	36.38	145.52	9610.33	36.38	145.50	72.76	9610.39	39.14
S6		37.76	151.02	9974.92	37.75	151.02	75.51	9974.92	46.91
S7		39.12	156.48	10335.51	39.12	156.48	78.23	10335.59	55.58
S8		40.04	172.17	11371.58	43.04	172.17	86.09	112371.6	61.04

ranges between 0.2 and 0.45, and modulus of elasticity varies between 16000 kPa and 700000 kPa. Maximum value of shear strain was 0.0023 which is an average value of all types of soil model considered for investigation. Table 1 summarizes the earthquake and soil data considered for different models ranging from very soft clay to highly dense sand.

The calculated values of thrust, bending moment and shear force using Wang and Penzien methods are shown in the following Table 2 for both upper and lower limits. It can be observed that the magnitude of error increases with increasing soil stiffness for both the methods having flexibility ratio less than 20. The error would be less than 6% for soft clay to hard sand and can be called acceptable. The conservative results are given for hard soils or soil with a flexibility ratio (F) greater than 4. The ΔT and ΔM are the magnitude of error between Wang and Penzien solution for thrust and bending moment, where subscript W-P refers to Wang and Penzien method. To compare the errors for different methods and flexibility ratio (F), the results are demonstrated in the following Fig. 2 (Table 3).

The maximum shear strain depends on shear wave velocity, which in turn is dependent on two strength parameters; modulus of elasticity (E) and Poisson ratio (ν). Due to the value change of modulus of elasticity (E) and Poisson ratio (ν), shear modulus (G), maximum shear strain (γ_{max}) and C_m will also change. Maximum acceleration during earthquake activities at the ground level assumed 0.4 g which can be estimated based on soil layer strata. As shown in Fig. 2, maximum shear strain (γ_{max}) increases with increasing modulus of elasticity (E) during starting phases. Later, it becomes constant for higher values of modulus of elasticity. Variation of thrust force using Wang's method and shear force and bending moment using Penzien's method are presented in the following Fig. 3.

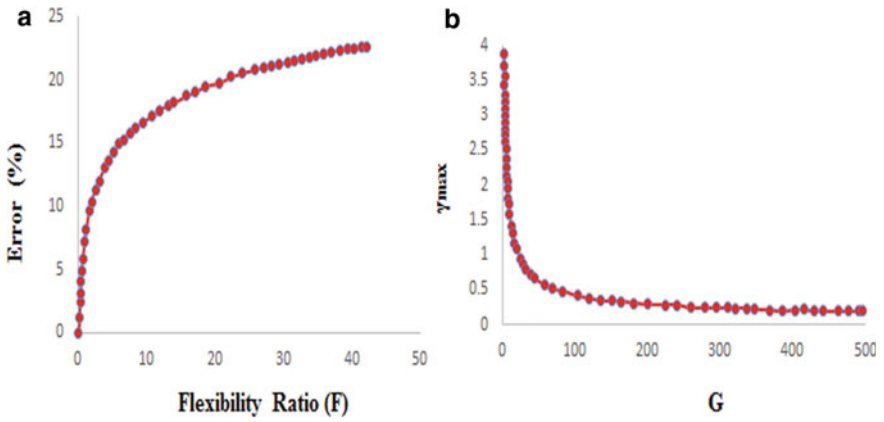

Fig. 2 **a** Variation of error between Wang and Penzien methods versus flexibility ratio; **b** Variation of maximum shear strain with shear modulus

Table 3 Error between Wang and Penzien methods

Soil Type	Model	$\Delta T_{W\text{-}P}$ (%)	$\Delta M_{W\text{-}P}$ (%)	F_{avg}
Very soft clay	S1	1.47	5.61	17.51
Soft clay	S2	2.16	5.13	27.34
Medium clay	S3	1.87	4.14	29.31
Hard clay	S4	0.91	3.64	36.46
Dense sand	S5	1.84	4.36	47.5
Sand and gravel	S6	1.93	4.53	56.11
Dense sand and gravel	S7	2.91	4.38	65.14
Highly dense sand	S8	1.87	4.45	71.19

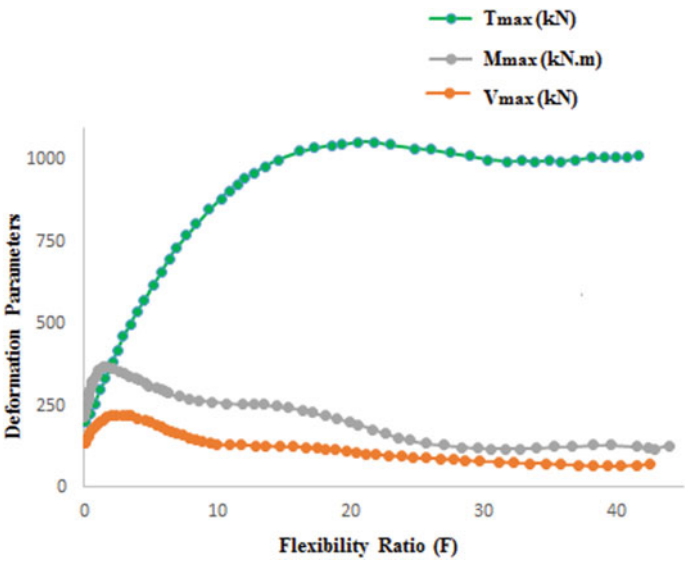

Fig. 3 Variation of deformation parameters with flexibility ratio

4 Conclusions

Tunnels constructed in a seismically active area are subjected to dynamic loading in terms of seismic forces. Tunnels can undergo different forms of deformation depending on the nature in which seismic waves propagate in soil medium. Basically, two modes of oval deformation are defined viz. full slippage and no slippage depending on the surficial behaviour. In this study, analytical solutions given by Wang and Penzien are compared to understand the seismic response of tunnel lining considering different soil media. Sensitivity analysis suggested that soil stiffness has direct effect on the magnitude of error between these two methods. For hard soils, conservative results are achieved in both methods. Analytical solutions are not useful

to estimate shear strain distribution, due to which maximum shear strain can be evaluated based on real-time seismic history. Deformation parameters including thrust and bending moment are dependent on flexibility ratio. For the safe design of tunnel lining when tunnels are subjected to earthquake loading, stress distribution must be considered for analysis and design.

References

1. Ansari, A., Satake, K., Malik, J.N.: Modelling the 2004 Indian Ocean Tsunami to estimate tsunami heights and its amplitude and to study its effects on coastal areas. ERI Earthquake Conference, University of Tokyo, Japan (2017)
2. Ansari, A., Rao, K.S., Jain, A.K.: Seismic hazard and risk assessment in Maharashtra: a critical review. In: Sitharam T.G., Kolathayar S., Sharma M.L. (eds.) Seismic Hazards and Risk. Lecture Notes in Civil Engineering, vol. 116, pp. 35–45. Springer, Singapore (2021). https://doi.org/10.1007/978-981-15-9976-7_4
3. Ameen, A. A. M. M.: Modeling the 2004 Andaman-Sumatra tsunami and historical tsunamis from Andaman and Nicobar Island: towards estimation of tsunami hazard along the adjoining areas of Indian Ocean. M.Tech., thesis, Indian Institute of Technology Kanpur, India (2018)
4. Owen, G.N., Scholl, R.E.: Earthquake engineering of large underground structures. Report No. FHWA/RD-80/195, Federal Highway Administration and NationalScience Foundation, 279 (1981)
5. Newmark, N.M.: Problems in wave propagation in soil and rock. In: Proceedings of International Symposium on Wave Propagation and Dynamic Properties of Earth Materials, New Mexico, University of New Mexico Press (1968)
6. St. John, C.M., Zahrah, T.F.: A seismic design of underground structures. Tunn. Undergr. Space Technol. **2**(2), 165–197 (1987)
7. Wang, J.N.: Seismic Design of Tunnels, A State-of-the-Art Approach. Monograph 7, Parsons Brickerhoff Quade and Douglas, Inc., New York (1993)
8. Penzien, J., Wu, C.: Stresses in linings of bored tunnels. Earthq. Eng. Struct. Dyn. **27**, 283–300 (1998)
9. Hashash, Y.M.A., Hook, J.J., Schmidt, B., Yao, J.I.C.: Seismic design and analysis of underground structures. Tunn. Underground Space Technol. **16**(2), 247–293 (2001)
10. Penzien, J.: Seismically induced racking of tunnel linings. Earthquake Eng. Struct. Dyn. **29**, 683–691 (2000)
11. BIS:1893.: Indian standard criteria for earthquake resistant design of structures, Part 1—General provisions and buildings, Bureau of Indian Standards, New Delhi, India (2002)

Development of Rational Method of Design of Soil Nailing System in Granular Soil

M. Nagalakshmi and C. N. V. Satyanarayana Reddy

1 Introduction

In urban areas, construction of multi-storied and high-rise structures with cellar and subcellar floors is necessitating for soil retention in nearly vertical excavation to ensure the stability of neighbouring structures and prevent soil slides from excavated surface into construction area for the safety of working personnel. Also, excavated steep slopes for constructions in hilly areas require soil retention. Soil nailing technique is being extensively used for stabilizing slopes and vertical cuts in deep excavations. Other methods of soil retention, namely, secant piles, contiguous piles, diaphragm wall are expensive while sheet piles are not readily available and have the limitations on driving of sheet piles in boulder strata. Relatively easier installation of nails makes the technique more advantageous over other reinforcing techniques.

The concept of soil nailing has originated from New Australian tunnel method where metallic rods with anchorages are used to support excavation in rocks during construction of a tunnel. Soil nailing is defined as the technique of reinforcing in-situ soil by a regular arrangement of closely spaced metal rods [1, 2]. The major components of a soil nail wall are the in-situ soil, reinforcing elements and facing. The nails are installed down the slope/excavation at regular intervals with an inclination of 10^0–15^0. Different types of nails such as driven, grouted, jet grouted, encapsulated corrosion protection nails, hollow bars [2] (FHWA) are used based on the site conditions. The nailed wall derives resistance from soil–nail interaction due to ground movement which results in the mobilization of tensile forces in the nailed wall. The potential failure mechanisms such as pull out failure, tension failure, shear, bending

M. Nagalakshmi (✉) · C. N. V. S. Reddy
Department of Civil Engineering, Andhra University College of Engineering, Visakhapatnam, India

C. N. V. S. Reddy
e-mail: prof.cnvsreddy@andhrauniversity.edu.in

C. N. V. Satyanarayana Reddy et al. (eds.), *Stability of Slopes and Underground Excavations*, Lecture Notes in Civil Engineering 185,
https://doi.org/10.1007/978-981-16-5601-9_30

and facing failure have been observed in a soil nailed wall. However, the effect of bending and shear strengths is considerably less (<10% [3]) on the overall stability of the nailed wall. The forces acting on the critical slip surface are to be computed to assess the safety of a soil nail wall. The critical slip surface may be circular or a two-wedge surface based on the type of soil, i.e. for soils with little cohesion, both slip circle and two-part wedge are nearly equivalent, whereas for soils with medium or high cohesion, circular slip surface is the least safe failure mechanism [4]. Different graphical and analytical methods are proposed for designing nailed wall based on limit state equilibrium (Gassler method, Davis method, FHWA, BS 8006, HA 68). With the gaining popularity for the soil nailing walls, there is need for development of simplified rational design methods.

The potential failure slip surface of nailed wall falls within the range of 0.3–0.4H at the top (Fig. 1) which confirms that it is similar to the failure slip surface of reinforced earth wall, i.e. the tensile force distribution is similar to that of reinforced earth wall (Clouterre 1991) [5]. Hence in the present study, concept of reinforced earth is adopted in designing soil nailed wall. Soil nailed walls for retaining granular soil of varying heights (4.5, 6, 8 and 10 m) are designed based on Gassler method and compared with the design details obtained from proposed design methodology under study.

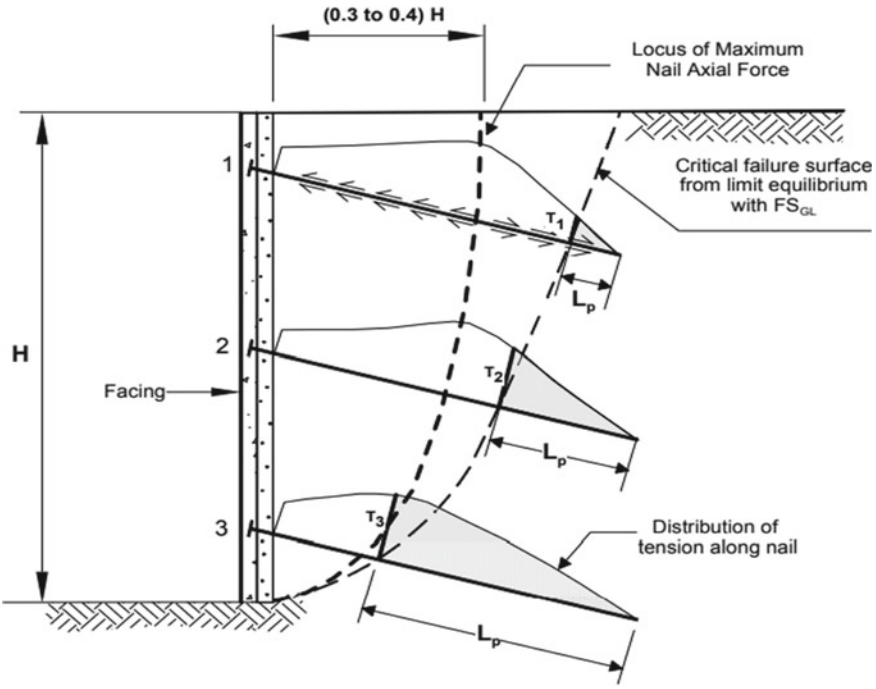

Fig.1 Behaviour of soil nail [8]

2 Methodology

2.1 Gassler Method

Gassler [4] developed design charts for nailed walls with varying slopes (α) and inclinations of end of nails (ρ) bearing different surcharge loads (q_d) in granular soils using partial safety factors based on Eurocodes. The method considers only reinforcement tensile forces. Pull out resistance is the major stabilizing force for which a partial factor of 1.3 was used in this method.

For a given geometry and soil properties, preliminary design of soil nail wall is carried out using Gassler's charts. Specific nailing density (μ) obtained from these charts is used to determine horizontal spacing using the following equation.

$$\mu = \frac{T}{\gamma \cdot S_v \cdot S_h} \tag{1}$$

where,

T= factored pullout force

S_v and S_h are vertical and horizontal spacings, respectively.

The design details obtained from charts are verified by considering equilibrium of polygon of forces acting on the critical failure wedge (two-wedge slip surface for granular soils). The design is safe if driving forces are less than or equal to resisting forces. The safety of wall against tension and pullout is verified.

2.2 Proposed Method for Design of Driven Nails System

It is proposed to consider soil nailed soil similar to reinforced earth wall as soil nailed soil system behaves as coherent gravity system by itself and helps in supporting the neighbouring soil. Hence, it is proposed to use the concept of coherent gravity method used in internal stability of reinforced earth walls for design of nailed soil system. The two-wedge failure surface of coherent gravity method nearly fits the failure surface pattern of soil nailed walls. Soil nailing systems are to be used only if soil has minimum cohesive strength of 7kN/m^2 to ensure stability of soil in excavation surface until facing is formed. The presence of cohesion in soil reduces the tension induced in nails. So, while adopting the coherent gravity method of analysis, Bell's (1915) equation is used for calculation of active earth pressure computation. The details of design coherent gravity structure are described below.

Coherent Gravity structure [6, 7]

Coherent gravity method derived from the monitored behaviour of various structures is used to verify the internal stability of reinforced earth wall in cohesionless soils.

The method considers a two-wedge failure plane in which the maximum tensile force falls within the range of 0.3 H at the top (Fig. 2). The variation of earth pressure coefficient is shown in Fig. 3. The factors of safety against tension and pull out failures are computed using the following equations.

1. Tension/rupture failure mechanism: The induced tensile force (T) at each reinforcement level is calculated as

$$T = K \sigma_{vj} S_v S_h \tag{2}$$

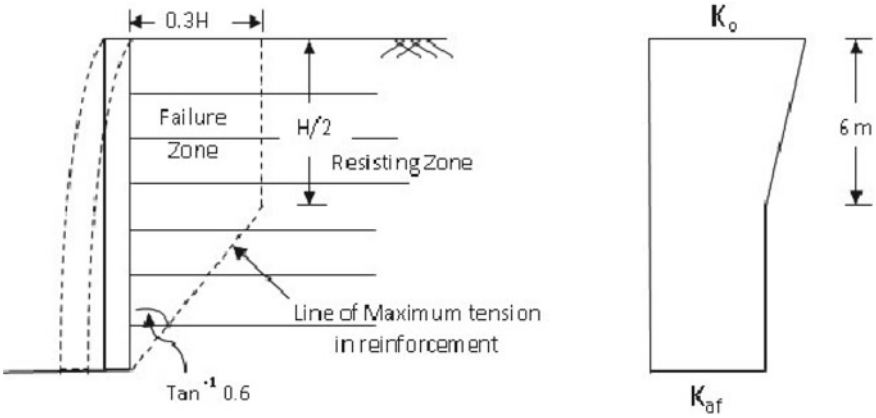

Fig.2 Line of maximum tension in reinforced earth wall

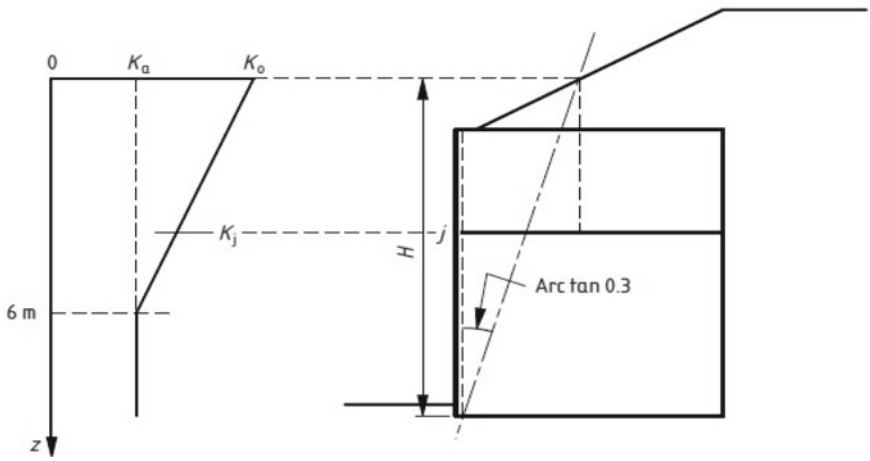

Fig. 3 Variation of earth pressure coefficient along the length of wall in coherent gravity method

$$\text{Factor of safety against tension} = T_f/T \tag{3}$$

where,
K= coefficient of earth pressure
σ_{vj} = vertical stress at selected reinforcement level
S_v and S_h are vertical and horizontal spacings, respectively
T_f = Ultimate tensile strength of nail

2. Pull out failure mechanism: Pullout resistance force (F) at each reinforcement level is calculated as

$$F = \gamma\, h_j \pi d L_e \tan\delta \tag{4}$$

$$\text{Factor of safety against Pull out} = F/T$$

where,
d=diameter of bar
L_e=length of the nail beyond failure zone

In the present proposed design methodology, the effect of cohesion of soil is considered in determination of induced tensile force in nail as given in Eq. 5

$$T = \left(K\sigma_{vj} - 2c\sqrt{k}\right) S_v \cdot S_h \tag{5}$$

FHWA [7] recommended minimum factors of safety for design of soil nailed walls for temporary and permanent excavations in static and seismic conditions given in Table 1 used in the proposed design based on coherent gravity analysis for pull out and tension failures.

Since the soil nail wall behaves similar to the reinforced earth wall, the design details obtained from Gassler's method are checked for safety against tension and pullout failures using the above equations.

Table 1 Minimum recommended factors of safety in pull out and tension failures of nails

Failure mechanism	Temporary walls		Permanent walls	
	Static	Seismic	Static	Seismic
Pull out failure	2.0	1.5	2.0	1.5
Tension failure	1.8	1.35	1.8	1.35

3 Design of Soil Nailing Walls

The properties of soil considered for the study are presented in Table 2. Based on gradation and plasticity characteristics, the soil is classified as SM-SC as per IS 1498–1970. Soil nailed walls of heights 4.5, 6, 8 and 10 m inclined at 10^0 with the vertical by considering the walls as temporary with no surcharge for driven nails inclined at 10^0 with horizontal and adopting L/H ratio of 0.6 are designed for supporting soil in excavations based on Gassler's method and the details are presented in Table 3. The pullout resistance is reduced by a factor of 1.3 and tensile strength is reduced

Table 2 Engineering properties of soil under study

Property	Value
Specific gravity grain size distribution	2.63
a. Gravel (%)	0
b. Sand (%)	84
e. Fines (%)	16
Plasticity characteristics	
a. Liquid limit	23
b. Plastic limit	18
c. Plasticity index I_p	5
IS classification compaction characteristics	SM-SC
a. Optimum moisture content (%)	6.8
b. Maximum dry density (kN/m^3)	18.0
Effective shear parameters	
a. Cohesion (kN/m^2)	8
b. Angle of internal friction	31^0

Table 3 Design details of soil nail walls obtained from Gassler's method

Parameter	Height of wall			
	4.5 m	6.0 m	8.0 m	10 m
Length of nails (m)	2.7	3.6	4.8	6
Inclination of end of nails	0	0	0	0
Grade of steel (Mpa)	415	415	415	415
Diameter of nail (mm)	25	25	25	25
Vertical spacing (m)	0.5	0.5	0.5	0.5
Horizontal spacing (m)	0.5	0.5	0.5	0.5
Factored pull out force (kN/m)	5.72	10.5	19	30
Max. Tensile force (kN)	9.7	25	72	126
Tensile strength (kN)	177	177	177	177
Global factor of safety	1.43	1.35	1.35	1.36

Table 4 Design details of soil nail walls obtained from coherent gravity method

Parameter	Height of wall			
	4.5 m	6.0 m	8.0 m	10 m
Length of nails (m)	**5.1**	**5.8**	**6.7**	**7.5**
Grade of steel (MPa)	415	415	415	**415**
Diameter of nail (mm)	**25**	**25**	**25**	**25**
Vertical spacing (m)	0.5	0.5	0.5	**0.5**
Horizontal spacing (m)	**0.5**	**0.5**	**0.5**	**0.5**
Max. Tensile force (kN)	**6.54**	**10.36**	**16.38**	**23.34**
Tensile strength (kN)	**203**	**203**	**203**	**203**
Factor of safety against pull out	**2.0**	**2.0**	**2.0**	**2.0**

by a factor of 1.15. The two-wedge critical slip surface required for design of soil nail walls using Gassler's method is computed either by trial and error method or by using a computer programme. In the present study, the critical slip surface is obtained from GEO 5 software. For a given geometry and soil profile, nailed wall model is created in GEO5, and the analysis is performed using partial factors of safety given by Eurocode. The induced tensile forces computed by considering equilibrium of critical failure wedge are also reported in Table 3.

The soil nailed walls designed based on coherent gravity analysis are presented in Table 4. Pull out resistance forces are computed at each reinforcement level for all heights of nailed walls under study, and the minimum obtained value factor of safety against pull out is reported.

Gassler design charts are given for L/H = 0.6 only. Further, Gassler considered that the soil behind the rectangular wedge only exerts lateral earth pressure, and the lateral earth pressure is computed based on Coulomb's theory. However, Rankine earth pressure theory [11] is more appropriate in flexible soil nailed wall in granular soil. From Table 4, the proposed design method based on coherent gravity analysis, it is observed that the L/H ratios of soil nailed walls vary between 0.75 and 1.13. It is observed that the L/H ratios of soil nailed walls decrease with increase in height.

4 Conclusions

The following conclusions are drawn from this study:

1. The geometry of nailed walls obtained from Gassler's method fails in mobilizing sufficient pullout resistance as recommended in coherent gravity method. Hence, longer nails are required than those obtained from Gassler's method to maintain minimum recommended factor of safety of 2 against pullout failure.

2. For a given soil, the length of nail obtained from coherent gravity method varies in between 0.75H and 1.2H for different heights of soil retention, whereas it varies in between 0.6H and 0.7.H in conventional design methods.
3. The value of L/H decreases with increase in height of the nailed wall in a given soil. However, driven nails are not preferred for supporting permanent structures of greater heights due to lower values of mobilized pullout resistance forces.

References

1. Gassler, G., Gudehus, G.: Soil nailing-some aspects of a new technique. In: Proceedings of 10th International Conference Soil Mechanics and Foundation Engineering, vol.3. Stockholm, pp. 665–670 (1981)
2. Juran, I.: Nailed-soil retaining structures: design and practice. In: Proceedings of Transportation Research Record, vol. 1119. Transportation Research Board, Washington D.C., USA, pp. 139–150 (1987)
3. Elias, V., Juran, I.: Soil nailing for stabilization of highway slopes and excavations. In: Publication FHWA-RD-89-198, Federal Highway Administration, Washington D.C., USA (1991)
4. Gassler, G.: Design of reinforced excavations and natural slopes using new European Codes. In: Keynote Lecture, International Symposium on Earth Reinforcement (IS Kyushu'96), Fukoka, Japan (1996)
5. Byrne, R.J., Cotton D., Porterfield, J., Wolschalag, C., Ueblacker, G.: Soil manual for design and construction of soil nail wall. In: Manual of Highway Administration Division No. FHWA0-SA-96-069R (1998)
6. AASTHO: Standard Specifications for Highway Bridges, 16th addition American association of State Highway and Transportation officials. Washington D.C, USA (1996)
7. BS 8006–1:2010: Code of Practice for Strengthened/Reinforced Soils and other Fills
8. FHWA 2003: Soil Nail Walls, Geotechnical Engineering Circular No.7, Report No. FHWA0-IF-03-017, Federal Highway Administration
9. Bell, A.L.: The lateral pressure and resistance of clay and the supporting power of clay foundations. In: Minutes Proceedings of Institution of Civil Engineers, vol. 199. IEEE, pp. 233–272 (1915)
10. IS: 2720, Methods of Test for Soils
11. Rankine, W.J.M.: On the stability of loose earth, vol. 147. In: Philosophical Transactions of the Royal Society of London, pp. 9–27 (1857)

Numerical Analysis on Interaction of Single Pile Tunnel System

Arnab Choudhury and Awdhesh Kumar Choudhary

1 Introduction

With rapid urbanization and economical development, heavy traffic congestions have become a problem for city planners and administrators. Due to scarcity of land, expansions of roads are also not possible for most of the urban areas. Underground rapid transport system came as a solution of above-mentioned problem. In rapid transit system, alignment of a proper tunnel path is a complex work. To avoid the interaction of foundation of several civil engineering structures, alignment of tunnel path is done through major roads, but problem arises when roads take a 90-degree sharp bend. Tunnel alignment has to take a curve turn towards a new road. At that time tunnel is bound to interact with pile foundation of high-rise building. Due to tunneling operation, ground movement takes place. Pile transfers its load to soil and presence of tunnel may disturb the load carrying mechanism of pile leading to the failure of structures. For these reasons, the position of tunnel with respect to pile is an important aspect which needs to be considered by practicing engineers for the better safety and serviceability of the structures.

In this regard, several researches have been carried out to get a better understanding on tunnel induced ground settlement and tunnel induced pile behaviour. Based on several experimental and numerical studies, it is found that maximum induced surface settlement occurred at the centre of tunnel and it decreases with increase in horizontal distance from tunnel centre Mair and Taylor [1–6]. It is also observed that single tunnel induced ground settlement can be represented by Gaussian distribution curve. Tunnel excavation also causes pile head settlement or reduction in pile load carrying

A. Choudhury (✉) · A. K. Choudhary
NIT Jamshedpur, Jamshedpur, India
e-mail: lncs@springer.com

A. K. Choudhary
e-mail: awdhesh.ce@nitjsr.ac.in

C. N. V. Satyanarayana Reddy et al. (eds.), *Stability of Slopes and Underground Excavations*, Lecture Notes in Civil Engineering 185,
https://doi.org/10.1007/978-981-16-5601-9_31

capacity like surface settlement in Greenfield condition. Bezuijen and Schrier [7] concluded from their studies that pile head settlement can be significant when tunnel pile distance is less than the tunnel diameter. It is also found that tunnel induced pile behaviour depends on tunnel position with respect to pile [1, 5, 8, 9]. Therefore, extensive study is required to investigate the insight behaviour of pile due to the construction of single tunnel for various tunnel pile configuration.

In view of this, present study aims to investigate the change in induced pile behaviour for different positions of single tunnel respect to pile through a series of numerical analysis in sand. The influence of several parameters such as single tunnel induced surface settlement at Greenfield condition, tunnel induced pile behaviour for different position of the tunnel on the overall behaviour of pile tunnel system are reported and discussed in this study.

2 Methodology

2.1 Numerical Studies

The objective of present study was achieved by performing numerical analysis using FLAC 2D software package. This is two-dimensional explicit finite difference program used to solve various complex geotechnical problem and complex boundary condition. Highly nonlinear and irreversible response of soil and rock can be analysed with the help of several constitutive models which are default in FLAC. A typical layout of FLAC 2D model with the details of loading and the boundary conditions are shown in Fig. 1, where L_P is the length of pile and Z_T is the depth of tunnel from soil surface. S is denoting the horizontal spacing in between pile toe and centre of tunnel.

2.2 Finite Element Mesh and Boundary Condition

The finite difference model for tunnel pile system used in this study is presented in Fig. 2. The dimensions of model used in this study were sufficiently large to minimize boundary effects in the numerical simulation. Besides, it is also observed that increase in number of grids beyond 50×50 did not influence computed results. For applying, boundary condition on the model, roller and pin supports were installed along the vertical sides and bottom sides of the mesh. So that, the horizontal movement for vertical boundaries and both horizontal as well as vertical movements for bottom boundaries were restrained. The elastic perfectly plastic Mohr–Coulomb model is used to model soil profile. Predefined structural elements, pile and liner are used to simulate pile and tunnel lining behaviour in this study. Pile has installed just middle

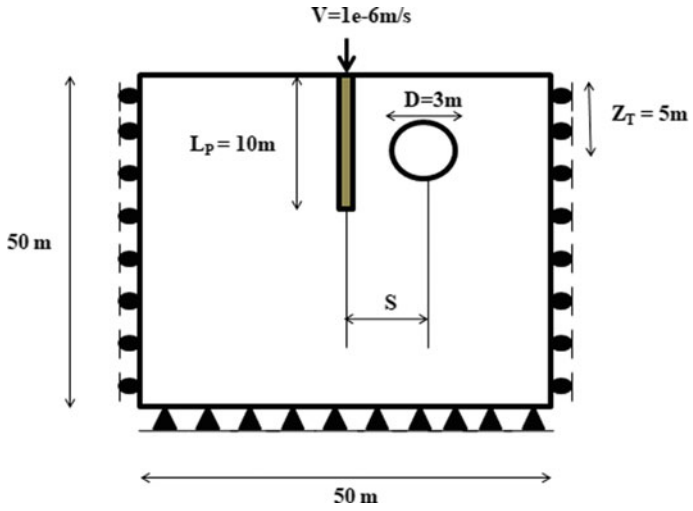

Fig. 1 Configuration of typical numerical model for case of $Z_T/L_P = 0.5$ (elevation view)

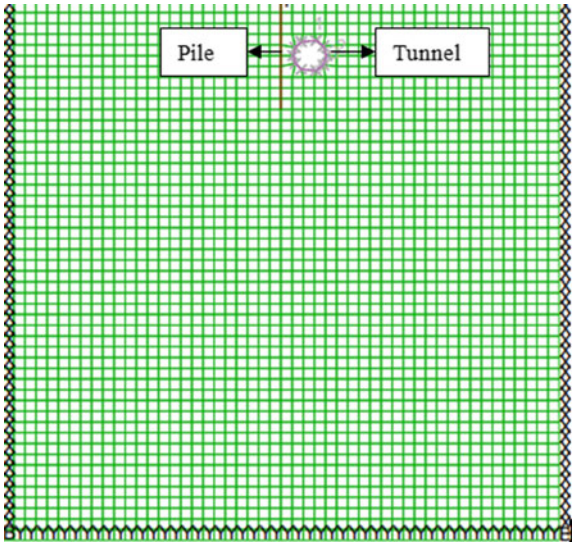

Fig. 2 Finite difference grids and boundary conditions of numerical model of $Z_T/L_P = 0.5$

of the model. The interaction between pile and soil has been controlled by shear and normal coupling spring of pile elements which were already designed in FLAC 2D software package. At a specified distance from pile, tunnel of 3 m diameter is simulated by excavating grids of initial model. This excavation is done using null commands. Liner elements are installed to simulate adequate tunnel support system. Tunnel is placed at 5 m depth from the top of the surface. As per requirement of study, tunnel position has varied vertically with respect to pile. As per requirement

Table 1 Parameters used in present study

Sl no	Properties	Value
1	Sand bulk modulus (Pa)	74e6
2	Sand shear modulus (Pa)	24.6e6
3	Friction angle (degree)	25°
4	Density (Kg/m^3)	1541
5	Stiffness of pile material (Pa)	2e11
6	Stiffness of liner material (Pa)	4e10

of study, tunnel has positioned at centre level of pipe and at the bottom of the pile consequently. Parameters used in present study are summarized in Table 1.

Mair and Taylor [6] reported typical volume loss up to 1% for sand when earth pressure balance shield is used for tunnel excavation. Based on this recommendation, tunnel volume loss of 1% is considered for present study.

Total five numerical models are simulated to represent Greenfield condition and various tunnel pile configurations as per requirement of present study. Single tunnel induced ground movement is investigated using Greenfield numerical model. Two different tunnel positions with respect to pile are simulated in tunnel pile system and represented by Z_T/L_P ratio (i.e., Z_T/L_P—0.5, 1). Tunnel induced pile behaviour is analysed for every Z_T/L_P ratio.

3 Results and Discussions

3.1 Validation of Numerical Model

Initially, it is necessary to compare computed numerical results with experimental results to verify the accuracy of the proposed numerical model. For this, load displacement response of single pile reported by Malhotra et al. [10] has been considered. The model dimensions and the properties of the material were adopted same as the experimental model. The comparison between load displacement response of pile obtained from present numerical model and experimental results reported by Malhotra et al. [10] is presented in Fig. 3. In general, it has been observed that a numerical results holds good agreement with experimental results. However, a little discrepancy between two results exits. This is probably due to the small error occurred while obtaining the soil properties in laboratory. Hence it can be said that the present numerical model can be used to simulate the pile behaviour in sandy soil conveniently. Subsequently, this model has been extended to study the tunnel pile interaction behaviour in details, which is presented in the following section.

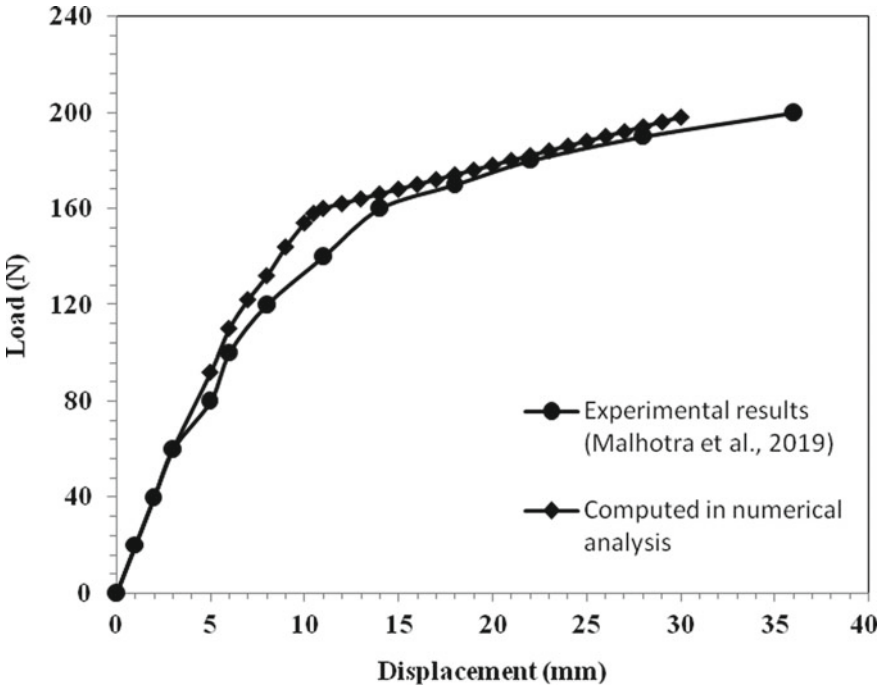

Fig. 3 Comparisons between experimental and numerical results

3.2 Ground Surface Settlement Due to Tunneling in Greenfield Condition

Tunnel excavation causes stress relaxation around a tunnel which leads to ground movement or surface settlement. Surface settlement profile due to single tunnel excavation is investigated in present study and presented in Fig. 4. It is seen that the maximum surface settlement of 0.58% of D (i.e., 17 mm) occurred at the centreline of the tunnel for C/D ratio of 1.2. Lu et al. [11] have reported similar behaviour through experimental analysis as well. The maximum settlement observed from centrifuge test for C/D ratio of 1.5 at centre line of the tunnel is about 0.5% of D [11]. Thus surface settlement data observed from present numerical analysis holds good agreement with experimental results as reported by Lu et al. [11]. Besides, the surface settlement curve due to tunnelling at Greenfield condition can be represented by Gaussian distribution curve. This curve was proposed by Peck [4]. Ground surface settlement S according to Peck [4] can be obtained using following equation.

$$S(x) = S_{max}\, exp\left(-x^{-2}/2i^2\right)$$

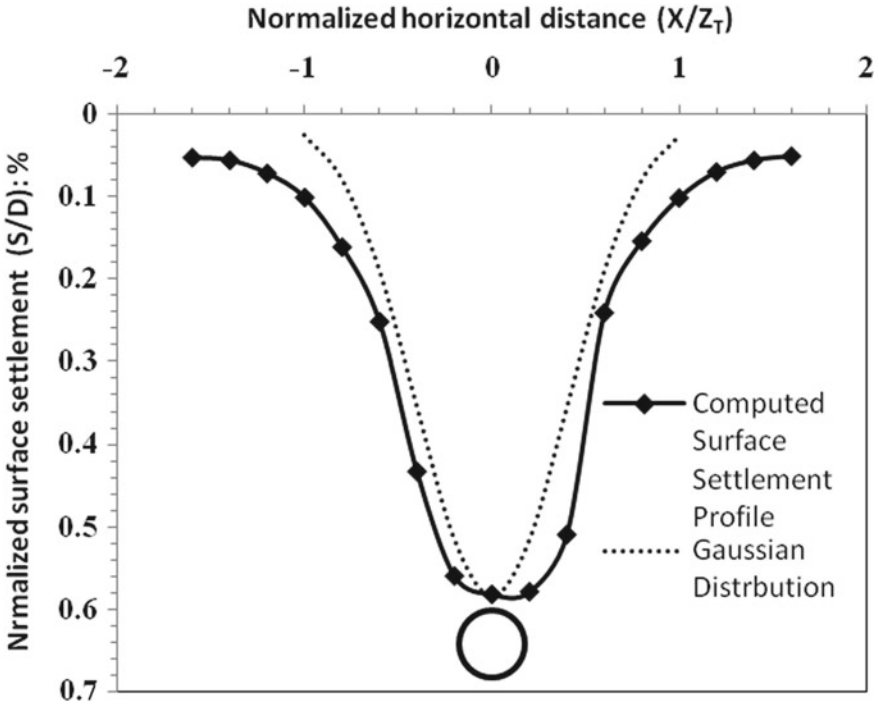

Fig. 4 Ground surface settlement due to single tunnel excavation at greenfield condition

where S_{max} represents the maximum ground surface settlement and i represent the distance between tunnel centreline to point of inflexion point. The value of i for present case is 2.25 m. Accordingly O'Reilly and New [3], i can be represented by KZ_T, where Z_T represents the depth of tunnel centre. The value of Z_T in present case is 5 m. Besides, width parameter K value can be obtained using following equation.

$$K = i/Z_T \text{or} K = 2.25/5 = 0.45$$

According Mair and Taylor [6], the typical value of K should be in between 0.25–0.45. Hence, the obtained K value for the present case is found to be 0.45, which is in the range.

3.3 Reduction in Ultimate Load Bearing Capacity of Pile Due to Tunnel

Figure 5 shows load displacement curves of pile before and after tunnelling when tunnel placed near the centre depth of pile (i.e., Z_T/L_P ratio 0.5). The ultimate load of

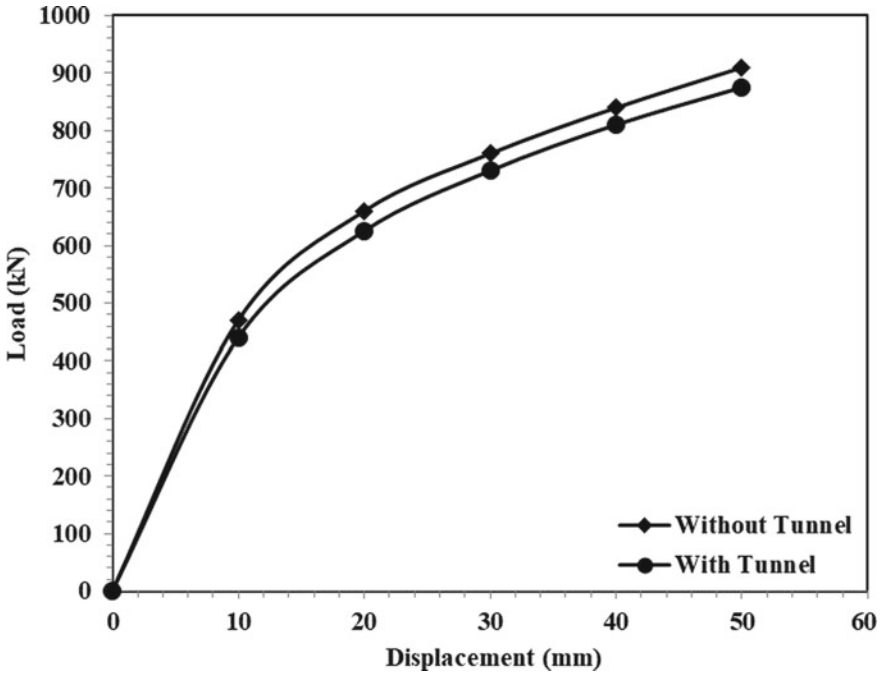

Fig. 5 Load displacement curve of pile: $Z_T/L_P = 0.5$

pile is obtained from load displacement response using double tangent method before and after tunnel excavations. Change in ultimate load bearing capacity of 3.07% is found at Z_T/L_P ratio 0.5. Similar observation on change in ultimate bearing capacity (i.e., change in bearing capacity = 4% at Z_T/L_P ratio 0.5) is also reported from by Malhotra et al. [10]. This is because the tunnel excavation causes stress reduction near the centre of the pile when tunnel is placed at Z_T/L_P ratio 0.5.

Vertical displacement contour of pile before and after tunnel excavation is shown in Figs. 6 and 7. The pattern of displacement contour without tunnel found to be similar in both side of pile (Fig. 6). However, the pattern of vertical displacement contour of pile after tunnel excavation found to be distorted on the right side of pile due to the tunnel excavation. Similar type of vertical displacement pattern has been reported by Malhotra et al. [10].

It is seen that higher load reduction of 6.92% is observed at Z_T/L_P ratio 1 which is presented in Fig. 8. This is because the tunnel excavation causes reduction in shaft resistance at lower portion of pile. Extra load due to decrement in shaft resistance transfers to the pile toe. To support this extra load, the end bearing resistance gets mobilized [9]. Consequently, a clear increment in vertical displacement near pile toe is found in vertical displacement contour of tunnel pile system (shown in Fig. 9). Change in vertical displacement contour is also found to be minimum at upper portion of pile which signifies lesser effect on upper portion of pile.

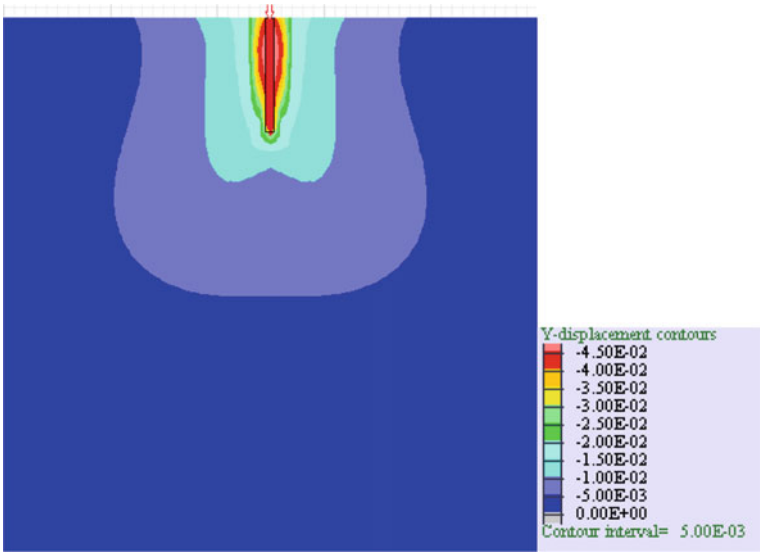

Fig. 6 Vertical displacement contour of pile without tunnel

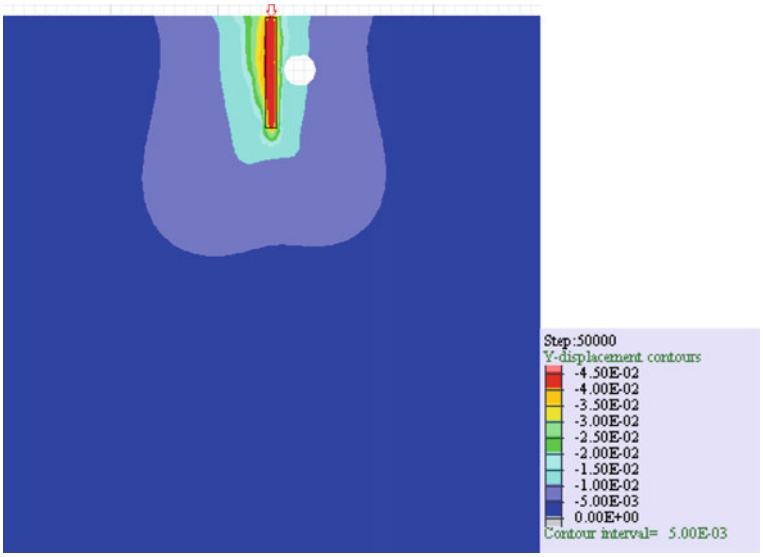

Fig. 7 Vertical displacement contour of pile with tunnel: $Z_T/L_P = 0.5$

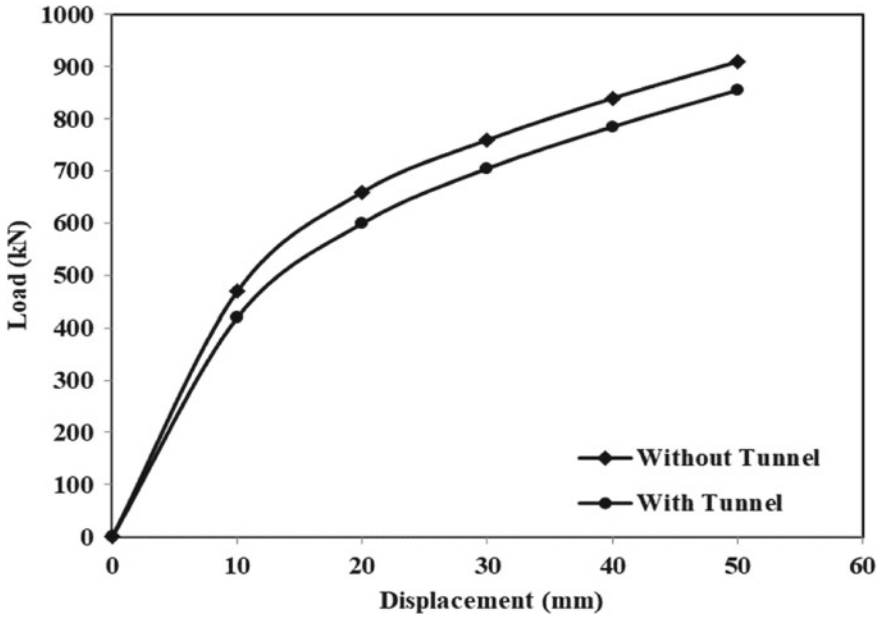

Fig. 8 Load displacement curve of pile: $Z_T/L_P = 1.0$

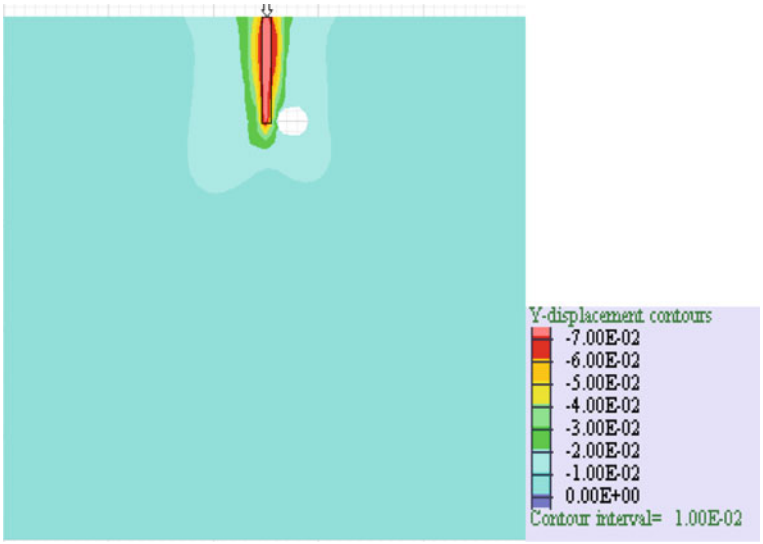

Fig. 9 Vertical displacement contour of pile with tunnel: $Z_T/L_P = 1$

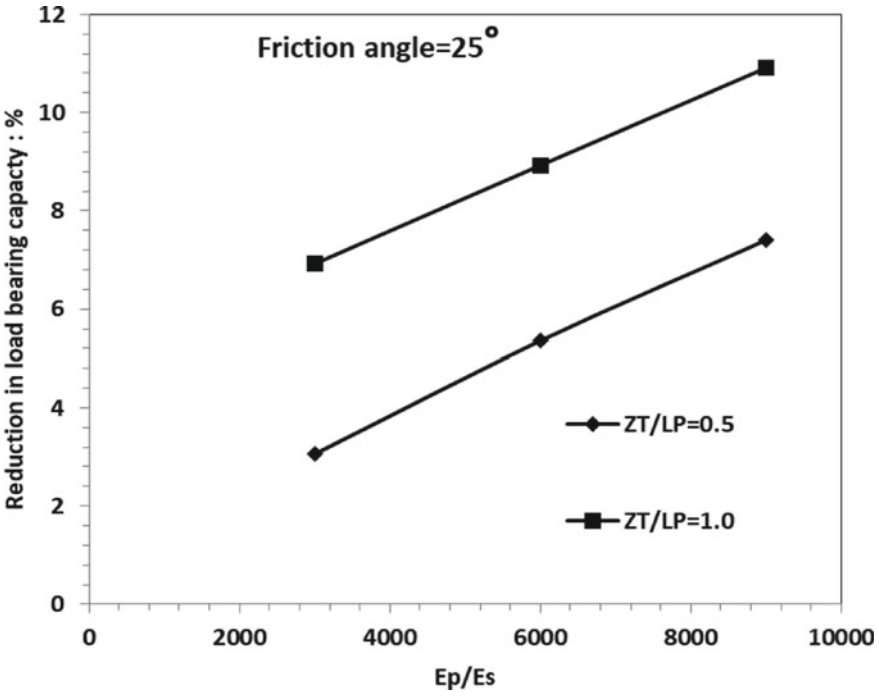

Fig. 10 Reduction in pile capacity with increasing Ep/Es ratio: friction angle = 25°

3.4 Parametric Study

Parametric study has been carried out to investigate the influence of sand stiffness and friction angle on the overall behaviour of pile-tunnel system. Figure 10 shows the reduction in load bearing capacity of pile for decreasing value of sand stiffness for every tunnel position when friction angle kept fixed at 25°. The change in load bearing capacity is calculated for two different sand stiffness values for every tunnel pile configuration (i.e., $Z_T/L_P = 0.5, 1$). Sand stiffness has been varied in terms of E_P/E_S ratio (i.e., $E_P/E_S = 3000, 6000, 9000$). E_p represents the elastic modulus of pile material, and E_S represents the elastic modulus of sand. It is observed from Fig. 10 that the reduction of load carrying capacity increases with increasing E_P/E_S ratio. This is because of more stress reduction around a tunnel due to decrease in sand stiffness which leads to more detrimental effect for low stiffness sand. For this reason, maximum reduction of load carrying capacity is found to be 7.2% when E_P/E_S ratio is 9000. The similar type analysis is also performed for friction angle 30, 35 and 40°. The relation in between pile behaviour and sand stiffness is found to be the same for all given values of friction angle which is presented in Fig. 10. It can be seen that the reduction in load bearing capacity due to tunnel excavation decreases with increase in friction angle of soil. This indicates that the stability of tunnel-pile system higher for greater friction angle of soil mass.

4 Conclusions

1. Surface settlement ground and load bearing capacity of pile is greatly influenced by the excavation of tunnel all around the pile.
2. Tunnelling induced surface settlement trough can be represented by Gaussian distribution curve. After single tunnel excavation, maximum surface settlement of 0.56% (i.e., 17 mm) is occurred at the centreline of the tunnel, and it decreases with the horizontal distance from tunnel centre.
3. Reduction in bearing capacity due to single tunnel excavation is maximum when tunnel placed at the adjacent to the pile toe (i.e., $Z_T/L_P = 1$). This reduction is found to be about 3.07% for $Z_T/L_P = 0.5$ and 6.92% for Z_T/L_P ratio 1.
4. Influence of sand stiffness and friction angle on tunnel induced behaviours of pile is analysed in this study. It is observed that reduction of load carrying capacity increases with decreasing vales of sand stiffness at a given friction angle of sand. Reduction in load carrying capacity increases from 3.07% to 7.41% with decrease in sand stiffness from 6.66–2.22 MPa at Z_T/L_P ratio 0.5 for friction angle of 25°. This observation indicates more detrimental effect for low stiffness sand. This is a result of more stress reduction around a tunnel due to decrease in sand stiffness.
5. Similar behaviours are also performed for higher values of friction angle (i.e., 30°, 35°, and 40°).

References

1. Loganathan, N., Poulos, H.G., Stewart, D.P.: Centrifuge model testing of tunnelling induced ground and pile deformations. Geotechnique **50**(3), 283–294 (2000)
2. Mair, R.J., Taylor, R.N., Bracegirdle, A.: Subsurface settlement profiles above tunnels in clay. Geotechnique **43**(2), 315–320 (1993)
3. O'Reilly, M. P., & New, B. M.: Settlements above tunnels in the United Kingdom-their magnitude and prediction. In Proceedings of the conference tunnelling, pp. 173 – 181. IMM London (1982)
4. Peck, R. B.: Deep excavation and tunnelling in soft ground. In Proceedings of the 7th international conference on soil mechanics and foundation engineering, pp. 225–90. Mexico (1969)
5. Soomro, M.A., Ng, C.W.W., Liu, K., Memon, N.A.: Pile responses to side-by-side twin tunnelling in stiff clay: effects of different tunnel depths relative to pile. Comput. Geotech. **84**, 101-116S (2017)
6. Mair, R.j., Taylor, R.N.: Bored Tunnelling in the urban environment. In Proc. 14th Int. Conf. SMFE, Hamburg, Vol. 4 (1977)
7. Bezuijen, A., Schrier, J.S.: The influence of a bored tunnel on pile foundations. Centrifuge 94, pp. 681–686, Singapore (1994)
8. Jacobsz, S.W., Standing, J.R., Mair, R.J., Hagiwara, T., Sugiyama, T.: Centrifuge modeling of tunnelling near driven piles. Soils and Foundation **44**, 49–56 (2004)
9. Ng, W.W.C., Lu, H., Peng, Y.S.: Three-dimensional centrifuge modelling of the effects of twin tunnelling on an existing pile. Tunnelling and Underground Space Technology (2013)

10. Malhotra, M., Sahu, V., Srivastava, A., Misra, K.A.: Impact of pile foundations adjacent to tunnels in sandy stratum. Sadhana **44**, 184 (2019)
11. Lu, H., Shi, J., Wang, Y., Wang R.: Centrifuge modeling of tunnelling-induced ground surface settlement in sand. Underground Space (2019)